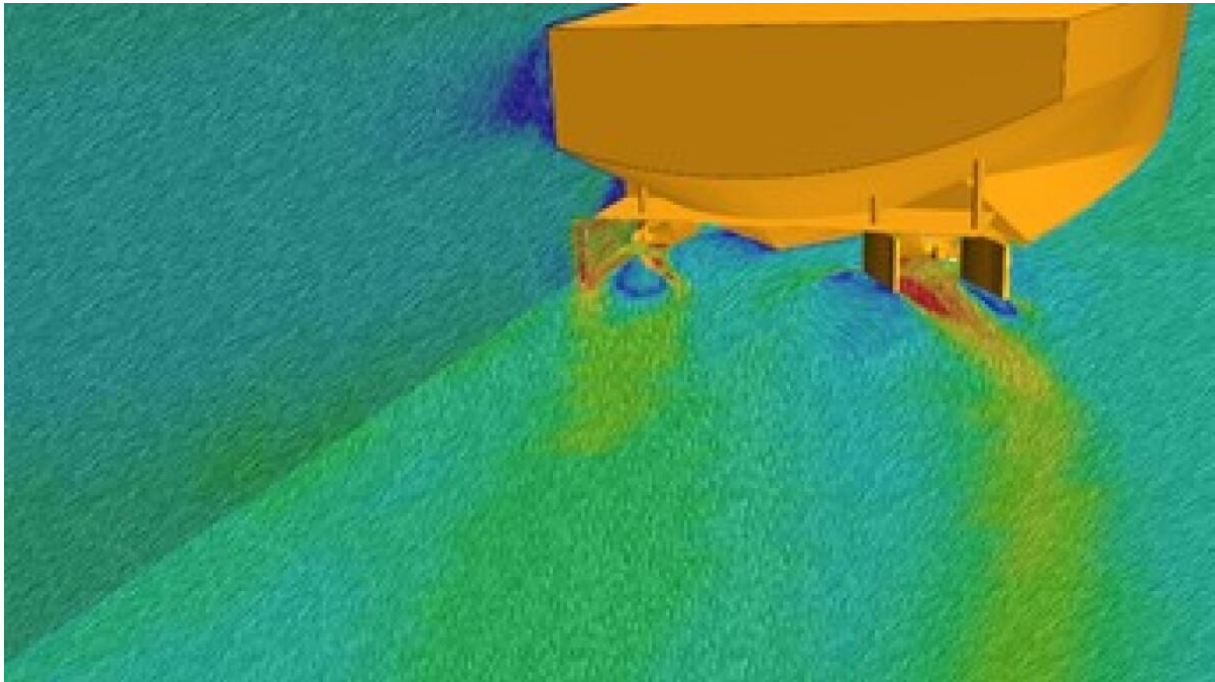


# **23<sup>rd</sup> Numerical Towing Tank Symposium**

**11-13 October 2021**

**Mülheim an der Ruhr/Germany**



**Ould El Moctar (Ed.)**

## Index of Papers

Jörg Albrecht

*Optimisation of the air circulation in the design of a solar houseboat catamaran*

Tiago Amaral, Manuel Rentschler, João Baltazar, Guilherme Vaz

*Hydrodynamic analysis of a floating vertical cylinder*

Andro Bakica, Nikola Vladimir, Hongil Im

*On the propeller modelling and its effect on hydrodynamic loading and structural response of ship hull appendages*

Jannes Berndt, Robinson Perić, Moustafa Abdel-Maksoud

*Recommendations on application of the HRIC scheme for simulation of free surface waves*

Volker Bertram, Milovan Perić

*Chronological and critical review of steady free-surface flow computations*

Yannick Eberhard, Age Nammensma

*Calculation method for aperiodic propeller designs in order to reduce underwater radiated noise*

Tiago Gomes, Sébastien Lemaire, Guilherme Vaz

*Verification study of sliding and overset grids methods*

Mohsen Irannezhad, Rickard E. Bensow, Martin Kjellberg, Arash Eslamdoost

*Towards uncertainty analysis of CFD simulation of ship responses in regular head waves*

Ebrahim Kadivar, Mikhail V. Timoshevskiy, Konstantin S. Pervunin, Bettar el Moctar

*Control of incipient cavitation on a benchmark hydrofoil using a Miniature Vortex Generator (MVG)*

Marek Kraskowski

*A method for optimization of Olympic canoes by global shaping*

Mariana Lopes Pinto, Felipe Ruggeri, Claudio Mueller Prado Sampaio, Kazuo Nishimoto, Philip von Pritzelwitz

*Numerical simulation of air lubrication system on large ore carrier*

Jacob E. Lotz, Marco F.P. ten Eikelder, Ido Akkerman

*Space-time simulation of a heaving and pitching foil with exact enforcement of time periodicity*

Stefano Lovato, Alex Kirichek, Serge Toxopeus, Just Settels, Arno Talmon, Geert Keetels

*The resistance of a plate moving through mud: experiments and simulations*

Sime Malenica

*Some aspects of the local hydro structure interactions during hydrodynamic impacts*

Philipp Mucha

*Application of hybrid-temporal LES to airwake analyses of the ONR tumblehome surface combatant*

Apostolos Papanikolaou

*Holistic ship design optimisation: what is the difference?*

Andreas Peters, Udo Lantermann, Bettar el Moctar

*Compressible and multi-scale simulations of cavitating flows*

Hoyte C. Raven

*Credibility of wave breaking computations by volume of fluid RANS codes*

Hemant Sagar, Bettar el Moctar

*A single cavitation bubble collapse in perspective of numerical simulations*

Carsten Schumann

*The validation of potential theory based predictions of full-scale resistance and propulsion characteristics*

Keun Woo Shin, Poul Andersen

*CFD prediction of cavitation inception on marine propellers*

Hendrik Simonis, Patrick Marleaux, Moustafa Abdel-Maksoud, Norbert Stuntz

*Dynamic stability analysis of a ship at high forward speed in calm water*

Heinrich Söding

*Nonlinear seakeeping by a potential method including hull vibrations and natural seaway*

Bram Starke

*On the relation between measurable (AHR) and modelled (sand-grain) roughness heights to full-scale ship resistance*

Joseph Praful Tomy, Stephan Berger, Keun Woo Shin, Harry Bingham, Poul Anderson

*Hydrodynamic and hydroacoustic simulations of propeller-induced URN in a hull wake-field*

Auke van der Ploeg

*Anderson acceleration for maritime applications*

Maurits van den Boogaard, Giacomo Alessi, Benoit Mallol, Dirk Wunsch, Nathan Clero, Dario Amadori, Luca Zampieri, Charles Hirsch

*Accelerating marine propeller development in early design stages using machine learning*

Arthur E.P. Veldman, Ronald A. Remmerswaal

*Piecewise parabolic reconstruction methods for free-surface flow*

Ville Viitanen, J. Peltola, A. Jaatinen-Värri

*Eulerian-Eulerian multiphase flow and turbulence modelling of hydrofoil cavitation*

Leonie Walter, Jann Strybny, Reinhard Hinkelmann

*Simulating the transport of suspended superquadric shapes with a fully-resolved CFD-DEM algorithm*

Dongni Yan, Arun Lakshminarayanan, Tommi Mikkola, Spyros Hirdaris

*Comparative study on numerical hydroelastic analysis of impact-induced loads*

Jiawei Yu, Chaobang Yao, Liwei Liu, Zhiguo Zhang, Dakui Feng

*Numerical simulations of KCS self-propulsion in regular head waves*

Lahbib Zentari, Simon Tödter, Bettar el Moctar

*Experimental and numerical investigation of gap flow between a pusher and a barge in deep and shallow water*

Yifu Zhang

*Evaluating the effects of drift angle on the self-propelled ship in waves using BEMt*

# Abstract

## "Optimization of the air circulation in the design of a solar houseboat catamaran".

*Dipl.-Ing. Jörg Albrecht · Schliemannstrasse 16 · D-10437 Berlin*  
*Mobil.:0176 –49581694 · Tel.:##49 - 30 - 449 28 00*  
*e-mail: [solarship@aol.com](mailto:solarship@aol.com) · home-page: [www.solarship.de](http://www.solarship.de)*

### 1. Occasion for constructive reasons



Foundation and financing: Schottenheim & Geiger  
Construction consulting: Dipl.-Ing. Burkhard Bader  
Engineering and design: Dipl.-Ing. Jörg Albrecht  
Visualization and interior design: Matteo Costa



The boat design, along with statics, CFD analysis and CE certification were carried out by the design engineer Dipl.-Ing. Jörg Albrecht.

The "optical pillars" in the bow area of the houseboat in particular posed a challenge to the field of vision, statics and aerodynamics.

In general, houseboats are often susceptible to wind and are therefore mostly used in inland waters, where wind loads do not occur as high as in open water areas at sea.

In the interior, the wind is often slowed down by buildings or vegetation or other obstacles, so that the load assumptions can be assumed to be moderate.

However, since houseboats have a relatively large area exposed to wind and are usually built lightly, gusts and permanent strong winds pose a real problem for the skipper. In particular, most houseboats are built very "angular", which act as spoiler edges and generate strong uncontrolled turbulence.

When in doubt, the boat begins to snake sharply, as the skipper has to perform constant corrective maneuvers.

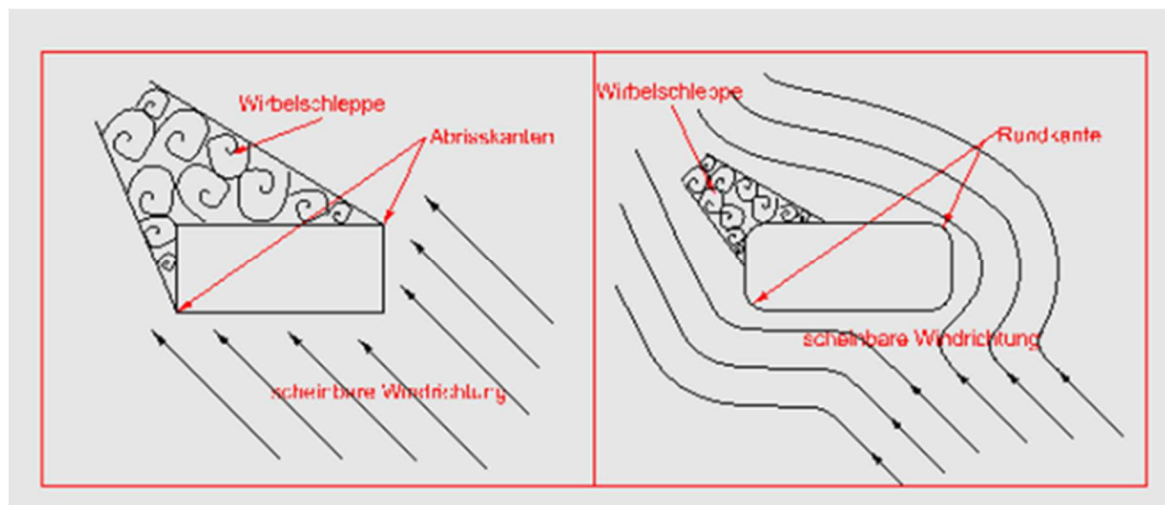
## 2. Considerations for the behavior of houseboats in cross winds

"Wind problems" as mentioned here are often solved in the area of the underwater hull.

Although this "wind problem" is well known and widespread, there are hardly any studies of the wind behavior of houseboats.

The client *Hausbootgeist* has therefore agreed to have a CFD examination, which results from the current design of the constructor and the required practical option.

According to the experience reports, e.g. by the catamaran builder Burkhard Bader, boats with a rounded front edge of the superstructure have better wind behavior, because the rounding off shifts the center of gravity of the area exposed to the wind to the rear and thus the boat can turn better into the wind. See sketch.



The houseboat should "turn into the wind" in cross winds. This is achieved when the lateral center of gravity of the superstructure lies behind the lateral center of gravity of the underwater hull (principle of the wind vane).

Since in most houseboat constructions, as in the current case, the forward deck in the bow area is designed as an open "veranda" and the structure is in the aft area, the lateral center of gravity of the aerodynamics is already shifted aft.

For optical reasons with regard to the design, however, two optically "wide" supports that are visible from the side should now be attached.

It therefore made sense to use these as aerodynamic "optimization tools" at the same time. These optical features were also part of the design in the stern area, where the aft deck,

however, is smaller than the forward deck. Here, too, you should use supports as additional "optimization tools".

These upstream guide surfaces in the bow area are primarily intended to guide the wind from the front around the structure in such a way that the resistance value of the structure is reduced or the wind behavior or maneuverability is improved.

The streamlines should also be positively influenced in the rear.

To test the effects of the profiles, several CFD simulations with different profile arrangements were tested. For reasons of time, the first virtual tests were carried out with the target speed of 13.5 km / h together with the hulls.

### 3. Implementation and considerations for modeling.

Streamlines are generally influenced by pressure fields and their different pressure potentials. If the streamlines are accelerated e.g. via profiles, a negative pressure is created and other streamlines are "sucked in". If the streamlines are decelerated, an overpressure arises which "pushes away" further streamlines. These are self-sustaining effects.

In the present case, the profiles can generally be arranged in two different ways. The position of the negative pressure field or the flow acceleration is selected here as a distinguishing feature.

In the first case, the negative pressure field can be directed outwards, away from the central longitudinal line, that is to say in the lateral outer area of the boat.

In the second case, the negative pressure field can be oriented inwards towards the central longitudinal line, so that there the streamlines are "sucked in".

It turns out that the rounding of edges also works according to the same principle. When an edge is rounded, it not only prevents the flow from separating and thus first of all makes the flow around the edge itself possible at all. Rather, by flowing around a round corner, as with the convex side of a wing, a negative pressure is generated by the acceleration of the flow, which in turn "sucks in" further streamlines and thus guides the flow elegantly around the corner.

### 4. Flow simulations

In the reference experiment, the houseboat was simulated without wind profiles as a reference.

A suggestion for improvement could already be made after this reference attempt.

#### 1. Profile attempt

In the first attempt, the front profiles should suck in the streamlines and accelerate out to the side between the profiles and the front wall. The resulting effects were not known until then.

The rear profiles, on the other hand, with the negative pressure areas on the outside, should lengthen the flow on the side wall, so to speak, to the mirror and thus also lengthen the structure towards the rear in terms of flow.

## 2. Profile attempt

The next attempt is to simulate the 1st arrangement when the boat moves reverse. The effect from experiment 1 is reversed here. The flow profiles also work "backwards".

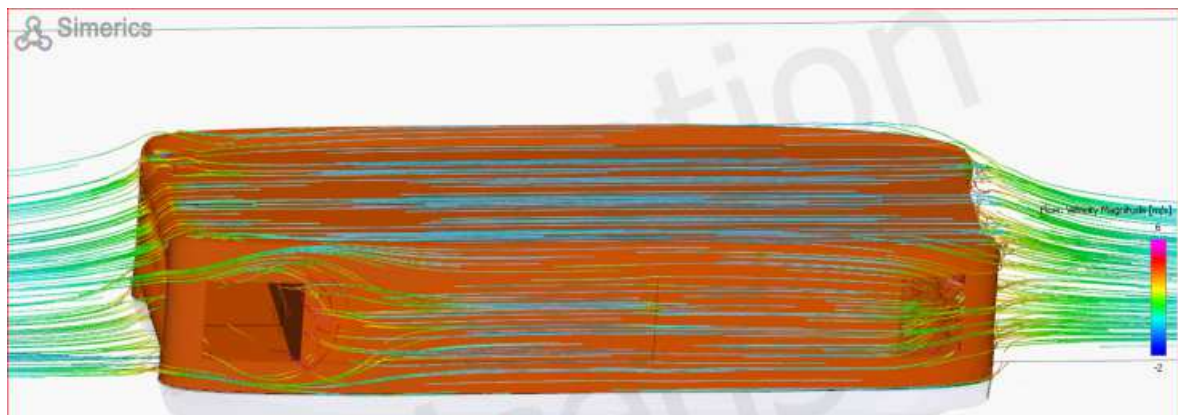
## 3. Profile attempt

This experiment was carried out with a considerable change in the construction with the aim of making it more optimal. The wind profiles in the bow area were turned.

The overpressure sides of the profiles have now pushed the streamlines outwards away from the central longitudinal and the suction side on the outside simultaneously sucks the streamlines in outwards as well.

## 4. Profile attempt

In this test, in addition to the third test arrangement, the design in the stern area was changed and minor corrections were made to the arrangement in the bow area.



## 5. Profile attempt

Here the influence of the roof stairs on the flow behavior of the entire houseboat system is examined. Furthermore, the influence of the draft on the current in the catamaran tunnel between the swimmers.

## 6. Profile attempt

At this point, the inclined wind flow onto the houseboat is examined.

## 5. Prospect for further applications

Afterwards, a prospect of similar aerodynamic problems in large shipping is given. Especially since ecological perspectives are also in the foreground here.

# Hydrodynamic Analysis of a Floating Vertical Cylinder

Tiago Amaral\*, Manuel Rentschler†, João Baltazar\*, and Guilherme Vaz† §

\*Instituto Superior Técnico, Lisbon/Portugal, †blueOASIS, Lisbon/Portugal, §Department of Civil, Maritime and Environmental Engineering, University of Southampton, UK  
tiago.clerigo.amaral@tecnico.ulisboa.pt

## 1 Introduction

The pitch free decay test response of a floating vertical cylinder will be studied throughout this paper. The present case is based on an experiment (Paredes et al., 2015) and subject of different CFD validation studies (Palm et al., 2015, Rivera-Arreba et al., 2017). Both have found significant discrepancies regarding the damping and natural period of the system for the pitch motion. The proposed test case will be verified and validated with the CFD solver ReFresco based on a cell-centered finite-volume discretisation with unstructured grids. The fully unstructured hexahedral grid generator commercial package NUMECA Hexaprep will be used. Furthermore the results will be compared with the experimental investigation performed by (Paredes et al., 2015).

## 2 Case description

A generic buoy was experimentally tested in a wave tank with a water depth of  $0.9m$  (Paredes et al., 2015). The buoy is a vertically truncated cylinder of mass  $M = 35.85kg$ , diameter  $D = 0.515m$ , and moment of inertia around the centre of gravity  $I_{xx} = 0.9kgm^2$ . The centre of gravity is placed  $0.0758m$  above the bottom of the buoy along the symmetry  $z$ -axis. These values are the ones used in setting up the numerical model and are modified from (Paredes et al., 2015) to include the extra mass ( $0.35kg$ ) and inertia ( $0.03kgm^2$ ) from the styrofoam lid and the metal supports of the moorings that were attached to the buoy (Palm et al., 2015). In this study a pitch free decay test will be conducted. The cylinder is rotated around its center of mass,  $8.88^\circ$  pitch from its vertical equilibrium position.

## 3 Numerical modelling

The computational fluid domain, represented in Fig. 1, is described as a rectangular box:  $x \in [-6, 9]m$ ,  $y \in [-2.5, 2.5]m$ ,  $z \in [-0.9, 0.9]m$ , with the buoy's centre of gravity initially located at  $(0, 0, -0.096)m$ . The initial draft of the buoy was set to  $0.172m$ , being the equilibrium of the free floating body. To support wave propagation without excessive wave damping there is a band of refined cells around the free surface. In the near-field area, the mesh is refined to resolve radiated waves and vortices generated by the flow separation at the cylinder edges. In the far-field, the mesh is coarser to decrease the computational cost.

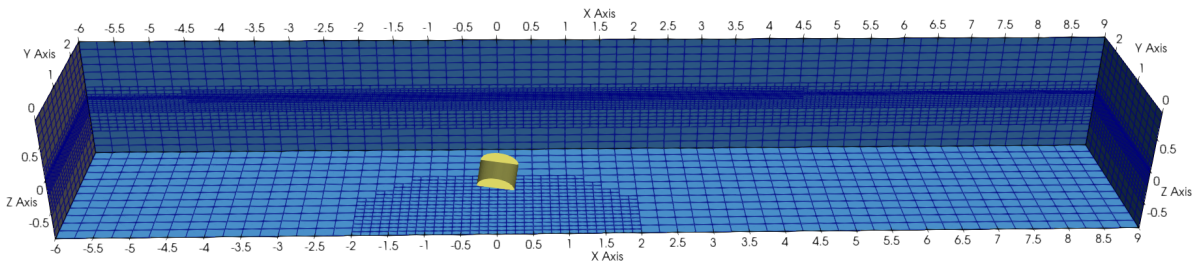
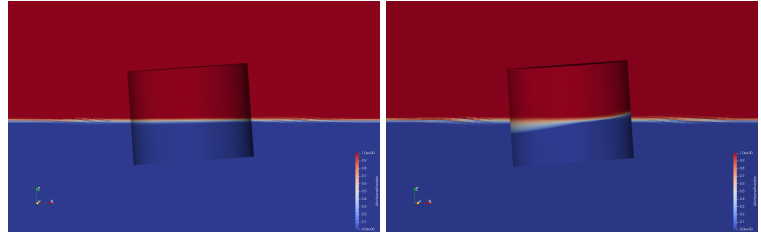


Fig. 1: Representation of the numerical model domain.

The shear-stress is determined at the wall from its definition, therefore it is required the usage of near-wall cells which are typically requested to present a non-dimensional height of  $y^+ \approx 1$ . The main (and only) drawback of this approach is the extremely small vertical size of the near wall cells that leads to higher cell counts and cells with high aspect ratio that make iterative convergence troublesome or even impossible (Eça et al., 2015). Due to the size of the cells near the cylinder's surface, it was noticed that the water remained attached to the buoy for a longer period of time, showing difficulties in flowing back to the free surface leading to an overestimation of the hydrodynamic damping. To avoid this it was necessary to apply a so-called Contact Line Correction, where a Neumann freeze near-wall approach



is applied to the volume-fraction variable. A visual representation of this phenomena is given in Fig. 2. The cylinder's motion was solved using a 3DOF solver, setting free the pitch, heave and surge DOFs. The implicit Euler (1<sup>st</sup> order) discretisation scheme was used in order to solve the unsteady terms. Furthermore, iterative solvers were applied for the resulting linear system of equations (GMRES or BCGS with Block-Jacobi or Jacobi preconditioning). Several interface capturing schemes are available for the discretisation of the convection term of the volume fraction and momentum transport equations. For the cylinder test case, the convection terms were



(a)  $t=2.8s$ , with Contact Line Correction. (b)  $t=2.8s$ , without Contact Line Correction.

Fig. 2: Air volume fraction comparison.

modelled using a Total Variation Diminishing (TVD) scheme (LIMITED QUICK) for the momentum and a second order TVD limiter (SUPERBEE) for the volume fraction. For the turbulence, the convection terms were modelled using a 1<sup>st</sup> order UPWIND scheme. Gradient operators were solved using the Gauss theorem. In all simulations it was required to have a maximum and average Courant numbers below 5 and 1, respectively. Furthermore, the residual norm  $L_2 < 10^{-6}$  and a maximum number of iterations of 200 were applied as the convergence criteria. Additionally, all simulations were supplemented by the two-equation turbulence model  $k - \omega SST$  (Menter et al., 2003).

Table 1: Numerical Settings used. Where NS represents the numerical solver and CDS the convection discretisation scheme.

Equation	Preconditioner	NS	CDS
Momentum	JACOBI	BCGS	LIMITED QUICK
Pressure	BJACOBI	BCGS	-
Turb. Model	BJACOBI	GMRES	1 <sup>st</sup> Order UPWIND
Free Surface	BJACOBI	BCGS	SUPERBEE

## 4 Results

The total hydrodynamic damping force may be decomposed in integrated pressure and shear stress on the wetted surface of the floating vertical cylinder. The pressure and shear stresses are influenced by wave radiation, eddy making and lift, skin friction and drag. The pressure loads are owing to radiated waves, viscosity, eddies or pressure drag. Moreover, energy losses in the boundary layer, vortices and flow separation contribute to the pressure loads (Mewes et al., 2020). In order to avoid overestimating the hydrodynamic damping it is fundamental to understand the influence of different grid refinement settings on the results. Several studies were carried out to investigate the influence of the grid refinement around the free surface and structure to prevent overestimating the contribution of the radiated waves, eddies and shear stresses on the cylinder's motion. Furthermore an uncertainty analysis will be performed.

Additionally, it has been seen in previous studies (Palm et al., 2015, Rivera-Arreba et al., 2017) that the system is highly sensitive to small changes in the structural properties of the cylinder due to its dimensions. The pitch response is closely linked to the position of the centre of gravity relative to the water line and the moment of inertia of the body.

### 4.1 Free surface refinement analysis

Different refinement levels (RL) for the refinement box around the free surface will be tested, while keeping constant the initial number of cells of the grid ( $N_x, N_y, N_z$ ), diffusion depth, first layer thickness, stretching ratio and number of layers of the viscous layer (Fig. 3). To analyse the free surface elevation capture, six monitor points have been deployed along the domain at the following locations:  $(0; 1.5; -0.9)m$ ,  $(0.3; 0; -0.9)m$ ,  $(0.5; 0; -0.9)m$ ,  $(1; 0; -0.9)m$ ,  $(3; 0; -0.9)m$  and  $(5; 0; -0.9)m$ . From the four refinement levels tested around the free surface it has been noted that the free surface ele-

Table 2: Grid settings used.

Grid	RL	Nx	Ny	Nz	Nb Cells
1	3	60	12	15	$0.71 \times 10^6$
2	4	60	12	15	$2.23 \times 10^6$
3	5	60	12	15	$3.58 \times 10^6$
4	6	60	12	15	$6.07 \times 10^6$

variation was captured in the same way except for the refinement level 3, showing differences in the monitor points closer to the cylinder  $(0.3; 0; -0.9)m$  and  $(0.5; 0; -0.9)m$ . However, it was possible to observe that the results obtained in terms of pitch were very similar (Fig. 4).

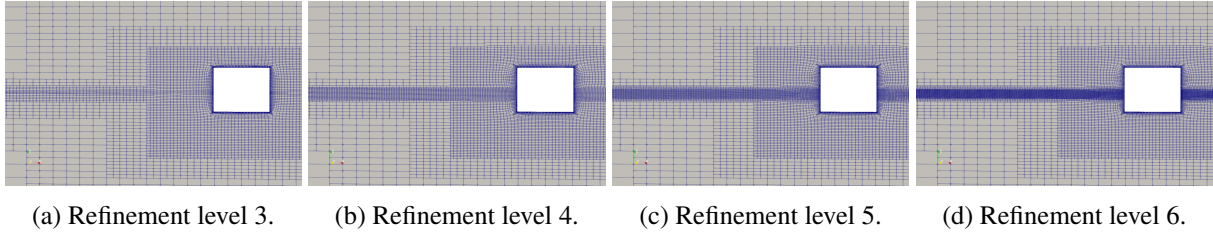


Fig. 3: Grid visualisation for the different refinement levels around the free surface.

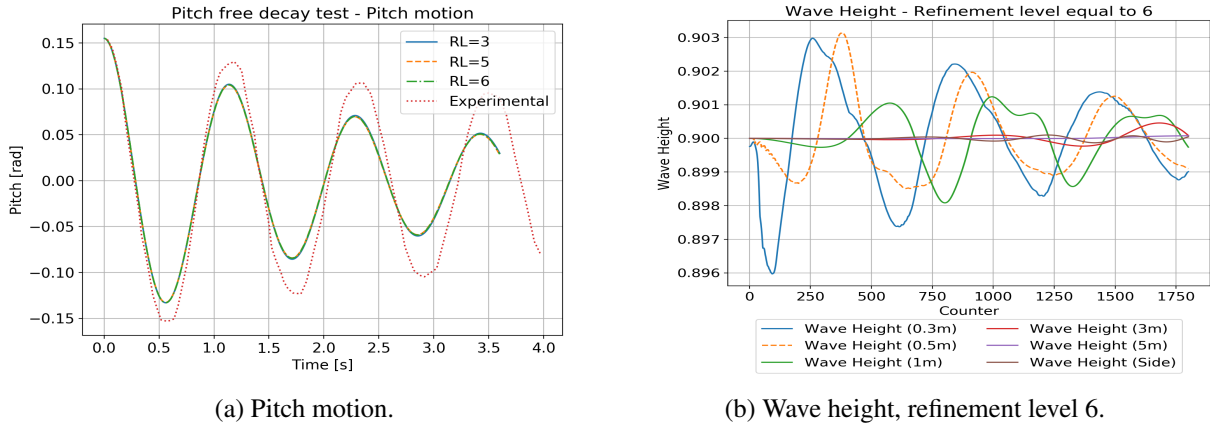


Fig. 4: Results obtained for the pitch motion and free surface elevation capture.

## 4.2 Body refinement analysis

With the intention of studying the eddy making and shear stresses effects on the cylinder's motion, different refinement levels around the structure have been tested, while keeping constant the initial number of cells of the grid, diffusion depth, first layer thickness, stretching ratio and number of layers of the viscous layer (Fig. 5). Throughout this study it was noted that the vortices near the edge of the cylinder were being poorly captured, specially for the refinement levels 3 and 4, revealing a need of increasing the refinement level around the structure. Furthermore, it was observed that as the refinement level around the cylinder increased, the hydrodynamic damping of the system decreased. At the same time the friction forces increased while the dynamic pressure forces remained fairly constant, showing only slightly different results in the y- and z-directions. However, the dynamic pressure forces revealed to be predominant, being two orders of magnitude larger than the friction forces (Fig. 6). Consequently, energy losses in the boundary layer, vortices and flow separation are the main contributions to the hydrodynamic damping of the system. The increase of the refinement level around the buoy led to a better capture of the vortices and its contribution to the cylinder's motion, minimising the overestimation of the hydrodynamic damping. In the same way, the poorly captured vortices for the lower refinement levels led to an overestimation of the hydrodynamic damping (Fig. 7).

Table 3: Grid settings used in the body refinement analysis.

Grid	RL	Nx	Ny	Nz	Nb Cells
1	3	60	12	15	$0.71 \times 10^6$
2	4	60	12	15	$1.21 \times 10^6$
3	5	60	12	15	$3.78 \times 10^6$
4	6	60	12 <td 15	$1.96 \times 10^7$	

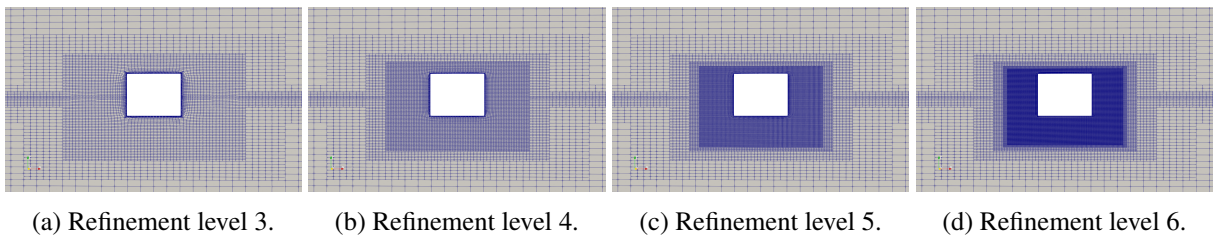


Fig. 5: Different refinement levels around the cylinder.

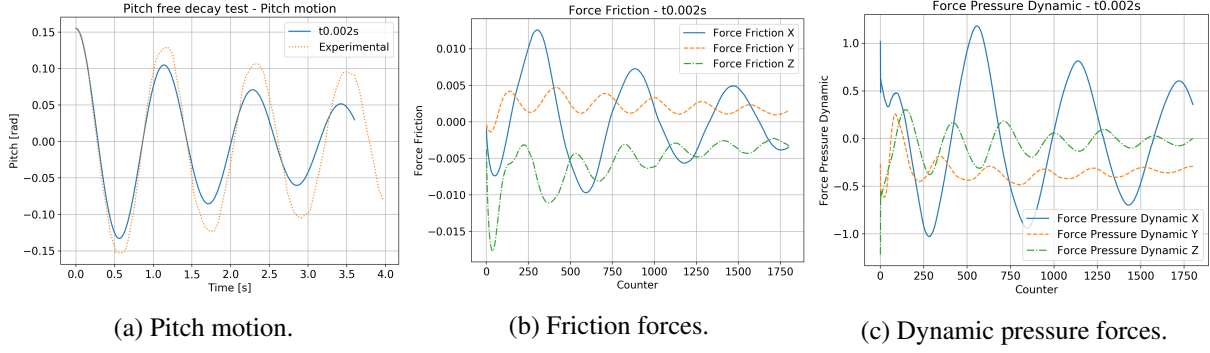


Fig. 6: Results obtained for the refinement level 3 simulation.

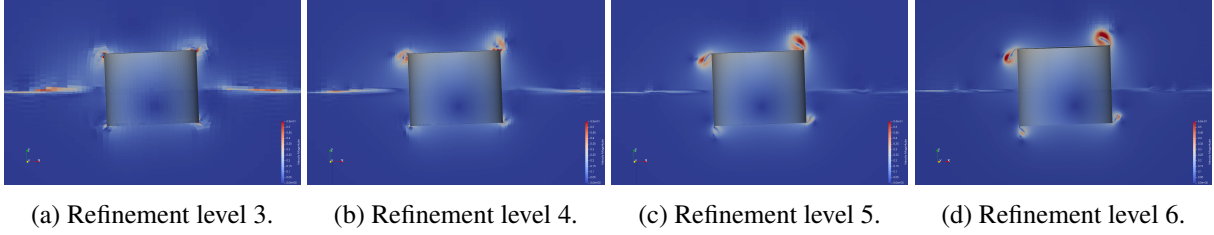


Fig. 7: Flow field around the cylinder for different refinement levels at  $t=0.8s$ .

### 4.3 Local refinement analysis

The computational cost increased with the increase of the refinement level around the buoy. With the intention to decrease the computational cost of the simulations there was a need to decrease the number of cells in the grids. At the same time it was noticed that the eddies and shear stresses above the free surface had little to none impact in the results obtained. Due to this observation it was possible to reduce the dimensions of the refinement box around the buoy. A second refinement box around the cylinder was created, surrounding solely the cylinder below the free surface with a refinement level of 6, while keeping a refinement level of 3 for the previous refinement box. Consequently, it was necessary to study the influence of the dimension of the second refinement box in the vortices capture. Three different refinement box dimensions were tested (Fig. 8).

Table 4: Grid settings used in the local refinement analysis.

Grid	RL	Nx	Ny	Nz	Nb Cells
Small 1	6	60	12	15	$3.01 \times 10^6$
Medium	6	60	12	15	$5.40 \times 10^6$
Large	6	60	12	15	$9.08 \times 10^6$
Small 2	7	60	12	15	$1.16 \times 10^7$

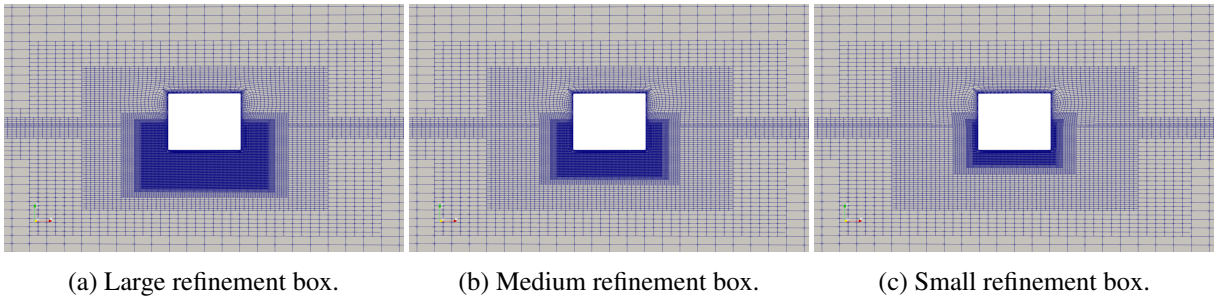
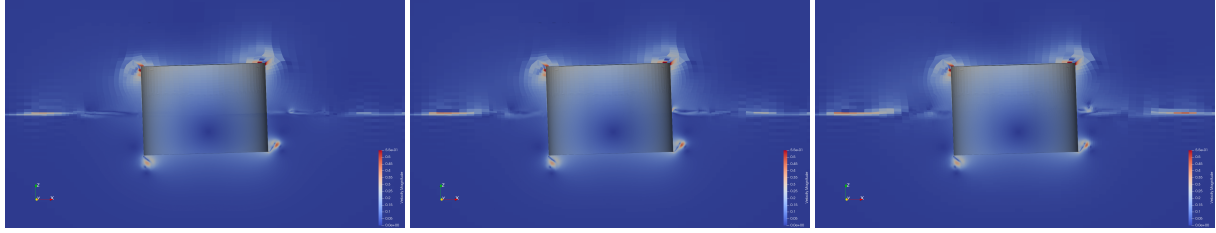


Fig. 8: Different local refinement boxes dimensions and refinement level 6.

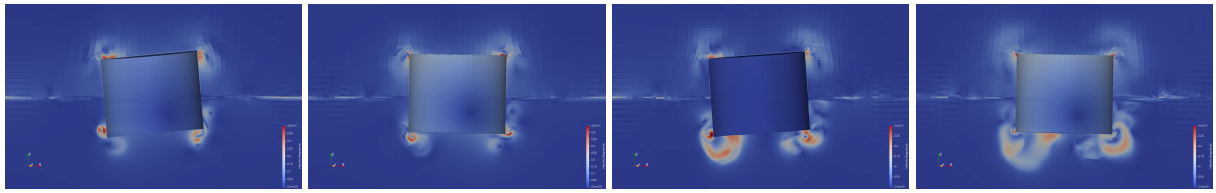
The three simulations revealed coincident results for the pitch motion. Furthermore, the vortices capture was fairly equal among the three different refinement boxes (Fig. 9). Moreover, the friction and pressure forces were found equal for all simulations. The same conclusion was taken for the free surface elevation capture. The three simulations agreed perfectly with the results obtained using the grid 4 of the section 4.2. As a result, the smallest local refinement box was used in the following simulations. Consequently, it became feasible to increase one more time the refinement level around the cylinder, with the objective of confirming that the results finally converged. Only the vortices showed a slightly different structure from the previous simulations, having almost zero influence on the results obtained in terms of pitch.

Nevertheless, the high aspect ratios of the near wall cells made iterative convergence troublesome, not being possible to fulfill the convergence criteria, specially for the air volume fraction in the viscous layer cells at the free surface. The high values obtained for the Courant number resulted in high  $L_\infty$  residuals (Fig. 11). However, the order of magnitude achieved in the residuals was assumed to be acceptable.



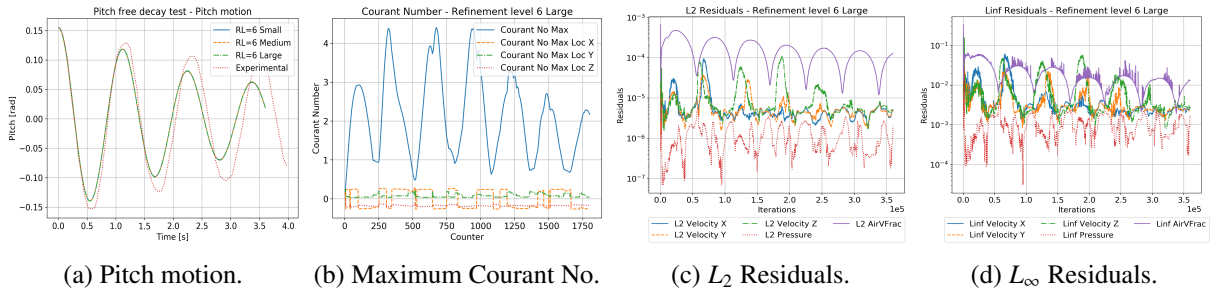
(a) Large refinement box. (b) Medium refinement box. (c) Small refinement box.

Fig. 9: Flow field for different refinement boxes dimensions and refinement level 6 at  $t=0.8s$ .



(a)  $t=1.6s$ . (b)  $t=2.0s$ . (c)  $t=2.8s$ . (d)  $t=3.6s$ .

Fig. 10: Time sequence of the flow field for the large refinement box and refinement level 6.



(a) Pitch motion. (b) Maximum Courant No. (c)  $L_2$  Residuals. (d)  $L_\infty$  Residuals.

Fig. 11: Residuals and Courant number data regarding the Large refinement box and refinement level 6.

#### 4.4 Uncertainty analysis

In the present study, the method proposed to generate as much as possible geometrically similar grids in (Crepier et al., 2017) will be followed in order to perform an uncertainty analysis (Eça et al., 2014). (Eça et al., 2014) proposed a method to estimate the numerical uncertainty of numerical simulations based on grid refinement studies of geometrically

similar grids. Generating the appropriate sets of grids is straightforward when using structured grids but it becomes more challenging when working with unstructured meshes. The main user input is the cell size for the initial grid, the refinement degree for each geometrical feature that should be captured, and the size of the transition zone between two refinement levels called diffusion depth  $d$ . Once a sufficient resolution is obtained at the places of interest, an anisotropic sub-layer of cells can be inserted to provide a grid suited to properly capture the boundary-layer on the walls presented in the grid. The grid sets built for this study are based on an initial coarse grid which is successively refined to obtain, in total, five grids (Fig. 12) (Crepier et al., 2017). The results from this analysis will be included in future work.

Table 5: Grid settings used in the uncertainty analysis. Where  $d$  represents the diffusion depth,  $r$  the stretching ratio,  $NbL$  the total number of layers of the viscous layer,  $FLT$  the first layer thickness in  $\times 10^{-5}m$ .

Grid	RL	$N_x$	$N_y$	$N_z$	Nb Cells	$d$	$r$	$NbL$	FLT
1	6	20	4	5	$0.21 \times 10^6$	1	1.728	9	14.560
2	6	40	8	10	$1.06 \times 10^6$	3	1.315	18	6.291
3	6	60	12	15	$3.01 \times 10^6$	5	1.200	27	4.000
4	6	80	16	20	$6.65 \times 10^6$	7	1.147	36	2.931
5	6	100	20	25	$1.26 \times 10^7$	9	1.116	45	2.312

similar grids. Generating the appropriate sets of grids is straightforward when using structured grids but it becomes more challenging when working with unstructured meshes. The main user input is the cell size for the initial grid, the refinement degree for each geometrical feature that should be captured, and the size of the transition zone between two refinement levels called diffusion depth  $d$ . Once a sufficient resolution is obtained at the places of interest, an anisotropic sub-layer of cells can be inserted to provide a grid suited to properly capture the boundary-layer on the walls presented in the grid. The grid sets built for this study are based on an initial coarse grid which is successively refined to obtain, in total, five grids (Fig. 12) (Crepier et al., 2017). The results from this analysis will be included in future work.

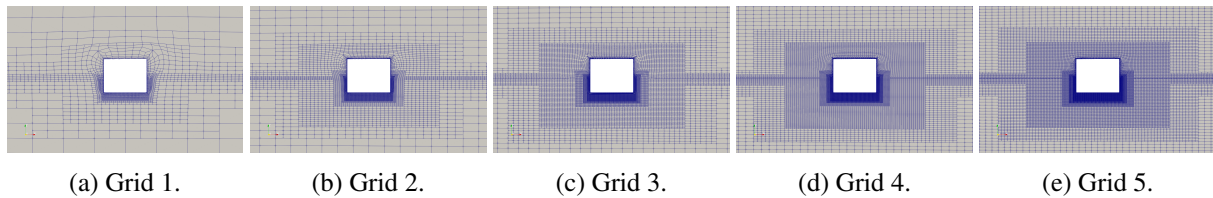


Fig. 12: Grids used in the uncertainty analysis.

## 5 Conclusion

A mismatch between the experimental data and CFD simulations using the CFD code ReFRESHCO regarding the damping of the system has been found. The hydrodynamic damping was over-predicted comparing with the experimental results. The main contribution to the hydrodynamic damping was revealed to be the pressure forces, induced by the radiated waves, viscosity and eddies (Mewes et al., 2020). For this reason, it is highly important to have enough refinements around the structure to minimize the overestimation of the damping of the system.

Nevertheless, there are always differences between the implementation of physical and numerical models. In this study, expected uncertainties in measured data can have a visible impact on the results. For reasons of implementation some known approximations are made in the setup of the numerical model. In the CFD simulations the buoy is perfectly truncated, but the experimental buoy was not perfectly so. The bottom corner was slightly rounded and bulged, and so was smoother than the right angle of the numerical model. The physical model also had protruding attachments for the moorings at the water level, thus changing the local flow pattern ever so slightly (Palm et al., 2015).

Further work will include investigation on the influence of the turbulence model on the results obtained, including a comparison without turbulence model. It is recommended for future studies to verify and validate the floating vertical cylinder test case against wave loads and mooring lines. Moreover, the convection discretisation schemes influence on the accuracy of the results obtained can be analysed. According to (Burmester et al., 2020) the REFRICS and HRIC convection schemes can provide significantly more accurate results for the free surface.

## Acknowledgements

The authors would like to acknowledge the use of the IRIDIS High Performance Computing Facility and associated support services at University of Southampton.

## References

- G. Paredes, J. Palm, C. Eskilsson, L. Bergdahl, and F. Taveira-Pinto. Experimental investigation of mooring configurations for wave energy converters, in: Proc. EWTEC 2015, 2015.
- J. Palm, C. Eskilsson, G. Paredes, L. Bergdahl, and F. Taveira-Pinto. Coupled mooring analysis for floating wave energy converters using CFD: Formulation and validation, 2015.
- L. Eça, F. S. Pereira, and G. Vaz. Viscous flow simulations at high Reynolds numbers without wall functions: Is  $y^+ \simeq 1$  enough for the near-wall cells?, 2017.
- P. Crepier. Ship resistance prediction: verification and validation exercise on unstructured grids. Proceedings on VII International Conference on Computational Methods in Marine Engineering MARINE 2017, Nantes, France.
- L. Eça, G. Saraiva, G. Vaz, and H. Abreu. The pros and cons of wall functions. Proceedings of the ASME 2015 34th International Conference on Ocean, Offshore and Arctic Engineering, St. John's, Newfoundland, Canada.
- I. Rivera-Arreba. Computation of nonlinear wave loads on floating structures. Master thesis, 2017.
- S. Mewes. Numerical Prediction on Hydrodynamic Loads and Damping of a Floating Offshore Wind Turbine. Dissertation, 2020.
- L. Eça and M. Hoekstra. A procedure for the estimation of the numerical uncertainty of CFD calculations based on grid refinement studies. Journal of Computational Physics, 2014.
- F. R. Menter, M. Kuntz and R. Langtry. Ten years of industrial experience with the SST turbulence model. Turbulence, Heat and Mass Transfer 4, 2003.
- S. Burmester, G. Vaz and O. el Moctar. Towards credible CFD simulations for floating offshore wind turbines. Ocean engineering, Vol. 209, 1 August 2020, 107237.

# On the propeller modelling and its effect on hydrodynamic loading and structural response of ship hull appendages

Andro Bakica <sup>a</sup>, Nikola Vladimir <sup>a</sup>, Hongil Im <sup>b</sup>

<sup>a</sup> Faculty of Mechanical Engineering and Naval Architecture, University of Zagreb, Croatia

<sup>b</sup> Hyundai Heavy Industries Co. Ltd., 1000, Bangeojinsunhwan-doro, Dong-gu, Ulsan, 44032, Korea

## 1. Introduction

Governed by changes in IMO regulations, shipping industry has turned to the non-standard and novel ways of reducing the ship fuel consumption. One way of improving the overall ship efficiency is by installing Energy Saving Devices (ESDs) which are located near the propeller. These devices operate by changing the flow near the propeller increasing the propeller efficiency, thus providing the same thrust at the lower rotation rate which directly has a positive impact on the ship fuel consumption.

When evaluating ESDs usually Computational Fluid Dynamics (CFD) is employed in order to solve the complicated flow field near the propeller considering the fluid viscosity, flow separation at the ship wake and the propeller rotation. Many authors have contributed to the validation of CFD for the ship equipped with the ESD (Kim et al., 2015; Sakamoto et al., 2019). Most of the work is usually related to the hydrodynamic efficiency of such devices or the influence of scale effects. Although these subjects are of importance for the overall evaluation of any ESD, their structural response remains vaguely investigated. Pre-Swirl Stator (PSS) type of ESD has been investigated through the joint international project GRIP (Paboeuf & Cassez, 2017; Prins et al., 2016). For the same device Lee et al. (2016) developed a design procedure which is further extended in Ju et al. (2018) to account for the different PSS shape. However, the overall coupling procedure features a simplified coupling of the CFD fluid loading to the structural FEM model and does not assess the propeller influence on the local PSS structure.

This study addresses the influence of the propulsion models on the PSS hydrodynamic loads and structural response in waves. Three models are investigated: without propeller (w/o propeller), with propeller (w/ propeller) and with the simplified propeller model of Actuator Disk (AD). The aim is to evaluate which of the propulsion models is necessary to properly investigate the ship-motion induced loads on the PSS from the perspective of the entire design procedure which should include the long-term wave statistical analysis. The hydrodynamic loads are obtained by means of OpenFOAM (Weller et al., 1998) with the in-house methods for free-surface flows. These loads are then imposed on the structural model through the careful interpolation procedure and computed stresses are evaluated using the FEM tool NASTRAN (Siemens, 2014). It is important to mention that there will be no thorough investigation of the PSS performance issues and propeller efficiency analysis since the main goal is to evaluate the difference of the propulsion models on the stresses of the PSS fin in the perspective of a statistical wave analysis.

## 2. Numerical model

Numerical hydrodynamic model is based on the Finite Volume (FV) discretization where the two-phase flow is considered incompressible. From the assumptions, flow is considered divergence-free, hence the continuity equation is defined as:

$$\nabla \cdot \mathbf{u} = 0, \quad (1)$$

where  $\mathbf{u}$  is the velocity in the fluid. The momentum equation reads:

$$\frac{\partial \mathbf{u}}{\partial t} + \nabla \cdot \mathbf{u} \otimes \mathbf{u} - \nabla \cdot (\nu_e \nabla \cdot \mathbf{u}) = -\frac{1}{\rho(\mathbf{x})} \nabla \cdot \mathbf{R}, \quad (2)$$

where  $\mathbf{u}$  is the position vector,  $\nabla p_d$  is the dynamic pressure gradient,  $\rho(\mathbf{x})$  is the density dependent on the spatial location,  $\mathbf{R}$  is the deviatoric part of the Reynolds stress tensor and  $\nu_e$  is the effective kinematic viscosity. Turbulence in the flow is modeled through the effective viscosity and with the two-equation  $k-\omega$  SST turbulence model. Interface between the two non-mixing fluids is modeled as a field bounded between -1 and 1 with a hyperbolic tangent profile. This field is written as a function of a signed distance called the Level-Set (LS) which is a shortest Euclidean distance from the free surface. More on the theory of the model can be found in Sun & Beckermann (2007), while the implementation details are described in Vukčević et al. (2016a, 2016b). In Vukčević et al. (2016a), the reader can also find the details on the numerical implementation of water waves. Wave reflection from the boundaries is resolved with the relaxation zones at domain edges (Jasak et al., 2015).

Regarding the ship propulsion models, the simpler AD approach features only a pressure and velocity tangential jumps at the position of the virtual disk. AD is simply introduced on the selected number of faces at the vicinity of the propeller plane. In this manner, the mesh w/o the propeller and w/ AD can have equal configurations. Full description and validation of the AD model can be found in Bakica et al. (2019). The most complex model w/ propeller is modelled through the sliding mesh interface. Mesh is separated in two regions, surrounding mesh and rotating mesh regions. The mesh in the vicinity of the propeller is allowed to rotate given the axis of rotation and rotation rate. The solution between the two meshes is merged on the General Grid Interface (GGI) where the interpolation of flow variables is computed. Description of the face-cut algorithm and variable averaging can be found in work by Beaudoin & Jasak (2008).

Regardless of the propulsion model, the obtained pressure field needs to be interpolated to the FEM structural model. Interpolation process is performed after the hydrodynamic solution is found meaning that there is no interaction between the flow and the motion of the structural nodes. This would classify the hydro-structural interaction as a one-way coupling. The pressure is interpolated onto the structural mesh by using the values at the Gaussian integration points which increases the accuracy of the field transfer. For each Gaussian point per FEM element there is an adjacent pair on the hydrodynamic mesh whose value is sought. This value is not readily available due to discontinuity of the flow field at the surface where zero gradient boundary condition is applied for the pressure and solution is known only at the surface face center. This requires computing the values at the CFD surface points in order to create a smooth pressure field which is performed by least square fit. After receiving the hydrodynamical values at all the integration points the FEM nodal forces can be computed depending on the plate element shape function. This enables the FEM model to be directly imposed with the nodal forces instead of the averaged pressure values. Finally, the stresses can be computed using linear static analysis. Interpolation process in full details is explained in Bakica et al. (2020).

### 3. Computational setup

The PSS investigated in this study is fitted on a well-known benchmark ship case KVLCC2. Ship particulars are given in Table 1. This type of fuller hull forms usually features a bilge vortex and other types of rotational losses at the stern wake, hence making it a good candidate for the ESD setup. However, as already mentioned hydrodynamic performance issues are not addressed in this study. All three propulsion models are shown in Fig 1. In order to make the study concise, only one fin is analyzed (shown in blue on Fig. 1). The procedure is straightforward to deduce for the other two fins.

Ship surrounding mesh is  $3.5L_{pp}$  long behind the ship,  $2.0L_{pp}$  to the inlet boundary and  $2.5L_{pp}$  to the sides. All three cases have the same near hull mesh geometry, while only the propeller case differs in the region of the propeller inclusion which ensures equal spatial comparison. In order to ensure the same time-step refinement in all three cases time-step is set to 1.5 degrees of propeller rotation. Rotation speed is adjusted with the PI controller for the AD case in a calm-water run until the thrust and hull drag force are equal. Same rotation rate is used for the direct propeller case. Wave parameters are chosen in order to excite ship pitching motion since the evaluation of the ship motion-induced loads compared to propulsion loads is a main subject of investigation. Chosen wave parameters include wavelength of  $0.9L_{pp}$  and the wave amplitude fixed at 10% of the ship draught.

Table 1. Ship particulars

Length between perpendiculars ( $L_{PP}$ )	320.0 m
Breadth ( $B$ )	58.0 m
Depth ( $D$ )	30.0 m
Draft ( $T$ )	20.8 m
Displacement ( $\Delta$ )	312622 m <sup>3</sup>
Design speed ( $U$ )	16.5 knots
Block coefficient ( $C_B$ )	0.81
Vertical centre of gravity ( $KG$ )	18.6 m
Moment of inertia ( $K_{XX}/B$ )	0.40
Moment of inertia ( $K_{YY}/L_{PP}, K_{ZZ}/L_{PP}$ )	0.25

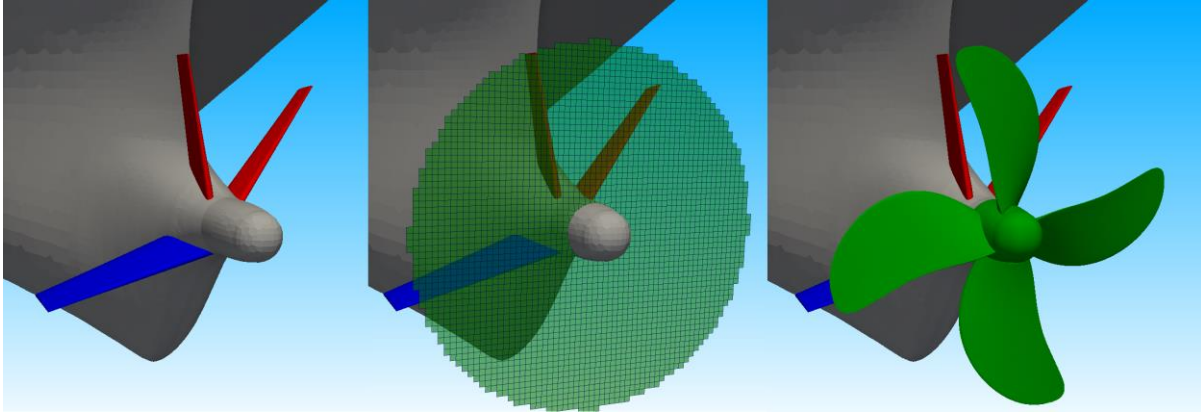


Figure 1. Three different propulsion models: w/o propeller (left), w/ AD (middle), w/ propeller (right).

For all three cases, 40 time-steps per encounter period is stored for structural analysis meaning that local higher frequency fluctuations from propeller blade passing will not be visible on the stress signal since this would include an unnecessarily large number of load cases for structural analysis. Also, the force in the local coordinate system of the fins is analyzed in order to compare the hydrodynamic loading impact in all of the hydrodynamic conditions.

#### 4. Results and discussion

First, the forces on the fin are analyzed. Lifting force is considered as a main contribution to the vertical bending moment of the PSS i.e., in the direction vertical to the two-dimensional section of the airfoil. Results are shown in Fig 2 in terms of lift coefficient. As can be observed, both the w/ AD and w/ propeller cases have a observable amount of force increase, but the trend of the hydrodynamic loading remains similar. Interestingly, the AD creates a similar suction effect on the fin profile, thus adding a reasonable amount of resemblance to the w/ propeller case. However, even the simplest case w/o propeller has a comparable lift loading curve which suggests that the dominant loading impact is created by the ship motion, particularly pitch motion has a leading influence on the currently observed fin. This is shown in Fig 2. by observing the pressure loading peak compared to the ship pitch motion which is with respect to the observed fin location intuitively expected.



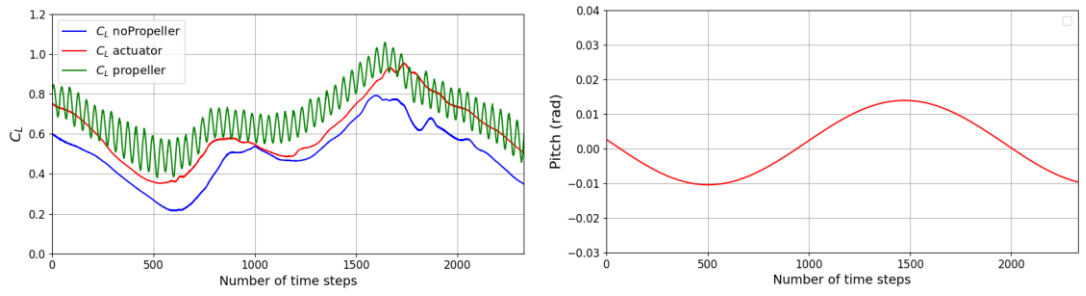


Figure 2. Lift coefficient ( $C_L$ ) on the selected fin (left), ship pitch motion (right)

Overall, by observing these results, their impact on the underlying structural configuration is not clear and can be investigated only by direct pressure transfer to the structural model. The field transfer is shown in Fig 3. for a particular time-step in a w/ propeller case where hydrodynamic and structural meshes are shown side by side. In order to reduce the amount of presented material, only the maximally loaded FEM element is selected, and its stress range is evaluated. The stress ranges for all three cases are shown in Fig 4. For the three cases stress ranges are 6.37 MPa, 6.31 MPa and 7.00 MPa for the w/o propeller, w/ AD and w/ propeller case, respectively. Peak stress is very similar in all three cases with the maximum of 53.98 MPa in the w/o propeller case while the other two cases have a difference of less than 3%. Most importantly, in all propulsion models the resulting stresses are sufficiently similar meaning that for the entire wave statistical analysis, the simplest w/o the propeller case results are adequate.

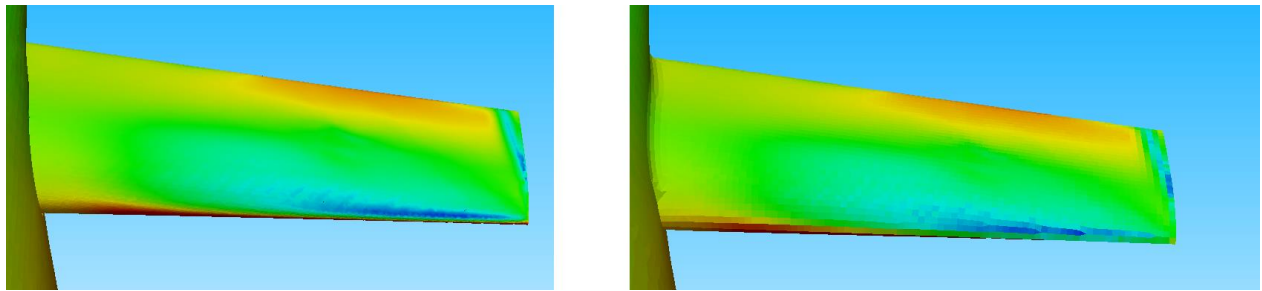


Figure 3. Pressure on the CFD hydrodynamic mesh (left), FEM element averaged pressure on structural mesh (right).

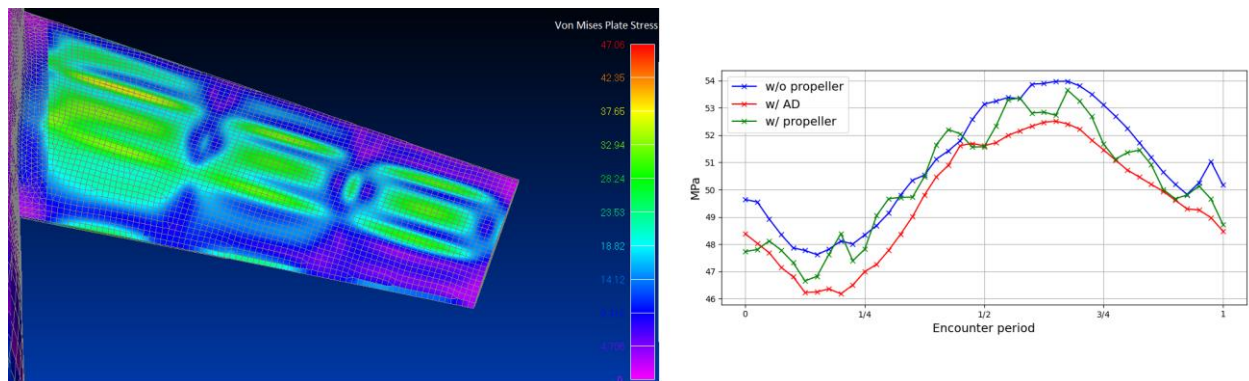


Figure 4. Stress at particular time-step (left), stress range for three propulsion models during encounter period (right).

## 5. Conclusion

This study investigated the influence of different propulsion models on the stresses of a PSS type of ESD. The aim of the study was to identify the necessary complexity in order to perform a valid long-term wave statistical analysis. The results have shown that the simplest model w/o propeller has sufficiently accurate results compared even to the most CPU demanding w/ propeller case. All this has shown that although there is a difference in the hydrodynamic loads emerging from the propeller suction effect, the final stress distribution remains quite similar with the stress peak roughly equal in all three cases. There is a slightly larger difference in stress ranges, but from the fatigue viewpoint this can be simply considered by including the calm-water propeller amplitude along the entire ship life cycle. Overall, the study has shown that the inclusion of the propeller is not mandatory when assessing the design wave parameters for the PSS ship motion induced loads.

## Acknowledgement

This research was supported by the Croatian Science Foundation under the project ‘Green Modular Passenger Vessel for Mediterranean (GRiMM)’ (Project No. UIP-2017-05-1253) and by the Hyundai Heavy Industries Co., Ltd., Ulsan, South Korea, within the project ‘A study on the structural integrity of the Energy Saving Devices (ESD) of the type Pre-Swirl Stator (PSS) and Flow Control Fin (FCF)’.

## Bibliography

- Bakica, A., Gatin, I., Vukčević, V., Jasak, H., & Vladimir, N. (2019). Accurate assessment of ship-propulsion characteristics using CFD. *Ocean Engineering*, *175*, 149–162. <https://doi.org/10.1016/j.oceaneng.2018.12.043>
- Bakica, A., Malenica, Š., & Vladimir, N. (2020). Hydro-structure coupling of CFD and FEM - Quasi-static approach. *Ocean Engineering*, *217*. <https://doi.org/10.1016/j.oceaneng.2020.108118>
- Beaudoin, M., & Jasak, H. (2008). Development of a Generalized Grid Interface for Turbomachinery simulations with OpenFOAM. *Open Source CFD International Conference*, 1–11. [papers3://publication/uuid/81CCD00D-DF48-4595-B591-C577955CEA06](https://doi.org/10.1016/j.oceaneng.2018.12.043)
- Jasak, H., Vukčević, V., & Gatin, I. (2015). Numerical Simulation of Wave Loads on Static Offshore Structures. *CFD for Wind and Tidal Offshore Turbines*, 95–105.
- Ju, H. B., Jang, B. S., Lee, D. B., Kim, H. J., & Park, C. K. (2018). A simplified structural safety assessment of a fin-typed energy saving devices subjected to nonlinear hydrodynamic load. *Ocean Engineering*, *149*(June 2017), 245–259. <https://doi.org/10.1016/j.oceaneng.2017.12.022>
- Kim, J. H., Choi, J. E., Choi, B. J., Chung, S. H., & Seo, H. W. (2015). Development of Energy-Saving devices for a full Slow-Speed ship through improving propulsion performance. *International Journal of Naval Architecture and Ocean Engineering*, *7*(2), 390–398. <https://doi.org/10.1515/ijnaoe-2015-0027>
- Lee, D. B., Jang, B. S., & Kim, H. J. (2016). Development of procedure for structural safety assessment of energy saving device subjected to nonlinear hydrodynamic load. *Ocean Engineering*, *116*, 165–183. <https://doi.org/10.1016/j.oceaneng.2016.02.038>
- Paboeuf, S., & Cassez, A. (2017). ESD structural issue - UPstream device. *International Shipbuilding Progress*, *63*(3–4), 291–314. <https://doi.org/10.3233/ISP-170135>
- Prins, H. J., Flikkema, M. B., Schuiling, B., Xing-Kaeding, Y., Voermans, A. A. M., Müller, M., Coache, S., Hasselaar, T. W. F., & Paboeuf, S. (2016). Green Retrofitting through Optimisation of Hull-propulsion Interaction - GRIP. *Transportation Research Procedia*, *14*(0), 1591–1600. <https://doi.org/10.1016/j.trpro.2016.05.124>
- Sakamoto, N., Kume, K., Kawanami, Y., Kamiirisa, H., Mokuo, K., & Tamashima, M. (2019). Evaluation of

hydrodynamic performance of pre-swirl and post-swirl ESDs for merchant ships by numerical towing tank procedure. *Ocean Engineering*, 178(February), 104–133. <https://doi.org/10.1016/j.oceaneng.2019.02.067>

Siemens. (2014). *NX NASTRAN User's Guide*.

Sun, Y., & Beckermann, C. (2007). Sharp interface tracking using the phase--field equation. *J. Comput. Phys.*, 220, 626–653.

Vukčević, V., Jasak, H., & Malenica, S. (2016a). Decomposition model for naval hydrodynamic applications, Part I: Computational method. *Ocean Eng.*, 121, 37–46. <https://doi.org/10.1016/j.oceaneng.2016.05.022>

Vukčević, V., Jasak, H., & Malenica, S. (2016b). Decomposition model for naval hydrodynamic applications, Part II: Verification and validation. *Ocean Eng.*, 121, 76–88. <https://doi.org/10.1016/j.oceaneng.2016.05.021>

Weller, H. G., Tabor, G., Jasak, H., & Fureby, C. (1998). A tensorial approach to computational continuum mechanics using object oriented techniques. *Computers in Physics*, 12, 620–631.

# Recommendations on application of the HRIC scheme for simulation of free surface waves

Jannes Berndt, Robinson Perić and Moustafa Abdel-Maksoud

Institute for Fluid Dynamics and Ship Theory, Hamburg University of Technology (TUHH), Am  
Schwarzenberg-Campus 4, 21073 Hamburg, Germany  
j.berndt@tuhh.de

## 1 Introduction

The simulation of multiphase flows with immiscible fluid phases is important for industrial flow simulations with ocean waves. Finite volume flow solvers employ the Volume-of-Fluid (VOF) method (Hirt and Nichols, 1981) to simulate multiple fluid phases on a single numerical grid. The properties of the fluid mixture are determined based on their volume fraction  $\alpha$  in the corresponding control volume (CV). The volume fraction  $\alpha$  takes a value between zero and one and indicates the phase distribution. It is zero if the corresponding phase is not present and one if only that phase and no other phase is present. The transport equation for the volume fraction of an incompressible fluid is given by

$$\frac{d}{dt} \int_V \alpha \, dV + \int_S \alpha (\mathbf{v} - \mathbf{v}_g) \cdot \mathbf{n} \, dS = \int_V q_\alpha \, dV, \quad (1)$$

with control volume (CV)  $V$ , surface  $S$ , fluid velocity  $\mathbf{v}$ , grid velocity  $\mathbf{v}_g$ , surface normal  $\mathbf{n}$  pointing outside the CV and volume fraction sources  $q_\alpha$ .

The key difficulty is to maintain a sharp interface between different phases. This problem results from the spatial discretization of volume fraction values on the CV faces for the approximation of the convective fluxes over the CV boundaries: First order upwind differences are unconditionally stable but diffusive and result in artificial numerical diffusion which can smear the interface. Downwind differences sharpen the interface but may result in numerical instability and unphysical interface distortions (see Leonard, 1991 and Muzaferija and Perić, 1998).

A widely used group of approaches for interface sharpening are the high resolution schemes based on the Normalized-Variable Diagram (NVD), such as ULTIMATE (Leonard, 1991), SURFER (Lafaurie et al, 1994), CICSAM (Ubbink and Issa, 1999), HRIC (Muzaferija and Perić, 1998) and STACS (Darwish and Moukalled, 2006). The general idea of high resolution schemes is the combination of upwind and downwind differences. The approaches differ in their choice of upwind and downwind schemes and their blending criteria.

The software implementation of these high resolution schemes usually includes certain case dependent parameters which can be modified by the user to optimize the interface-sharpening for the specific numerical setup. There are several publications that compare the performance of different high resolution schemes for particular applications (e.g. Darwish and Moukalled, 2006 and Waławczyk and Koronowicz, 2008). In general however, different schemes perform well for different applications and it is expected that most schemes can be tuned by a proper selection of the case dependent parameters to perform reasonably well. A significant drawback is the case dependency of these parameters. Optimum values are not readily available and a proper setup requires either a very experienced user or an extensive trial-and-error procedure.

*The aim of this work is to provide guidance for estimating the optimum value for the case dependent parameters of the HRIC interface-sharpening scheme in flow simulations with free-surface waves.* The findings are expected to apply to all interface-sharpening schemes based on the NVD diagram.

This paper focuses on the HRIC scheme in finite-volume-based flow simulations of free-surface waves. The HRIC scheme contains the user-defined parameter  $C_\theta$  (angle factor). This user defined parameter modifies the shape of the blending function based on the interface orientation relative to the cell face under consideration. With an extensive parameter study, the influence of the angle factor is analyzed for different cell sizes and cell aspect ratios of the numerical grid near the interface. Recommendations on appropriate choices for the angle factor for the simulation of relatively steep ocean waves are made based on the cell geometry.

## 2 High resolution interface capturing (HRIC) scheme and interface angle correction

The high resolution interface capturing (HRIC) scheme (Muzaferija and Perić, 1998) is based on the normalized variable definition describing the volume fraction  $\alpha$  at cell center C and cell face f relative to the volume fraction of the next cell in upwind and downwind direction (U and D; cf. Figure 1):

$$\tilde{\alpha}_C = \frac{\alpha_C - \alpha_U}{\alpha_D - \alpha_U}, \quad \tilde{\alpha}_f = \frac{\alpha_f - \alpha_U}{\alpha_D - \alpha_U} \quad . \quad (2)$$

In this way, the discretization of the normalized face value  $\tilde{\alpha}_f$  can be defined only as a function of the cell value  $\tilde{\alpha}_C$  as plotted in the Normalized-Variable Diagram (NVD) in Figure 2. Corrections are employed for Courant-numbers  $Co > 0.3$  and for the interface orientation  $\theta$ . The Courant-numbers in the previous study are  $< 0.3$  and the influence is therefore not included.

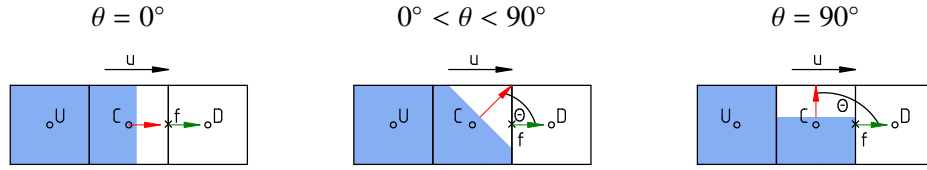


Fig. 1: One-dimensional volume fraction transport for different interface orientations  $\theta$  with two phases indicated by a blue and white shading;  $\theta$  is given by the angle between interface normal (red) and cell face normal (green); cell centers of upwind, center and downwind cell, defined by the velocity vector  $\mathbf{u}$ , are denoted by U, C and D respectively; the flux through the cell face f can be approximated by the wetted part of the face for small Courant-numbers

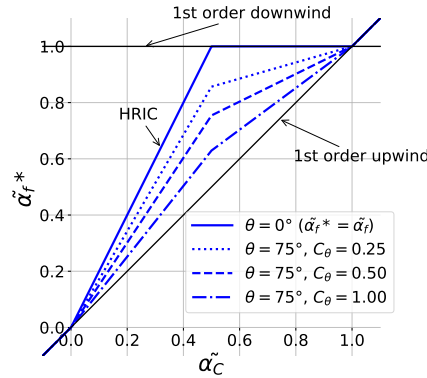


Fig. 2: Normalized-Variable Diagram for the HRIC scheme with the normalized corrected volume fraction on cell face  $\tilde{\alpha}_f^*$ , normalized volume fraction on cell center  $\tilde{\alpha}_C$  and exemplary curves for their dependency for different interface orientations  $\theta$  and angle factors  $C_\theta$ ; first order upwind and downwind schemes are included as black lines

The interface orientation is defined by the angle  $\theta$  between the normal vector of the free surface to the normal vector of the face under consideration as illustrated in Figure 1. If  $\theta$  approaches  $90^\circ$ , the face value  $\alpha_f$  is obtained by first order upwind differencing. This can be quickly understood by considering the fluxes of the blue shaded phase through cell face f in Figure 1.

The following blending function modifies the mixture between upwind and downwind differences as a function of  $\theta$ :

$$\tilde{\alpha}_f^* = \tilde{\alpha}_f \cdot \cos(\theta)^{C_\theta} + \tilde{\alpha}_C \cdot [1 - \cos(\theta)^{C_\theta}] \quad . \quad (3)$$

A larger angle factor  $C_\theta$  results in a curve closer to the diagonal and therefore a higher weighting of the first order upwind differencing schemes. The influence of different angle factors for the simulation is analyzed in the following chapters.

### 3 Simulation Setup

The numerical simulations are performed with the finite-volume-based flow solver Star-CCM+ 14.06.012 from Siemens. For the interface capturing, the Volume-of-Fluid (VOF) method (Hirt and Nichols, 1981) is used. A sharp interface is achieved with the high resolution interface sharpening HRIC scheme (Muzaferija and Perić, 1981) for discretization of the the volume fluxes over the control volume boundaries. The angle factor  $C_\theta$  influencing the blending function of upwind- and downwind schemes within the HRIC scheme is varied between 0 and 0.5 in steps of 0.05. Temporal discretization is of second order accuracy and the time step is chosen low enough to result in Courant-numbers of  $Co < 0.3$  for all cases.

Two-dimensional regular free surface-waves with wave height  $H = 0.15$  m and wave length  $\lambda = 1.5$  m are simulated. The wave period is  $T = 0.933$  s and the wave steepness is  $H/\lambda = 0.1$  (corresponding to 70 % of maximum steepness). Figure 3 (left) shows the computational domain which extends  $10\lambda$  in horizontal direction and  $10/3\lambda$  in vertical direction. The water depth is  $8/3\lambda$  resulting in *deep water* conditions. The coordinate system is set with its origin at the left side of the domain at stillwater level with the  $z$ -axis pointing positive upwards and  $x$ -axis pointing to the right. Waves traveling in positive  $x$ -direction are generated at the left side of the domain according to Stokes 5th-order wave theory. At the right boundary, a forcing zone with a width of  $2\lambda$  is attached to minimize wave reflections. The solution for velocity and volume fraction in the forcing zone is forced to a reference solution for the calm surface. The forcing strength and blending function are optimized according to (Perić, 2019) with an exponential blending function and a forcing strength of  $\gamma = 7.5$  s<sup>-1</sup>.

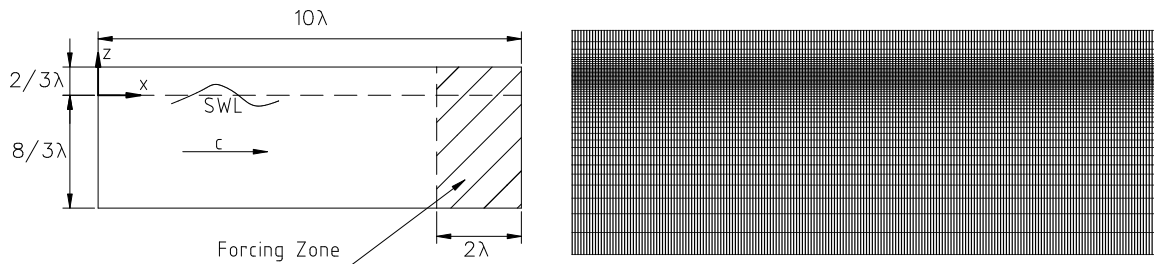


Fig. 3: Left: Domain geometry with dimensions given as multiples of the wave length  $\lambda$ , position of the stillwater line SWL and wave phase propagation direction indicated by vector  $c$ ; the forcing zone for wave damping is indicated by a hatched pattern; Right: numerical grid refinement level *very coarse*

A block-structured grid with local mesh refinement as depicted in Figure 3 (right) is used. Near the water surface, the reference grid (*very coarse*) has 5 cells per wave height and 20 cells per wave length. The grid size gradually increases with increasing distance from the water surface. In  $y$ -direction, the grid is only one cell wide resulting effectively in a two-dimensional case.

For mesh sensitivity studies differently refined meshes are generated based on the coarse mesh presented above (see Table 1). Firstly, the mesh is uniformly refined in both  $x$ - and  $z$ -direction with refinement factors  $1/\sqrt{2}$  (*coarse*),  $1/2$  (*medium*),  $1/(2\sqrt{2})$  (*fine*) and  $1/4$  (*very fine*) meaning that the cell size in each direction is multiplied by the refinement factor. To analyze the influence of the aspect ratio, also nonuniformly refined meshes are created by refining the cells only in  $x$ -direction or  $z$ -direction by factors of  $1/2$  and  $1/4$ .

mesh	refinement factors		total number of cells	cells per wave height	cells per wave length	aspect ratio
	$f_{r,x}$	$f_{r,z}$	$n_c$	$H/\Delta z$	$\lambda/\Delta x$	$\Delta x/\Delta z$
<i>very coarse</i>	1	1	9400	5	20	2.5
<i>coarse</i>	$1/\sqrt{2}$	$1/\sqrt{2}$	18678	7	28.3	2.5
<i>medium</i>	$1/2$	$1/2$	37600	10	40	2.5
<i>fine</i>	$1/(2\sqrt{2})$	$1/(2\sqrt{2})$	74712	14	56.6	2.5
<i>very fine</i>	$1/4$	$1/4$	150400	20	80	2.5
<i>refined X 2.0</i>	$1/2$	1	18800	5	40	1.25
<i>refined X 4.0</i>	$1/4$	1	37600	5	80	0.625
<i>refined Z 2.0</i>	1	$1/2$	18800	10	20	5
<i>refined Z 4.0</i>	1	$1/4$	37600	20	20	10

Table 1: Mesh parameters;  $f_{r,x}$  and  $f_{r,z}$  denote the refinement factors in  $x$ - and  $z$ -direction, respectively -  $f_{r,x} = f_{r,z}$  indicates uniform refinement;  $\Delta x$  and  $\Delta z$  are the cell sizes in  $x$ - and  $z$ -direction near the water surface

## 4 Results and Discussion

The numerical simulations are analyzed in terms of wave height losses and distortion of the free surface. For this purpose, the free surface between  $x = 6\lambda$  and  $7\frac{1}{3}\lambda$  is examined for a time interval of one wave period  $T$  after  $t = 12.5T$  simulation time. The time interval is selected so that the wave energy, propagating with the group velocity  $c_g = 0.5c$ , in terms of phase velocity  $c$ , must have traveled from the wave inlet through the region of consideration.

The wave height  $H(x)$  at a specific  $x$ -coordinate is calculated as the difference of maximum and minimum surface elevation  $\zeta$  over one wave period  $T$ . Wave height losses are given by the ratio of the mean wave height  $H$  (see Figure 5 left) to the wave height  $H_0$  prescribed at the inlet boundary. Distortions are quantified by the maximum wave height differences  $\Delta H_{\max} = H_{\max} - H_{\min}$  (see Figure 5 right). Results for  $H/H_0$  and  $\Delta H_{\max}/H_0$  in Figure 4 show that a large angle factor  $C_\theta$  increases the wave height losses. These result from increased artificial diffusion due to a higher weighting of the upwind scheme for the approximation of the volume fraction face values as described in section 2, effectively resulting in a situation with the volume fraction being advected in horizontal direction faster than the propagation speed of the wave itself as shown in Figure 6 (left). Also angle factors approaching to zero (no or small interface orientation correction) result in wave height losses due to the reduced volume fraction transport in vertical direction. Minimum losses are observed for angle factors between  $C_\theta = 0.05$  and  $0.20$  depending on the mesh refinement level.

The local changes of the wave height  $\Delta H_{\max}$  are mostly reduced with increasing angle factors  $C_\theta$ . The explanation is the lower weighting of the downwind (compressive) scheme. If the compressive scheme is weighted too high however (smaller  $C_\theta$ ), distortions of the free surface occur as shown in Figure 5 (top right) and Figure 6 (right).

The nonuniform refinement demonstrates that cells with a small aspect ratio  $\Delta x/\Delta z$  (*refined X 2.0* and *refined X 4.0* in Figure 4) produce lower wave height losses but significantly higher wave height differences. Second can also be explained with the fact that the HRIC scheme aims to restrict the interface to one cell. However, a free surface with a relatively gentle slope as presented in Figure 6 (right) can geometrically not be limited to one cell in horizontal direction for cells an aspect ratio close to one. This can only be counteracted by a large weighting of the upwind scheme for the face value approximation (larger  $C_\theta$ ).

Examples of the surface elevation plots for a case with significant wave height diffusion (A), free surface distortion (B) and close-to-optimum parameters are presented in Figure 5. The corresponding points in Figure 4 are marked by a black circle and the letter A, B and C.

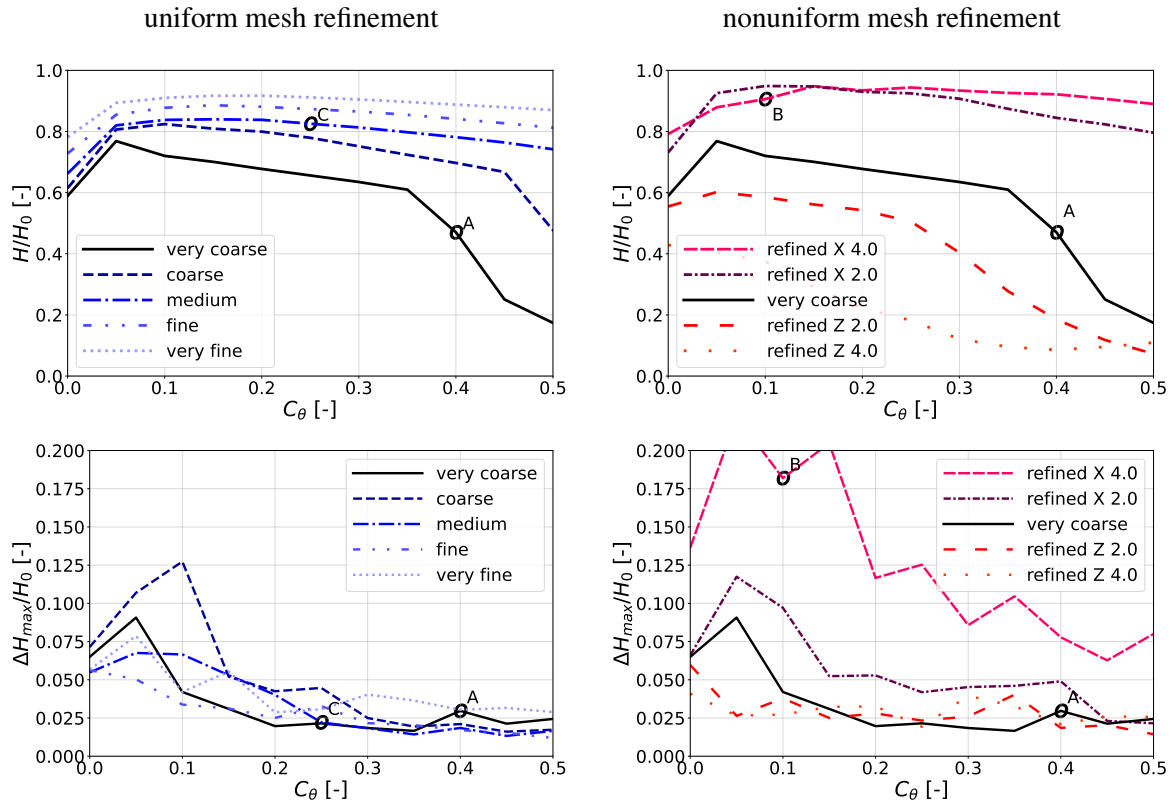


Fig. 4: Wave height  $H$  (top row) and local wave height changes  $\Delta H_{\max} = H_{\max} - H_{\min}$  (bottom row) per reference wave height  $H_0$  as a function of angle factor  $C_\theta$  evaluated within  $6\lambda$  and  $7\frac{1}{3}\lambda$  for a time interval  $12.5T$  to  $13.5T$  in terms of wave period  $T$ ; left column: uniform refinement levels, right column: nonuniform refinement levels; for  $\Delta H_{\max}/H_0 > 0.05$ , noticeable disturbances in the wave height envelope occur; for  $H_{\max}$  and  $H_{\min}$  see Figure 5

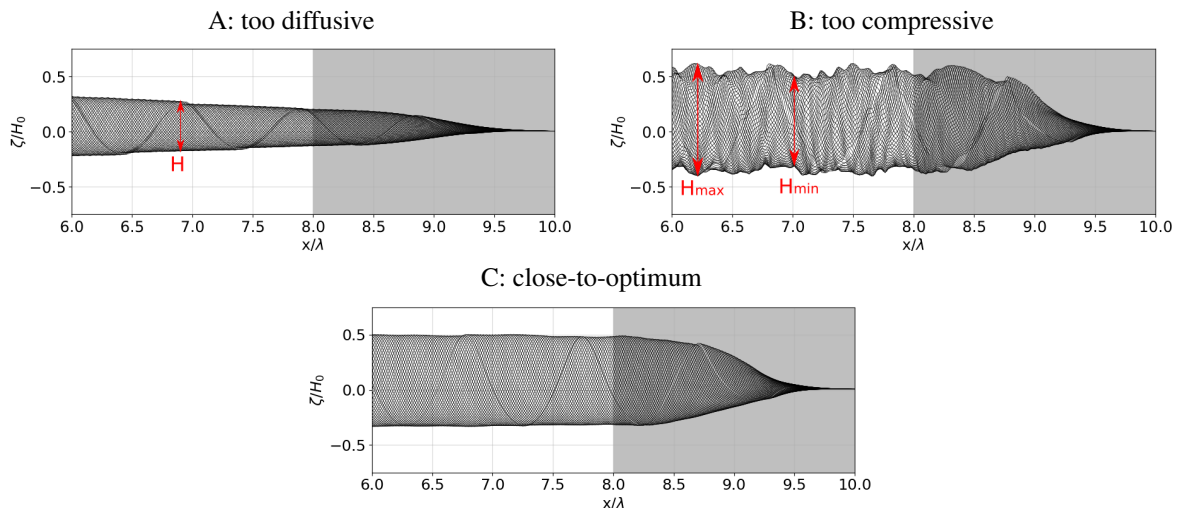


Fig. 5: Surface elevation as a function of wave propagation direction  $x$  for equally spaced time intervals during one wave period near the right side of domain; the forcing zone for wave damping is shaded in grey; smooth surface but significant wave height losses (top left), seriously distorted surface with low wave height losses (top right) and close-to-optimum tuning (bottom); note that even for optimum tuning some loss in wave height occurs due to discretization and iteration errors, which vanish for finer discretization



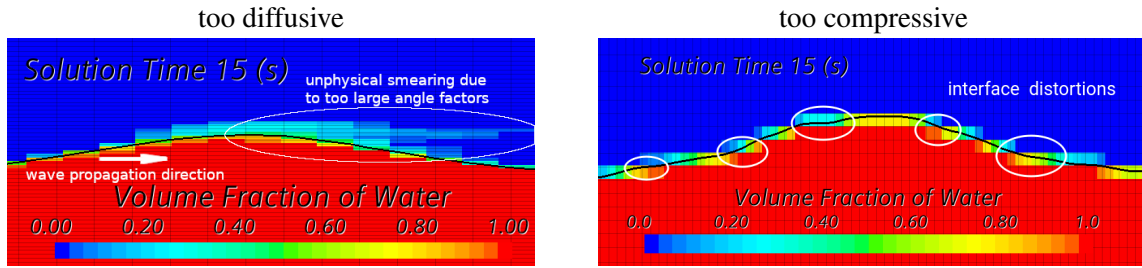


Fig. 6: Volume fraction field with unphysical diffusion of the wave crest (left) and interface distortion due to a small cell aspect ratio  $\Delta x/\Delta z$ , in terms of cell sizes  $\Delta x$  and  $\Delta z$  in  $x$ - and  $z$ -direction respectively (right); the black line indicates the approximated free-surface

The optimum angle factor depends on the cell size and especially on the aspect ratio of the cells in the vicinity of the interface. For a finer mesh, optimum angle factors are slightly higher as the problem of interface distortion is increased. Wave height losses increase for larger angle factors. For the present case of a wave steepness of  $H/\lambda = 0.1$  and a cell aspect ratio of  $\Delta x/\Delta z = 2.5$ , the optimum angle factor was ca. 0.1 for the *very coarse* and *coarse* mesh and 0.15 – 0.25 for the finer meshes. For an aspect ratio lower than 2.5 (*refined Z 2.0* and *refined Z 4.0*), the wave height losses increase by upto 90 %.

## 5 Conclusion

This work demonstrated that the interface-sharpening scheme HRIC contains a case-dependent parameter, the angle factor  $C_\theta$ . If  $C_\theta$  is not optimally selected, disturbances in the free-surface elevations can occur in flow simulations with wave propagation, leading to a loss in wave height and distortions in the wave height envelopes, which can produce substantial errors in the results (local changes in wave height of 20 % or more resulting in 44 % or more changes in wave induced forces in the results). Theoretical considerations suggest that these problems occur for other NVD-based interface-sharpening schemes as well. A systematic procedure was presented to determine the optimum value for  $C_\theta$  via computationally inexpensive 2D-flow simulations. For waves with steepness  $H/\lambda = 0.1$ , the optimum  $C_\theta$  was ca. 0.1 on coarser and 0.15 – 0.25 on finer grids provided that the cell aspect ratio  $\Delta x/\Delta z$  is about 2.5. A more extensive parameter study for other wave steepnesses is planned for future work.

## Acknowledgements

The authors gratefully acknowledge the financial support by the Deutsche Forschungsgemeinschaft (DFG) (project AB 112/11-2) for this study.

## References

- Darwish, M., Moukalled, F., 2006. Convective Schemes for Capturing Interfaces of Free-Surface Flows on Unstructured Grids. *Numer. Heat Tr. Part B-Fundamentals*, 49(1), 19-42.
- Ferziger, J., Perić, M., 2002. *Computational Methods for Fluid Dynamics*, Springer, Berlin.
- Hirt, C. W., Nichols, B. D., 1981. Volume of fluid (VOF) method for the dynamics of free boundaries. *J. Comput. Phys.*, 39(1), 201-225.
- Lafaurie, B., Nardone, C., Scardovelli, R., Zaleski, S., Zanetti, G., 1994. Modelling Merging and Fragmentation in Multiphase Flows with SURFER. *J. Comput. Phys.*, 113, 134-147.
- Leonard B.P., 1991, The ULTIMATE conservative difference scheme applied to unsteady one-dimensional advection, *Comput. Method. Appl. Mech. and Eng.*, 88, 17-74.
- Muzaferija S., Perić, M., Sames, P., Schelin, T., 1998, A two-fluid Navier- Stokes solver to simulate water entry, *Proc. Twenty-Second Symposium on Naval Hydrodynamics*
- Perić, 2019. Minimizing undesired wave reflection at the domain boundaries in flow simulations with forcing zones. Doctoral dissertation, Technical University of Hamburg, Germany.
- Ubbink, O. ,Issa, R. I. , 1999. A Method for Capturing Sharp Fluid Interfaces on Arbitrary Meshes. *J. Comput. Phys.*, 153, 26-50.
- Wacławczyk, T. , Koronowicz, T. , 2008. Comparison of CISAM and HRIC high-resolution schemes for interface capturing. *J. Theor. and Appl. Mech.* , 46, 325-345.

# Chronological and Critical Review of Steady Free-Surface Flow Computations

**Volker Bertram**, DNV, Hamburg/Germany, [volker.bertram@dnv.com](mailto:volker.bertram@dnv.com)  
**Milovan Peric**, CoMeT GmbH, Bad Reichenhall/Germany, [milovan@comet-cfd.de](mailto:milovan@comet-cfd.de)

The beginning of computational methods in shipbuilding can be seen with the work of the Australian mathematician John Henry Michell, who in 1898 proposed an integral expression to compute the wave resistance. Michell's "wonderful" integral delighted mathematicians for at least 100 years after his publication, even though Michell's thin-ship theory (including all subsequent refinements) is in essence unacceptably wrong for real ship geometries and ship speeds. (Michell's thin ship theory is very good if your ship looks like a razorblade or goes at 200+ knots.) On rare occasion, it still comes in handy. An example may be the prediction of the wave resistance of a submarine near the free surface with a streamlined snorkel piercing the free surface. The snorkel itself has a Froude number around 2 and then thin-ship theory can be used in good conscience (and the snorkel does not need to be geometrically modelled in the CFD-model for the submarine.) *Söding (1995)* gives a FORTRAN code to compute Michell's integral.

After Michell, many other great names developed wave resistance theories, slender body, Kelvin-Neumann conditions, etc. Instead of razor blades, the research community offered Wigley hulls as computationally friendly options to industry. But industry stubbornly refused to build ships that were computationally friendly like Wigley hulls and insisted on researchers adapting to reality, rather than the other way around. That didn't impress most researchers much. We were too busy discussing which of our wrong assumptions was least wrong. Should it be consistently wrong on all counts, or just wrong on the water surface and right on the ship? The debates of the 1970s and 1980s were on whether a Neumann-Kelvin model (Neumann condition correct on hull, but linearized free-surface condition on water surface) was an improvement or not.

In the meantime, *Hess and Smith (1964)* had opened the door to panel methods and *Dawson (1977)* had pioneered a solution for enforcing downstream wave radiation in panel codes, fuelling the arguments of the Neumann-Kelvin faction. This apparent Gordian knot was finally cut in the late 1980s with so-called fully nonlinear wave resistance codes, which fulfilled the Neumann condition on the (dynamically trimmed) hull and the nonlinear free-surface condition (which was iteratively approximated through a consistent linearization around the previous solution).

*Jensen (1988)* was one of a new generation of numerical ship hydrodynamicists to cut the Gordian knot, presenting a wave resistance model that was both consistent on the hull and the free surface. Key breakthroughs were (i) the new free-surface condition that allowed iterative fulfilment of the nonlinear condition, again consistently at the free surface and (ii) a new technique to fulfil the radiation condition that waves travel only downstream. The origins of this "shifting technique" shed characteristic light on *Söding* and how research happened 'back then'. "One day, Prof *Söding* came into Jensen's office, handed him a piece of paper and said: Try this! It was the idea of shifting the collocation points by one panel length. It worked like a charm. Simpler and more accurate than anything else tried before. To this date, we don't know how the master [Prof. *Söding*] had this inspiration," Gerd Jensen in personal communication. Such second-generation wave resistance codes which became quickly state of the art in ship design, were adopted by leading model basins such as MARIN, SSPA, HSVA, and INSEAN.

But, alas, fully nonlinear wave resistance codes are not truly fully nonlinear. The fundamental equation neglects viscosity, thus modelling propellers in detail makes no sense, and breaking waves cannot be handled either. Too bad that all ships have propellers and feature breaking waves. We needed to move to the next game level, and we did so in the late 1990s, when NuTTS started in 1998 to bring a new generation of marine CFD-researchers together.

CFD became a research field in the late 1960s. First commercial CFD software appeared in the 1980s including codes like PHOENICS, FLUENT, STAR-CD, CFX, TASCFLOW, and FLOW3D. By today's standards, these codes were very limited in terms of complexity of geometry and physics, but they could handle viscous effects and turbulence by solving the Reynolds-averaged Navier-Stokes equations (RANSE) with a choice of turbulence models. Applications were also severely limited by the available computer power in those days.

The first research for RANSE solutions with wave-making for ships appeared in the late 1980s. By the late 1990s various research groups also presented results for ships free to trim and sink. The state of the art in marine CFD has been documented in a series of benchmark workshops. Initially, the focus was on the boundary layer and turbulence modelling, with detailed validation data coming from wind tunnel tests, i.e. single-phase flows were studied with focus on predicting forces and important flow features. Fig.1 shows an example of comparison of experimental data and simulation results.

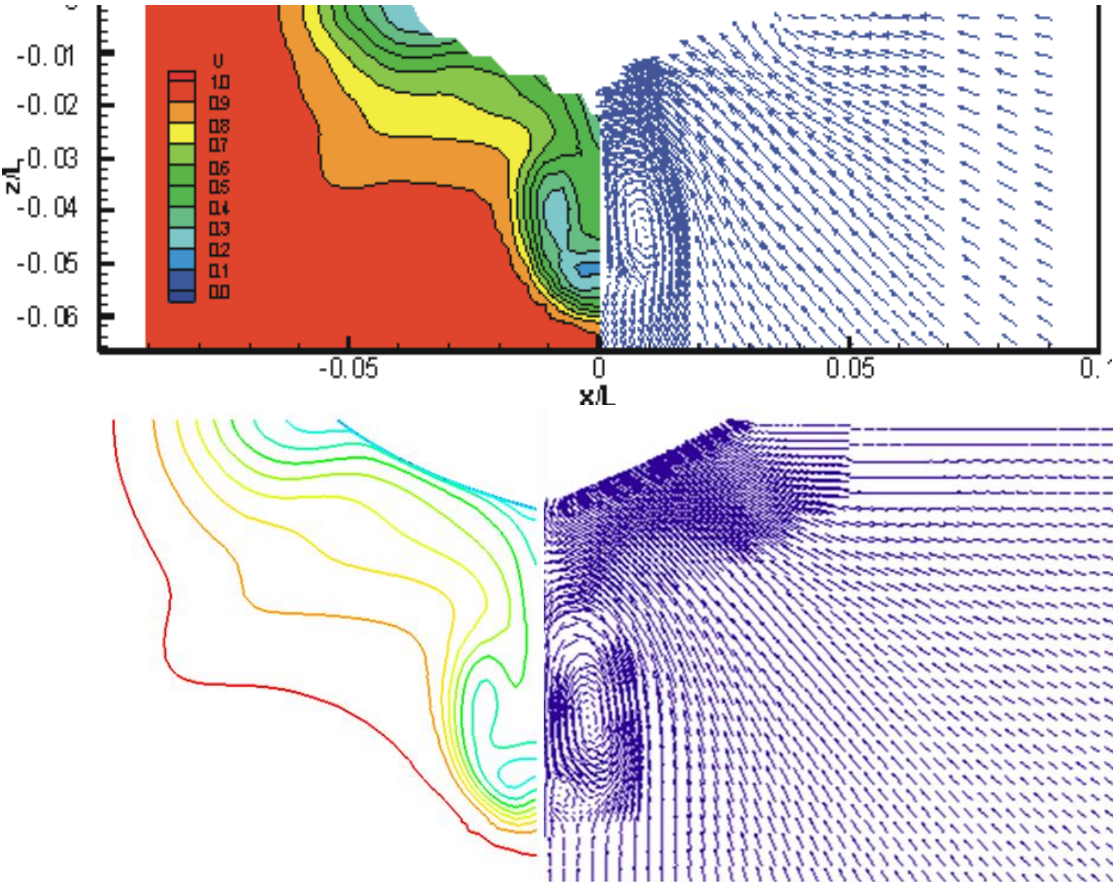


Fig.1: Prediction of secondary flow in the wake of KLVCC hull model: data from wind tunnel test (top) and the result of CFD-simulation using Reynolds-stress turbulence model (bottom)

Turbulence modelling was in the “villain” of the 1980s and 1990s. Unsatisfactory results were often blamed on turbulence modelling. The CFD validation workshops shed more light on adequacy and inadequacy of turbulence modelling for marine flows, Figs.1-3. Arguably, the importance of the ability of turbulence models to predict features like those shown in Fig.1 has been over-rated. Turbulence models play a significant role in predicting the flow structures (like the kidney-shaped isolines of streamwise velocity component showed in Fig.1) in the wake of a bare hull. Best prediction is usually provided by Reynolds-stress turbulence models, which solve 7 additional equations and converge very slowly because of the stiff equation system. However, the propeller behind the ship dominates the flow field in the aftbody and reduces the importance of the turbulence modelling. It is often more important to account for appendages and other geometry details, and to refine the grid locally where higher resolution is needed, than to use a sophisticated turbulence model.

For at least 10 years now, the user-friendly eddy-viscosity type turbulence models offered as standard options by commercial CFD software have proven sufficient for predicting resistance, trim and sinkage of ships.

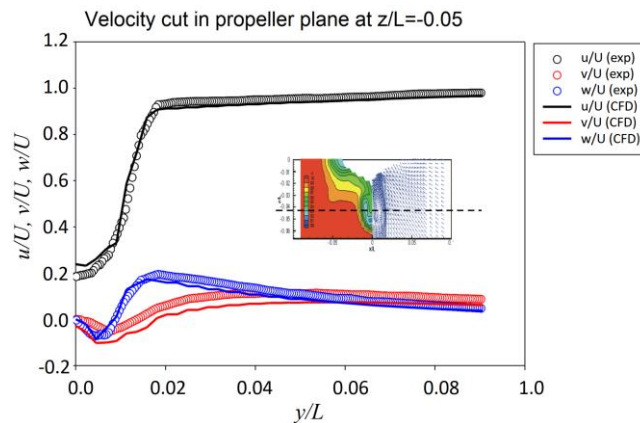


Fig.2: Measured and predicted velocity profiles at one horizontal cut in propeller plane

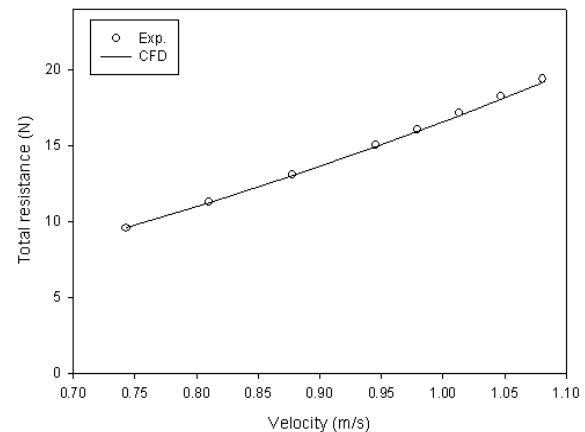


Fig.3: Measured and predicted resistance for KLVCC without free surface

The focus of the CFD validation workshops changed to free-surface simulations with the Gothenburg 2000 workshop, where CFD simulations for a containership geometry (Hamburg Test Case) were benchmarked against detailed model basin resistance tests, *Larsson et al. (2000)*. The early attempts in free-surface RANSE simulations for ships featured wave patterns that looked a bit like Christmas trees. Due to insufficient grid resolution and simplified free-surface models there was too much numerical (unphysical) damping and the divergent waves disappeared rapidly behind the ship, even if the wave profile directly at the hull was mostly captured quite well. ‘Mostly’ meant that directly at the bow CFD and experiments differed often; this gave rise to discussions on what was documented from experiments and where the free surface was to be defined when larger areas of foam on top of a breaking waves appeared at the bow. But it also gave insight into numerical schemes and required grid resolution to capture crisp wave crests. Collectively we progressed.

Interface-tracking algorithms were replaced by interface-capturing algorithms which allowed significant progress whenever larger wave breaking was involved. While ruling supremely for unsteady breaking waves, such as in sloshing and seakeeping applications, for steady free-surface flow computations, the progress was moderate. *Peric and Bertram (2011)* describe the state of the art a decade ago: “Interface-capturing methods (volume of fluid, two-phase flow, level-set, etc.) allow the simulation of highly nonlinear free-surface flows. Where the two fluids (typically water and air) are not expected to mix, a sharp interface (within one control volume) can be obtained. This minimizes numerical mixing. [...] Despite the significant progress in free-surface modelling, research continues in this field, as the modelling of breaking waves can still be improved in terms of air mixing and turbulence interaction with the free surface. In regions, where in reality white foam appears (a mix of air and water), current CFD simulations show smeared surfaces and predict the propagation of these waves less accurately”, Fig.4.

The last decade may be described as a decade of streamlining the commercial application of steady free-surface RANSE applications for ships. Large-scale applications of ‘resistance & propulsion’ CFD simulations include:

- Ship hull optimization (incl. Design of Experiments) often combines low-fidelity simulations (such as wave resistance codes) for a wider search with high-fidelity CFD simulations for final, limited search and/or accurate power prediction for the found optimum hull, *Bertram and Campana (2020)*.
- Trim optimization tools vary speed, trim and draft to generate hydrodynamic ‘knowledge bases’. Using response surfaces, these knowledge bases then allow quasi-instantaneous

interpolation to give operational decision support for most energy efficient trim of ships, *Bertram and Hochkirch (2015)*.

- The same type of hydrodynamic ‘knowledge bases’ is needed in performance monitoring, where it is often referred to as ‘base lines’, *Bertram (2020)*.

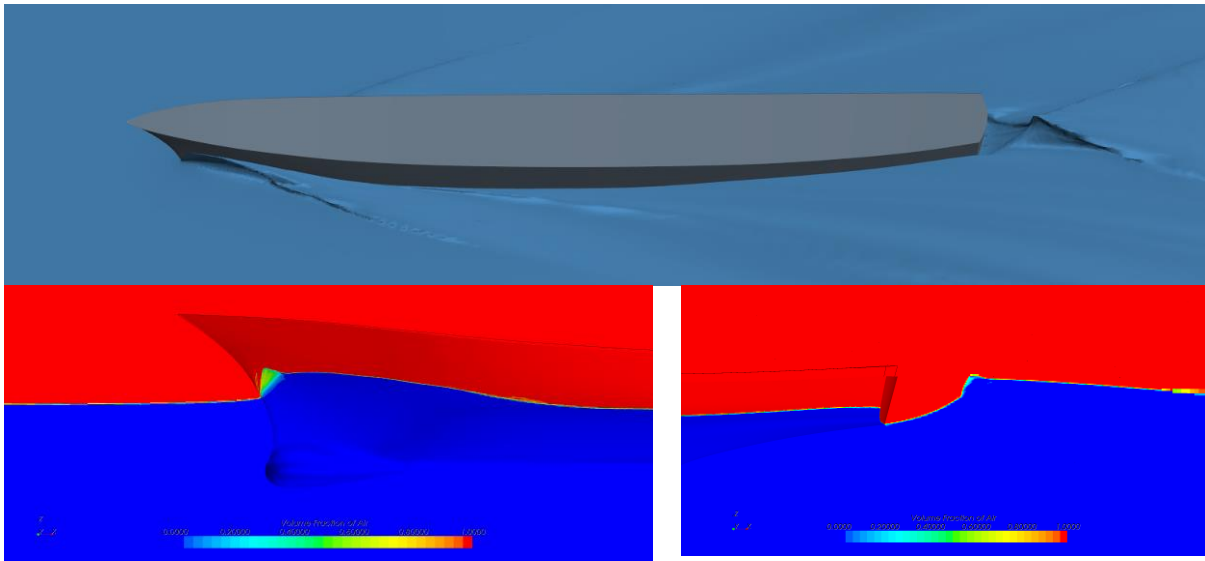


Fig.4: Computed wave field around DTMB 5415 (destroyer geometry; upper picture); smeared interface at bow and stern where waves break, sharp interface elsewhere (lower pictures with details at bow and stern); *Peric and Bertram (2011)*

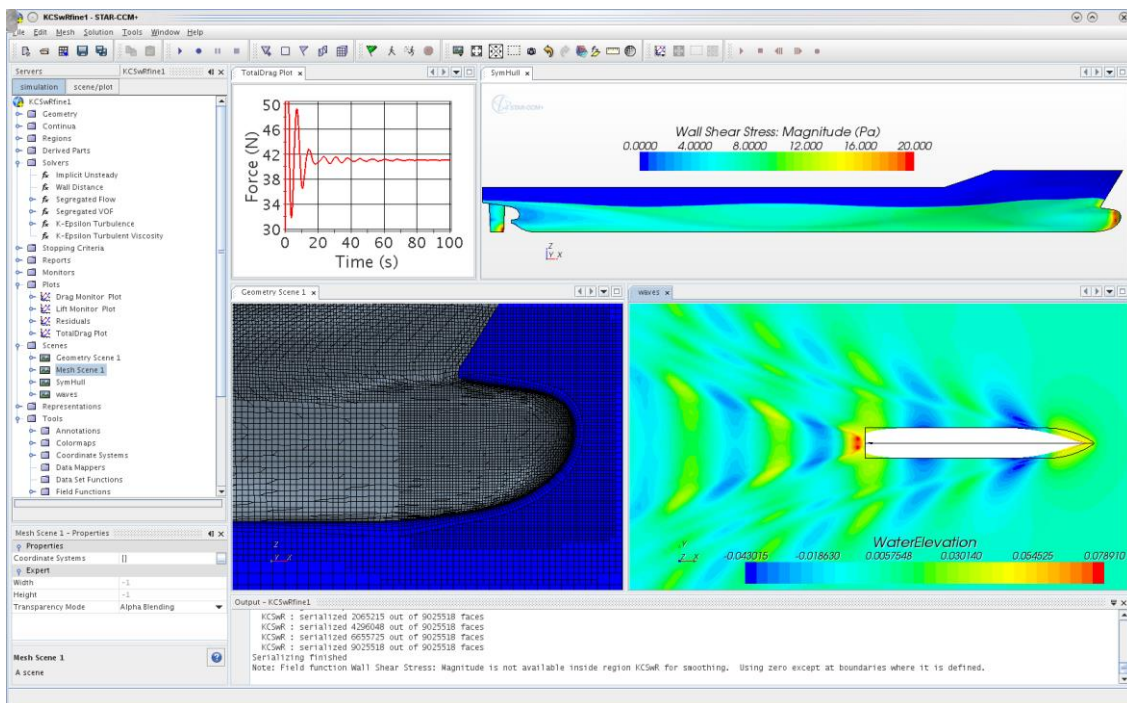


Fig.5: Analysis tools integrated in a user-friendly interface allow simulation-driven designs

Various developments have contributed to bringing down costs and response times as prerequisites for large-scale commercial applications:

- (Largely automatic) Grid generation has been improved, making it easier to generate high-quality grids for accurate CFD simulations. This includes tools for automatic and user-friendly manual repair of CAD models (which are often imperfect IGES files), as well as tools

for automatic generation of polyhedral, trimmed hexahedral or extruded meshes. As grid generation used to be the most time-consuming part of CFD analyses driving also the costs (as man-time accounted for the largest part of overall CFD project costs), the significant improvement in grid generation has been crucial for cost and response time improvements in the last decade.

- Adaptive meshes and local grid refinement algorithms have matured. The main impact at first glance is on computational times, but for adaptive grids, also the initial grid generation is often easier and faster.
- License and hardware costs have come down. OpenFOAM, first released in 2004, played an important part in bringing down CFD license costs, especially for large-scale parallel licenses. But also the trend towards renting parallel computing capacity along with pay-by-demand licence fees has brought down costs significantly for occasional users. Along with more user-friendly processes and often free instructions in on-line tutorials and webinars, the ‘democratization’ of CFD simulations has opened the field to a much wider audience.
- Design tools like CAESES offer integrated ship design environments, *Harries (2020)*. The integrated design environment combines ship hull description using parametric modelling, interfaces to most modern CFD solvers, optimization algorithms, and software to handle process management across various operating systems. The user-friendliness of this approach has certainly lowered thresholds in using CFD by designers for design of experiments and optimization applications.

BERTRAM, V. (2020), *CFD for Performance Monitoring – Current Capabilities and Limits*, 5<sup>th</sup> Hull Performance & Insight Conf. (HullPIC), Hamburg, pp.111-119

BERTRAM, V.; CAMPANA, E.F. (2020), *Ship Hull Optimization – An Attempt to Determine Position and Course of the State of the Art*, 19<sup>th</sup> COMPIT Conf., Pontignano, pp.271-279, [http://data.hiper-conf.info/compit2020\\_pontignano.pdf](http://data.hiper-conf.info/compit2020_pontignano.pdf)

BERTRAM, V.; HOCHKIRCH, K. (2015), *Optimization for ship hulls - Design, refit and operation*, 6<sup>th</sup> Int. Conf. on Computational Methods in Marine Engineering (MARINE), Rome, pp.210-217

DAWSON, C.W. (1977), *A Practical Computer Method for Solving Ship-Wave Problems*, 2<sup>nd</sup> Int. Conf. Numerical Ship Hydrodynamics, Berkeley, pp.30-38

HARRIES, S. (2020), *Practical Shape Optimization Using CFD: State-Of-The-Art in Industry and Selected Trends*, 19<sup>th</sup> COMPIT Conf., Pontignano, pp.196-222, [http://data.hiper-conf.info/compit2020\\_pontignano.pdf](http://data.hiper-conf.info/compit2020_pontignano.pdf)

HESS, J. L.; SMITH, A. M. O. (1964), *Calculation of nonlifting potential flow about arbitrary three-dimensional bodies*, J. Ship Research 8, pp.22-44

JENSEN, G. (1988), *Berechnung der stationären Potentialströmung um ein Schiff unter Berücksichtigung der nichtlinearen Randbedingung an der Wasseroberfläche*, PhD Thesis, Report 484, Institut für Schiffbau, University Hamburg

LARSSON, L.; STERN, F.; BERTRAM, V. (Ed.) (2000), *Gothenburg 2000 Workshop*, Chalmers Technical University, Gothenburg

PERIC, M.; BERTRAM, V. (2011), *Trends in Industry Applications of CFD for Maritime Flows*, 10<sup>th</sup> COMPIT Conf., Berlin, pp.8-18, [http://data.hiper-conf.info/compit2011\\_berlin.pdf](http://data.hiper-conf.info/compit2011_berlin.pdf)

SÖDING, H. (1995), *Wave resistance by Michell integral*, Ship Technology Research 42, pp.163-164

# Verification Study of Sliding and Overset Grid Methods using the Method of Manufactured Solutions on a Wind Turbine flow

Tiago Gomes\*, Sébastien Lemaire<sup>†</sup> §, Guilherme Vaz<sup>‡</sup> <sup>†</sup> \* ¶, and Fernando Lau\*

\*Instituto Superior Técnico, Lisboa/Portugal, <sup>†</sup>Maritime Engineering Group, University of Southampton, Southampton/UK, <sup>‡</sup>WavEC, Lisbon/Portugal, § MARIN, Wageningen/Netherlands,

<sup>\*</sup>ISMT, Universität Duisburg-Essen, Duisburg/Germany, ¶ blueOASIS, Lisbon/Portugal  
tiago.gomes.21@tecnico.ulisboa.pt

## 1 Introduction

Sliding Grids (SG) and Overset Grids (OG) are two CFD methods for discretizing the domain with several sub-grids, with the potential of: 1) simplifying the mesh generation process; 2) increase their individual quality; 3) improve accuracy of unsteady simulations with moving objects. Their fundamental difference lies on the sub-grid placement, fitted into each other (SG) or overlapped (OG), which ends up impacting the information transfer mechanism that couples them. During the last few years, both methods have been specially useful in many areas, including the simulation of offshore wind turbines, where a Sliding Grid might be used to accommodate the motion of the rotor and an Overset Grid to capture the overall movement of the platform with the ocean waves (Tran and Kim, 2018). However, very few studies exist comparing SG with OG, despite their versatility and interchangeability in various situations. Even within the available literature, as (Francois et al., 2011), they mostly focus on practical test cases, with no Code Verification (Eça and Hoekstra, 2013) performed. Therefore, a detailed analysis is necessary, where the flow analytical solution is known, so that discretization errors can be evaluated in isolation. For that an inedit wind turbine flow manufactured solution is designed and used, taking advantage of the Method of Manufactured Solutions (Roache, 2019) to produce an arbitrarily complex flow with a known analytical solution. With it, Code Verification can be performed, to assess and compare the impact of SG and OG in typical wind turbine flow conditions. Based on this work, some more light can be shed on possible improvements and good practices for industrial uses, potentially extendable to other CFD solvers with similar capabilities.

## 2 ReFRESKO

ReFRESKO (Vaz et al., 2009) is a CFD solver based on a finite-volume discretization with cell-centered collocated variables and unstructured grids, capable of handling hanging nodes. It solves the unsteady, multi-phase and incompressible RANS equations, in addition to turbulence models and volume-fraction transport equations for each phase. Moreover, it has the capability to simulate moving objects through the use of Sliding Grids and more recently the Overset Grids method (Lemaire et al., 2021). These methods depend on the interpolation schemes implemented, with a considerable number of options available in the solver. Some of them include Inverse Distance (1st order), Nearest Cell Gradient (2nd order) and Least Squares ( $n$ -th order with a  $n - 1$ th degree polynomial) (Lemaire et al., 2021).

## 3 Sliding Grids Method

The Sliding Grids method uses several sub-grids to discretize the domain (Rai, 1985). Despite being individually generated, they have a certain degree of dependence, since they need to fit into each other to cover the entire domain. Therefore, the sub-grids communicate between each other through the interfaces, which might slide relative to one another in the case they are animated. Considering this, they are inherently limited to simple movements, including unidirectional translation or rotation over cylindrical or conical surfaces of revolution.

A key aspect of the implementation of this method is the information transfer between each sub-grid through the interface. Several methods exist in the literature, but in ReFRESKO the one implemented is based on Halo Cells (Ramírez et al., 2015). In the Halo Cell method the new cell center is projected from a given parent boundary cell at the interface to the other contiguous sub-grid. The properties of the flow at the halo cell center are interpolated from a stencil of surrounding cells in the sub-grid to which it was projected to, based on the selected interpolation scheme. These will act as Dirichlet boundary conditions,

closing the respective system of equations and coupling the sub-grids. In ReFRESHCO the halo cells are determined on-the-fly, being by default projected over the line connecting the parent cell center and the respective face center. Therefore, no eccentricity exists between both. Moreover, the halo cell is defined to have the same size as the parent cell.

#### 4 Overset Grids Method

The Overset Grids method (Benek et al., 1986) also uses several sub-grids to discretize the domain. However, since they are overlapped, they don't need to fit into each other, potentially easing the grid generation process and allowing virtually any type of movement because of that same characteristic. Nevertheless, they are known to be numerically more expensive and also more complex to implement than the Sliding Grids method (Francois et al., 2011).

This method uses the Domain Connectivity Information (DCI), which assigns to each cell in the domain one of three possible status: *In*, *Fringe* or *Hole* Cell. *In* Cells are regular, active cells in the domain. *Hole* Cells are the ones that are ignored by the solver, since they are substituted by cells of other sub-grid that is overlapping that region or because they are just outside the domain. Finally, *Fringe* cells are placed in between the two other types of cells, receiving the interpolated information and coupling the different sub-grids.

#### 5 Wind Turbine MMS Test Case

The wind turbine flow solution was created based on the Method of Manufactured Solutions (MMS). A CFD simulation of an Actuator Disk was used as reference to model the velocity and pressure fields, which in turn had as inputs the reference operating conditions of the NREL 5MW (Jonkman et al., 2009) wind turbine: free-stream flow velocity,  $V_0$ , of 11.4 m/s, rotor angular speed,  $\omega$ , of 1.2698 rad/s and respective values of thrust and torque. The  $z$  axis represents the flow direction, perpendicular to the rotor disk.

After extensive testing, Equation (1) was obtained, providing a  $V_z$  field with reasonable features and a power net flux,  $P_{net}$ , over the selected domain of around 5.008 MW (harvested). This process included tuning the values of the blending functions in the axial and radial directions, Equations (3) and (4), respectively, where  $R_a$  is the radius of the wind turbine, 63 meters. In order to respect the continuity equation, the integral of Equation (2) was solved using the algebraic toolbox Sympy, obtaining the radial velocity distribution  $V_r$ . While the tangential component  $V_\theta$  did not contribute to mass conservation, it was not considered to simplify the solution process.

$$V_z(r, z) = V_0 - 0.2715 \cdot V_0 \cdot \gamma_z(z, 0.7, 4.0) \cdot \gamma_r(r, 1.2) + 0.2000 \cdot V_0 \cdot \gamma_z(z, 0.7, 4.0) \cdot \gamma_r(r, 2.5) - 0.1000 \cdot V_0 \cdot \gamma_z(z, -2.0, 1.0) \cdot \gamma_r(r, 3.0) \quad (1)$$

$$V_r = \frac{1}{r} \left( \int_0^r -r \frac{\partial V_z}{\partial z} dr \right) \quad (2)$$

$$\gamma_z(z, a, b) = \frac{1}{1 + e^{\left(\frac{z}{R_a} + a\right) \cdot b}} \quad (3) \quad \gamma_r(r, c) = e^{\left(-c \cdot \frac{r}{R_a}\right)^2} \quad (4)$$

As for the pressure field,  $p$ , the strategy adopted was based on the Bernoulli's Principle, presented in Equation (6). Assuming that the total pressure  $H$  is constant along a streamline, a reasonable approximation given the flow characteristics, all flow regions will have the same value as the free-stream flow,  $H_0$ , with  $p_0$  equal to 0 Pa. The only exception will be in the wake, since energy was extracted from the flow by the turbine. Based on dimensional analysis, Equation (5) was obtained to estimate that drop in total pressure, obtaining  $H_{wake}$  with previously known quantities. Afterwards, the two total pressure values obtained,  $H_0$  and  $H_{wake}$ , were blended in a similar fashion to  $V_z$ , allowing for a pressure field equation to be obtained through Equation (6).

$$H_{wake} = H_0 + \frac{P_{net}}{Q_{disk}} \quad (5) \quad p(r, z) = H(r, z) - \frac{1}{2} \rho V(r, z)^2 \quad (6)$$

$$H(r, z) = (H_0 \cdot (1 - \gamma_z(z, 0.0, 4.0)) + H_{wake} \cdot \gamma_z(z, 0.0, 4.0)) \cdot \gamma_r(r, 1.2) + H_0 \cdot (1 - \gamma_r(r, 1.2)) \quad (7)$$

Having created a set of equations describing the velocity and pressure fields in the domain, pyMMS



(Lemaire, 2021) was used to obtain the source terms that forced them to become the exact solutions of the Navier-Stokes equations. These source terms are in turn provided to the flow solver, which eventually outputs a simulation with errors that can be easily assessed by comparison with the known analytical solution provided initially - therefore enabling Code Verification. A slice of the obtained velocity and pressure fields are presented in Figure 1.

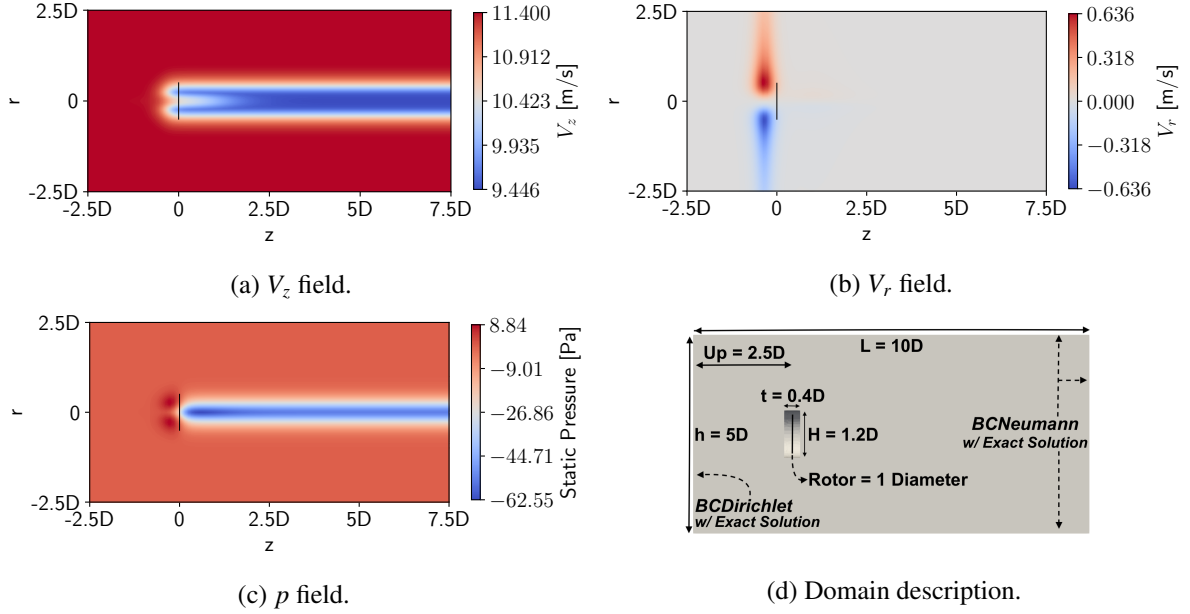


Fig. 1: Exact solution fields of Wind Turbine MMS, based on Actuator Disk solution with NREL 5MW characteristics. Slice over  $rz$  plane, in cylindrical coordinates.

While solution realism is not essential to a MMS (Roache, 2019), it was still sought during the creation process. Nevertheless, issues with the stability of MMS that did not respect continuity severely limited the flow features that could be recreated. Therefore the present MMS represents a compromise, which can have some critics established: (1) the wake has no swirl,  $V_\theta = 0$ ; (2) the wake has no expansion; (3) the flow starts decelerating too early upstream of the turbine, which leads to premature radial velocity component. In the end the authors acknowledge the limitations of the current MMS, but hope to further improve it in the future after identifying and solving the stability issues stated. Yet, it is considered that the current version is already suitable to perform Code Verification.

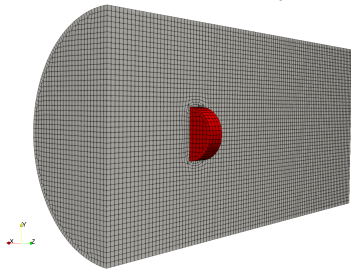


Fig. 2: Typical SG grid setup. Slice over  $yz$  (or  $rz$ ) plane of Hole subgrid (gray), fitted with Rotor subgrid (red). G1 refinement. Cylinder grid is identical to Hole, but without space to fit Rotor.

Grid	Refin. ( $h_i$ )	Size	Cell Count ( $N_i$ )		
			Cylinder	Rotor	Hole
G1	2.49	100 x 50 x 50	203 600	512	204 144
G2	1.66	150 x 75 x 75	682 350	1680	682 839
G3	1.25	200 x 100 x 100	1 604 000	3840	1 603 700
G4	1.00	250 x 125 x 125	3 125 250	7520	3 123 035

Table 1: Sub-grid refinements description. Baseline: Cylinder grid only. Sliding Grids: Hole mesh fitted with Rotor grid. Overset Grids: Cylinder and Rotor grids overlapped.

To discretize the domain, three main types of grids had to be created. The first is a simple, Cylinder grid with mostly cubic cells, which is used as a benchmark, since it is a single mesh. This grid will also

be used in OG, together with a second sub-grid, Rotor, overlapped in the region of the wind turbine, which can rotate. Finally, for the SG, the Rotor sub-grid will also be used, but the Cylinder one is substituted with another that has a hole in the middle, so that they can fit into each other. All grids are unstructured, created using Hexpress, aiming at geometric similarity through all refinements, resulting in a set of systematically refined grids necessary to perform Code Verification. Moreover, they do not have hanging nodes. Their characteristics are presented in Figure 2 and Table 1.

The boundary conditions (BC) were defined as follows: a Dirichlet BC for the inlet and a Neumann BC for the other exterior surfaces, all based on the analytical solution of the MMS. Regarding the adopted numerical setup, for the discretization of the convection fluxes a 2nd order, limited, QUICK scheme was selected. For the time discretization the 2nd order Implicit Three Time Level is used, with a default angular rotation per time step of 8 degrees (maximum  $CFL$  is 0.25 in grid G4, with a time step of 0.11 s). The iterative residuals are reduced up until all  $L_\infty$  norms are below  $10^{-6}$  at each time step, which yield iterative errors negligible for all flow quantities after an iterative study was performed. Finally, for both SG and OG the default interpolation scheme used is the Least Squares with a second degree polynomial function, which is a third order accurate scheme (LS3).

## 6 Results

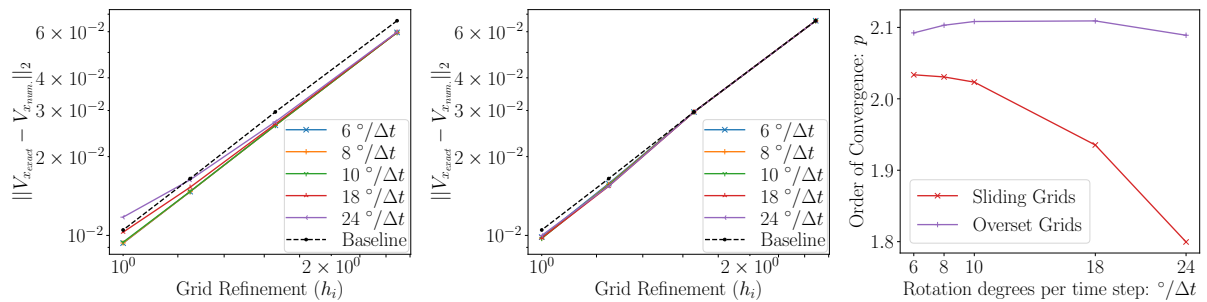
### 6.1 Baseline

The first simulation used a single grid for the entirety of the domain, serving as a benchmark when SG and OG methods are introduced. Overall, at least second order of accuracy was obtained for pressure and radial velocity components ( $V_x$  and  $V_y$ ). However, for the axial velocity,  $V_z$ , reduced order of accuracy occurred ( $p = 1.37$ ). Due to a yet unknown source, high errors concentrated at the outlet of the domain, degrading the overall velocity error order. Hence, focus will be given to the  $L_2$  error norms throughout this work to assess the impact of the SG and OG, instead of  $L_\infty$ , which are dominated by these outlet errors. Nevertheless, no significant impact is expected on the conclusions of the present paper.

### 6.2 Time Step

One of the parameters tested was the influence of the time step. Assuming that the rotor has a fixed angular speed during operation ( $\omega = 1.2698$  rad/s), the time step is determined in order for the rotor to advance a pre-determined amount of degrees. The values tested ranged from 6 to 24 degrees per time step ( $6$  to  $24^\circ/\Delta t$ ). The movement of the rotor leads to unsteadiness of the results, which need to be averaged. To quantify the respective statistical uncertainty the TST method is used (Brouwer et al., 2015), as implemented in the software pyTST (Lemaire and Klapwijk, 2021). In this particular case that quantity was always kept at least two orders of magnitude lower than the obtained mean by taking into account the last four rotations of the rotor in the simulation.

The grid refinement plots of  $V_x$  error for different time steps are presented in Figures 3a and 3b, for SG and OG, respectively. Based on the methodology of Code Verification (Eça and Hoekstra, 2013), a linear regression was used to estimate the order of convergence,  $p$ , presented in Figure 3c.



(a)  $V_x$  error ( $L_2$  norm). Sliding Grids. (b)  $V_x$  error ( $L_2$  norm). Overset Grids. (c) Order of Convergence,  $p$ .

Fig. 3: Time Step sensitivity study: 6 to 24 degrees of rotation per timestep. Analysed quantity:  $V_x$  error.

It can be concluded that the order of convergence of  $V_x$  is degraded with coarser time steps when

SG are used, whereas OG appears to be more robust in preserving it. Analyzing the error curves, neither of the methods seem to be introducing a significant source of error. In fact, the slight error reduction perceived in some grids when compared to the Baseline case is likely related to the reduced amount of cells of the latter. Moreover, the OG results match the Baseline for G1 and G2: this is due to the lack of Fringe cells in the domain, given that these meshes are too coarse, therefore errors from the rotor are not transmitted to the rest of the domain. Besides, this consideration is behind a slight overprediction of the order of convergence in Figure 3c for OG.

Overall, as finer grids are used with SG, the convergence decreases if coarse time steps are adopted. On the other hand, OG is practically not influenced by that. Regarding other flow quantities,  $V_y$  presented the exact same results, since the flow is axysymmetric. As for pressure and axial velocity, no significant differences were found in both methods.

### 6.3 Interpolation Scheme

The other parameter tested was related to the interpolation schemes to couple the sub-grids. The default time step is constant,  $8^\circ/\Delta t$ . Besides the Least Squares with a second order polynomial (LS3), the default scheme used until this point, Nearest Cell Gradient (NCG2) and Inverse Distance (ID1) were also tested. Note that the algorithm in the acronym denotes the accuracy order of the method. In Figure 6 the error distribution of  $V_z$  in the rotor region are presented for the three interpolation schemes (ID1, NCG2 and LS3) for both SG and OG methods. It can be assessed that ID1, a first order method, is introducing

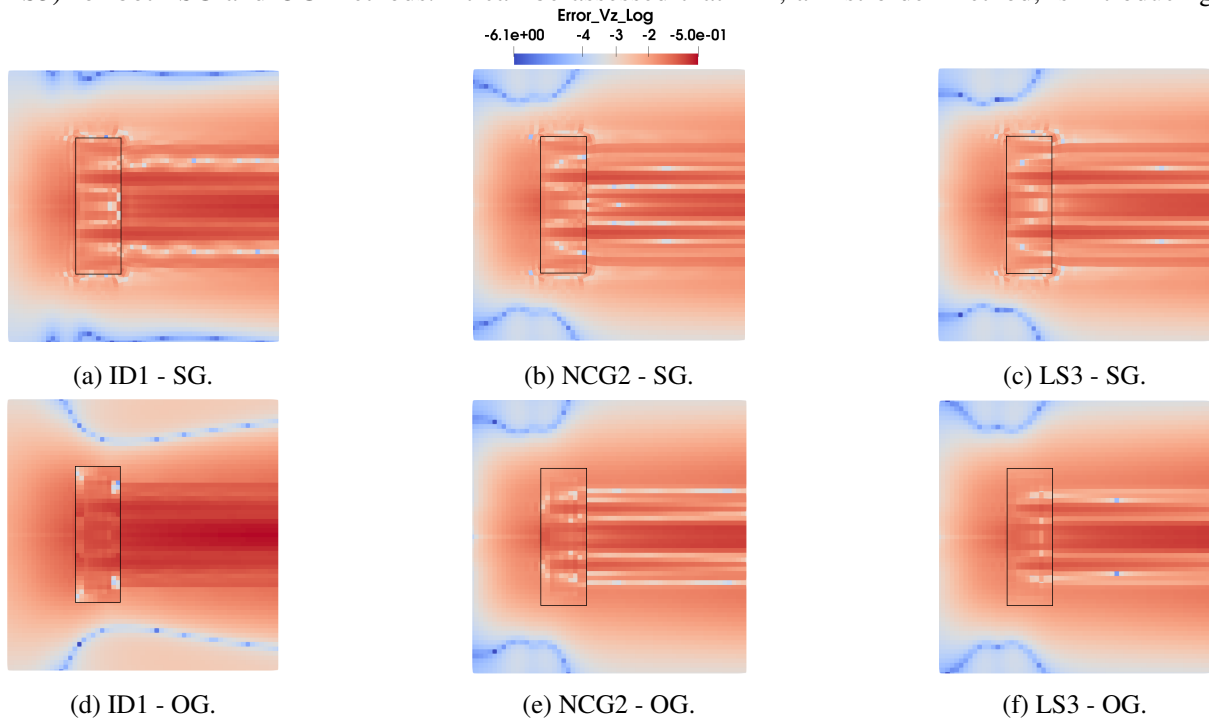


Fig. 4: Error distribution of axial velocity,  $V_z$ , nearby the rotor region in log scale. Slice over  $yz$  plane. Black line encloses rotor region. Top row: Sliding Grids. Bottom row: Overset Grids.

the highest amount of errors. These are in turn convected downstream, since this flow is convection dominated. On the other hand, only slight differences can be perceived between the error distribution of NCG2 and LS3, with the second order method introducing a less smooth distribution. Comparing the results between SG and OG, the error wake is wider in the first method, since SG always transfers information at the interface. As for OG that transfer depends on the Fringe cells locations, which in this case are more packed inside the rotor region.

Mass conservation was also investigated, since both SG and OG do not respect it in the intergrid communication process. It is quantified with the absolute value of the sum of mass fluxes going in and out of the domain, with the respective history over the last four rotations presented in Figure 5.

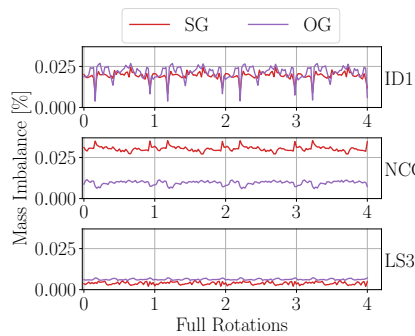


Fig. 5: Mass Imbalance over last rotations: percentage of mass flow rate through the rotor. Grid G4 with different interpolation schemes.

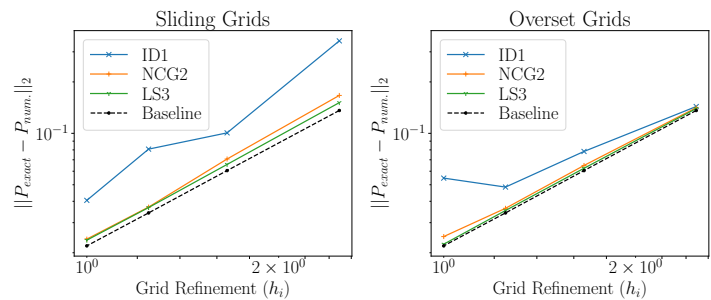


Fig. 6: Pressure errors ( $L_2$  norm) with grid refinement and different interpolation schemes.

Overall, the mass imbalance introduced is minimal: less than 0.03%. Also, the difference between that value using either SG and OG is also small, except for NCG2. However, it is important to point out the differences between each interpolation scheme. While no clear trend exists regarding higher order schemes and lower mean value of mass imbalance (*vide* ID1 vs. NCG2 with SG), the same cannot be said concerning the oscillations. In fact, the higher the order of accuracy of the scheme, the smaller the oscillations. Bear in mind that oscillations in mass imbalance translate into pressure fluctuations, since both quantities are coupled in the pressure correction equation in incompressible flows. These pressure fluctuations are in turn translated to force oscillations. Therefore, while a constant mass imbalance might not be important to the solution accuracy, having oscillations in pressure might have a negative impact when acoustics or forces are under analysis. In fact, Figure 6 reflects this same consideration: ID1 has the highest pressure errors, with SG not being in the asymptotic range and OG errors stagnating in finer grids. On the other hand, NCG2 and LS3 are able to have similar error trends in terms of pressure for both methods, keeping it low and preserving the order of convergence.

## Acknowledgements

This project has received funding from the EPSRC Centre for Doctoral Training in Next Generation Computational Modelling (EP/L015382/1) at the University of Southampton including financial support from MARIN. The authors acknowledge the use of WavEC resources and facilities for this work.

## References

- Benek, J., Steger, J., Dougherty, F., and Buning, P. (1986). Chimera: A Grid-Embedding Technique. *Technical Report AEDC-TR-85-64*.
- Brouwer, J., Tukker, J., and van Rijsbergen, M. (2015). Uncertainty analysis and stationarity test of finite length time series signals. In *4th International Conference on Advanced Model Measurement Technologies for the Maritime Industry*.
- Eça, L. and Hoekstra, M. (2013). Verification and validation for marine applications of CFD. *International Shipbuilding Progress*, 60(1-4):107–141.
- Francois, B., Costes, M., and Dufour, G. (2011). Comparison of Chimera and Sliding Mesh Techniques for Unsteady Simulations of Counter Rotating Open-Rotors. In *20th International Society for Airbreathing Engines Conference*.
- Jonkman, J., Butterfield, S., Musial, W., and Scott, G. (2009). Definition of a 5-MW Reference Wind Turbine for Offshore System Development. Technical Report NREL/TP-500-38060, 947422.
- Lemaire, S. (2021). pyMMS. DOI: 10.5281/zenodo.4428181.
- Lemaire, S. and Klapwijk, M. (2021). pyTST. DOI: 10.5281/zenodo.4428158.
- Lemaire, S., Vaz, G., Deij - van Rijswijk, M., and Turnock, S. R. (2021). On the Accuracy, Robustness and Performance of High Order Interpolation Schemes for the Overset Method on Unstructured Grids. *International Journal for Numerical Methods in Fluids*. DOI: 10.1002/flf.5050.
- Rai, M. (1985). An Implicit, Conservative, Zonal-Boundary Scheme for Euler Equation Calculations. *NASA Contractor Report 3865 - Ames Research Center*.
- Ramírez, L., Foulquié, C., Nogueira, X., Khelladi, S., Chassaing, J. C., and Colominas, I. (2015). New high-resolution-preserving sliding mesh techniques for higher-order finite volume schemes. *Computers and Fluids*, 118:114–130.
- Roache, P. J. (2019). The Method of Manufactured Solutions for Code Verification. In Beisbart, C. and Saam, N. J., editors, *Computer Simulation Validation: Fundamental Concepts, Methodological Frameworks, and Philosophical Perspectives*, chapter 12, pages 295–318. Springer International Publishing, Cham.
- Tran, T. T. and Kim, D. H. (2018). A CFD study of coupled aerodynamic-hydrodynamic loads on a semisubmersible floating offshore wind turbine. *Wind Energy*, 21(1):70–85.
- Vaz, G., Jaouen, F., and Hoekstra, M. (2009). Free-Surface Viscous Flow Computations: Validation of URANS Code FreSCo. In *Proceedings of the ASME 2009 28th International Conference on Ocean, Offshore and Arctic Engineering*, Volume 5: Polar and Arctic Sciences and Technology; CFD and VIV, pages 425–437.

# Towards Uncertainty Analysis of CFD Simulation of Ship Responses in Regular Head Waves

Mohsen Irannezhad<sup>1,\*</sup>, Rickard E. Bensow<sup>1</sup>, Martin Kjellberg<sup>2</sup>, and Arash Eslamdoost<sup>1</sup>

<sup>1</sup>Chalmers University of Technology, 412 96, Gothenburg, Sweden

<sup>2</sup>SSPA Sweden AB, 412 58, Gothenburg, Sweden

\*Corresponding author, E-mail: [mohsen.irannezhad@chalmers.se](mailto:mohsen.irannezhad@chalmers.se)

## INTRODUCTION

Ship hydrodynamic performance prediction in waves is a common practice in the early stages of the ship design process as the interaction between the ship and waves may adversely affect the hydrodynamic responses of the ship in comparison to calm water. Various well-established numerical and experimental methods are often utilized for prediction of ship performance in waves. Although the model tests are expensive and time-consuming, a high level of accuracy is often achieved in such experiments. On the other hand, with respect to the increased computational power, prediction of ship performance in waves by the numerical methods based on Computational Fluid Dynamics (CFD) techniques are gradually acquiring more popularity. However, the validity of the incorporated discretization schemes and modelling assumptions in these state-of-the-art CFD methods are often overlooked and the method accuracy is mainly assessed through the validation of the results based on the respective model test data. Validation as an engineering exercise aims to show that the right equations are solved, while verification (mathematical exercise) is required to demonstrate that equations are solved right [1].

The eventual objective of this research is to perform verification and validation exercises of a ship performance prediction in regular head waves using CFD, whereas in this paper, the working progress is presented which may be subjected to significant revisions. To this end, extensive attempts have been made to investigate numerical wave propagation without the presence of the hull. Ship responses in waves are significantly influenced by the wave excitation forces. Therefore, not only high level of accuracy is required for the simulation of the numerical waves, but also quantification of the numerical uncertainties are of a great importance. This becomes even more challenging when the ship hydrodynamic responses, such as motions and added resistance in waves, exhibit dependencies on wave steepness. In this paper, the main focus of such uncertainty analyses is on the systematic grid convergence study.

## APPROACH

The second variant of the MOERI tanker (KVLCC2) in model-scale (scale factor = 100) and operating in fresh water at the design speed (Froude number  $Fr = 0.142$ ) in a regular head wave (wave height  $H = 0.06$  m and wave length  $\lambda/L = 0.6$ ) is considered. The model tests are carried out in Osaka University Towing Tank [2].

In this paper, a commercial CFD solver, Simcenter STAR-CCM+ (version 2020.3.1), is used with an Unsteady Reynolds-Averaged Navier-Stokes (URANS) approach. Unstructured grids including the trimmed hexahedral meshes with local refinements near the free surface and near the hull as well as prism layer meshes along the hull surface are generated using STAR-CCM+ automatic mesh generator. Different cautions are taken into account to eliminate/diminish undesired grid refinement diffusion depths (transition zone between two local refinement zones) and also to generate "as geometrically similar as possible" set of unstructured grids. The computational domain in each grid is discretized employing an Overset Topology which consists a moving overset region and a stationary background region with specific treatment of cell sizes near the overlapping zone (where the information is exchanged between the background and overset regions).

The simulations are mainly carried out for five different grid sets shown in Table 1, in which the effects of different local refinement zones as well as the quality of the cell size and overset interpolations in the overlapping zones are evaluated. The simulations are carried out in three different computational domain widths, i.e., Quasi-2D (only one cell in  $Y$  direction), Small Width SW-3D (one third of the full domain in  $Y$ ) and Full Width FW-3D (full domain size in  $Y$ ). The reason behind choosing one third of the domain size for the SW-3D case is to eliminate undesired grid refinement diffusion depths that may be introduced by the grid generator. In GS4, a sinusoidal pitch

motion with an amplitude of 3 (deg) and a frequency equal to the wave encounter frequency is predefined for the overset region.

Table 1: Grid sets details.

Grid Set	Simulation Type	Regions		Local Refinement Zones					Prism Layers
		Background	Overset	Free Surface	Kelvin Wedge	Overlapping	Around Overset	Inside Overset	
GS1	Wave Propagation	✓	—	✓	—	—	—	—	—
GS2	Wave Propagation	✓	—	✓	✓	✓	✓	—	—
GS3	Wave Propagation	✓	✓ Restrained	✓	✓	✓	✓	✓	—
GS4	Wave Propagation	✓	✓ Predefined Motions	✓	✓	✓	✓	✓	—
GS5	Hull Performance	✓	✓ Hull Motions	✓	✓	✓	✓	✓	✓

In each grid set, four systematically refined grids are considered which are determined by the refinement levels  $n = 0.5$  (coarsest), 1.0, 1.5 and 2.0 (finest). Trimmed hexahedral meshes (isotropic volume meshes) are generated in both background and overset regions, where every two cells are divided into  $2n$  cells in each direction (except in  $Y$  for Quasi-2D simulations) to derive a geometrically similar grids. Figure 1 shows the grids ( $n = 1.0$  and 1.5) in GS2 where different local refinement zones are illustrated by different colors. The total number of cells in SW-3D domain in each grid in GS1, GS2 and GS3 (equal to GS4) is exactly 984384, 4122656 and 6606944 multiplied by  $n^3$ , respectively.

In order to achieve geometrically similar anisotropic sub-layer (prism layer) meshes, the methodology presented by P. Crepier [3] is employed. In this method, the total thickness of prism layers remains the same between the grids but both the first layer cell thickness and the growth ratio between the layers are adjusted accordingly. The total number of layers in each grid will be  $nN_t$ , in which  $N_t$  is the total number of layers for the coarsest grid, see Figure 2. The prism layers are generated such that the non-dimensional wall distance  $y^+$  remains above 30 over the major part of the hull wetted surface area during the ship simulations in waves (for all grids in GS5), hence a wall function is utilized for treatment of the near-wall region. The undesired transition zone between the prism layers and their neighbouring isotropic cells are inevitable in GS5, consequently, the total number of cells are 987823, 7868343, 26542331 and 62866494 for  $n = 0.5 - 2.0$ , respectively.

An overview of the computational domain size and the imposed boundary conditions are shown in Figure 3. Moreover, 16 wave probes (located at 4 X-positions and 4 Y-positions) are considered in order to analyze the numerical wave elevation. The longitudinal location of probes are, (1) at the end of wave forcing zone (will be explained further in the paper), (2) before the overset region, (3) within the overlapping zone and, (4) inside the overset region close to the hull fore perpendicular. Notice that the hull was not present in the wave propagation simulations in GS1-GS4. Although the Quasi-2D simulations are computationally much cheaper than 3D simulations, it was found that the Quasi-2D results for the wave propagation simulations are not necessarily similar to that of the 3D cases. Therefore, the wave propagation simulations are mainly performed in SW-3D domain in order to gain similar results as of FW-3D while keeping the computational costs low. Thereafter, the hull performance simulations are carried out only in the FW-3D domain.

The Volume of Fluid (VOF) model is used to capture the free surface. A wave forcing function is used in the vicinity (distance equal to  $L$ ) of all vertical boundaries with velocity inlet boundary conditions in order to force the solution of the discretized Navier-Stokes equations towards the theoretical 5<sup>th</sup> order Stokes wave solution minimizing the wave reflection from the boundaries. An implicit unsteady solver is used with a second order temporal discretizational scheme (time step  $t = 0.003/n$ , hence similar Courant number between the grids in each grid set). The chosen time step results in Courant numbers smaller than 0.3-0.4 on the free surface which also fulfils the ITTC recommendations of at least 100 time steps per encountered wave period [4].

In the wave propagation simulations, both the background and overset regions are moved with a constant speed translation motion representing the hull expected velocity. On the other hand, in the experimental model tests, the hull was towed with a light weight carriage connected to the main carriage by means of a weak spring in order to allow the ship to surge in conjunction with heave and pitch. This weak spring mass system is also numerically replicated in the simulations, therefore the hull actual velocity and hence the translation motion of the background and overset regions in the hull performance simulations is marginally oscillate around the hull

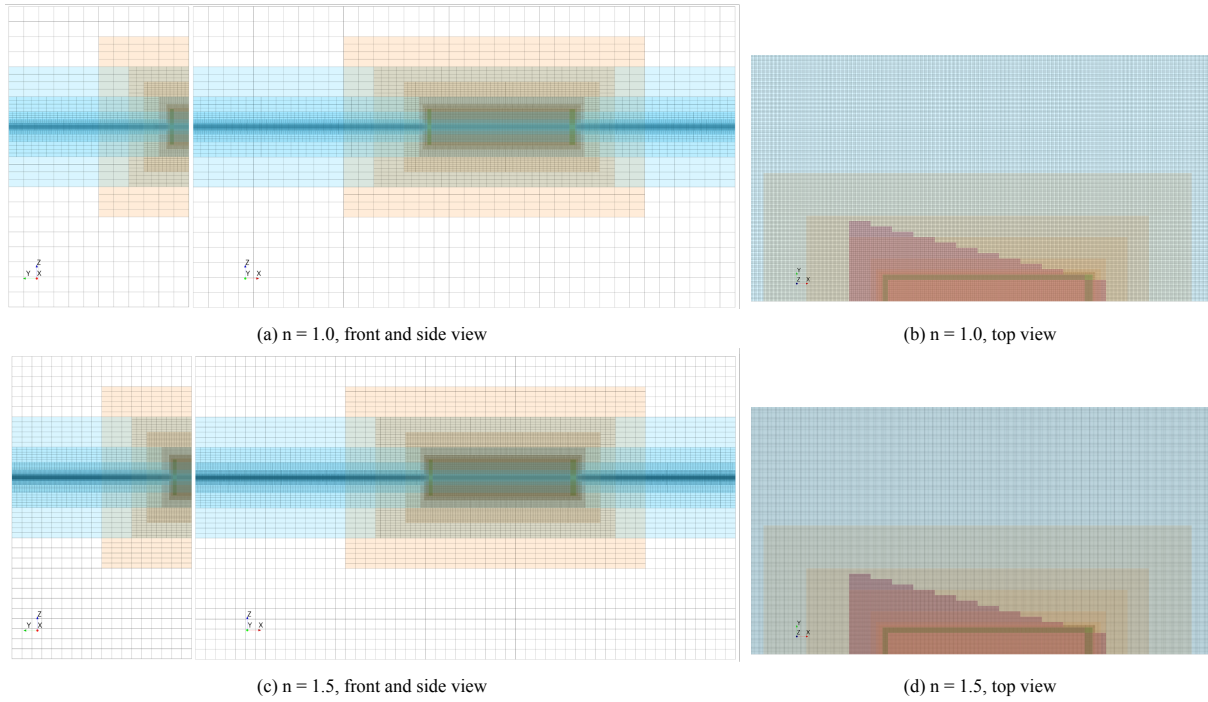


Figure 1: Overview of the grids and local refinement zones ( Free Surface Around Overset Overlapping Kelvin Wedge ) for GS2 in FW-3D domain.

expected velocity.

## RESULTS

The numerical wave elevation  $\zeta$  and its error (relative to the analytical representation of the 5th order Stokes wave) after 30 encountered waves are presented for GS1 (in SW-3D domain) in Figure 4a. Moreover, the longitudinally averaged absolute error (in percentage of the wave height) for Laminar and Turbulent flow ( $k-\omega$  SST) simulations are presented in Figure 4b. The results of the turbulent flow simulations are similar to that of laminar flow. Wave propagation is a laminar phenomenon by its nature, while turbulent simulations are required when the hull performance is being studied.

The averaged absolute error is rather low for both laminar and turbulent flow simulations in GS1. Moreover, the error converges approximately after a few encountered wave periods. Therefore, the simulations deemed converged after 12 encountered waves and the Fourier analysis of the wave elevation at the probes are carried out for GS1-GS4 over the 12-20 encountered wave periods time window. The 1<sup>st</sup> harmonic amplitude as the domi-

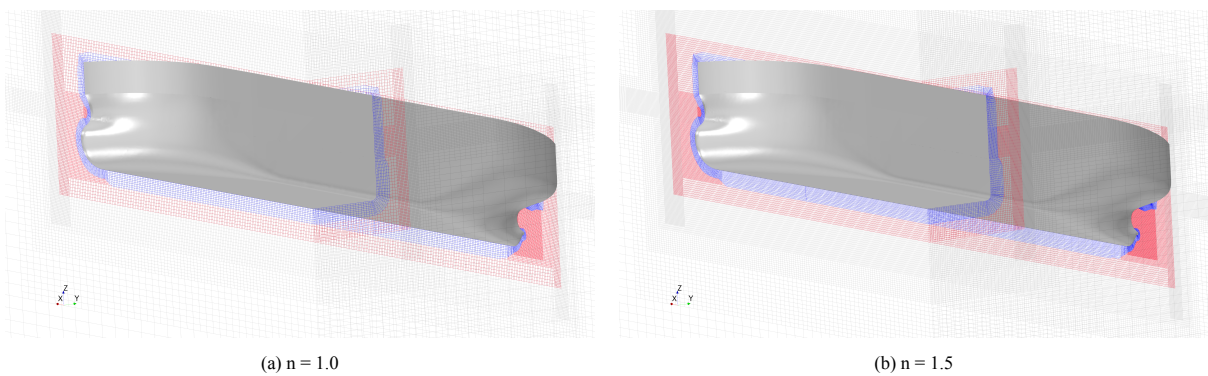


Figure 2: Overview of the grids near the hull in GS5. Gray lines represents the mesh in the background region. Blue and red colors represent the isotropic and prism layer meshes in the overset region, respectively. Local refinement zones inside the overset can also be observed.

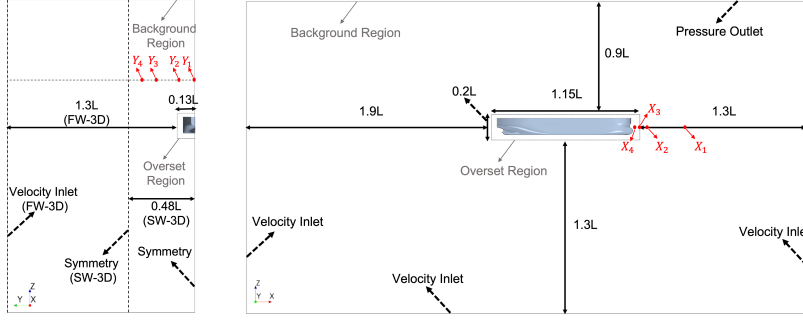


Figure 3: Computational domain size, applied boundary conditions and wave probes locations.

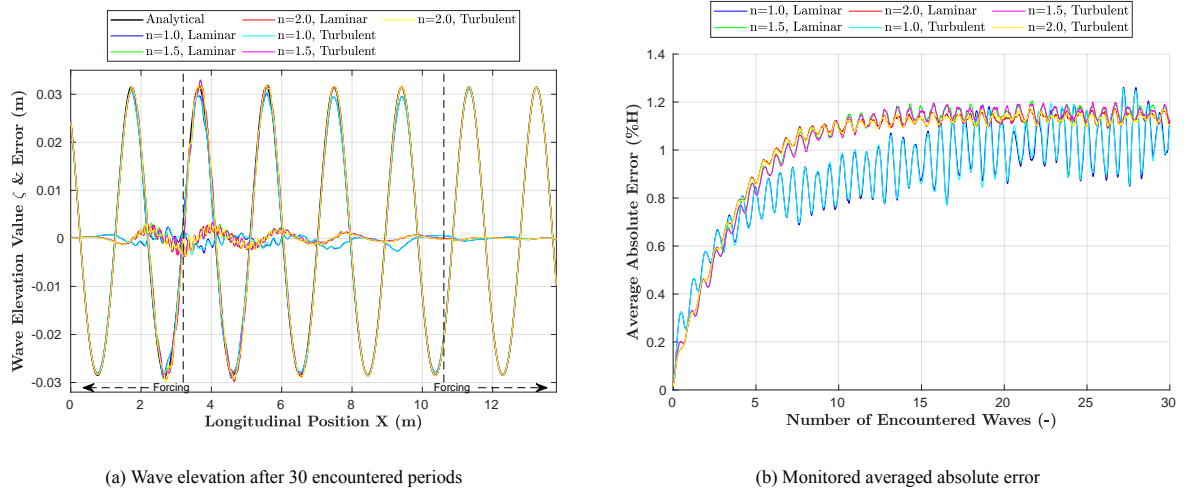


Figure 4: Wave elevation near symmetry plane ( $Y_1$ ) and its error with respect to the analytical wave elevation for GS1 in SW-3D domain.

nating component is shown in Figure 5. It should be noted that the magnitudes of the higher harmonic components are very small, thereby small differences yield large errors.

It can be clearly seen that for all the grid sets and all the probes, the magnitude of the error for  $n = 0.5$  is considerably larger than the finer grids. For  $X_1$  probes (located at the end of forcing zone), shown in Figure 5a, the magnitudes of errors decrease from coarsest to finer grids in all grid sets. Moreover, the results for different grid sets and an specific refinement level are very similar, hence no significant effects from the local refinements and overset region at that longitudinal location are observed. The results are also similar for different Y probes in each refinement level.

For  $X_2$  probes (before the overset region), shown in Figure 5b, the magnitude of error for GS1 decreases from coarser grids towards finer grids, while for GS2, GS3 and GS4 the behaviour varies depending on the grid refinement and the probes Y location. On the other hand, the magnitude of the error is relatively smaller for  $n = 1.5, 2.0$  compared to the coarser grids. Interestingly, for GS4 in all refinement levels for  $Y_1$  and  $Y_2$  (located closer to the pitching overset region) the change of error is towards positive values which results in decreased error in  $n = 0.5, 1.0$  and increased error in  $n = 1.5, 2.0$  (although negligible).

For  $X_3$  probes (only  $Y_1$  and  $Y_2$  are located within the overlapping zone for the grid sets including overlapping refinement), shown in Figure 5c, almost similar trend as of  $X_2$  probes is seen, however, with a more pronounced change of errors in  $Y_1$  and  $Y_2$  for GS4. This may imply that the overset interpolations are affected more significantly in the case of the existing pitch motion than the restrained overset region in GS3. For probes located at  $X_4$  (only  $Y_1$  and  $Y_2$  are located inside the overset region after the overlapping zone), shown in Figure 5d, the change of error between different refinement levels is towards positive values in all grid sets with more pronounced effects on  $Y_1$  and  $Y_2$  probes.

In general, larger errors are seen in each grid set and for X probes further away from the inlet ( $X_1$  to  $X_4$ ). To a large extent, GS2 and GS3 in all X probes are similar in each refinement level showing better interpolations between the overset and the background regions for the restrained overset. The errors in  $Y_3$  (and respectively  $Y_4$ )



in GS4, GS3 and to some extent also GS2 for each specific X probe are almost similar, which imply that the results are affected less from the refinements related to the overset region. The errors of  $n = 2, 1.5$ , and to some extent  $n = 1$ , in  $X_4$  and GS1 in all Y probes are larger than those of  $X_3$ , possibly because the error moves towards positive values from  $X_1$  to  $X_3$ , hence in  $X_3$  the error magnitude becomes smaller and then for  $X_4$  the errors are become positive. On the other hand, for  $n = 0.5$  the error increases in negative values. It should be mentioned that no significant wave encounter period change is seen in the wave propagation simulations and it remains below 0.2% of the wave encounter period. More observations could be discussed in future including the analysis of the 2<sup>nd</sup> harmonic amplitudes.

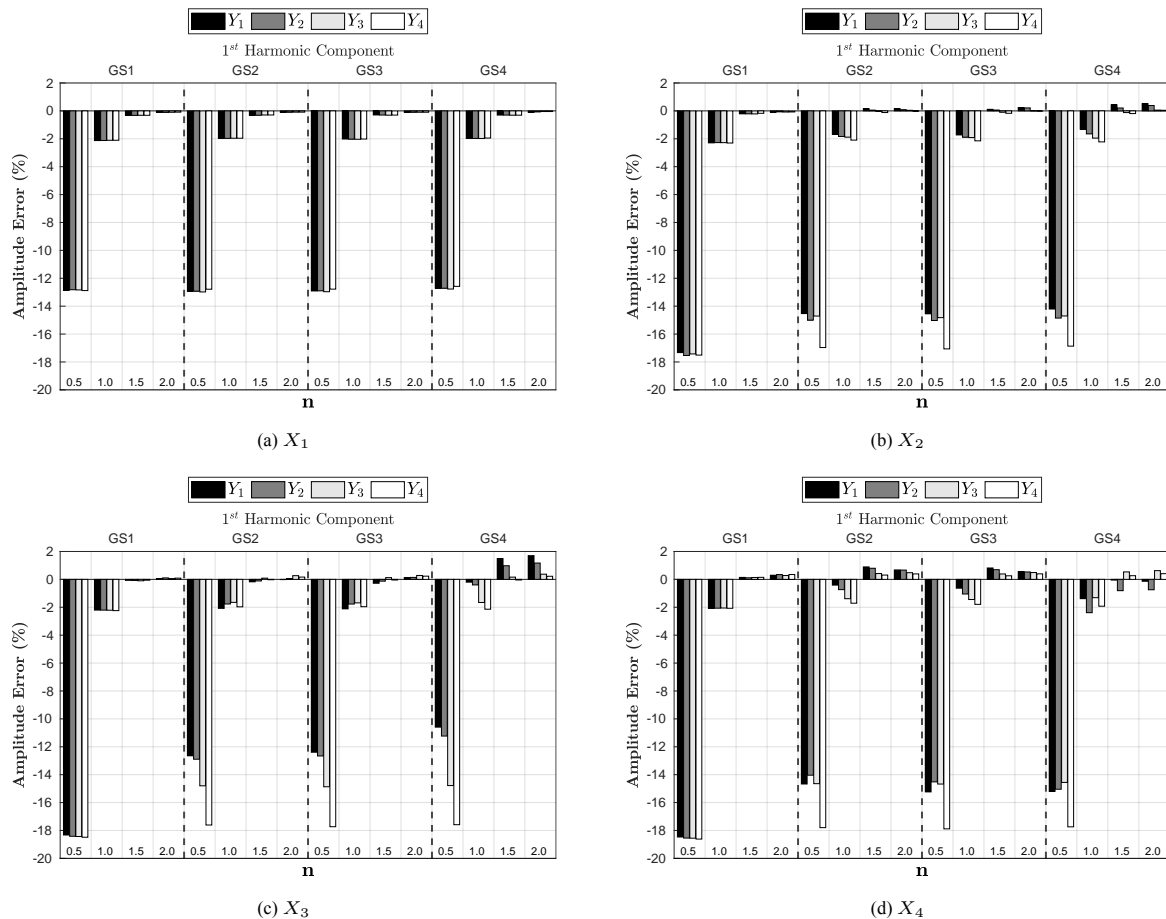


Figure 5: The Fourier analysis results of the wave elevation at the probes for turbulent flow simulations in SW-3D.

The Fourier analysis is carried out for the hull performance simulations in GS5 for 6 encountered wave periods for convergence (under discussion) in each refinement level. The numerical uncertainty analysis of the grids is carried out by a method proposed in [5]. The mean (0<sup>th</sup> harmonic amplitude) of resistance (for a half hull) and the first harmonic amplitudes of heave and pitch motions for different refinement ratios, are presented in Figure 6. The mean value of the heave and pitch motions are very small (close to the calm water sinkage and trim), therefore, the incorporated uncertainties of such parameters would become unjustifiably large and therefore not presented here.

The numerical uncertainty of mean resistance for the finest grid ( $n = 2$ ) is close to 16% and the highest uncertainty is seen for  $n = 1.0$ . The resistance values computed in all grids are relatively similar which are close to the experimental value. The uncertainty of the 1<sup>st</sup> harmonic amplitude of heave motion is similar in all grids and the heave motion exhibits a stable trend in all grids even though the magnitude of such parameter is very small. An interesting grid convergence is seen for the pitch 1<sup>st</sup> harmonic amplitude with largest uncertainty at coarsest grid  $n = 0.5$  and smallest at the finest grid  $n = 2.0$ . The experimental data related to motions are not included in the plots due to very small and rounded values.

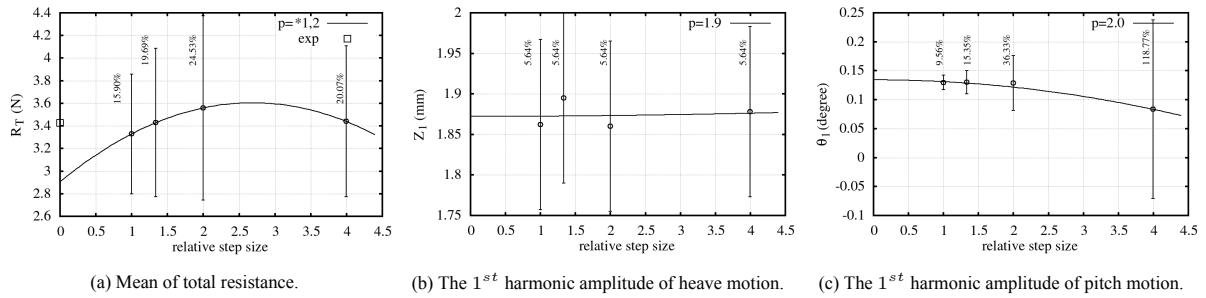


Figure 6: The uncertainty analysis of the hull performance in waves in GS5.

Mean of the surface averaged  $y^+$  over the wetted surface area of the hull during one wave encounter period is approximately 208, 102, 66, 49 for  $n = 0.5 - 2.0$ , respectively. The computational costs per each encountered wave period in terms of core-hours are provided in Figure 7. The computational costs are clearly much higher for the finer grids in each grid set.

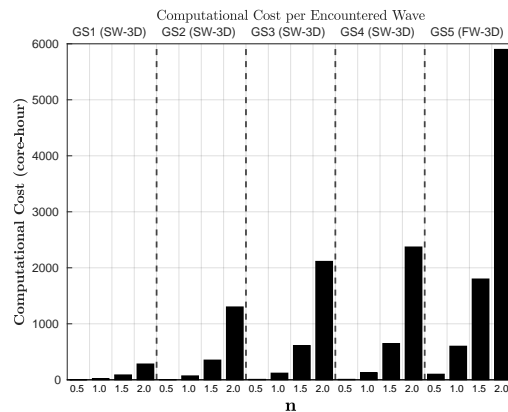


Figure 7: Computational costs per encountered wave period of simulation.

## CONCLUDING REMARKS and FUTURE WORK

The numerical uncertainties of the finest grid is about 16%, 6% and 10% for the ship resistance and the first harmonic of heave and pitch motions, respectively. The uncertainties increase for the coarser grids. The computational cost of the finest mesh is several times larger than the other coarser grids which makes it impractical for further investigations with respect to the available computational resources. However, it should be highlighted that the hull motions are very small for  $\lambda/L = 0.6$ . Therefore, small changes in the final result cause large uncertainties. We expect that the uncertainties decrease for the longer wave lengths where the motions are more dominant. The validity of this hypothesis will be investigated in the continuation of this study.

## REFERENCES

- [1] P. Roache. Verification of codes and calculations. AIAA Journal, 5:696-702, 36, (1998).
- [2] K. Ho. Phase-Averaged SPIV Wake Field Measurement for KVLCC2 Propeller Plane in Waves. PhD Thesis, Osaka University, Japan. (2014)
- [3] P. Crepier. Ship Resistance Prediction: Verification and Valication Exercise on Unstructured Grids. MARINE 2017, Wageningen, The Netherlands.
- [4] ITTC, 2014. International Towing Tank Conference. Recommended Procedures and Guidelines 7.5-03-02-03, "Practical Guidelines for Ship CFD Applications", 27<sup>th</sup> ITTC, 2014.
- [5] L. Eça and M. Hoekstra, A procedure for the estimation of the numerical uncertainty of CFD calculations based on grid refinement studies, Journal of Computational Physics, Volume 262, Pages 104-130, doi:10.1016/j.jcp.2014.01.006. (2014)

# Control of Incipient Cavitation on a Benchmark Hydrofoil Using a Miniature Vortex Generator (MVG)

<sup>1</sup>Ebrahim Kadivar, <sup>2</sup>Mikhail V. Timoshevskiy, <sup>2</sup>Konstantin S. Pervunin, <sup>1</sup>Ould el Moctar

<sup>1</sup>Institute of Ship Technology, Ocean Engineering and Transport Systems, University of Duisburg-Essen, 47057 Duisburg, Germany

<sup>2</sup>Kutateladze Institute of Thermophysics, Siberian Branch of the Russian Academy of Sciences, 630090 Novosibirsk, Russia

Email: [ebrahim.kadivar@uni-due.de](mailto:ebrahim.kadivar@uni-due.de)

**Abstract:** Cavitation occurrence can cause undesirable effects on the operation and performance of marine propellers and rudders as well as hydraulic machinery and pumping systems as it is the main factor of surface erosion, vibration and noise. In this study, we manipulate incipient cavitation using a passive method of cavitation control based on a miniature vortex generator. The idea of this passive control is adapted from aerospace engineering applications where similar controlling elements are commonly used to manage boundary layer characteristics and flow separation on airfoils. This method was previously investigated numerically on a benchmark hydrofoil and experimentally on a semi-circular leading-edge flat plate under unsteady flow conditions. It is shown that a proper size and position of a vortex generator on the suction side of a test body can significantly change the dynamics of unsteady cloud cavitation and cavitation surge. In this study, we use a CAV2003 section with and without a wedge-type vortex generator as test models. The miniature wedge-type vortex generator is located on the hydrofoil suction side close to its leading edge near the cavitation inception point (Fig. 1). The experiments are carried out in the cavitation tunnel in Institute of Thermophysics SB RAS. Dynamics of incipient cavitation on the hydrofoil suction side at different angles of attack and effect of the control device on the cavitating flow are studied by high-speed imaging using a Photron FASTCAM SA5 high-speed camera at a 20 kHz frame rate and a 768×480 pixels resolution. In addition to the visual data analysis, we perform hydroacoustic measurements with a hydrophone Brüel&Kjær Type 8103 to capture pressure pulsations in the hydrofoil wake. The results show that the cavitation inception on the hydrofoil suction side can be shifted downstream and successfully hampered, with only some small cavitating vortices observed behind the vortex generator. Thus, the miniature vortex generator allows delay of cavitation inception and decrease high-amplitude wall-pressure fluctuations in a wake region of the hydrofoil.



Figure 1. The photo of the benchmark hydrofoil CAV2003 with a miniature wedge-type vortex generator on the suction side of the hydrofoil.

Figure 2 shows the instantaneous photo of cavitation inception formed on the hydrofoil surface without and with the miniature vortex generator. The results revealed that, the cavitation inception was suppressed on the hydrofoil surface and only some small cavitating-vortices in the aft part of the miniature vortex generator can be observed. Therefore, it can be deduced that the cavitation inception near the leading edge on the unmodified hydrofoil was suppressed for the case with cavitation control using a miniature wedge-type vortex generator.

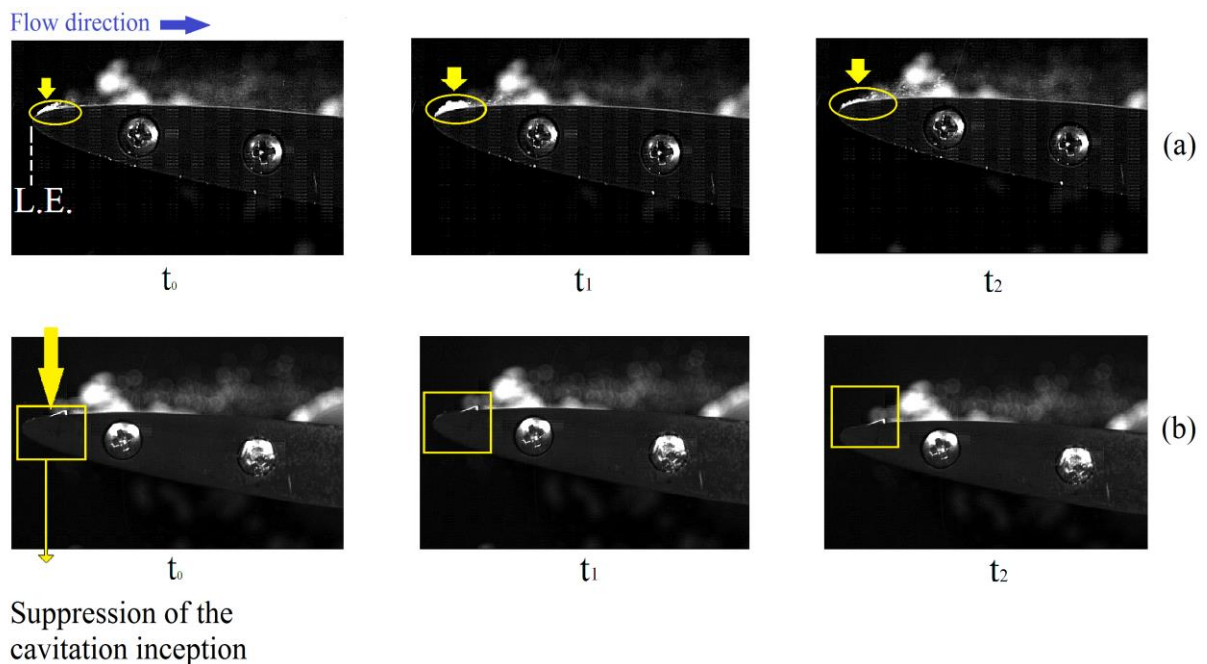


Figure 2. Instantaneous photograph of the side-view of the incipient cavitation formation on the hydrofoil surface for the case a) without miniature vortex-generator and b) with miniature vortex-generator. The flow direction is from left to right.

**Keywords:** passive control, miniature vortex generator, cavitation inception, benchmark hydrofoil, high-speed visualization, pressure measurements.

# A method for optimization of Olympic canoes by global shaping

Marek Kraskowski

<sup>a</sup> Maritime Advanced Research Centre, CTO S.A, 80-392 Gdańsk, Szczecińska 65, Poland

<sup>b</sup> Gdansk University of Technology, 80-233 Gdańsk, Narutowicza 11/12, Poland  
marek.kraskowski@cto.gda.pl

## 1. Introduction

From the point of view of CFD optimization in respect of resistance in calm water, the canoes used by professional competitors turn out to be very challenging. Unlike merchant ships, where the optimization can be efficiently realized in check-and-correct manner, based on visual analysis of pressure distribution, wave interaction and streamlines, the canoes are so simple in respect of body form and so slender that there are in fact no qualitative differences between their wave patterns and pressure distribution on the hull surface. Their distinctive features are: extreme slenderness of the waterplane (app. 14) and convex bodylines in each region of the hull. Fixed length and the breadth minimized so as to fit the competitor (thus also fixed in practice) together with the regulations leave very little room for the design optimization. Moreover, relatively small contribution of pressure component to total resistance makes it really hard to capture any dependence between acceptable modifications of the shape and resulting resistance. This paper presents an attempt on the shape optimization based on parametrized *a-posteriori* transformation of available hull surface definition, referred to as "global shaping". An efficient approach to the transformation is proposed, in which both the displacement volume and the longitudinal centre of buoyancy remain unchanged, so that all the analysed variants are by definition within the range of acceptable solutions. The analysis is realized by coupling the NX CAD software with the STAR-CCM+ solver. The results show the possibility of efficient fine-tuning of most promising canoe shapes in cases where intuitive optimization is no longer possible.

## 2. Approach

The presented work is aimed at optimization of the shape of the canoes for the Olympic games in Paris, 2024. An excessive CFD study was undertaken to search possible dependencies between the hull shape features and its performance at various conditions (speed, displacement). Large variety of existing hulls were analysed to enable formulating possibly general conclusions. The findings were as follows:

- in each class of analysed classes (K1 men, K1 women, K2 men, K2 women), the difference between worst and best shapes is of the order of 1%;
- no clear tendency was found in the influence of global shape parameters (prismatic coefficient, longitudinal centre of buoyancy) on total resistance;
- there is also no unique way in which the shapes characterized by lowest resistance achieve their good performance; in other words, best shapes can be characterized either by lowest pressure resistance or lowest friction resistance;
- in general, the proportions between friction resistance and pressure resistance was related to the character of the sectional area curve; in Fig.1, two examples are presented: the "sharp" sectional area curve (red) results in low friction resistance and high pressure resistance, and opposite tendency was observed for smooth sectional area curve;
- location of the LCG is crucial for selection of the best shape; analysis of the resistance for just one LCG for each shape can be very misleading.

General finding was that best performance of the canoe hull is achieved by advantageous combination of several factors, but conscious controlling this combination to achieve even better performance turns out to be really hard. On the other hand, it is clear that the performance of today's best canoes, optimized for decades based on experience, intuition and sometimes luck of the top designers, is already very close to absolute optimum.

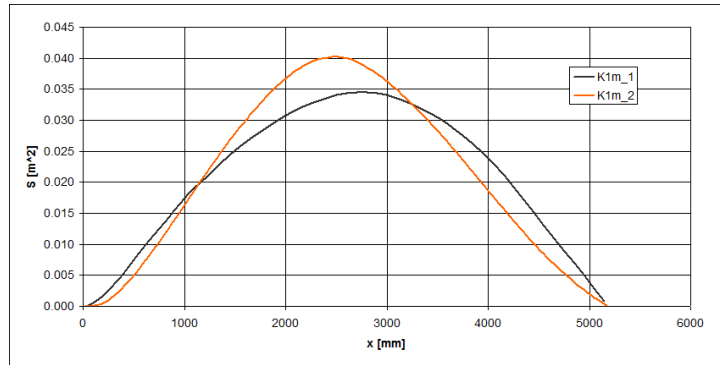


**Fig. 1 Examples of sectional area curves**

A proposed approach to further optimization of the canoe shapes thus consisted in a two-step procedure: start with selecting the most promising shape of available existing ones (making sure that they are compared at their optimum LCG) and then fine-tune this shape by introducing modifications to its longitudinal volume distribution. A method for these modifications, described below, was selected so that the displacement volume and the longitudinal centre of buoyancy remain constant.

### 3. Hull parametrization

As mentioned in the introduction, the selected approach is based on the *a-posteriori* transformation of existing hull surface definition; an attempt on modelling the shape with fully parametric definition turns out to be inefficient - it is either very hard to obtain required consistency with parent shape, or the definition becomes extremely complex [1]. Parametric transformation of the existing geometry was realized using the Global Shaping feature of the NX software. The method of the transformation is explained on the basis of Fig. 5.

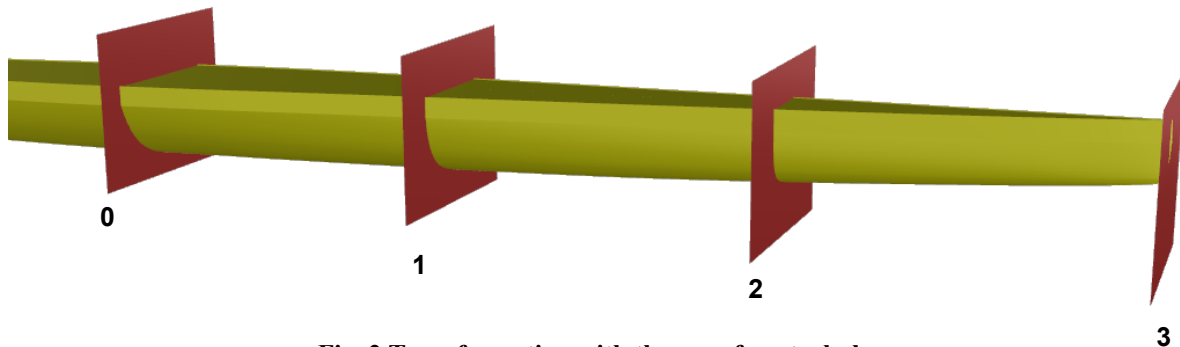


**Fig. 2 Transformation with the use of control planes**

Arbitrary number of control points is assigned to the transformed region. In presented case, the transformation is applied to the region between the midship section and the fore perpendicular. The location of the ones located at the ends of the region (0 and 3 in presented case) remains unchanged. All the control points located between them (1-2) can be shifted arbitrarily, which results in continuous shift of the hull sections in the region between points 0 and 3. The resulting shift of individual sections relative to their initial position is evaluated using the Bézier curve formulation. This formulation is explained in detail below.

Let us define the vector of initial locations of control points:

$$X_{BASE} = [x_0 \quad x_1 \quad x_2 \quad x_3]$$

The transformation is realized by shifting the control points to new locations:

$$X_{TR} = [x_{0\_TR} \quad x_{1\_TR} \quad x_{2\_TR} \quad x_{3\_TR}]$$

In presented case,  $x_0 = x_{0\_TR}$  and  $x_3 = x_{3\_TR}$ , however, in generic case, this does not necessarily hold true.

The difference between initial and transformed location of the control points is denoted as:

$$\Delta X = X_{BASE} - X_{TR} = [\Delta x_0 \quad \Delta x_1 \quad \Delta x_2 \quad \Delta x_3]$$

Our goal is to evaluate the shift of arbitrary point located between  $x_0$  and  $x_3$  based on the values of  $\Delta X$ . For this purpose, let us introduce the parameter  $t \in [0,1]$  and parametrize the length of the transformed region, so that  $x_0$  corresponds to  $t=0$  and  $x_3$  corresponds to  $t=1$ . The shift of arbitrary point between  $x_0$  and  $x_3$  is evaluated using the formula:

$$dx(t) = \sum_{i=0}^n \Delta x_i B_i^n(t) \quad (1)$$

where  $B_i^n(t)$  are so-called Bernstein polynomials defined as:

$$B_i^n(t) = \begin{cases} \binom{n}{i} t^i (1-t)^{n-i} & \text{for } i = 0 \dots n \\ 0 & \text{for } i < 0, i > n \end{cases} \quad (2)$$

Let us now present an example of shape transformation based on 4 control points ( $n=3$ ). The graph below (Fig.6) shows the form of Bernstein polynomials for  $i=0 \dots 3$ .

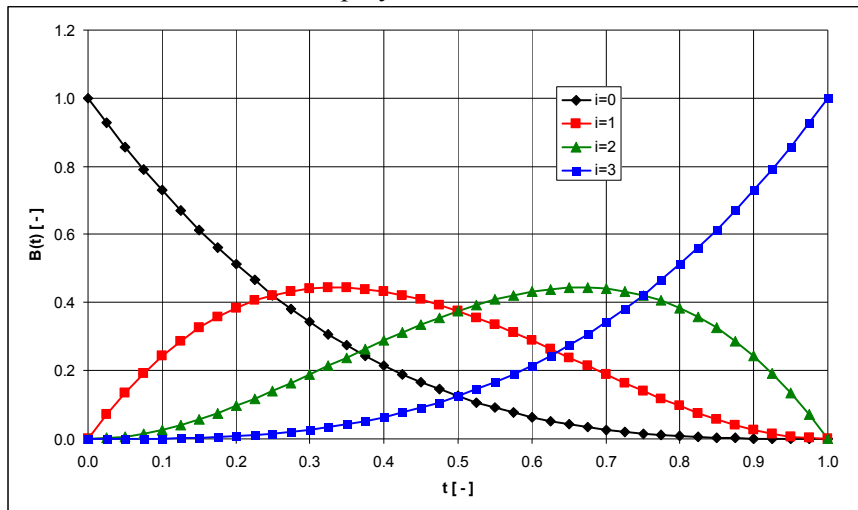


Fig. 3 Bernstein polynomials

Formulation of the transformation results in the fact that the location of the control points has no influence on the transformation result - it is only the number of control points which affects the transformation form. The control points are thus evenly distributed along the modified region, which results from technical requirements of the applied NX software (we use midship as zero point and fore perpendicular as end point,  $x=2.790$  m):

$$X_{BASE} = [0 \quad 0.930 \quad 1.860 \quad 2.790]$$

We then introduce the following transformation based on single parameter  $p$  (values of vector  $\Delta X$ ):

$$\Delta X = [0 \quad -a \cdot p \quad p \quad 0]$$

The coefficient  $a$  is selected so that within required range of modifications the displacement volume remains constant. Once the sectional area values are available, the value of  $a$  can be easily calibrated in an iterative manner. The LCB was not directly controlled, but it was found that once this procedure of iso-volumetric transformation is correctly applied both to fore part and the aft part, the LCB also remains constant. The example of resulting modifications of the sectional area curve for extreme values of parameter  $P$  for selectet K1-men canoe are presented in figure below

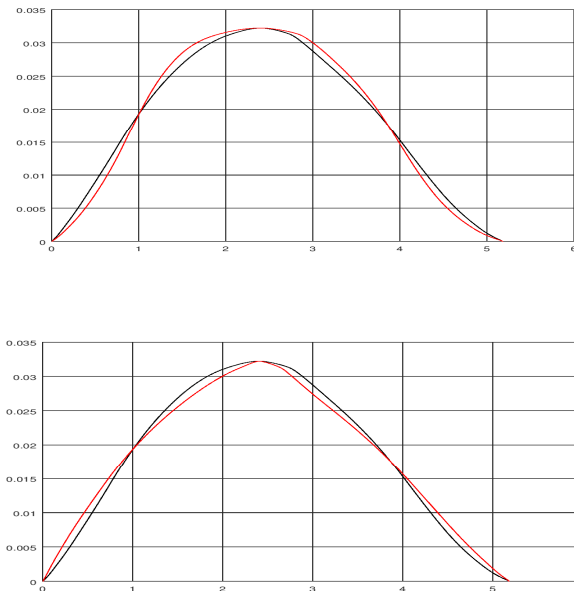


**Fig. 4 Considered range of modifications of the longitudinal volume distribution**

#### 4. Computational model

The resistance for subsequent variants of the selected K1 canoe was computed with the use of STAR-CCM+ solver. The CFD solver was coupled with the CAD software NX, and the computational procedure was executed in the following manner:

- a table of required range of parameter  $p$  to be analysed was pre-defined and imported to the CFD solver;
- the CFD solver manages the process by sending the command to CAD software at the beginning of each analysis, to execute another modification;
- the modified shape is imported to CFD solver, which executes remeshing and analysis.

As the computational time is of high priority, and the focus was primarily on differences in resistance rather than absolute values of the resistance, relatively coarse mesh was used and the dynamic trim and sinkage were neglected. Initial trim and draught were adjusted based on the computations for the parent shape, and remained unchanged for all other variants, assuming that their variation will be small due to constant displacement and LCB. Nevertheless, this simplifications seems really crude due to high Froude number of the Olympic canoes, so the result was further verified by repeating the computations for the parent shape and the optimal one with detailed model, using dense mesh and directly taking into account the dynamic trim and sinkage.

The number of mesh cells for optimization process and verification was XXX and XXX, respectively. The visualizations of the meshes is presented in figures below.



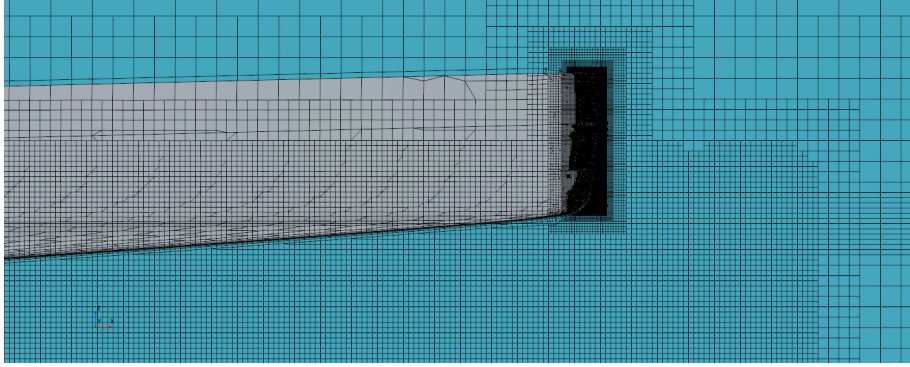


**Fig. 5 Computational mesh for optimization**

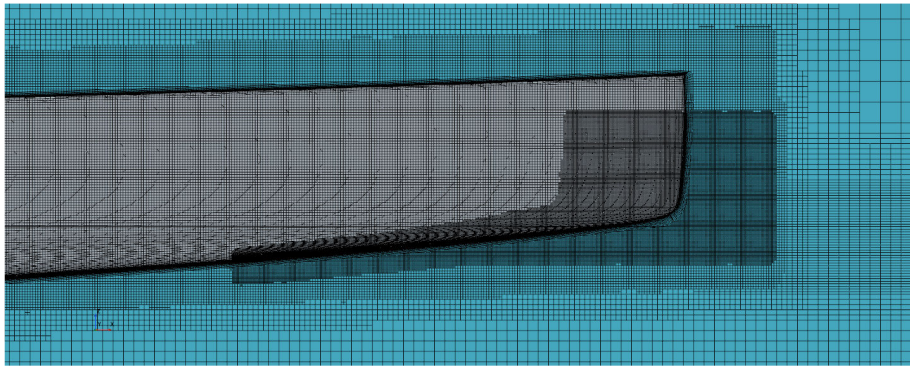


**Fig. 6 Detailed computational mesh**

## 5. Results and conclusions

Primary result of the analysis is the total resistance for subsequent variants. This result for analysed example of a K1 canoe is presented in figure below. The resistance value was normalised using the resistance of a parent shape.

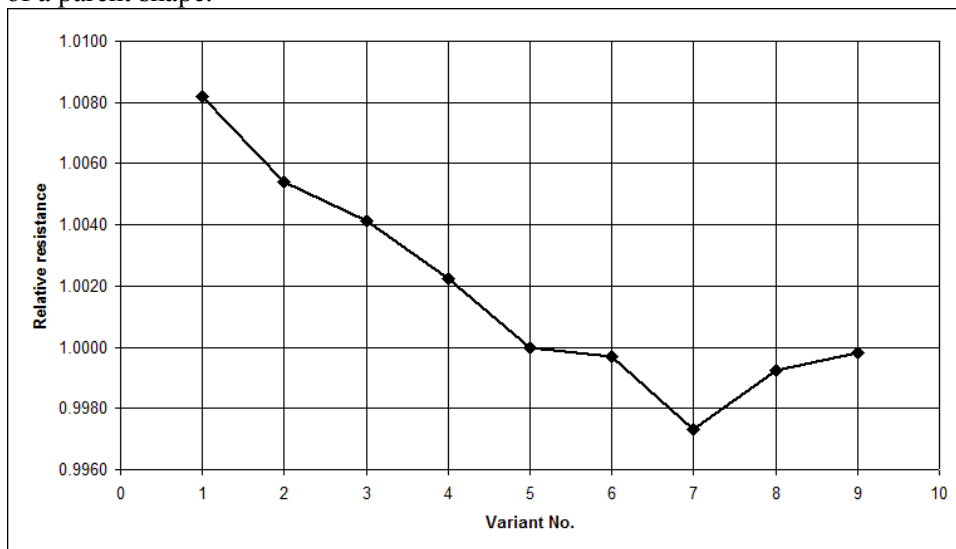


**Fig. 7 Result of the optimization**

The parent shape corresponds to Variant No. 5 in the figure above. Achieved reduction of resistance for optimal variant is only 0.3%, however, this is the order of magnitude of variation expected in

optimization of Olympic class canoes. This result was confirmed by computations realized with the use of detailed model.

The resulting work can thus be summarized as follows:

- a method for optimization based on *a-posteriori* transformation of existing shape was proposed; it is based on a global shaping feature of the CAD software;
- the optimization is realized by selecting the best of the pre-defined variants, analysed subsequently;
- formulation of the transformation method is such that all the variants are within the range of acceptable solution, as the displacement and LCB remains constant;
- the method turned out to be efficient as a tool for fine-tuning of a shape by minor adjustments of the longitudinal volume distribution; slight reduction of resistance was achieved for the best of the analysed existing shapes of K1 canoes.

## **6. Acknowledgement**

The presented work was co-funded by the National Centre for Research and Development, and realized within the framework of the project No. POIR.01.01.01-00-0103/19 "Innovative Olympic and Paralympic class boats for canoeing sprint events". The author would like to express his gratitude to Ryszard Seruga and Tomasz Bugalski from Water Sport Equipment Group - the producer of the canoes and leader of the project.

## **7. References**

1. Vernengo G., Villa D., Gaggero S., Viviani M., "Interactive design and variation of hull shapes: pros and cons of different CAD approaches", International Journal on Interactive Design and Manufacturing, 2019

**CFD CALCULATIONS OF AIR LUBRICATION SYSTEM ON LARGE ORE CARRIER**  
**Mariana Lopes Pinto<sup>1</sup>, Felipe Ruggeri<sup>2</sup>; Claudio Mueller Prado Sampaio<sup>1</sup>; Kazuo Nishimoto<sup>1</sup>;**  
**Philip von Pritzelwitz<sup>3</sup>;**

<sup>1</sup>Numerical Offshore Tank, University of São Paulo, Brazil;<sup>2</sup>Argonautica Engineering & Research, Brazil;<sup>3</sup>Vale Institute of Technology (ITV), Brazil  
[marianalopes@usp.br](mailto:marianalopes@usp.br)

**1. INTRODUCTION**

The ship emissions are a key target in marine industry since IMO set short- and long-term measurements to reduce carbon emissions of the current and new fleet [1]. Among several technological alternatives to reduce ship emissions on large vessels (tanker/ore/container), a promised one is the air lubrication system (ALS).

The air lubrication system is an active system that injects compressed air into the flat bottom area of the ship. In the area covered by air, frictional drag could be reduced more than 80% [2]. As large ore carriers have a wide flat bottom, this technology is an interesting g alternative to gas emissions reduction.

Air flow rate and air injection position are the most important parameters for air lubrication system. There is an ideal combination of air flow rate and position, usually, high flow rate and air injection far from the ship centerline could be inefficient as air leaks through hull side and pressure resistance increases [3] [4]. In the literature, most of studies are based on model experiments and drag reduction is about 10-15%. However, power net savings in full scale are often omitted as there isn't a consolidated methodology for extrapolation data for model to full scale. [3] proposed an extrapolation method, which assumes air layer thickness and friction drag reduction should be the same in model and full scale. Net power savings are 5-6% based on model test for a 66k DWT ship with air lubrication system.

In this paper, the main goal is estimate net savings due to air lubrication system in a larger ore carrier under full loading draft and at different ship velocities. For this purpose, CFD calculations are carried out for a larger ore carrier in model scale with an air lubrication system. Initially the ALS is off in order to obtain the baseline resistance, once the ALS is switched on, drag reduction and net savings are calculated for each condition. In order to establish the ALS layout, a preliminary study is performed to define its parameters, such as: air

injection direction, position and quantity of air injectors, air flow rate and injector breadth.

**2. LARGER ORE CARRIER AND ALS**

The larger ore carrier and its main characteristics are showed in Figure 1 and Table 1, respectively. Froude similarity is adopted, which are commonly used for ship and offshore structures, and scale ratio is  $\lambda = 46.045$ .



Figure 1 – Geometry of the larger ore carrier.

Table 1 – Main characteristics of the ships.

	Full Scale	Model Scale
Length overall [m]	362 m	7.73 m
Beam [m]	65 m	1.39 m
Draft Loaded [m]	23 m	0.49 m
Velocities of the ship [knots]	8 - 18 knots	1.17 – 2.63 knots
$F_n$	0.069 - 0.155	0.069 – 0.155
$Re$	$1.7 - 3.9 \times 10^9$	$5.3 - 12.2 \times 10^6$

The final ALS layout is presented in Figure 2, the dimensions correspond to full scale. Air injectors are rectangular, 0.1m wide, their positions and breadth defined based on the preliminary study (Section 5).



Figure 2 – The ALS layout.

**3. NUMERICAL SETTINGS**

The StarCCM+ package is used in these calculations, which includes the grid generation, solver and post-processing features. It is a Finite Volume based code, which handles incompressible, steady, multiphase flows with

second order scheme in space. In this study, RANS and  $k - \omega SST$  turbulence model equations are solved by segregated manner based on SIMPLE-algorithm.

The calculation domains are rectangular in shape, outlined in Figure 3, with inflow and outflow boundaries. Mass flow inlet is applied on air injector boundaries whereas a no-slip condition is enforced for the ship surface. In this analysis, as Froude number is low, the wave resistance may play a smaller role in total resistance, for this reason and computational costs, symmetry condition was applied at waterline. Furthermore, symmetry conditions are applied at bottom and side boundaries, as well in the longitudinal axis of the ship, since ship's geometry and ALS layouts are symmetrical over this axis.

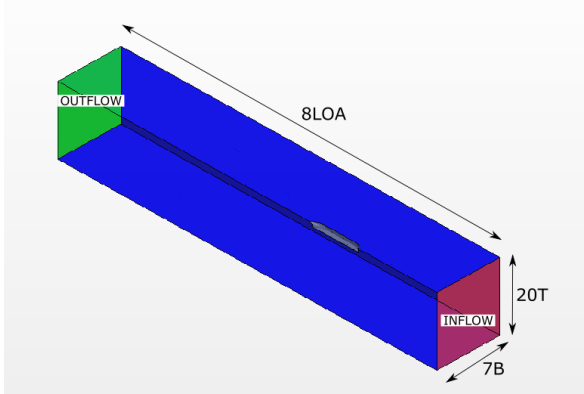


Figure 3 – Computational domain for the calculations.

The grids are hexaedrical with refinement blocks in the regions of greatest details. Additionally, a prismatic layer is applied on the ship walls to allow proper calculation of the boundary layer. Its first layer is set to  $y^+ \approx 1$ , allowing proper performance of the wall functions. A grid convergence analysis was done in order to ensure enough grid resolution and over 10 million cells grid is set. The grid layout and details are shown in Figure 4.

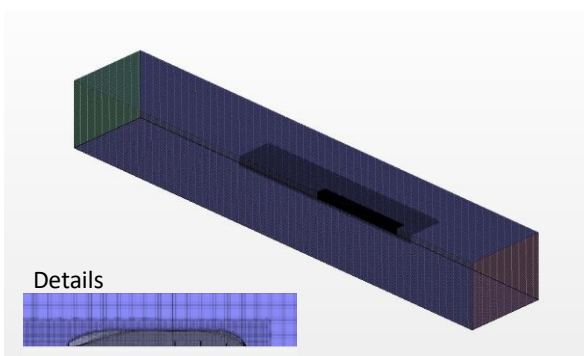


Figure 4 – Grid layout for the calculations.

#### 4. EXTRAPOLATION OF MODEL SCALE DATA TO FULL SCALE DATA

For this analysis, the model total resistance ( $R_{T,m}$ ) is a sum of friction and form drag, where the form drag is expressed by a fraction ( $k$ ) of the friction coefficient ( $C_{f,m}$ ).

$$\text{without ALS: } R_{T,m} = C_{f,m} (1 + k) 0.5 \rho V^2 S$$

$$\text{with ALS: } R_{T,m}^{AIR} = C_{f,m}^{AIR} (1 + k) 0.5 \rho V^2 S$$

$V, S, \rho$  are, respectively, ship velocity, wetted surface area and water specific mass.

The friction drag reduction ( $k_2$ ) is defined by:

$$k_2 = \frac{C_{f,m}^{AIR}}{C_{f,m}}$$

The hypotheses adopted for extrapolation of model scale resistance to full scale resistance are: the form drag fraction ( $k$ ) and the friction drag reduction ( $k_2$ ) are the same in model and full scale for each case. Also, friction coefficient in full scale ( $C_{f,r}$ ) is calculated by ITTC 57.

$$C_{f,r} = \frac{0.075}{(\log Re - 2)^2}$$

The total resistance in full scale ( $R_{T,r}$ ) is therefore expressed as:

$$\text{without ALS: } R_{T,r} = C_f (1 + k) 0.5 \rho V^2 S$$

$$\text{with ALS: } R_{T,r}^{AIR} = C_f (1 + k + k_2) 0.5 \rho V^2 S$$

And total drag reduction (DR) is defined by:

$$DR = \frac{R_{T,r} - R_{T,r}^{AIR}}{R_{T,r}}$$

The delivered power ( $P_d$ ) is calculated assuming a constant global efficiency of  $\eta = 0.7$ .

$$\text{without ALS: } P_d = \frac{R_{T,r} V}{\eta}$$

$$\text{with ALS: } P_d^{AIR} = \frac{R_{T,r}^{AIR} V}{\eta}$$

The net power savings (NPS) is the difference between delivered power without and with ALS minus the power demanded by the air compression system.

$$NPS = \frac{P_d - P_d^{AIR} - P_{comp}}{P_d}$$

The compressor' power is estimated by assuming a polytropic process to compress the air in standard conditions (1atm and 25°C) with an efficiency of  $\eta_c = 0.7$ .

$$P_{comp} = \frac{Q}{\eta_c} p_1 \left( \frac{n}{n-1} \right) \left\{ \left( \frac{p_2}{p_1} \right)^{\frac{n-1}{n}} - 1 \right\}$$

Where  $p_1$  is atmospheric pressure,  $p_2$  is the hydrostatic pressure under the keel,  $n$  is 1.4, assuming an isentropic process, and air flow rate is quantified in terms of air layer thickness ( $t$ ) as the following equation.

$$Q = tVB$$

$B$  is breadth of the air injector. The assumption is that air layer thickness remains the same in model and full scale.

## 5. PRELIMINARY STUDY

For the preliminary study, ship velocity is assumed 14 knots, with rectangular injectors (5m x 0.1m) positioned over the hull as shown in Figure 5. The injectors are identified by the letters “C” and “L”, which means central and lateral, respectively, as well as by number of the station that they are installed.

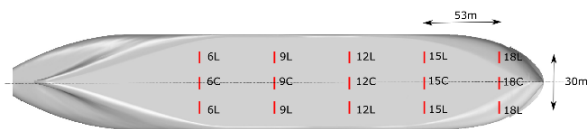


Figure 5 – Injector positions for the preliminary study.

Several preliminary studies are made to determine the best parameters for the injectors:

### Angle of air injection

Angle of injection analysis is performed for injector ‘15C’ and 5mm of air layer thickness. The angle of air injection is varied from 20° to 90° (i.e. air is injected perpendicular to ship velocity). The optimal angle is 30°, however there are only minor differences for higher angles, as shown in Figure 6.

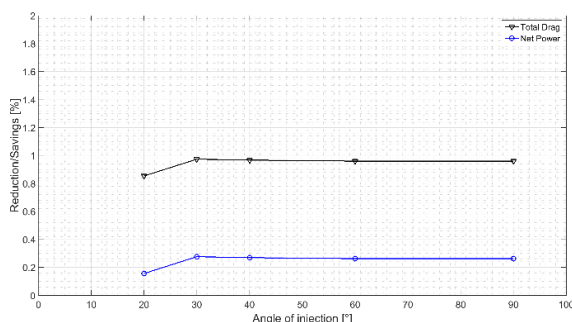


Figure 6 – Angle of injection results.

### Position of Air Injectors

The effect of injector position is investigated in this section. The injectors are distributed as shown in Figure 5 (stations 6, 9, 12, 15 and 18),

the air layer thickness is kept 5mm and injection angle, 30°.

First, the influence of the lateral injection is investigated considering single working rows. Figure 7 shows net power savings (blue line) and total drag reduction (black line) for central injection (full line) alone and of the central and lateral injection combined (dashed line) for each single station. As shown in the figure, central injection is more efficient in forward regions (station >12). When the lateral injection is turned on, drag reduction increases however net power savings remains almost the same for the middle stations, with significant reductions for stations 18 and 6. For station 18, the lateral injection isn’t in flat bottom area, also, air escapes at hull sides, increasing the form drag. For station 6, flat bottom area is short and air escapes similarly.

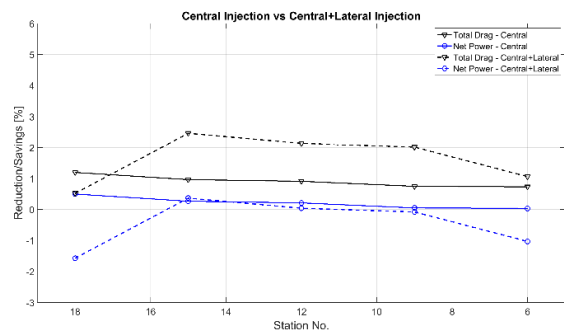


Figure 7 – Central injection vs. Central+Lateral injection results

As a next step, multiple injection rows of injection are investigated. (note: for station 18 only central injection was considered due to inefficient lateral injection). Figure 8 shows that drag reduction and net power savings, the nomenclature used in the figure representing the set of multiple row, for example “18E15E12” meaning injectors at stations 18, 15 and 12 are turned on. .

Once again drag reduction increases with lateral injection but net power savings decrease as compress air power increases substantially. The multiple rows arrangement of air injection is better than the one row (see Figure 7), especially, for central injection case, where the 18E15E12 is marginally the best combination.

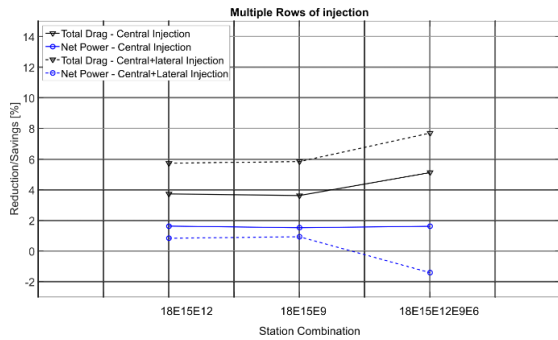


Figure 8 – Multiple row of injection results

### Air-Flow Rate

Air-flow rate is analyzed based on ‘18E15E12’ central injection layout. As air-flow rate is expressed by air layer thickness,  $t$  is defined 3mm, 5mm and 7mm. There are 27 combination of  $t$  and station injection, the results for each combination are presented in Figure 9, where each subtitle “t18” is associated a different air layer thickness for the injectors at the 18 station. Analogously, the same applies to the other row stations.

As can be observed in the figure, that the lowest air-flow rate ( $t=3\text{mm}$ ) at the forward station (station 12) is the best selection for multiple injection, while the configuration involving high air-flow rate are always less effective in all station. The optimal air layer thickness corresponds to the  $t_{12}=3\text{mm}$  with  $t_{18}$  and  $t_{15}$  equal to 5mm.

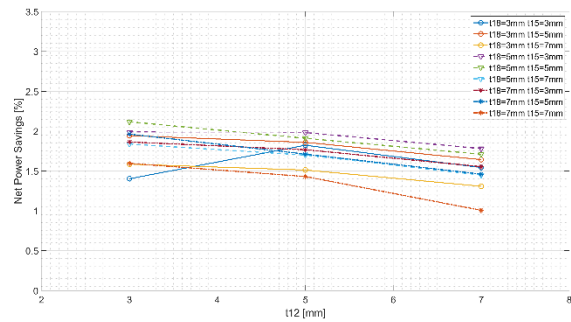


Figure 9 – Air-Flow Rate Results

### Air Injector Breadth

The final investigation is air injector breadth. The central injector at station 15 (‘15C’) is chosen and three breadths are tested: 5m, 10m and 20m. Larger breadth injector improves drag reduction and net power savings, as shown in Figure 10.

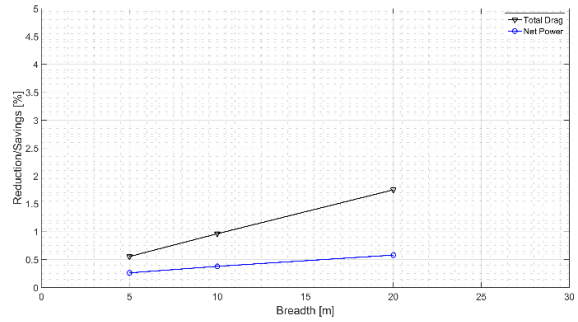


Figure 10 – Air injector breadth results

## 6. RESULTS AND DISCUSSION

Based on the preliminary study, the final ALS layout is defined, Figure 2, and the main parameters are summarized in Table 2, in full scale.

Table 2 – Main parameters of ALS

Station Position	18	15	12
Breadth [m]	10	20	20
Air layer thickness [mm]	5	5	3
Angle of injection [°]	30	30	30

The CFD study is carried out for full loading draft and ship velocities between 8 knots and 18 knots. Figure 11 shows drag reduction and power net savings. Drag reduction remains almost constant for all the ship velocity range while the net power savings increase with ship velocity and reached 6% for the highest one, in spite of the negative power savings at low ship velocities, where the compressor power is higher than delivered power savings.

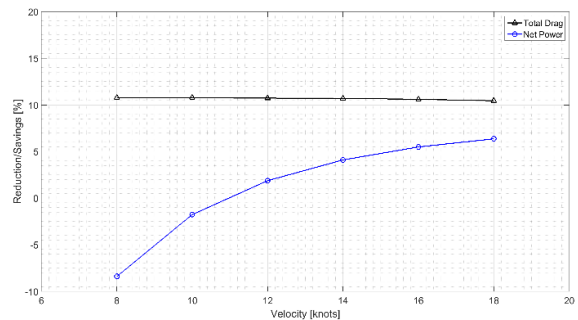


Figure 11 – Large ore carrier net power savings in full loaded draft.

## 7. CONCLUSIONS

Based on CFD calculations, a preliminary study is conducted to define main parameters of a ALS system. The effect of various ALS parameters are extensively analyzed, the main conclusions being:

- 1) Optimal angle of injection is 30°;
- 2) Air injector should be located in flat bottom area, near the ship's longitudinal axis and around the parallel middle body;
- 3) Air injection in multiple (three) rows is better than only one row;
- 4) High air-flow rate could decrease power net savings and optimal air flow rate is roughly for an air layer thickness of 5mm;
- 5) Larger injector breadth increases power net savings.

Power net savings and drag reduction are, respectively, about 6% and 10%, which is in accordance with others results in literature.

For air layer thickness of 5mm and ship velocities less than 10 knots, the power net savings are negative, i.e., the amount of energy consumed by air compressor is higher than energy savings.

## ACKNOWLEDGEMENTS

This research is supported by Vale Institute of Technology ("Ecoshipping Project").

## REFERENCES

- [1] IMO, "Module 2 - Ship Energy Efficiency Regulations and Related Guidelines," London, 2016.
- [2] B. R. e. a. ELBING, "Bubble-induced skin-friction drag reduction and the abrupt transition to air-layer drag reduction," *Journal of Fluid Mechanics*, vol. 612, pp. 201-236, Oct 2008.
- [3] J. e. a. JANG, "Experimental investigation of frictional resistance reduction with air layer on the hull bottom of a ship," *International Journal of Naval Architecture and Ocean Engineering*, vol. 6, pp. 363-379, Jun 2014.
- [4] S. H. PARK e I. LEE, "Optimization of drag reduction effect of air lubrication for a tanker model," *International Journal of Naval Architecture and Ocean Engineering*, vol. 10, pp. 427-238, Jul 2018.

# Space-Time Simulation of a Heaving and Pitching Foil with Exact Enforcement of Time Periodicity

Jacob E. Lotz<sup>1</sup>

Marco F. P. ten Eikelder<sup>2</sup>

Ido Akkerman<sup>1</sup>

<sup>1</sup> Delft University of Technology, The Netherlands

<sup>2</sup> Leibniz University Hannover, Germany

Email: j.e.lotz@tudelft.nl, marco.ten-eikelder@ibnm.uni-hannover.de, i.akkerman@tudelft.nl

## 1 Introduction

In recent years there has been a renewed interest in hydrofoils, particularly for leisure craft. For a wider adoption of hydrofoils in commercial vessels it is desirable to have a better handle on the behavior of the vessel in waves. Therefore the effect of waves on hydrofoils, and their actuators, has to be studied in detail. In particular, the presence of wave orbital motions is essential. This induces an unsteady inflow which can be characterized as a combined heave and pitch motion. These motions are assumed to be periodic in time.

We use residual-based variational multiscale (RBVMS) turbulence modelling [1] in a time-periodic space-time formulation for the simulation of heaving and pitching submerged hydrofoils. This is implemented in our in-house code DelFI using the MFEM library [2]. We apply NURBS-based isogeometric analysis [3] for the spatial discretization. This provides a better representation of both the curvature at the leading edge of the hydrofoil and of the prescribed mesh motion. We employ a second-order periodic NURBS C-mesh which is C1-continuous in the interior temporal domain.

The no-slip boundary condition of the moving foil is enforced weakly [4]. We introduce a mesh dependent boundary velocity for the no slip boundary condition of the moving boundary of the hydrofoil. We use an essential boundary condition for a uniform flow in horizontal direction as an inflow boundary condition. The outflow boundary condition is enforced naturally as a uniform flow in horizontal direction.

This extended abstract consists of five parts. First, the strong incompressible space-time Navier-Stokes equations are discussed. Second, a method to determine the boundary velocity for the no-slip boundary condition is introduced. Third, our periodic space-time mesh of the heaving and/or pitching hydrofoil is presented. Fourth and fifth, results and conclusions are provided.

## 2 Incompressible space-time Navier-Stokes equations

In the incompressible space-time Navier-Stokes equations, time  $t$  is considered a spatial coordinate. The space-time coordinate  $\hat{x}$  can be defined as:

$$\hat{\mathbf{x}} = \begin{bmatrix} \mathbf{x} \\ t \end{bmatrix} = \begin{bmatrix} x_1 \\ x_2 \\ t \end{bmatrix} = \begin{bmatrix} x_1 \\ x_2 \\ x_3 \end{bmatrix} \quad (1)$$



with  $x_3 = t$ . Furthermore a space-time velocity vector is defined:

$$\hat{\mathbf{u}} = \begin{bmatrix} \mathbf{u} \\ 1 \end{bmatrix} = \begin{bmatrix} u_1 \\ u_2 \\ 1 \end{bmatrix} = \begin{bmatrix} u_1 \\ u_2 \\ u_3 \end{bmatrix}. \quad (2)$$

Note that:

$$u_3 = \frac{\partial x_3}{\partial t} = \frac{\partial x_3}{\partial x_3} = 1. \quad (3)$$

Now the incompressible space-time Navier-Stokes equations can be derived from the two-dimensional incompressible Navier-Stokes equations:

$$\rho \left( \frac{\partial \mathbf{u}}{\partial t} + (\mathbf{u} \cdot \nabla_{\mathbf{x}}) \mathbf{u} \right) - \nabla_{\mathbf{x}} p - \mu \nabla_{\mathbf{x}}^2 \mathbf{u} = \mathbf{f}, \quad (4)$$

$$\nabla_{\mathbf{x}} \cdot \mathbf{u} = 0. \quad (5)$$

Using  $t = x_3$ , the space-time coordinate  $\hat{\mathbf{x}}$  and space-time velocity  $\hat{\mathbf{u}}$ , the first two terms on the left-hand side of the momentum equation can be rewritten:

$$\rho \left( \frac{\partial \mathbf{u}}{\partial x_3} + (\mathbf{u} \cdot \nabla_{\mathbf{x}}) \mathbf{u} \right) = \rho (\hat{\mathbf{u}} \cdot \nabla_{\hat{\mathbf{x}}}) \mathbf{u}. \quad (6)$$

Using equation (6), equation (5) can be rewritten to:

$$\rho (\hat{\mathbf{u}} \cdot \nabla_{\hat{\mathbf{x}}}) \mathbf{u} - \nabla_{\mathbf{x}} p - \mu \nabla_{\mathbf{x}}^2 \mathbf{u} = \mathbf{f}, \quad (7)$$

$$\nabla_{\mathbf{x}} \cdot \mathbf{u} = 0 \quad (8)$$

which can be interpreted as steady Navier-Stokes equations.

### 3 Mesh dependent boundary velocities

To apply the no-slip boundary condition a boundary velocity is required. The no-slip boundary condition on the hydrofoil  $\Gamma_{\text{foil}}$  is defined as:

$$\mathbf{u} = \mathbf{g} \quad \text{on} \quad \Gamma_{\text{foil}} \quad (9)$$

where  $\mathbf{g}$  is the velocity of the boundary.  $\mathbf{g}$  depends on the motion of the hydrofoil in the mesh:

$$\mathbf{g} = \frac{\partial \mathbf{x}}{\partial t} = \frac{\partial \mathbf{x}}{\partial x_3} \quad \text{on} \quad \Gamma_{\text{foil}}. \quad (10)$$

To determine this derivative we use the definition of a NURBS volume. The geometry of a NURBS volume depends on a set of control points, three knotvectors and three coordinates  $\boldsymbol{\xi} = [\xi_1, \xi_2, \xi_3]$  in the reference space [3]:

$$\mathbf{x} = \mathbf{x}(\xi_1, \xi_2, \xi_3) \quad (11)$$

where  $\xi_3$  is the coordinate corresponding with the time direction  $x_3$ .

The surface of the hydrofoil is the face of a three-dimensional NURBS Patch. Therefore,  $\mathbf{x}$  on  $\Gamma_{\text{foil}}$  is only a function of the controlpoints, the two knotvectors and the two coordinates in the reference space corresponding to the face of the NURBS patch. The coordinates are chosen to be  $\xi_a$  and  $\xi_b$ :

$$\mathbf{x} = \mathbf{x}(\xi_a, \xi_b) \quad \text{on} \quad \Gamma_{\text{foil}}. \quad (12)$$

where  $a, b = 1..3$  and  $a \neq b$ . A graphical representation of a NURBS patch in the physical and reference space is given in figure 1, where  $a = 1$  and  $b = 3$ . The three-dimensional NURBS patch is visualized in dashed lines and its face is represented in solid lines.

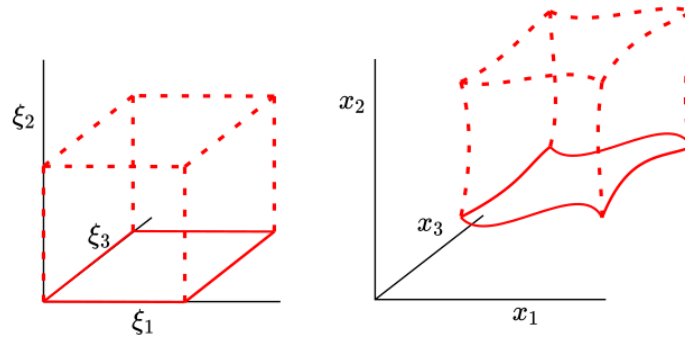


**Figure 1:** Reference space (l) and physical space (r) in three dimensions.

Now equation (10) can be rewritten using the chain rule and assuming that  $\xi_a$  or  $\xi_b$  is aligned with  $x_3$  ( $a = 3$  or  $b = 3$ ), equation (10) is rewritten to

$$\mathbf{g} = \sum_{i=a,b} \frac{\partial \mathbf{x}}{\partial \xi_i} \frac{\partial \xi_i}{\partial x_3} \quad \text{on} \quad \Gamma_{\text{foil}} \quad (13)$$

where  $\frac{\partial \mathbf{x}}{\partial \boldsymbol{\xi}}$  is the Jacobian of the mapping from reference space to physical space and  $\frac{\partial \boldsymbol{\xi}}{\partial \mathbf{x}}$  is its inverse. Rewriting gives:

$$\mathbf{g} = \sum_{i=a,b} \frac{\partial \mathbf{x}}{\partial \xi_i} \left( \frac{\partial x_3}{\partial \xi_i} \right)^{-1} \quad \text{on} \quad \Gamma_{\text{foil}}. \quad (14)$$

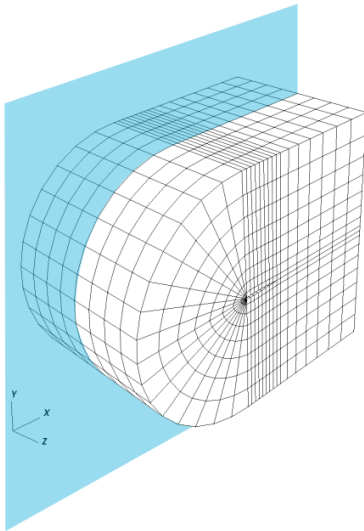
## 4 Time periodic space-time mesh

The three-dimensional space-time mesh can be seen in figure 2. The mesh is an extruded two-dimensional C-shaped mesh in the time ( $x_3$ ) direction and employs second order NURBS. The hydrofoil is displaced in the  $[x_1, x_2]$ -plane such that it is given a motion. This motion can be heave, pitch or a combination of both. A result for a heaving and pitching motion can be seen in figure 4.

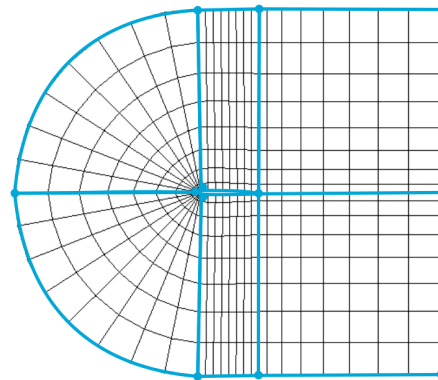
The mesh or solution at a given moment in time can be viewed by means of slicing. The slicing plane can be seen in blue in figure 2 and its result, showing the C-shaped mesh, in figure 3.

Figure 3 shows the side view of the six employed NURBS patches. The second order NURBS patches are  $C^1$ -continuous internally and  $C^0$ -continuous across patches. The mesh motion is  $C^1$ -continuous on the internal temporal domain since the extrusion uses only one NURBS patch. The periodicity is enforced by means of a periodic boundary condition.

The resulting orientation of a heaving and pitching hydrofoil can be seen in figure 4 for three moments in time,  $t = [0.24, 1.80, 3.02]$ , and an extrusion length of 4.00.



**Figure 2:** View of the mesh showing the slice.



**Figure 3:** Slice of the mesh and the six NURBS patches.

## 5 Results

Results for a heaving and pitching hydrofoil are shown at three moments in time:  $t = [0.24, 1.80, 3.02]$ . Figure 5 shows results for  $|\mathbf{u}|$  and figure 6 shows results for pressure  $p$ . At  $t = 0.24$  the hydrofoil moves downward and has a nose up angular velocity. At the next moment in time,  $t = 1.88$ , the hydrofoil moves upward and has a nose up angular velocity. At the last moment in time,  $t = 3.02$ , the hydrofoil is at the top of the sinus of the heave motion and has a nose down angular velocity.

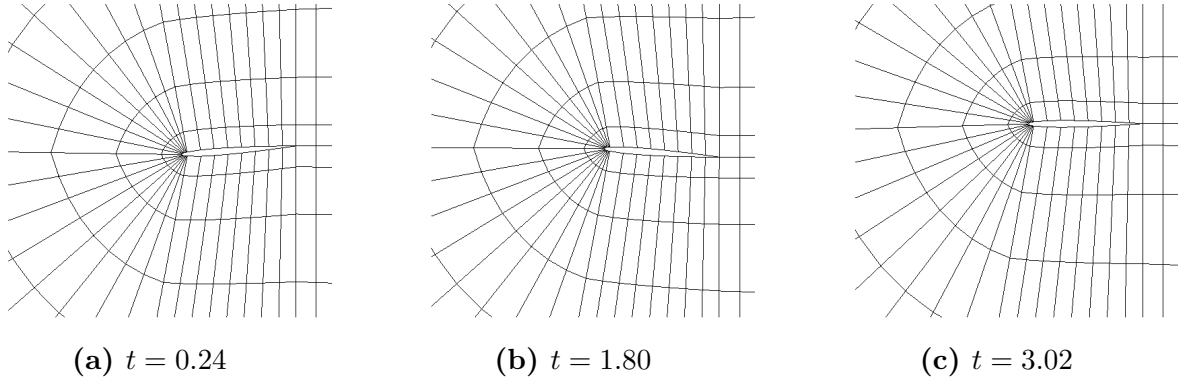


**Figure 4:** Orientation of a heaving and pitching hydrofoil at three moments in time.

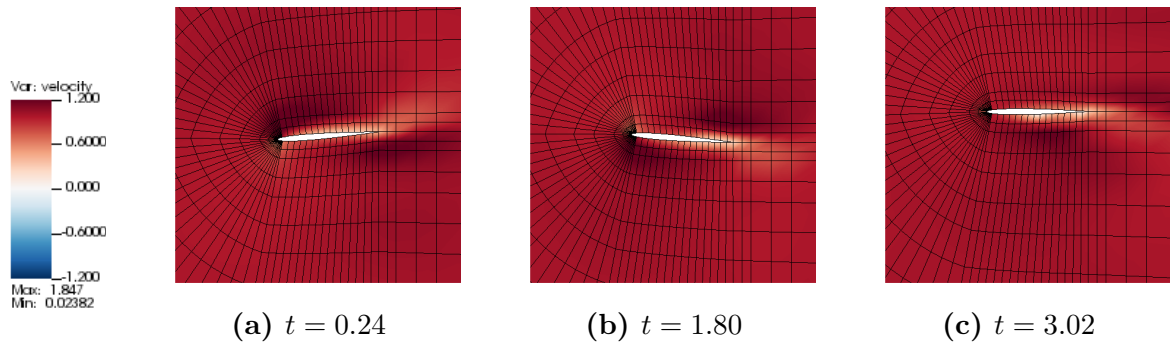


**Figure 5:** Results for velocity  $|\mathbf{u}|$  at three moments in time.

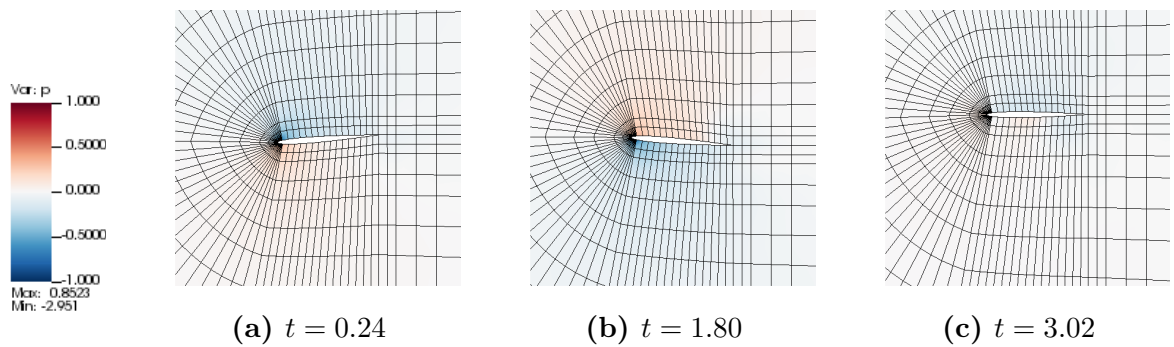


**Figure 6:** Results for pressure  $p$  at three moments in time.

## 6 Conclusions

A space-time formulation of the Navier-Stokes equations has been successfully implemented. Using a time periodic second order NURBS mesh, weak boundary conditions and mesh dependent boundary velocities we were able to simulate the flow around a heaving and pitching foil with  $C1$ -continuity on the internal time domain.

## References

- [1] Y. Bazilevs et al. “Variational multiscale residual-based turbulence modeling for large eddy simulation of incompressible flows”. In: *Computer Methods in Applied Mechan-*

- ics and Engineering* 197.1-4 (2007), pp. 173–201. ISSN: 00457825. DOI: 10.1016/j.cma.2007.07.016.
- [2] R. Anderson et al. “MFEM: A modular finite element methods library”. In: *Computers and Mathematics with Applications* 81 (2021), pp. 42–74. ISSN: 08981221. DOI: 10.1016/j.camwa.2020.06.009. arXiv: 1911.09220.
- [3] T. J.R. Hughes, J. A. Cottrell, and Y. Bazilevs. “Isogeometric analysis: CAD, finite elements, NURBS, exact geometry and mesh refinement”. In: *Computer Methods in Applied Mechanics and Engineering* 194.39-41 (2005), pp. 4135–4195. ISSN: 00457825. DOI: 10.1016/j.cma.2004.10.008.
- [4] Y. Bazilevs et al. “Weak Dirichlet boundary conditions for wall-bounded turbulent flows”. In: *Computer Methods in Applied Mechanics and Engineering* 196.49-52 (2007), pp. 4853–4862. ISSN: 00457825. DOI: 10.1016/j.cma.2007.06.026.

# The resistance of a plate moving through mud: experiments and simulations

Stefano Lovato<sup>1</sup>, Alex Kirichek<sup>1</sup>, Serge Toxopeus<sup>2</sup>, Just Settels<sup>2</sup>, Arno Talmon<sup>1,3</sup>, Geert Keetels<sup>1</sup>

<sup>1</sup>Delft University of Technology, Delft/Netherlands.

<sup>2</sup>Maritime Research Institute Netherlands, Wageningen/Netherlands.

<sup>3</sup>Deltares, Delft/Netherlands

s.l.lovato@tudelft.nl

## 1 Introduction

Safe navigation in restricted areas is ensured, among others, by setting a minimum under keel clearance (UKC), which is the distance between the ship's keel and the bottom. However, in many ports and waterways around the world the seabed is covered by mud (Fig. 1) and the position of the bottom is not longer clearly defined. In this case, the depth is determined based on the *nautical bottom*, defined as “the level where physical characteristics of the bottom reach a critical limit beyond which contact with a ship's keel causes either damage or unacceptable effects on controllability and manoeuvrability”(PIANC).

A complete implementation of the nautical bottom concept therefore requires a good understanding of the possible effects of muddy bottoms on the navigation of marine vessels. Although some model-scale (Delefortrie et al. (2005)) and full-scale (Barth et al. (2016)) trials have been carried out in the past decades, results are difficult to generalise because of the large number of parameters involved (UKC, mud layer thickness, rheological properties, ship's geometry and speed, fairway cross-section, etc). Thus, for practical reasons, port authorities define the nautical bottom as the level where the mud reaches either a critical density (e.g.  $1200 \text{ kg/m}^3$ ) or a critical rheological property, based on the experience acquired over the years. These criteria, however, may be too conservative in some cases, which either lead to unnecessary maintenance and environmental costs, or to excessive restrictions on the allowed draughts of the vessels.



Fig. 1: A ship moving through a muddy seabed (snapshot from [www.youtube.com/watch?v=LSbQhUJMBJw](http://www.youtube.com/watch?v=LSbQhUJMBJw)).

A research project was thus started with the aim to build a Computational Fluid Dynamic (CFD) framework that would allow more systematic studies on this topic (Lovato et al. (2021)). One of the main difficulties of the CFD approach, however, is that mud exhibits a very complex non-Newtonian rheology (see e.g. Shakeel et al. (2021)). Nevertheless, for engineering purposes, mud is often modelled as a Bingham fluid as it is the simplest rheological model capable of capturing one of the main features of mud, i.e. viscoplasticity. These type of fluids start to flow only when the level of shear stress exceeds a certain threshold, called yield stress. Below the yield stress, viscoplastic fluids behave as solid-like materials. Other examples of these fluids are gels, drilling fluids, cosmetic and food products (e.g mayonnaise).

The main goal of this research is to establish whether, in spite of its simplicity, the Bingham model is suitable for prediction of the forces acting on marine vessels moving through mud. Since experimental data for such scenarios are rather difficult to obtain, a simpler problem is considered here. In this paper, an experimental and numerical study on the resistance of a thin plate moving through homogeneous mud in laminar regime will be presented.

## 2 Experimental methods

### 2.1 Facility and setup

The experimental data were obtained in the “water-soil flume” (Fig. 2 (a)) at the research institute Deltares. The flume, which is 30 m long, 2.5 m high and 2.4 m wide, was filled with natural mud previ-

ously dredged from the seabed in the port of Rotterdam.

The experiments consisted in towing a smooth plywood plate through mud and measuring the total resistance. The towing speed of the carriage was varied between  $0.25$  and  $1.0 \text{ m s}^{-1}$  and, for each speed, the tests were repeated 8 times. The plate has been reinforced with vertical and horizontal wooden beams to increase its stiffness and to reduce possible bending. The main information about the experiments are summarised in [Table 1](#).

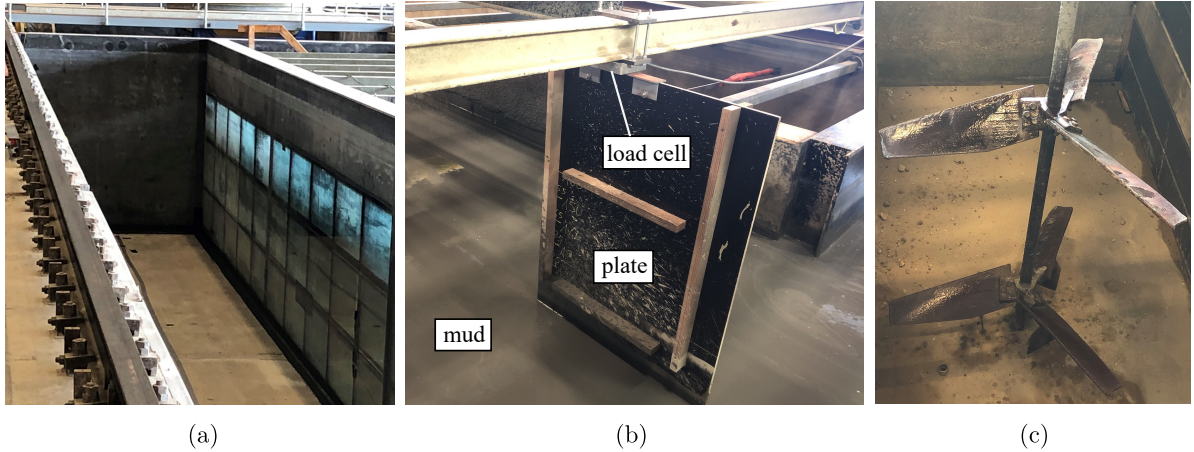


**Fig. 2:** (a) Water-soil flume at Deltares, Netherlands. (b) Plywood plate immersed in mud. (c) Mixer used to homogenise the mud in the flume.

## 2.2 Uncertainties

The uncertainties due to the calibration of the load cell was estimated by pulling the plate with a thread attached to a dynamometer previously calibrated using weights. The force was increased from 4 to 24 N by constant increments of 2 N. The maximum observed discrepancy between the load cell and the dynamometer was about 3.5%.

It was thus decided to adopt  $U_{cal} = 4\%$ , as a ‘Type B’ uncertainty. Another source of uncertainty originates from the scatter of the mean force obtained from the stationary part of the load cell signal. Thus, each test was repeated 8 times and the uncertainties due to the repeated tests,  $U_{rep}$ , was estimated by statistical methods, similarly to the procedure proposed by the ITTC. Assuming that the mean force follows the Student’s  $t$ -distribution,  $k = 2.306$  was adopted as coverage factor, which ensures a 95% confidence level with the 8 repetitions (degrees of freedom). The uncertainty due to the experimental setup was not estimated as the time required would have been incompatible with the time available to complete the experiments. The final experimental uncertainties  $U_{exp}$  in the mean force is thus obtained from the RMS of  $U_{cal}$  and  $U_{rep}$ , and it is within 5.1% of the experimental data for all cases.

**Table 1:** Main information about the experiments. Note that the mud level is 1.96 m for the thickest mud and 2.0 m otherwise.

Plate		Flume	
Chord (m)	0.8	Length (m)	30.0
Thickness (m)	0.012	Width (m)	2.4
Submerged span (m)	0.96 or 1.0	Mud level (m)	1.96 or 2.0
Speed (m/s)	0.27, 0.52, 0.77, 1.02	Height (m)	2.5

## 2.3 Mud preparation

The mud was collected from the Calandkanaal (port of Rotterdam) and it was transported to the water-soil flume. In order to analyse the effect of different mud rheologies, the mud was diluted with sea water (having same salinity as the natural system) to obtain three densities that correspond to target yield stress values of approximately 30, 20 and 10 Pa. To ensure the homogeneous properties within the water-soil flume, the mud was stirred using a rotating mixer ([Fig. 2 \(c\)](#)) that was towed three times back-and-forth prior the experiments with each mud. After the homogenisation, six samples of each mud were collected.

## 2.4 Mud rheology

The HAAKE MARS I rheometer was used to perform the rheological experiments on the mud samples using concentric cylinder geometry and keeping the temperature at 20 °C. The flow curves of the mud samples were obtained in controlled shear rate mode with the following protocol: (i) shear rate ramp-up from 0 to 300 s<sup>-1</sup> in 180 s, (ii) constant shear rate of 300 s<sup>-1</sup> for 60 s, and (iii) shear rate ramp-down from 300 to 0 s<sup>-1</sup> in 180 s. This type of test is quite fast and repeatable to obtain the yield stress of remoulded samples (Shakeel et al. (2021)). The ramp-down curve for shear rates above 200 s<sup>-1</sup> was then used for the least-squares fitting of the Bingham model (Fig. 3), which, for simple shear flow, reads:

$$\begin{cases} \tau = \tau_B + \mu_B \dot{\gamma} & \text{for } \tau_B \leq \tau, \\ \dot{\gamma} = 0 & \text{for } \tau < \tau_B, \end{cases} \quad (1)$$

where  $\tau$  (Pa) is the shear stress,  $\dot{\gamma}$  (s<sup>-1</sup>) is the shear rate  $\tau_B$  (Pa) is the yield stress and  $\mu_B$  (Pa s) is the Bingham (or plastic) viscosity. The density and the Bingham parameters that were obtained from the mud samples and used in the CFD computations are reported in Table 2.

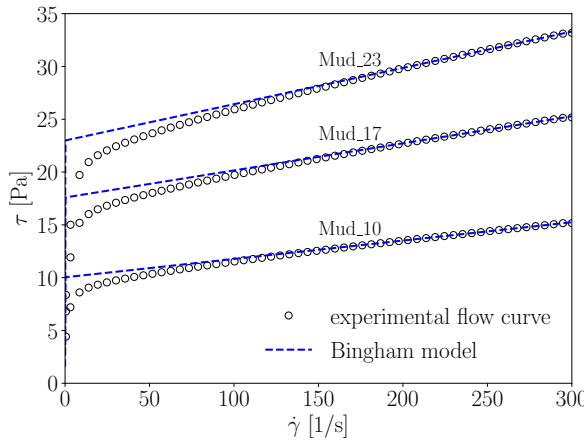


**Table 2:** Mean values of density and Bingham parameters over the six sample for each mud.

Mud case	$\rho$ (kg/m <sup>3</sup> )	$\tau_B$ (Pa)	$\mu_B$ (Pa s)
Mud_10	1171	9.96	0.0172
Mud_17	1190	17.3	0.0249
Mud_23	1200	23.0	0.0344

**Fig. 3:** Mud flow curves and Bingham fit for one of the six samples of each mud.

## 3 Numerical methods

### 3.1 Governing equations

Preliminary calculations have shown that the effect of the free surface with no angles of attack is within the numerical uncertainties. Therefore, double-body calculations were performed by solving the incompressible continuity and momentum equations combined with the Bingham constitute equation. However, in order to avoid numerical difficulties caused by the infinite viscosity when  $\dot{\gamma} = 0$  in Eq. (1), the regularisation approach of Papanastasiou (1987) was used. The non-differentiable constitutive equation Eq. (1) was thus replaced by

$$\tau = \tau_B(1 - e^{-m\dot{\gamma}}) + \mu_B \dot{\gamma} \quad (2)$$

where  $m$  is the regularisation parameter. In the limit of  $m \rightarrow \infty$ , Eq. (2) tends to Eq. (1), therefore large values of  $m$  are required in order to mimic the behaviour of the ideal (non-regularised) Bingham model (Eq. (1)). For this work,  $m$  was chosen such that  $m\tau_B/\mu_B = 12000$ , which represents the ratio of the possible maximum and minimum viscosity attainable by the fluid.

### 3.2 Grids and boundary conditions

The computational domain was discretised with a series of multi-block structured H-type grids, with 1.77 million cells in the finest grid. The size of the first cell away from the plate surface is  $2 \times 10^{-4}$  m. For the boundary conditions, the inflow velocity was applied at the inlet boundary, whereas the no-slip/no-penetration condition was applied to the plate surface. At the outlet, Dirichlet condition was imposed for the pressure, and symmetry conditions were applied to the top and symmetry planes. Preliminary calculations showed that the presence of the plate is not ‘felt’ by the side and bottom walls, thus symmetry conditions were applied also to these boundaries (Fig. 4).



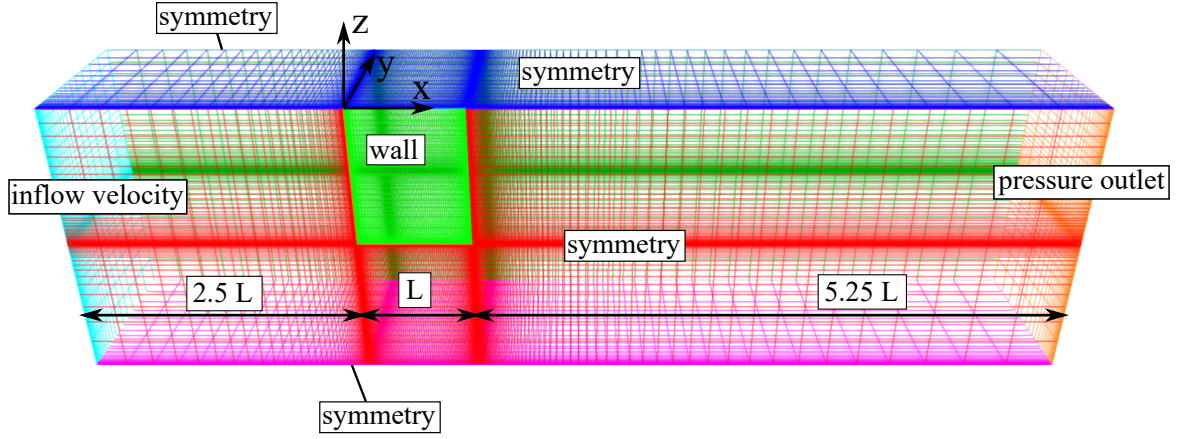


Fig. 4: Computational domain and boundary conditions.

### 3.3 Flow solver

The CFD code used for the present work is ReFRESKO (Vaz et al. (2009)), a viscous-flow code currently being developed and verified for maritime purposes by the Maritime Research Institute Netherlands (MARIN) in collaboration with several non-profit organisations around the world. Originally developed for Newtonian fluids, ReFRESKO has been recently extended and verified (Lovato et al. (2021)) to include the Herschel-Bulkley model, of which Bingham is just a particular case. Equations are discretised in strong-conservation form with a second-order finite-volume method for unstructured meshes with cell-centred co-located variables. Mass conservation is ensured with a pressure-correction equation based on a SIMPLE-like algorithm. The convective fluxes of the transport equations are linearised with the Picard method and discretised with the Harmonic scheme (Van Leer (1979)).

### 4 Validation procedure

According to the validation procedure proposed by ASME (2009), the modelling errors,  $\delta_{model}$ , can be estimated by comparing two quantities: the (expanded) validation uncertainty,

$$U_{val} = \sqrt{U_{num}^2 + U_{exp}^2 + U_{input}^2} \quad (3)$$

and the comparison error,  $E = S - D$ , where  $S$  is the simulation value and  $D$  is the experimental value,  $U_{num}$  and  $U_{exp}$  are the numerical and experimental uncertainty, respectively, and  $U_{input}$  is the uncertainty in the simulation input parameters.  $E$  and  $U_{val}$  define an interval within which  $\delta_{model}$  falls, i.e.  $E - U_{val} \leq \delta_{model} \leq E + U_{val}$ .

### 5 Input parameter uncertainties

Numerical simulations require input parameters that are experimentally determined and that have uncertainties associated with them. The input parameter uncertainties,  $U_{input}$ , were estimated using the perturbation method and by approximating the numerical data with analytical formulas for the friction and pressure components (not discussed here). For the present work, the input parameters are the: plate's draught  $H$ , carriage's speed  $V$  (inflow velocity), mud density  $\rho$ , Bingham yield stress  $\tau_B$  and viscosity  $\mu_B$ . For all the cases, the estimated input parameter uncertainties combined are within 2.8% of the CFD results.

### 6 Solution verification

Solution verification was carried out to estimate the numerical errors and uncertainties. For steady flows, numerical errors are usually divided in round-off, iterative and discretisation errors. Round-off errors arise from the finite precision of computers and, for this work, they can be neglected by using double-precision machines. Iterative errors stem from the use of iterative methods to find the solution of the discretised equations. For this work, iterations were stopped when the  $L_\infty$  norm of the normalised residuals dropped below  $10^{-7}$ . However, this convergence tolerance was actually hardly met, thus, in practice,

calculations were stopped when the maximum number iterations was reached. As a result, iterative errors could not be neglected and the uncertainties,  $U_{it}$ , were estimated using the method proposed in Eça and Hoekstra (2009), whereas the discretisation uncertainties,  $U_d$ , were estimated with the method described in Eça and Hoekstra (2014). The total numerical uncertainty,  $U_{num}$ , was finally obtained by arithmetic summation of  $U_{it}$  and  $U_d$ . Overall, the numerical uncertainties do not exceed 2.4%.

The use of regularisation methods produces an additional error, the regularisation error, which is the difference between the solution of the regularised and the ideal (non-regularised) model. In absence of validated methods to estimate the regularisation uncertainty,  $U_{reg}$ , from numerical data, we have estimated  $U_{reg}$  adopting the same method used for  $U_d$  by replacing the grid size with  $1/m$ . Overall, the estimated regularisation uncertainties do not exceed 3.9%. Since the regularisation parameter affects both discretisation and iterative errors,  $U_{reg}$  was arithmetically (no RMS) added to  $U_{num}$ .

## 7 Results and discussion

The estimated comparison errors and the validation uncertainties are reported in Table 3 together with the upper bounds of the modelling errors, whereas the total resistance is plotted in Fig. 5 against the inflow velocity. Table 3 shows that the comparison error is often close or within the validation uncertainties, except at the lowest speed, where the comparison errors always exceed the uncertainties. In any case,  $E$  is never sufficiently larger than  $U_{val}$  to allow a direct estimate of the modelling errors and, for all the cases, only the upper bound of the modelling error could be estimated. For a few cases, also the sign of the modelling error could be determined.

**Table 3:** Comparison error, validation uncertainty and the upper bounds of the modelling errors in percentage of CFD data.

$V$ (m/s)	$E$	$U_{val}$	$ \delta_{model}  \leq$	$E$	$U_{val}$	$ \delta_{model}  \leq$	$E$	$U_{val}$	$ \delta_{model}  \leq$
			Mud_10			Mud_17			Mud_23
0.27	10.1	6.3	16.4 (+)	9.8	6.4	16.2 (+)	8.7	7.7	16.4 (+)
0.52	5.4	6.0	11.3	4.7	6.6	11.3	3.4	7.1	10.4
0.77	0.1	6.7	6.7	0.6	5.9	5.9	-1.0	6.1	7.2
1.02	-5.5	6.4	12.0	-7.7	6.9	14.6 (-)	-5.5	6.3	11.7

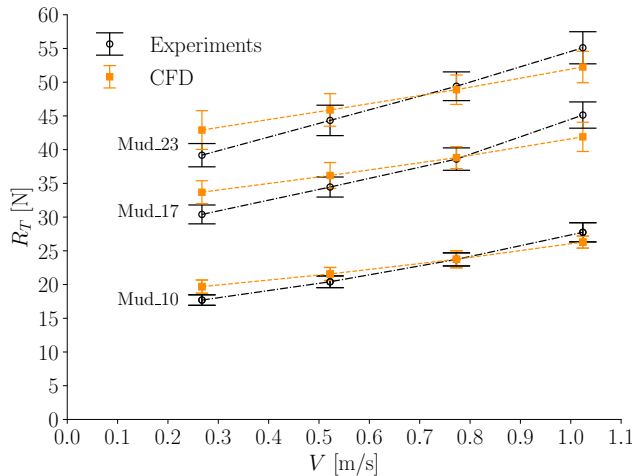


**Fig. 5:** Total resistance of the plate moving through mud against the inflow velocity (or towing speed).

about 7% of the CFD data. If more information about the modelling error is required, the uncertainty (especially the experimental) needs to be reduced.

Further preliminary calculations (not reported here) were carried out with the aim to reduce the comparison error and better capture the trend of the experimental data. Better agreement with experimental data was achieved when calculations were performed with (i) a small rotation (about  $1.5^\circ$ ) of the plate around the vertical axis; (ii) the effect of the free surface; (iii) lower regularisation parameters that were determined directly from the mud flow curves to better capture the behaviour at low shear rates. This suggests that the experiments, especially at the high speed, could have been contaminated by small rota-

The larger comparison errors are found at  $V = 0.27 \text{ m s}^{-1}$ , and the upper bound of the modelling errors is about 16%. The lowest upper bound of the modelling errors is found for  $V = 0.77 \text{ m s}^{-1}$  because of the very small comparison error for all the three mud concentrations. At this speed, there seems to be an intersection of the numerical and experimental data (see also Fig. 5). In fact, numerical data tends to overpredict the resistance at low speed and to underpredict at high speed. Figure 5 suggests that  $E$  will increase in magnitude for increasing speed, meaning that the trend in the experiments is not correctly captured by CFD. In any case, validation is achieved for nearly all the cases (i.e. for the cases where experimental and CFD uncertainties overlap) at the level of

tions of the plate, and that rheology of mud is better captured by the regularised Bingham model rather than the ideal Bingham.

## 8 Conclusions

The purpose of this study was to assess the performance of the Bingham model for numerical predictions of flow of mud over a plate. This was done by comparing numerical predictions with the measured resistance of a plate moving through the mud collected from the seabed in the port of Rotterdam.

Comparison with numerical data showed a fairly good agreement, with maximum discrepancies of about 10%. Since the validation uncertainty is around 6-7%, only the lower and upper bounds of the modelling errors could be estimated. The maximum upper bounds of the modelling errors are about 16% and they are found at the lowest speed considered in this study. In particular, CFD seems to overpredict the resistance at low speed, whereas underprediction is observed at high speed. However, preliminary calculations revealed that experimental data may have been contaminated by small rotations of the plate, which enhanced the free surface deformation, especially at the highest speed. These preliminary calculations also showed that the Bingham model appears to overpredict the experimental data, whereas using lower regularisation parameters might significantly improve the prediction at all speeds. In any case, results showed that, in spite of the discrepancies between experiments and CFD, the changes in the forces due to variation of the mud properties is consistent with the experiments.

In conclusion, a first step has been made to establish that the regularised Bingham model may be a good compromise between accuracy and simplicity for predicting the forces due to the laminar flow of mud over slender bodies. Future work is needed to investigate whether these conclusions are valid also for applications concerning the navigation of ships in presence of muddy seabeds, which involve turbulent flows of a water-mud system over more complex geometries.

## Acknowledgement

This work is supported by the Dutch Research Council (NWO), Port of Rotterdam (PoR) and MARIN. Calculations were performed on the Marclus4 cluster (MARIN). The experimental work was carried out within the Prisma project and is funded by PoR, TU Delft, Port of Hamburg and Topconsortium voor Kennis en Innovatie (TKI) Deltatechnologie subsidy. Special thanks to Pavan Goda, Marcel Busink and Lynyrd de Wit for their contribution to the experimental part. This study was carried out within the framework of the MUDNET academic network: <https://www.tudelft.nl/mudnet/>.

## References

- ASME PTC Committee (2009). Standard for Verification and Validation in Computational Fluid Dynamics and Heat Transfer: ASME V&V 20. The American Society of Mechanical Engineers (ASME).
- Barth, R., Van der Made, C.J.A.W., Bourgonjen, L., Van Dijken, J., Vantorre, M. and Verwilligen, J. (2016). Manoeuvring with negative underkeel clearance: 2nd full scale field test in the port of Delfzijl. 4th MASHCON-International Conference (pp. 262-271).
- Delefortrie, G., Vantorre, M. and Eloot, K. (2005). Modelling navigation in muddy areas through captive model tests. *Journal of marine science and technology*, 10(4), pp.188-202. doi:[10.1007/s00773-005-0210-5](https://doi.org/10.1007/s00773-005-0210-5)
- Eça, L. and Hoekstra, M. (2009). Evaluation of numerical error estimation based on grid refinement studies with the method of the manufactured solutions. *Computers and Fluids*, 38(8), 1580–1591. doi:[10.1016/j.compfluid.2009.01.003](https://doi.org/10.1016/j.compfluid.2009.01.003)
- Eça, L. and Hoekstra, M. (2014). A procedure for the estimation of the numerical uncertainty of CFD calculations based on grid refinement studies. *Journal of Computational Physics*, 262, 104–130. doi:[10.1016/j.jcp.2014.01.006](https://doi.org/10.1016/j.jcp.2014.01.006)
- Harbour approach channels design guidelines (2014), PIANC Report No. 121. PIANC.
- van Leer, B. (1979). Towards the ultimate conservative difference scheme. V. A second-order sequel to Godunov's method. *Journal of Computational Physics*, 32(1), 101–136. doi:[10.1016/0021-9991\(79\)90145-1](https://doi.org/10.1016/0021-9991(79)90145-1)
- Lovato, S., Toxopeus, S. L., Settels, J. W., Keetels, G. H., and Vaz, G. (2021). Code Verification of Non-Newtonian Fluid Solvers for Single- and Two-Phase Laminar Flows. *Journal of Verification, Validation and Uncertainty Quantification*. 6(2), 021002. doi:[10.1115/1.4050131](https://doi.org/10.1115/1.4050131).
- Papanastasiou, T.C. (1987). Flows of materials with yield. *Journal of Rheology*, 31(5), pp.385-404. doi:[10.1122/1.549926](https://doi.org/10.1122/1.549926)
- Shakeel, A., Kirichek, A., Talmon, A. and Chassagne, C. (2021). Rheological analysis and rheological modelling of mud sediments: What is the best protocol for maintenance of ports and waterways? *Estuarine, Coastal and Shelf Science*, 257, 107407. doi:[10.1016/j.ecss.2021.107407](https://doi.org/10.1016/j.ecss.2021.107407)
- Vaz, G., Jaouen, F. and Hoekstra, M. (2009). Free-Surface Viscous Flow Computations: Validation of URANS Code FRESKO. *Proceedings of OMAE2009, Honolulu, Hawaii, USA*, 425–437. doi:[10.1115/OMAE2009-79398](https://doi.org/10.1115/OMAE2009-79398)

# Some aspects of the local hydro-structure interactions during hydrodynamic impacts

Malenica S.<sup>(1)</sup>, Gatin I.<sup>(2)</sup>, Seng S.<sup>(1)</sup>, Jagite G.<sup>(1)</sup>, Diebold L.<sup>(1)</sup>,  
Khabakhpasheva T.<sup>(3)</sup> & Korobkin A.A.<sup>(3)</sup>

<sup>(1)</sup> Bureau Veritas, Paris, France

<sup>(2)</sup> Faculty of Mechanical Engineering and Naval Architecture, University of Zagreb, Croatia

<sup>(3)</sup> University of East Anglia, Norwich, UK

## 1. Introduction

There exist many practical situations in offshore and marine operations where the hydrodynamic impacts occur (Figure 1): slamming, sloshing, green water, wave impact, free-fall, underdeck impact ...



Figure 1: Practical hydrodynamic impact situations.

Both the experimental measurements and the numerical simulations show that extremely large local pressures might occur during the impacts. Due to the extreme sensibility of the maximum impact pressures to the local details of the impact, the physical experiments show large variability and at the same time the numerical tools cannot properly reach the convergence in terms of pressure. However the difficulties in evaluating the maximum impact pressures do not necessarily represent an important practical problem when it comes to the evaluation of the structural response. Indeed, the localized extreme pressures are usually of extremely short durations and their spatial extents are also very small, so that the extreme pressure peaks are naturally filtered by the structural dynamics.

The well-known dependency of the structural response on the ratio between the excitation time and the first structural natural period (Dynamic Amplification Factor – DAF) is shown in Figure 2 where the three different interaction regimes are identified: impulsive, dynamic and quasi-static ones. Quasi-static response means the static structural response under hydrodynamic pressure loading obtained for rigid structure. It can be seen that in the case of an impulsive regime the structural response can be easily overestimated by several hundred percent if the quasi-static approach is used.

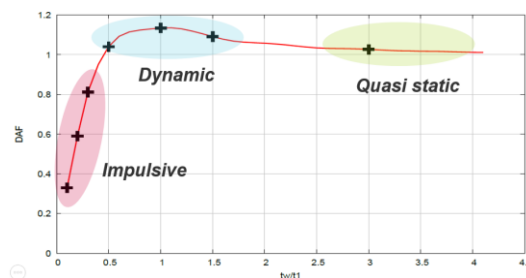


Figure 2: Dynamic amplification factor and 7 impact conditions considered in the present work.

In order to properly model the hydro-structure interactions in impulsive and dynamic regimes, full hydroelastic coupling is necessary. The main purpose of the present work is to investigate if the CFD on the hydrodynamic side and the FEM on the structural side can be coupled and used to efficiently simulate the hydro-structure interactions for all three interaction regimes. For simplicity, the 2D impact conditions are considered only.

## 2. Numerical modelling

### 2.1 Hydrodynamic modelling

From numerical modelling point of view, the body impacting the water or water hitting the body are fully equivalent and only the relative geometry and the relative velocities matter. This means that the same

numerical models are applicable to different types of impact provided that the relative geometry of the impact is properly interpreted. During the impact it is reasonable to assume potential flow and neglect the viscosity. However, even within the potential flow assumptions, due to the violent deformations of the free surface and the presence of the jets, the modelling of the hydrodynamic impact remains very complex especially in 3D. Two types of hydrodynamic models are employed in the present work: the potential flow-based Wagner model and a CFD model within the OpenFoam framework.

### 2.1.1 Potential flow modelling and Wagner approach

The potential flow assumptions allow for robust and accurate numerical modelling which usually relies on Boundary Integral Equation Method (BIEM). In addition, for some simple geometries and, under some additional hypotheses, analytical solutions can be obtained. The most popular analytical model is known as Wagner model. The basic assumption of the Wagner model is that the penetration depth (i.e. the distance between the impacting body surface and the water surface) is much smaller than the dimension of the wetted part of the body surface. Then the Boundary Value Problem (BVP) can be linearized at each time instant. The detailed theoretical description of the Wagner model can be found in [7]. Here we recall some basic features of this model for a 2D symmetric elastic wedge with deadrise angle  $\gamma$  entering water with constant velocity  $V$ .

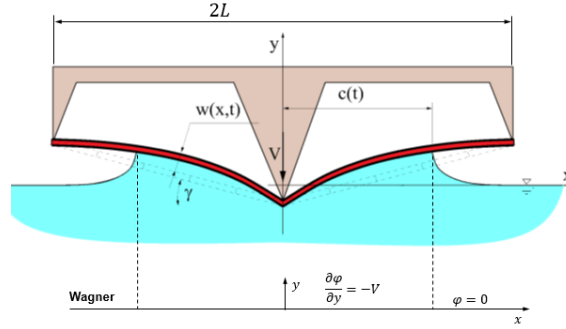


Figure 3: Wagner impact model.

A sketch of the problem is shown in Figure 3. The critical physical quantity is the half-length of the wetted part of the body surface  $c(t)$  which is found from the Wagner's condition:

$$c(t) = \frac{\pi}{2}t - \int_0^{\pi/2} w[c(t) \sin \theta, t] d\theta \quad (1)$$

The case of rigid body is particularly interesting since it gives the basic characteristics of the pressure distribution which is described by [7]:

$$p = \rho V \frac{c\dot{c}}{\sqrt{c^2 - x^2}} - \rho V \frac{c\dot{c}}{\sqrt{2c(c-x)}} + 2\rho\dot{c}^2 \frac{\sqrt{\tau}}{(1+\sqrt{\tau})^2} \quad 1 \leq \tau \leq \infty \quad (2)$$

$$p = 2\rho\dot{c}^2 \frac{\sqrt{\tau}}{(1+\sqrt{\tau})^2} \quad 0 \leq \tau \leq 1 \quad (3)$$

where the variable  $\tau$  and the coordinate  $x$  are related by the following expression:

$$x = c + \frac{\delta}{\pi} (-\ln \tau - 4\sqrt{\tau} - \tau + 5) \quad , \quad \delta = \frac{\pi}{8} \frac{c}{\dot{c}^2} V^2 \quad (4)$$

The maximum pressure is given by  $p_{max} = 0.5\rho\dot{c}^2$ .

For symmetric impact of a rigid wedge with deadrise angle  $\gamma$  with constant impact velocity  $V$ , the velocity of expansion of the contact point is given by  $\dot{c}(t) = 0.5\pi V / \tan \gamma$  which leads to the maximum pressure of  $p_{max} = 0.125\rho\pi^2 V^2 / \tan^2 \gamma$ . This implies very large velocities of expansion of the contact point and extremely large maximum pressures when the deadrise angle approach zero (flat impact). These physical features of the impact problem, together with very sharp deformations of the free surface close to the contact points, represent the major difficulties for the numerical modelling.

The expressions (2) and (3) can be used to produce the pressure distribution at each time instant during impact. In Figure 4 the pressure distributions for different impact conditions are presented. In the left part of the figure the maximum pressure is kept constant and 3 different deadrise angles are considered:

$\gamma = 5, 10$  and  $15$  degrees, while in the right part of the figure, impact velocity is kept constant for the same 3 deadrise angles. It is interesting to observe that, even if the maximum impact pressure is the same, the pressure distributions are significantly different. At the same time, very small changes of the deadrise angle leads to very different maximum pressures and the corresponding pressure distributions. This feature of the hydrodynamic impact should always be kept in mind when calculating the structural response [1]. Also, when interpreting the experimental results, we should not make conclusions based on the maximum pressures only, because the same maximum pressure can occur for very different impact conditions!

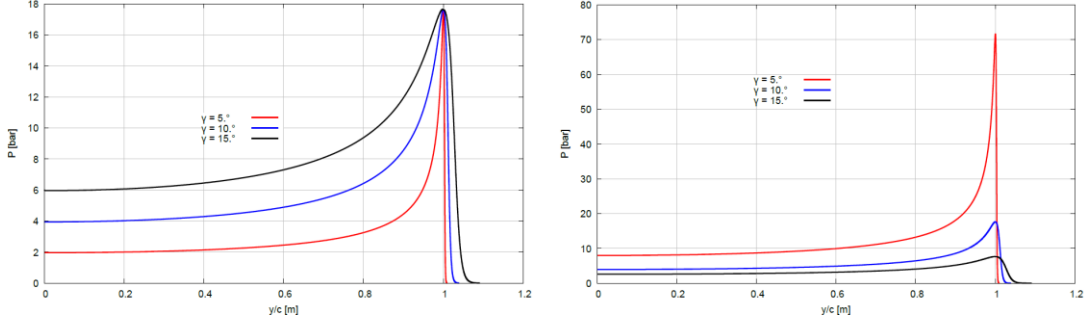


**Figure 4:** Impact pressure for wedge impact and for different combinations of impact velocities and deadrise angles. Left – maximum pressure is kept constant, Right – impact velocity is kept constant.

### 2.1.2 CFD hydrodynamic model within OpenFoam framework

The OpenFoam based numerical CFD models of water impact do not make any particular additional assumptions compared to the classical modelling of the fluid flow in the presence of the free surface. However, the convergence issues and the mesh requirements become much more critical now due to the large velocity of expansion of the wetted surface  $\dot{c}(t)$  and the local sharp free-surface deformation close to the contact points. In the present work two different approaches for surface capturing were employed. The first one is the classical Volume of Fluid (VOF) method while the second one is the so called Ghost Fluid Method (GFM). More details about the two methods can be found in [5],[6]. Both compressible and incompressible flow solvers were employed [2].

## 2.2 Structural modelling and coupling

There exist two main approaches to hydroelastic modelling: the direct approach and the modal approach. Within the direct approach the coupling is performed at the level of finite element and the informations (deformations for CFD and the forces for FEM) are exchanged locally. The advantage of the direct approach is that it allows for considering both the linear and the nonlinear type of the structural response, however the drawback is that the FE structural problem need to be solved at each time step which leads to large increase in CPU time. In case of the linear structural response a more efficient modal approach can be used. Within this approach the coupling is performed at the level of structural natural modes which are pre-calculated prior to the simulations. The advantages of the modal approach are the reduction of the CPU time and better stability, however only the linear structural problems can be considered in an easy way. The modal approach is usually preferred for linear problems which are most often encountered in practice. However, the nonlinear structural analysis can be required for the situations where the plastic deformations can occur or where the structural behavior is nonlinear by nature such as the cargo containment system of LNG tanks. For those cases only the direct approach is applicable.

### 2.2.1 Modal approach

Within the modal approach, the beam deflection is represented as a sum of the modal contributions:

$$w(x, t) = \sum_{n=1}^{\infty} a_n(t) \psi_n(x) \quad (5)$$

where  $a_n(t)$  are the time dependent modal amplitudes and  $\psi_n(x)$  are the space dependent mode shapes. The mode shapes can be chosen in many different ways and most often the dry natural modes are used. The dry natural modes depend on the type of beam model which is adopted and on the boundary conditions. In the present case the Euler Bernoulli model of simply supported beam is used:

$$\alpha \frac{\partial^2 w}{\partial t^2} + \beta \frac{\partial^4 w}{\partial x^4} = p(x, t) \quad , \quad 0 < x < L \quad , \quad t > 0 \quad (6)$$

where  $w(x,t)$  is the beam normal deflection,  $\alpha$  and  $\beta$  are the mass and the stiffness coefficients respectively. The initial conditions are  $w = \partial w / \partial t = 0$  at  $t = 0$  for  $0 < x < L$  and the boundary conditions at beam ends for simply supported beam are  $w = \partial^2 w / \partial x^2 = 0$  for  $t \geq 0$  and  $x = -L, 0, L$ . The coupling procedure consist in projecting the hydrodynamic pressure on the mode shapes and in integrating it over the wetted part of the body i.e. from  $-c(t)$  to  $c(t)$ . The equilibrium between the loading and the structural response, at each time step, is ensured through the enforcement of the body boundary condition at the wetted surface. This boundary condition requires that the normal velocity of the fluid and the velocity of the beam are equal to each other. The fact that the wetted body domain changes in time introduces non trivial convergence issues which should be properly handled. When using the analytical Wagner hydrodynamic model, it is possible to produce highly accurate and robust solution, as described in [3]. The use of the Wagner model allows for clear separation of the hydrodynamic loading into the time dependent added mass and the pure excitation parts, so that the dynamic beam equation (6) can be easily integrated in time together with the hydrodynamic part of the problem. However, when using the CFD for solving the hydrodynamic problem, it is not possible to explicitly identify the added-mass part of the load and an iteration procedure is required in order to satisfy the body boundary condition at each time step.

## 2.2.2 Direct FE approach and coupling

In the case of the direct FE approach, the structural deformation is represented with the help of local shape functions (usually polynomials) which are associated with the nodal degrees of freedom (deflection and slope) using the well-established FE procedure [4]. From the coupling point of view the basic principles remain the same as in the modal approach, except that the degrees of freedom changes: amplitudes of the natural modes in modal approach become nodal deflections and slopes in the direct FE approach. This implies different numerical issues when projecting and integrating the pressure over the wetted part of the body. When using the modal approach the pressure can be taken directly from the CFD solution and integrated over the mode shape while in the case of the direct FE approach the pressure needs first to be interpolated onto the Gauss points of each finite element. In addition, special care has to be taken when integrating the pressure over the partially wetted finite elements because of the large peak values close to contact point  $c(t)$ . From theoretical point of view the modal and the direct approaches are fully equivalent for the linear structural model.

## 3. Results and discussions

### 3.1 Test cases

One of the main goals of the present work was to check the efficiency of the CFD – FEM coupling for different hydro-structure interaction regimes: impulsive, dynamic and quasi-static. For that purpose, 7 ratios of the excitation time and the first wet structural natural period were chosen (see Figure 2). The beam characteristics were fixed to match the typical plating of the bow part of the Ultra Large Container Ship (ULCS) which gave the values presented in Table 1 – left. The range of the impact velocities was fixed between 0 and 25m/s and the range of the deadrise angles between 0 and 25 degrees. The excitation time was defined as the time when the whole beam becomes wet under rigid body assumptions, and the period of the 1<sup>st</sup> wet natural mode is defined with the added mass associated with the fully wetted beam conditions [3]. In total 21 test cases were selected for comparisons, see Table 1 – right. The blue cells indicate the cases for which more detailed results are presented here.

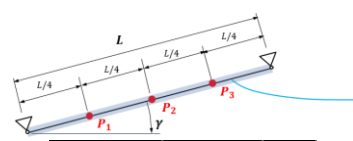


Plate characteristics	
Length (L)	0.8 m
Thickness (t)	0.02 m
Young module	2.10E+11 Pa
Density	7850 kg/m <sup>3</sup>

V Impact		Gamma [deg]				
		5.0	10.0	15.0	20.0	25.0
tw/t1	0.1	16.328				
	0.2	8.164	16.454			
	0.3	5.443	10.970	16.670		
	0.5	3.266	6.582	10.002	13.586	17.406
	1.0		3.291	5.001	6.793	8.703
	1.5		2.194	3.334	4.529	5.802
	3.0				2.264	2.901

**Table 1 :** Left – beam characteristics, Right – test cases. Impact velocities for different deadrise angles and different interaction regimes are defined by the ratio  $t_w/t_1$ , see also Figure 2.

### 3.2 Numerical setup

The finite element based numerical tool Dyana2 [4], was used for beam modelling. It was shown that 7 structural natural modes are enough to represent the structural response correctly within the Wagner model for all interaction regimes. The numerical FE model Dyana2 showed that 20 finite elements are sufficient to calculate the lowest 7 natural modes with an error of less than 1%. Finally the comparisons

of the numerical and the analytical results for the quasi-static response showed that 3 Gauss points per finite element are enough to correctly evaluate the structural response.

On the hydrodynamic side, in total 5 different meshes were used to check the convergence of the CFD results. The refinement was mainly controlled by the number of cells over the length of the wedge which was chosen to be 64, 89, 133, 200 and 300. This means that in all cases the CFD mesh is finer than the structural mesh which was fixed to 20 finite elements. The extent of the CFD model was about 25 wedge lengths in the horizontal and the vertical directions. Convergence tests showed that the convergence was reasonably achieved with the mesh of 133 cells per beam length. As expected, the worst convergence was observed for the impulsive impact conditions.

### 3.3 Representative results

Large amount of results was produced during this investigation program. Only some representative results are presented here. When mentioning different interaction regimes defined by the ratios  $t_w/t_1$ , the test cases marked by blue color in Table 1 are concerned. In Figure 5 the comparisons of the time history of the pressure at 3 points along the beam (see Table 1 – left) are presented. The analytical results (marked by A) are presented both for the rigid (QS) and flexible (HE) beam while the numerical results are presented for the flexible beam only. The analytical values of the pressure are cut at their maximum theoretical values for rigid beam case i.e.  $p_{max} = 0.125\rho\pi^2V^2/\tan^2\gamma$ . Significant differences can be observed between the numerical (N) and the analytical results, in particular when the pressure peaks are concerned. The impulsive case ( $t_w/t_1 = 0.1$ ) is particularly interesting since it gives the maximum pressure value close to 450 bars analytically and 230 bars numerically! If applied in a quasi-static way these pressure would obviously lead to severe local beam failure. In reality the structural dynamics will naturally “filter” these localized pressure peaks, which can be correctly modelled numerically using the fully coupled hydroelastic models only.

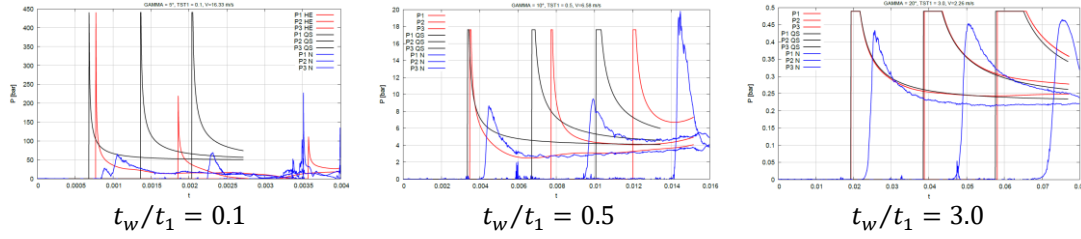


Figure 5: Time history of the pressure at 3 representative points for different impact conditions.

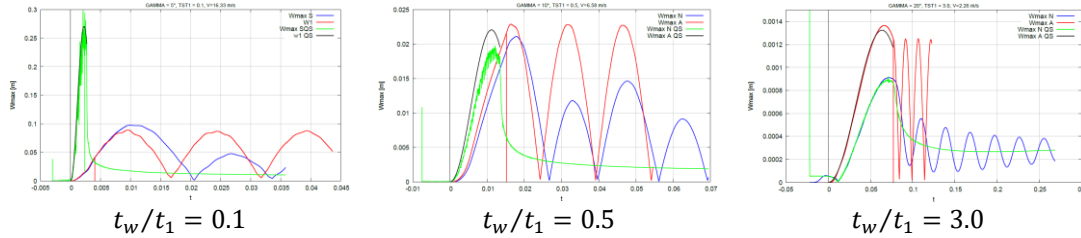


Figure 6: Time history of the maximum deflection of the beam for 3 different regimes.

In Figure 6 the typical results for the maximum deflection are shown for the same impact conditions. Numerical results show significant noise, especially in the impulsive case, which needs to be filtered. Fair agreement can be observed between the numerical and the analytical results. As expected, the difference between the hydroelastic and the quasi-static results is large in the impulsive case.

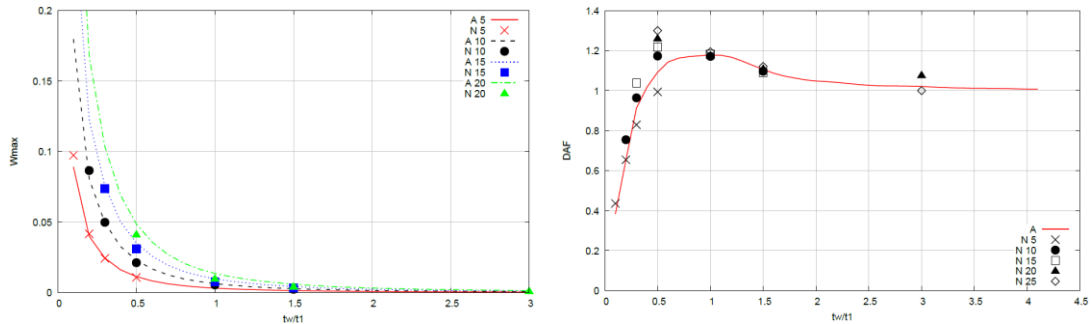


Figure 7: Comparison of numerical (N) and analytical (A) results for maximum deflection (left) and the corresponding DAF (right) for different test cases from Table 1.



The results for the absolute maximum deflection for all 21 test cases are summarized in Figure 7 both in terms of the maximum deflection (left) and in terms of the DAF (right). The differences between the analytical and the numerical results can be attributed both to the validity of the Wagner approach as well as to inaccuracies of the numerical modelling. For the cases of 5 and 10 degrees the Wagner model is known to be an accurate approximation and these test cases are probably the most representative ones. It can be seen that, in spite of the numerous numerical difficulties especially for impulsive interaction regime, the agreement between the numerical and the analytical results is fairly good both in terms of the maximum deflection as well as in terms of the DAF.

## 4. Conclusions

From the results obtained within the present investigations, the following main conclusions can be drawn:

- The numerical model based on CFD – FEM coupling is able to simulate hydroelastic interactions, which occur during hydrodynamic impacts, with acceptable accuracy and for all hydro-structure interaction regimes.
- The coupling procedures based on modal and direct approaches give close results. The modal approach shows better convergence properties. The direct approach can be safely extended to model the nonlinear response of the structure.
- The CFD methods based on either GFM or VOF free surface capturing methods, show some small differences between them but both agree well with the analytical results. GFM method appears to be more unstable in the present cases.
- All numerical models converge properly in terms of the structural response even though the pressure distribution can be very different. This is particularly true for impulsive regime. This means that the pressure, especially the maximum pressure, should not be used as a single parameter for indicating the severity of the impact in terms of the structural response!
- Compressibility does not play an important role for the cases considered here.
- The effects of gravity can be safely neglected for the cases considered here. For milder impacts (larger deadrise angles and lower impact velocities) the effects of gravity might become important.
- The CFD – FEM coupling procedure which was demonstrated using the in-house numerical code Dyana2 can be easily extended for coupling with more general FE codes (ABAQUS, NASTRAN ...)
- Compared to the quasi static hydro-structure interaction simulations, which are based on the pre-calculated hydrodynamic loading for the rigid structure, the CPU time required for fully coupled hydroelastic simulations increases from 3 to 4 times.

Among other issues, the future work should consist of:

- Comparisons/validations with experimental results
- Investigation of 3D effects
- Investigation of the effects of compressibility when larger amount of air is entrapped
- Coupling of CFD with the general FEM codes (ABAQUS, NASTRAN ...)
- Practical applications (slamming, sloshing, green water ...)

## 5. References

- [1] Faltinsen O.M., 2000. “*Hydroelastic slamming.*” J Mar Sci Technol Vol. 5, pp. 49–65
- [2] Gatin I., 2018. : “*Multiscale nonlinear and viscous numerical modelling of wave impact loads*”, PhD thesis, Faculty of Mechanical Engineering and Naval Architecture, University of Zagreb.
- [3] Khabakhpasheva T. & Korobkin A.A., 2013. : “*Elastic wedge impact onto a liquid surface: Wagner’s solution and approximate models.*”, J. of Fluids and Structures, Vol. 36 pp. 32–49
- [4] Jagite G., 2020. : “*Analysis of slamming induced whipping effects over the ultimate strength of ships*”, PhD thesis, Ecole Centrale de Nantes.
- [5] Seng S., 2013. : “*Slamming and whipping analysis of ships*”, PhD thesis, Technical University of Denmark.
- [6] Vukcevic V., Jasak H. & Malenica S., 2016.: “*Decomposition model for naval hydrodynamic applications, Part I: Computational method*”, Ocean Engineering, Vol. 121, pp. 37-46
- [7] Zhao R. & Faltinsen O.M. 1993 “*Water entry of two-dimensional bodies*”, J. Fluid Mechanics, Vol. 246, 593-612.

# Application of Hybrid-Temporal LES to Airwake Analyses of the ONR Tumblehome Surface Combatant

**Philipp Mucha**

Siemens Digital Industries Software - Waltham, MA  
philipp.mucha@siemens.com

A Computational Fluid Dynamics (CFD) analysis is presented of the airwake of the ONR Tumblehome (ONRT) surface combatant using a novel turbulence model from the class of hybrid Reynolds-averaged Navier-Stokes (RANS) - Large Eddy Simulations (LES) called Hybrid-Temporal LES (HTLES). Airwake analyses are critical to the design of surface combatants for the efficient and safe operation of aircraft during landing and departure. CFD predictions of meaningful flow statistics within the wake of the deckhouse over the hangar and flight decks were compared to experiments. In HTLES the delineation between RANS and LES is not based on near-wall versus freestream regions, but rather, the largest structures in the freestream are resolved with LES whilst smaller structures are modeled with RANS, and thereby allowing for coarser grid resolution in freestream regions and a continuous transition between RANS and LES.

The advance of knowledge about turbulent flow simulations for ships and offshore structures resulting from numerous verification and validation exercises within the community in conjunction with the increase in computational resources have shifted the focus to Scale-resolving Simulations (SRS) to better capture secondary flow effects attributable to turbulent flow, commonly encountered in lifting flow conditions for ships with bilge keels, sonar domes, or with submarines and superstructures of ships. High-fidelity CFD-based aero- and hydro-acoustic analyses also require flow resolution to scale. Among SRS Direct Numerical Simulation (DNS) is cost-prohibitive for industrial applications. Large Eddy Simulation (LES) is widely used in academia, but due to discretization requirements still too expensive for industrial settings, Liefendahl et al. (2020). Methods based on the solution of the unsteady RANS equations are not designed to provide statistical information. Therefore, the emergence of hybrid RANS-LES has created anticipation to benefit from the best of both methods to enable SRS in industrial context. Detached Eddy Simulation (DES) represents a popular hybrid method. Grey-area mitigation, incapability to handle larger time steps, and challenges associated with discretization sensitivity are impairing reliable application of DES at scale, as required for design

exploration and optimization exercises called for by the industry. Recently, alternative hybrid methods such as Scale-adaptive Simulation (SAS) and Stress-blended Eddy Simulation (SBES) have been introduced to the field claiming to be competitive on grids designed for unsteady RANS simulations, making them comparatively cheaper than DES, for which discretization requirements are stricter, Menter (2018), Menter and Egorov (2010). The concept of HTLES ties into above motivation by establishing a continuous connection between RANS and LES models by controlling the energy partition between resolved and modeled scales through temporal filtering. HTLES assumes an analogy between statistical averaging and low-pass filtering. Following this notion, the stress tensor would be modeled such that it resorts to the Reynolds stresses in regions where RANS modeling suffices, and subgrid-scale LES modeling is in place only in regions where scale-resolution is enabled through finer grids. Thus, for sufficiently fine grids and time steps, a continuous switch from RANS to LES mode is enabled based on the filter time-width. Between these time scales, the time step and the mesh size determine the resolution of the turbulent structures. Such simultaneous filtering was suggested by Duffal et al. (2021). Duffal et al. (2021) provide a rigorous derivation of the novel HTLES approach associated with eddy-viscosity closures. The approach enjoys a strong theoretical foundation with empiricism employed only in the shielding functions used in near-wall regions.

Airwake analyses of naval ships have aroused interest to inform the design process in the context of the interaction between ships with vertical and short take-off and landing (V/STOL) aircraft for an array of combat, rescue and expeditionary operations in adverse conditions. For conventional superstructures the hangar and flight decks are located aft of the deckhouse. From the standpoint of fluid dynamics tumblehome bodies with multiple backward-facing steps behind the deckhouse already suggest complex wake characteristics for uniform flow conditions, but they are further complicated by atmospheric boundary layer turbulence, ship responses to waves and dynamic interaction with the aircraft

encountered in real-world scenarios. Such flow problems stand out as suitable candidates for SRS validation exercises because the mean flow characteristics are driven by large-scale time-dependent features including a recirculation zone arising from the detached shear layer for which RANS models fail to produce statistical information. Gnanamanickam et al. (2020) presented an experimental analysis of the airwake over the Simplified Frigate Shape 2 (SFS2), confirming a pronounced recirculation zone over the flight deck and the hypothesis of the large-scale nature of energetic flow structures. The study of Shukla et al. (2019) is an example of the application of SAS to the flow around SFS2. Thedin et al. (2020) is a comprehensive extension of airwake analyses of SFS2 based on SRS, including rigorous treatment of atmospheric boundary layers. Buchholz et al. (2016) present a study on the wake characteristics across the range of relevant Reynolds numbers and associated scaling problems. Dooley et al. (2019) discuss a detailed study on the effects of motions and atmospheric turbulence on the airwake of the ONR Tumblehome surface combatant. Delayed DES (DDES) was applied to derive statistics of the wake deficit and vertical velocity profiles downstream of the deckhouse in the hangar and flight deck regions. Favorable comparison was drawn to experimental measurements. Both the capabilities and high cost of SRS became evident, with most favorable results obtained using a 154M grid. Assessment of grid sensitivity of mean flow statistics used to inform important simulation parameters, e.g. the time required to attain a desired sample error bound, remains a challenge, especially considering aforementioned issues with DES. Linton and Thornber (2021) address numerical uncertainty quantification associated with finite sample errors encountered in SRS, as lack thereof impairs conclusive validation based on comparison to experiments. A comprehensive literature survey can be found in Dooley (2019) and Linton and Thornber (2021).

The goal of the present investigation was to assess the efficacy of HTLES by applying a new turbulence modelling method as implemented in Simcenter STAR-CCM+, called Scale-resolving Hybrid (SRH), to the airwake analysis of ONRT as presented by Dooley et al. (2019). In Simcenter STAR-CCM+, solution methods for variants of the Navier-Stokes equations are available. Their volume integral representation reads

$$\frac{\partial}{\partial t} \int_V \rho dV + \int_S \rho \mathbf{v} \cdot \mathbf{n} dS = 0 \quad (1)$$

$$\frac{\partial}{\partial t} \int_V \rho \mathbf{v} dV + \int_S \rho (\mathbf{v} \mathbf{v}) \cdot \mathbf{n} dS = \int_S \mathbf{T} \cdot \mathbf{n} dS + \int_V \rho \mathbf{b} dV \quad (2)$$

where  $\mathbf{v}$  denotes the fluid velocity vector,  $\mathbf{n}$  is the normal vector of  $S$ , which represents the area of the surface of control volume (CV)  $V$ ,  $\mathbf{T}$  denotes the stress tensor and  $\mathbf{b}$  a vector representing a force per unit mass. The fundamentals of FV-based methods are abundantly covered in Ferziger and Peric (2001). The computational mesh contained hexahedral CVs which were arranged in an unstructured way. Surface and volume integrals representing convective and diffusive fluxes were approximated using the mid-point rule. Values at cell faces were found from interpolation. In Simcenter STAR-CCM+, upwind-biased approximations of first and second order are available, based on variable values and their gradients at CV centers upstream of the cell faces. Bounded-central differencing (BCD) is available for LES. A hybrid BCD scheme is offered for hybrid RANS-LES methods. A Semi-Implicit Method for Pressure Linked Equations (SIMPLE) algorithm was used for the segregated solution of the velocity-pressure coupling problem. An implicit three-level time integration scheme of second order was applied. RANS modelling relied on the Realizable Two-Layer  $k\varepsilon$ -turbulence model as implemented in Simcenter STAR-CCM+. The generic SRH transport equations for the energy partition read

$$\frac{Dk_m}{Dt} = P_m - \epsilon_m + D_{k_m} \quad (3)$$

$$\frac{D\epsilon_m}{Dt} = C_{\epsilon_1} \frac{\epsilon_m}{k_m} P_m - [C_{\epsilon_1} + r(C_{\epsilon_2} - C_{\epsilon_1})] \frac{\epsilon_m^2}{k_m} + D_{\epsilon_m} \quad (4)$$

$P_m$  is the production of modeled energy  $k_m$ .  $D_{k_m}$  and  $D_{\epsilon_m}$  are the diffusion of modeled energy and modeled dissipation rate, respectively. The RANS-LES transition is based on the second term in Eq. (4), the so-called hybridization function with modeled-to-total energy ratio  $r = k_m/k$ . It serves as a measure of the energy partition between resolved and sub-filter scales. Along these lines,  $r = 1$  means operation in RANS mode. As  $r$  decreases, modeled energy and viscosity decrease, enabling a gradual transition to LES. Wall treatment followed a novel dual shielding function approach outlined in Duffal et al. (2021); see also and Simcenter STAR-CCM+ User Guide (2021).

ONRT model 5613 (Figure 1) is a representative design of a modern surface combatant and publicly available to the community, ONR (2021). No full-scale ship exists. The model features  $10^\circ$  tumblehome sides. Superstructures include the deck house, hangar, and flight decks. The detailed experimental setup and properties of the 1/77 scale model ( $L=2\text{m}$ ) used in the present investigation are described in Dooley (2019) and Dooley et al. (2019). The study of straight-ahead condition and uniform inflow, i.e. absent of atmospheric boundary layer (ABL) effects, was

addressed. Tests were conducted at Reynolds number  $Re=1 \cdot 10^6$ . Particle Image Velocimetry (PIV) and Laser-Doppler Anemometry (LDA) measurements were available for locations indicated by Figure 2, coinciding with the center plane ( $y=0$ ). Line probes and a point probe of mean and RMS of velocity in streamwise and vertical directions were available. Contour plots of the center plane were also available. The air flow around the superstructure of ONRT resembles in part the characteristics of the well-established backward-facing step and Ahmed body test cases, Driver (1985) and Ahmed (1984). Taking a viewpoint from the center of the deckhouse toward the stern there are three backward-facing steps; the first one off the deckhouse and the last one at the stern are slanted. The second step between the hangar and flight deck is located within the recirculation zone of the first step where potential reattachment is obstructed by the presence of this step. A further distinction to the canonical case lies in the fact that the superstructure is three-dimensional with additional slanted surfaces to the sides of the deckhouse and decks.

To assess the reliability of predictions through the SRH model simulations were performed using three grid refinement levels and three time steps. Simulations encompassed six flow-through periods over the 2m long

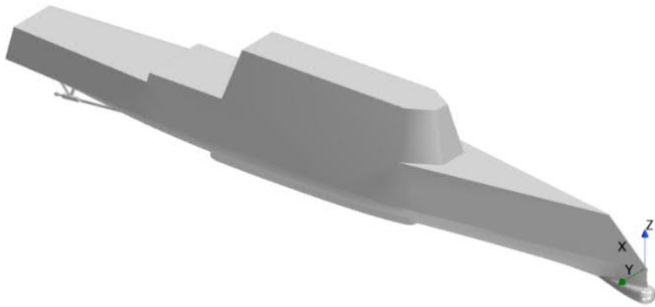


Figure 1 Perspective view of ONRT and coordinate system.

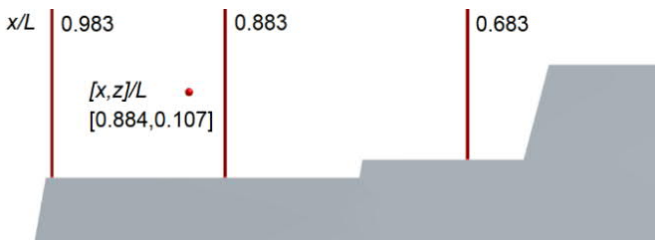


Figure 2 Point and line probe locations in the wake of ONRT.

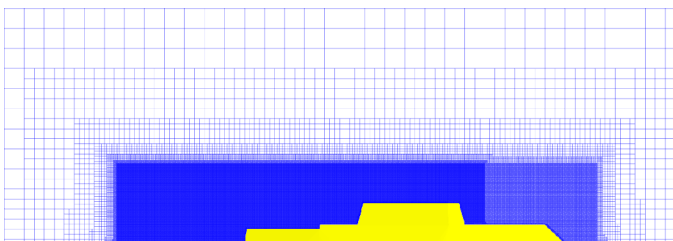


Figure 3 Grid in focus region and transition to far-field.

model at 0.5m/s, based on which mean and RMS of velocity were derived. Grids with 10M, 29M and 80M CVs were generated. Time steps were chosen to 1e-3s, 1e-4s and 5e-5s. The mesh was built with coarser discretization in the freestream region, where code operation in RANS mode was desirable, and finer grid spacing in the focus region (FR), based on established concepts for hybrid RANS-LES. They were less strict in Euler and departure regions (ER and DR), Spalart (2001), with faster growth to larger grid spacing than what is specified in Spalart (2001) for DES. Time step choice was based on a time scale proposed by Linton and Thornber (2021) taking into account both flow-through periods and closed-loop pilot response characteristics. Non-dimensional wall distance  $y^+$  was equal to or smaller than 1 on surfaces of the hangar and flight decks, using twelve prismatic layers on surfaces in FR, and six prismatic layers on remaining surfaces of the ship model across a height of  $z/L=0.005$ . These settings remained constant across all grids. A rectangular solution domain was built around the model of ONRT, with lower vertical boundary coinciding with the waterplane at the height of the draft. The domain extended 2.5 ship lengths upstream and six ship lengths downstream measured from the forward perpendicular. It extended one ship length vertically into the air phase and 1.5024m laterally, consistent with the width of the experimental wind tunnel. The upstream boundary of the domain served as an inlet, where velocity and turbulence boundary conditions were specified directly. Simulations were run in turbulence-free inflow conditions while honeycomb screens were used to condition the inflow in experiments with reported RMS values of approximately 3% and 2% for streamwise and vertical velocity, respectively. The downstream boundary served as an outlet, where pressure was specified directly, and velocities were found from interpolation of neighboring cells. Remaining boundaries were walls. Figure 6 shows streamwise and vertical profiles of mean velocity for the three levels of grid resolution and a given time step of 1e-4s. Overall, sensitivity to spatial discretization was weak for the streamwise velocity at sections  $x/L=0.883$  and  $x/L=0.983$ , and more pronounced at  $x/L=0.683$ . For the vertical velocity the middle section  $x/L=0.883$  exhibited largest variations based on discretization levels. A detailed plot across all grids and time steps is provided by Figure 5 for above sections where sensitivity to discretization was notable. Table 1 summarizes results of the discretization sensitivity study in terms of mean velocities at the point probe above the flight deck. While simulations across all grids and time steps showed little differences for mean velocity profiles and the point probe, Figures 5 and 6 and Table 1, field contour plots

revealed notable differences in terms of RMS values. Most favorable comparison was achieved on the finest grid, where grid spacing in FR was 3mm. It was 6mm and 12mm for the 29M and 10M grids, respectively. No notable difference was observed between different levels of temporal discretization for the coarser grids. Simulations using 10M cells showed characteristics of a statistically averaged flow field, indicating tendency to RANS modelling. This was reflected by the field contour plot of the energy partition, Figure 4. Here, a significant zone after separation remained in RANS mode ( $r=1$ ) with a downstream wake of low resolved energy. This zone was diminished as grid spacing decreased in this region. In general, the largest differences to experimental measurements were encountered at section  $x/L=0.883$  in the center of the flight deck. Comparison of simulation results to experiments was favorable for sections  $x/L=0.683$  and  $x/L=0.983$ . CFD results resembled the airwake behind the deckhouse phenomenologically correct. The transition from freestream to boundary layer in terms of mean streamwise velocity was captured well across all simulations. The pronounced recirculation zone over the hangar deck ( $x/L=0.683$ ) was accounted for across large parts of the boundary layer, with maximum percentage differences of -20% seen only in the magnitude of the highest recirculation velocity encountered in the immediate layers off the wall. The transition point of recirculation ( $u=0$ ) was predicted well with +5.6% difference at  $z/L=0.101$ . Profiles of mean velocity in the streamwise direction overall compared well with experiments above the flight deck, with largest comparison errors of -15% encountered in the immediate layers off the wall over a distance approximately equal to the height of the step from the hangar to flight deck at the middle section ( $x/L=0.883$ ). Capturing of the reattachment point is critical to an accurate prediction of velocity profiles in this location, and simulation predictions indicated that it occurred further downstream compared to the experiment. Toward the end of the deck at  $x/L=0.983$  the effect of the second step and associated recirculation was diminished, and results compared significantly better. Largest differences for the vertical velocity were encountered in the first section  $x/L=0.683$  behind the deckhouse in terms of the magnitudes of downward flow, while the s-like shape of the profile was resembled. Scrutiny of section  $x/L=0.883$  revealed a mismatch of predictions between simulations and experiment in a small region located at the height of the edge of the second step between the hangar and flight deck, where simulations overpredicted the downward flow. This occurrence tied into the assessment of the capturing of the reattachment zone. Contour plots generated with the

discretization level of 80M cells and time step of  $1e-4s$  were compared to experiments, Figures 7 and 8. The contour plots of mean streamwise velocity in the region of interest showed good qualitative agreement, with accordant recirculation zone predictions and close agreement for the transition to freestream behind the deckhouse. RMS values of streamwise velocities phenomenologically matched. However, fluctuations near the second step from the hangar to the flight deck were underpredicted by simulations, while the field over the flight deck was concordant with measurements. The characteristic distribution of the mean vertical velocity was well reflected by simulations. Recirculation manifested itself in a strong upward wash over the rear side of the deckhouse and two large zones of downward flow above the second step. Local underprediction of mean vertical velocity around  $z/L=0.12$  of the downward flow at  $x/L=0.683$  was evident. The upward wash of the rear side of the deckhouse was captured well in extension and magnitude. Experiments revealed large-scale fluctuations of vertical velocity in the zone above the second step, which did not occur to this extent in simulations. While fluctuations were predicted across similar zones and with similar distribution, magnitudes of RMS values were smaller in zones of maximum fluctuation.

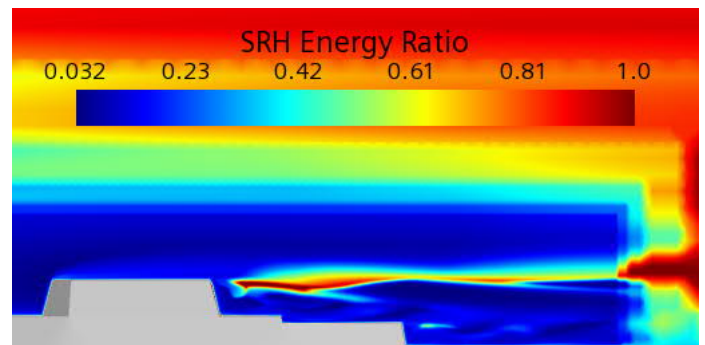


Figure 4 Energy ratio for coarsest spatial discretization level (10M,  $1e-04s$ ).

Table 1 Mean velocities at point probe for various discretization levels

$\Delta t$ [s]	1e-3	1e-4	5e-5
<b>10M CVs</b>			
$\bar{u}$ [m/s]	0.443	0.443	0.442
$\bar{w}$ [m/s]	0.0531	0.0531	0.0530
<b>29M CVs</b>			
$\bar{u}$ [m/s]	0.443	0.443	0.442
$\bar{w}$ [m/s]	0.0532	0.0531	0.0530
<b>80M CVs</b>			
$\bar{u}$ [m/s]	0.437	0.423	0.432
$\bar{w}$ [m/s]	0.0483	0.0453	0.0469
<b>EFD</b>			
	LDA	PIV	
$\bar{u}$ [m/s]	0.453	0.462	
$\bar{w}$ [m/s]	0.0456	0.0484	

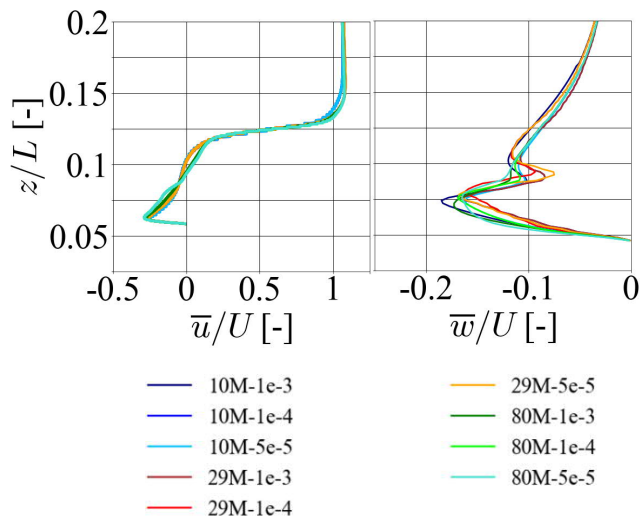


Figure 5 Sensitivity of mean velocity profiles to discretization,  $x/L=0.683$  (l.h.s.) and  $x/L=0.883$  (r.h.s.)

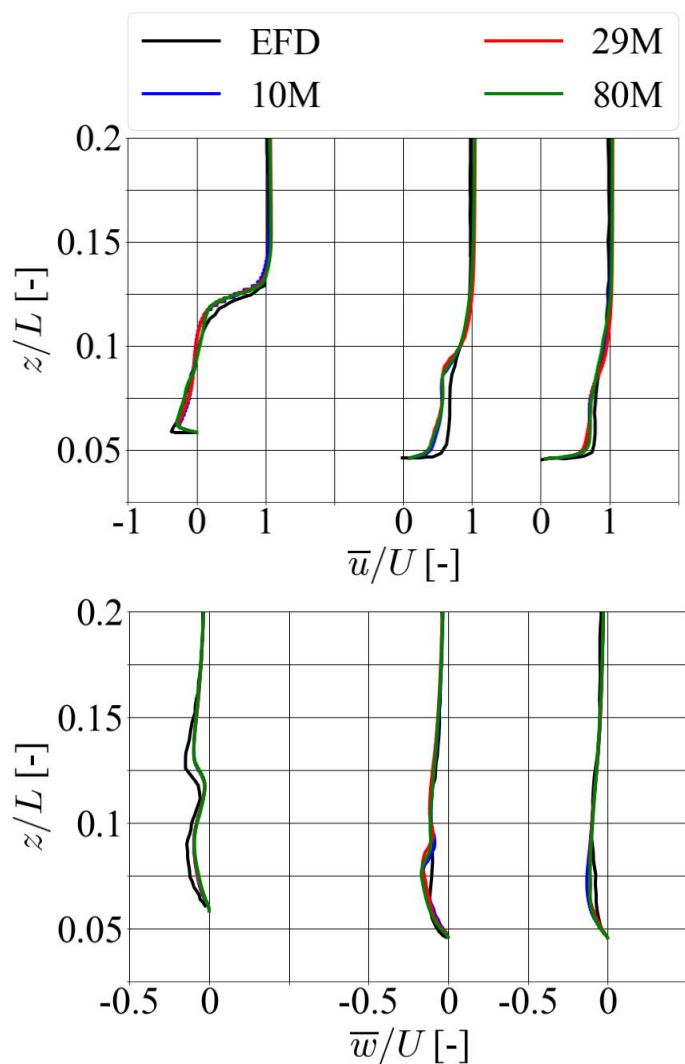


Figure 6 Mean streamwise (top) and vertical (bottom) velocity profiles at  $x/L=0.683$ ,  $x/L=0.883$ ,  $x/L=0.983$  (left to right). Time step  $1e-04s$ .

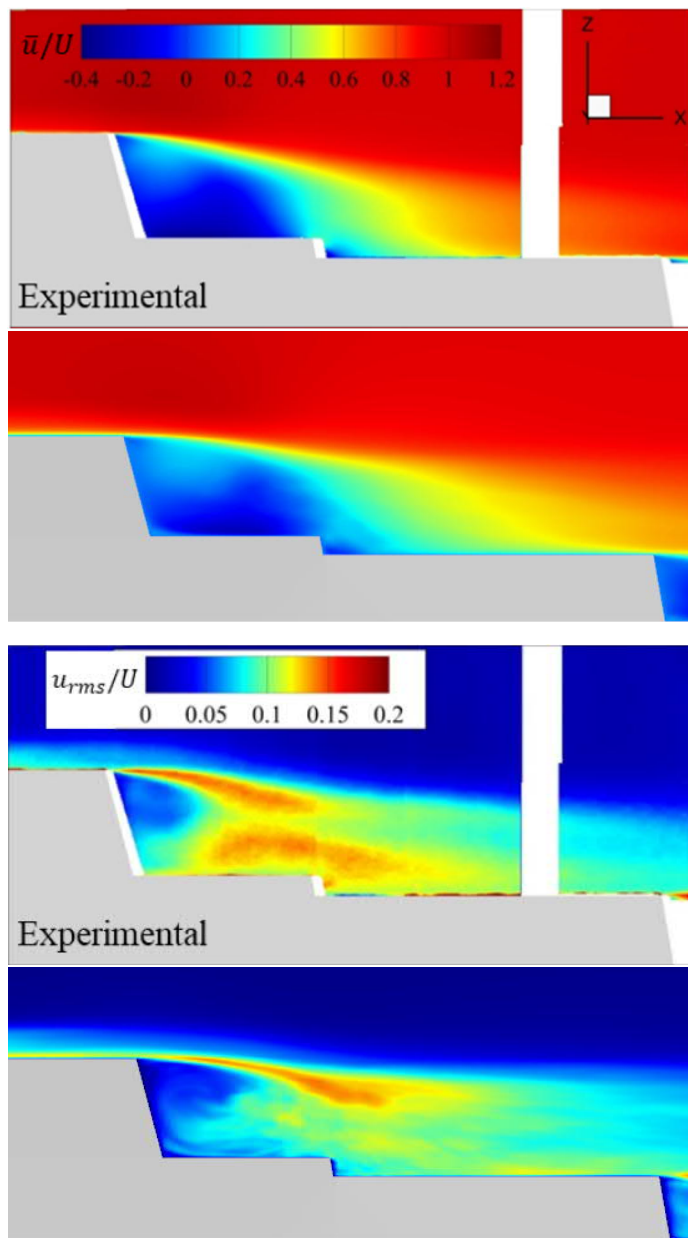


Figure 7 Contour plots of mean (top) and RMS (bottom) of streamwise velocity from experiments and CFD (80M, time step  $1e-04s$ ).

The observed larger deviations in RMS values of velocities warrant an investigation into the sensitivity to freestream conditioning, as well as extending the simulated time beyond the six flow-through periods set for the finest grid and smallest time step to quantify the error associated with finite sampling along the lines of Linton and Thornber (2021). Besides, the sensitivity of results to near-wall shielding function parameters remains to be evaluated. Specifically, the suitability of parameter  $r_{sd}$  (Simcenter STAR-CCM+ User Guide) – set to 45 by default based on calibration from canonical cases in Duffal et al. (2021) – should be examined against the background of unstructured meshes for arbitrary geometries commonly used in industrial settings. Tying into this point is the interest of comparing achieved results to simulations using

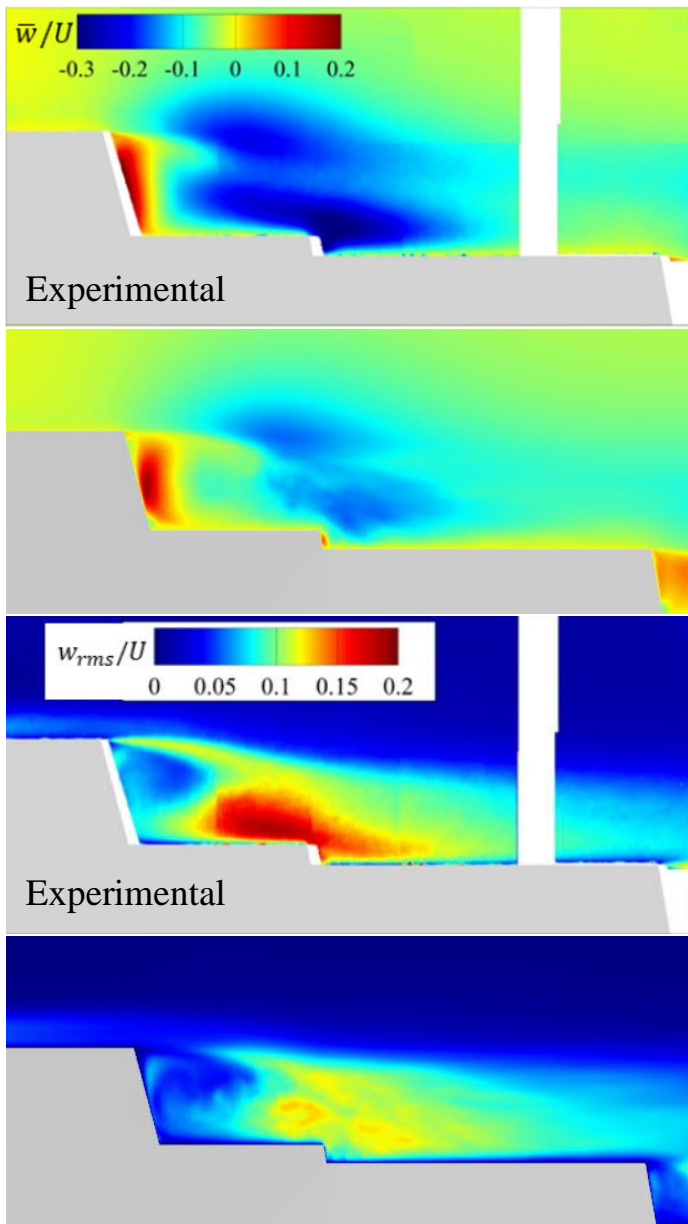


Figure 8 Contour plots of mean (top) and RMS (bottom) of vertical velocity from experiments and CFD (80M, 1e-04s).

a structured mesh and higher-order convection schemes. All in all, the test case at hand confirmed the prospective benefits of SRH for industrial use in terms of less constrained mesh building, potential reduction of total cell count and increase of time step. Meaningful flow statistics can be derived based on grids well below 100M with time steps of up to one order of magnitude greater than employed in equivalent DES. Using 1000 cores meaningful statistics were available for six flow-through periods on the 80M grid with a time step of 1e-04s in a day, which is within reach for forensic analysis of existing designs or scrutiny of up to a dozen design variations within realistic project time frames. While comparison to wall-resolved LES is infeasible, comparison to a wall-modelled LES approach is instructive for conclusion of the problem,

given a rigorous scrutiny of the raised SRH-specific questions. Both issues are currently investigated.

Ahmed, S.R., Ramm, G. 1984. Some Salient Features of the Time-Averaged Ground Vehicle Wake, SAE-Paper 840300

Buchholz, J., Martin, J. E., Krebill, A., Dooley, G., Carrica, P. M., 2018. Structure of a Ship Airwake at Model Scale and Full Scale. AIAA SciTech 2018 Forum (AIAA 2018-1263)

Dooley, G. 2019. Ship airwakes in waves and motions and effects on helicopter operation. PhD Thesis. The University of Iowa

Dooley, G., Carrica, P., Martin, E., Krebill, A., Buchholz, J. 2019. Effects of Waves, Motions and Atmospheric Turbulence on Ship Airwakes. AIAA Scitech 2019 Forum (AIAA 2019-1328)

Driver, D. M. and Seegmiller, H. L. 1985. Features of Reattaching Turbulent Shear Layer in Divergent Channel Flow," AIAA Journal, 23(2):163-171

Duffal, V., de Laage de Meux, B., Manceau, R. 2021. Development and Validation of a New Formulation of Hybrid Temporal Large Eddy Simulation. Flow, Turb. and Comb.

Ferziger, J., Peric, M. 2002. Computational Methods for Fluid Dynamics, Springer

Gnanamanickam, E., Zheng, Z., Seth, D., Leishman, G. 2020. Structure of the Ship Airwake in a Simulated Atmospheric Boundary Layer. AIAA Aviation 2020 Forum

Liefendahl, M., Revstedt, J., Fureby, C. 2020. A Critical Survey of Turbulence Modeling Methods for Ship Aero- and Hydrodynamics. 33<sup>rd</sup> Symposium on Naval Hydrodynamics, Osaka

Linton, D., Thornber, B. 2021. Quantifying uncertainty in turbulence resolving ship airwake simulations. Ocean Engineering 229, 2021.108983

Menter, F., Egorov, Y. 2010. The Scale-Adaptive Simulation Method for Unsteady Turbulent Flow Predictions. Part 1: Theory and Model Description. Flow Turbulence and Combustion 85(1):113-138

Menter F. (2018) Stress-Blended Eddy Simulation (SBES)—A New Paradigm in Hybrid RANS-LES Modeling. In: Progress in Hybrid RANS-LES Modelling. HRLM 2016. Notes on Numerical Fluid Mechanics and Multidisciplinary Design, vol 137. Springer

Office of Naval Research (ONR) Tumblehome Surface Combatant. <https://t2015.nmri.go.jp/onrt.html> called 9/16/2021

Shukla, S., Singh, S.N., Sinha, S.S., Vijayakumar, R. 2020. An Investigation of Ship Airwakes by Scale Adaptive Simulation. J. Marine Navigation and Safety of Sea Transportation 14(2):471-475

Siemens. 2021. Simcenter STARCCM+-User-Guide 2021.1

Spalart, P., 2001. Young-Person's Guide to Detached-Eddy Simulation Grids. Technical Report CR-2001-211032, NASA.

Thedin, R., Murman, S., Horn, J., Schmitz, S. 2019. Effects of Atmospheric Turbulence Unsteadiness on Ship Airwakes and Helicopter Dynamics. AIAA Aviation 2019 Forum (AIAA 2019-3032)

# Holistic Ship Design Optimisation: What is the Difference?!

Apostolos Papanikolaou  
National Technical University of Athens  
papa@deslab.ntua.gr

The paper introduces a holistic approach to ship design, as it was developed in the Horizon 2020 EU project HOLISHIP ([www.holiship.eu](http://www.holiship.eu), 2016-2020). The project dealt with the development of design and virtual prototyping simulation platforms, which integrate software tools for all major ship design disciplines and optimization objectives, namely, building and operational cost, energy efficiency, safety, environmental footprint, and life cycle cost/impact assessment. It enables the seamless mathematical multi-objective optimization of ship design with governing design constraints and the exploration of the huge design space by parametric modeling of the ship design system and its components (“digital siblings”).

The paper focuses and comments on the differences between the conventional and the HOLISHIP ship design approach by comparing their basic capabilities, advantages and disadvantages with respect to a series of criteria referring to

- the concept design process,
- the preliminary and contract design,
- the accuracy of the employed numerical methods (and software tools),
- the design lead time and person man-month effort,
- the early assessment of cost,
- the quality of design,
- the safety of ship and of the marine environment,
- the energy efficiency,
- the assessment of ship’s life-cycle performance,
- the development of innovative designs,
- the utilization of the employed software platforms,
- the coding of design workflow procedures,
- the distributed working and cloud computing,
- the virtual prototyping and
- the acceptance by the industry.

## References:

1. Papanikolaou, A. (ed), A Holistic Approach to Ship Design, Vol. 1: Optimisation of Ship Design and Operation for Life Cycle, SPRINGER Publishers, ISBN 978-3-030-02809-1, January 2019.
2. Papanikolaou, A., Harries, S., Hooijmans, P., Marzi, J., Le Néna, R., Torben, S., Yrjänäinen, A., Boden, B., A Holistic Approach to Ship Design: Tools and Applications. Journal of Ship Research, 65 (2020) JSR-12190070, The Society of Naval Architects and Marine Engineers.
3. Papanikolaou, A. (ed), A Holistic Approach to Ship Design, Vol. 2: Application Case Studies, SPRINGER Publishers, ISBN 978-3-030-71090-3, June 2021.



# Credibility of wave breaking computations by Volume of Fluid RANS codes

Hoyte C. Raven, Maritime Research Institute Netherlands, h.c.raven@marin.nl

Wave breaking is a frequent phenomenon in the flow around ships, as part of the steady wave pattern. Both plunging (overturning) breakers occur, mainly at a sharp ship bow; and spilling breakers as found at blunter bows, fore and aft shoulder, and aft of transom sterns.

In ship wave computations using Volume of Fluid codes common today, wave breaking seems to occur naturally; and we notice some confidence of users in the wave breaking phenomena as predicted, e.g. Wang & Wan [2017]. It is sometimes supposed that other classes of methods, such as surface-fitting codes or single-phase formulations, would not be able to predict this. But spilling breakers are in principle well representable by surface-fitting codes. Starke et al [2007] show results for spilling breakers aft of transom sterns in 2D flow, computed with the steady iterative surface-fitting code PARNASSOS. There are also several papers on computation of breaking waves using single-phase methods; e.g. Hino [2004] computed the wave pattern of a blunt body and obtained qualitative agreement for the spilling breakers at bow and shoulder. Two-phase surface-capturing formulations, such as Volume of Fluid, would seem to be more suited to the calculation of wave breaking due to the ability to include the air entrainment and the easier incorporation of overturning waves. However, that is not evident at all, as we shall show.

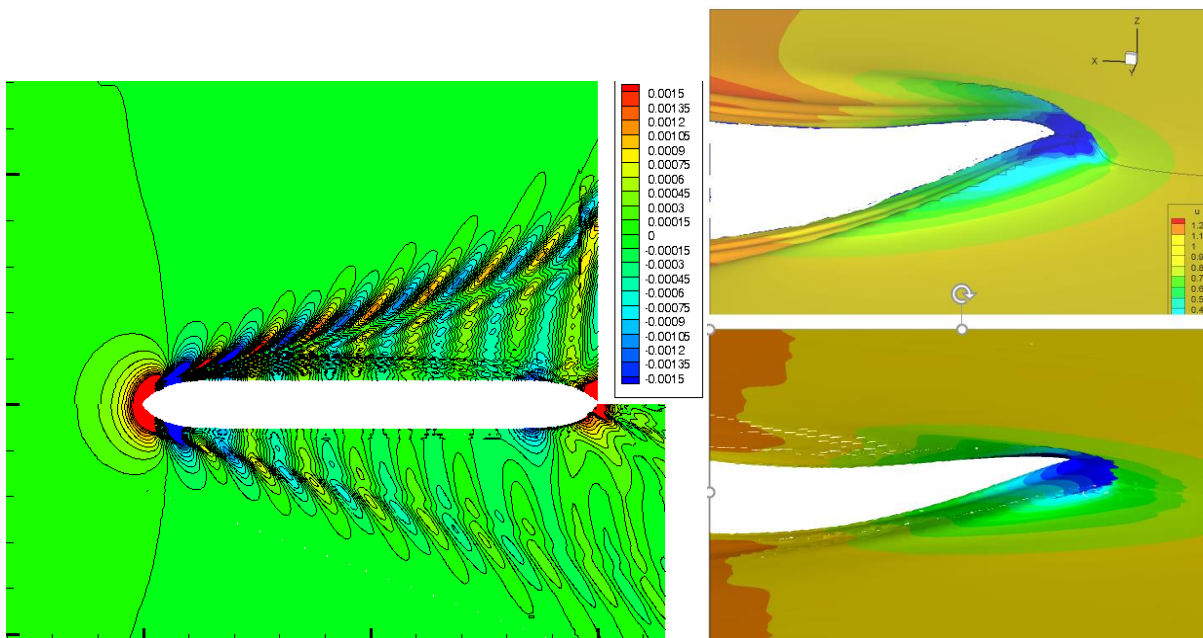


Fig. 1 Computed wave pattern of inland vessel. Top half: Parnassos. Bottom half: Refresco. In the graphs at the right, colours indicate longitudinal velocity

The incentive for the present study was Fig.1. It compares the flow around an inland ship computed using PARNASSOS (surface-fitting, single-phase, steady) and REFRESKO (surface capturing, two-phase, Volume of Fluid, transient). A spilling breaker is found at the bow, with an almost stagnant area upstream of the bow and a sort of plateau of the water surface. The local bow wave form and the velocity field under it are very similar between both predictions. Even so there appears to be a large difference in the amplitude of the radiated bow wave system. It is not caused by a difference in numerical wave damping, as there is already a factor 2 difference close to the ship. It seems that for the spilling breaker at the bow, REFRESKO computes a flow with more dissipation than PARNASSOS. This is confirmed by the total-head loss, which in the bow area appears to be an order of magnitude larger for REFRESKO. What causes this much larger dissipation? And which prediction is correct?

To clarify this, we take a simpler 2D test case, from the experiments by Duncan [1983]. This is a NACA0012 foil with chord length  $c = 0.203$  m at 5 deg incidence (nose-up), towed at 0.8 m/s in a rather shallow tank, at a fixed distance of  $0.86 c$  above the bottom. The foil submergence was varied by varying the water level. For larger submergence, a regular, non-breaking wave train is formed, for smaller ones the crest following the deep wave

trough above the foil starts breaking with a steady spilling breaker, and the downstream wave train is reduced in amplitude.

### **A simple model of a spilling breaker**

In Duncan [1981,1983] a simple model of a spilling breaker has been given. It describes the breaker as a recirculating eddy riding on top of the underlying wavy flow, staying in place on a wave front. Due to its weight, the breaker would slide forward down the wave face; but it is held in place by the aft-directed shear stress exerted by the underlying flow. Conversely, the breaker exerts forces on the underlying flow: its weight gives a pressure force on the wave surface that reduces the downstream waves; the shear stress causes a surface wake. Thus, part of the momentum defect due to the trailing waves is converted to a momentum defect in a surface wake. Tulin and Cointe [1986] have extended this model and derived empirical relations for several quantities. While, of course, this model plays no role in our computations, it is a useful reference to compare with.

### **Computational settings**

We have computed all cases from Duncan [1983], to check the accuracy of the regular wave trains, the submergence at which wave breaking starts, and the trailing wave amplitude. The code used is REFRESCO, an unstructured finite-volume RANS code with a SIMPLE-based solution approach. The water surface is treated by a Volume of Fluid formulation. Therefore, steady free-surface cases are solved in transient mode. The air volume transport equation was discretised by the Refrics scheme (Klajj et al, 2018). In most of the present calculations, an SST turbulence model has been used. The domain extended from 12 chord lengths upstream of the trailing edge, to 16c downstream. An unstructured grid was generated using Hexpress, with strong refinement around the foil and in a band around the free surface. Longitudinal grid spacing here was 1/130 of a transverse wave length.

On the foil, a no-slip condition was imposed. At the outflow, an undisturbed hydrostatic pressure was imposed, and Neumann conditions for other quantities. At the bottom of the domain a free-slip condition was imposed, ignoring the weak boundary layer that should be present.

### **Results**

For the larger submergence values, the computed non-breaking wave amplitude was a bit smaller than from the data. Probably connected with this, for decreasing submergence wave breaking started somewhat later than in the experiment. We do not discuss all results here, but just consider the submergence of 0.159 m, the smallest from Duncans data. In the experiment, substantial wave breaking and a large reduction of the downstream wave amplitude occurred. In the computations, the first wave trough is too shallow, the following peak is 40% too high (Fig. 2). The downstream wave amplitude is in reasonable agreement with the data, but is far more regular. Therefore, the large reduction of the wave amplitude due to breaking is there. But where is the breaking?

Fig. 3 is a close-up of the velocity field in the first wave crest, where we would expect to find the recirculating flow as in the simple flow model. There is a retarded flow, with x-velocity dropping to 25% of the inflow speed, but no stagnation or backflow. A weak wake behind the first wave crest can be observed, with a velocity deficit of about 10%. A substantial level of eddy viscosity is found from the first wave crest, slowly decaying aft. So there are some signs of a spilling breaker: dissipation of wave energy, a large reduction of the downstream wave amplitude, and turbulence production. Also, the total-head loss distribution clearly shows increasing losses from the wave trough aft until the wave crest. But it remains quite puzzling that the flow gives no indication of the mechanism that causes this head loss and wave reduction, and that nothing of the flow behaviour described by Duncan and by Tulin & Cointe is found.

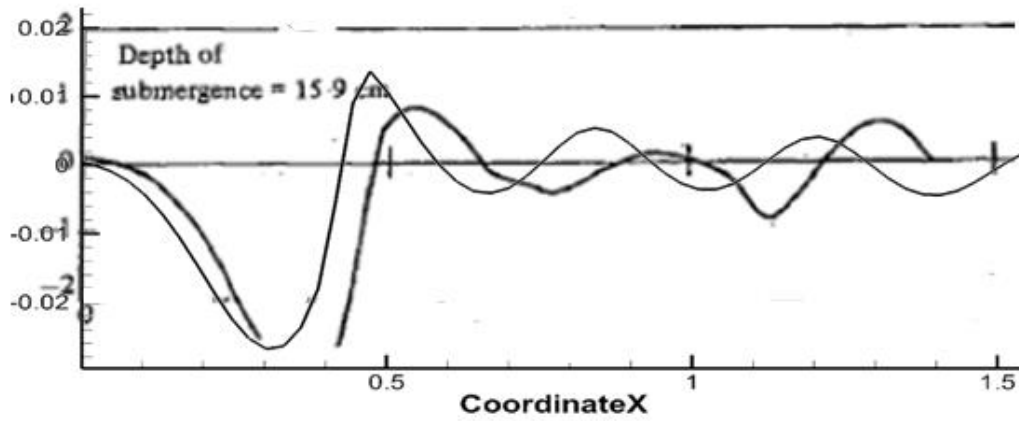


Fig. 2. Measured (heavy line) and computed (thin line) wave profile for submergence 0.159 m.

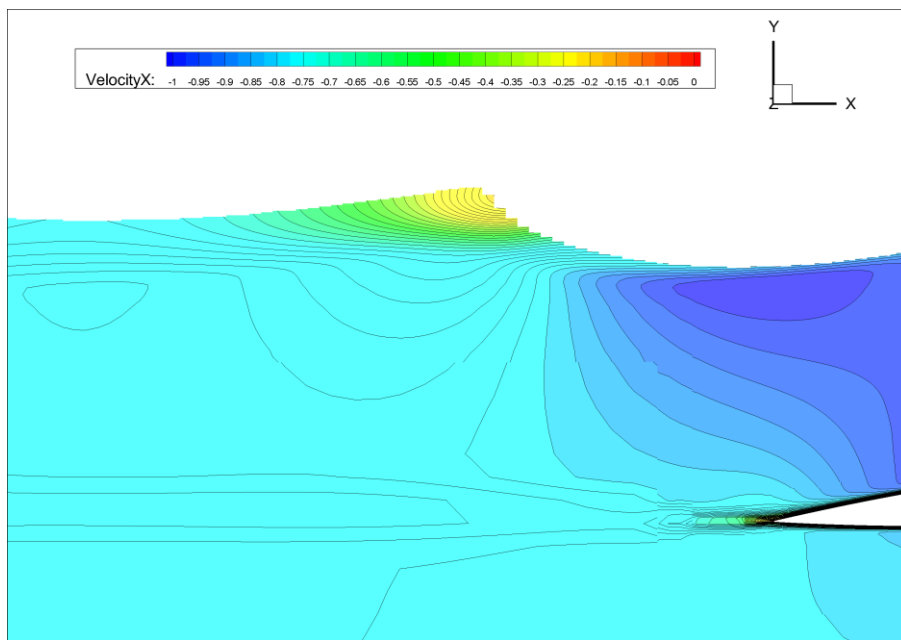


Fig. 3. Distribution of longitudinal velocity, submergence 0.159 m.

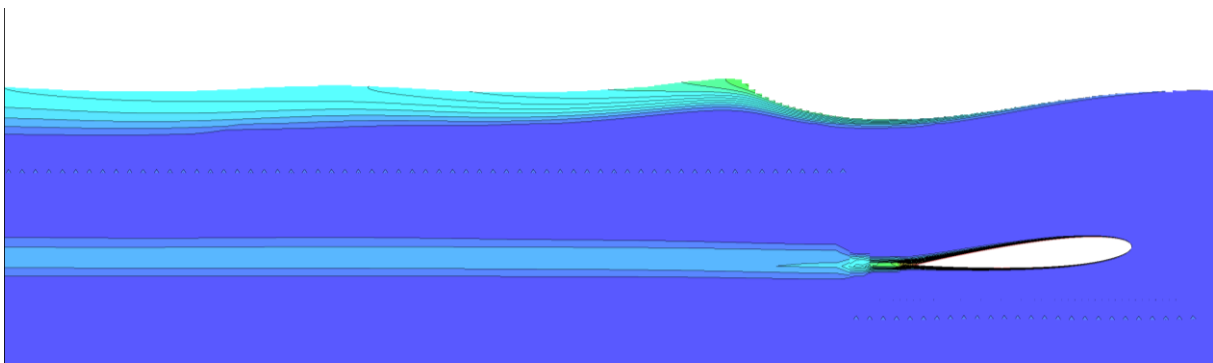


Fig. 4. Total head loss distribution. Submergence 0.159 m.

The explanation comes once we inspect the pressure distribution on the wave surface, as usual defined as the surface of 0.5 volume fraction. The pressure on this surface should be essentially constant, equal to atmospheric pressure. Small deviations always occur in two-phase methods, and are found here as well for the greater foil submergences. But for submergence 0.185 m, and even more for 0.159 m, there is a clear overpressure at the wave surface; indicated in colour on the wave surface in Fig.5. It starts near the deepest point of the wave trough and

increases up to the first wave crest, where it ends. This overpressure has a magnitude up to  $C_p=0.18$ ! In the same figure, on the back wall the distribution of the air volume fraction is indicated. Above the wave surface, there is a large cloud of a mixture of air with 10-15% of water. The hydrostatic pressure this gives corresponds very well with the pressure on the wave surface. As this overpressure on the wave surface adds momentum to the flow, reducing the momentum deficit in the waves, it reduces the waves. At the same time, the shear stress between the cloud and the underlying flow causes a surface wake. Therefore, it is this cloud of wet air above the wave surface that explains the total head loss and the reduction of the waves. As Fig.6 shows, this air cloud does display the expected recirculation and forms a closed bubble, very similar to the flow type we expect, except that it is located above the wave surface!

Next, several tests have been done with variation of computational parameters. A moderate grid refinement by a factor 2 in  $\Delta x$  did not change much. For a larger immersion, 0.193 m, which had incipient breaking in the experiment, also a drastic refinement has been made, by a factor of 10 longitudinally and 2 vertically. This led to an increase of the extent and water content of the breaker and a further reduction of the downstream wave amplitude, thereby moving away from the experimental data.

Also, various turbulence models have been tried. The Spalart-Allmaras model gave a result similar to that of SST, but slightly closer to the experiment; the  $k-\sqrt{k} L$  model gave a much larger and heavier recirculation and a worse agreement. The amplitude of the trailing wave system differed by more than a factor 2 between turbulence models.

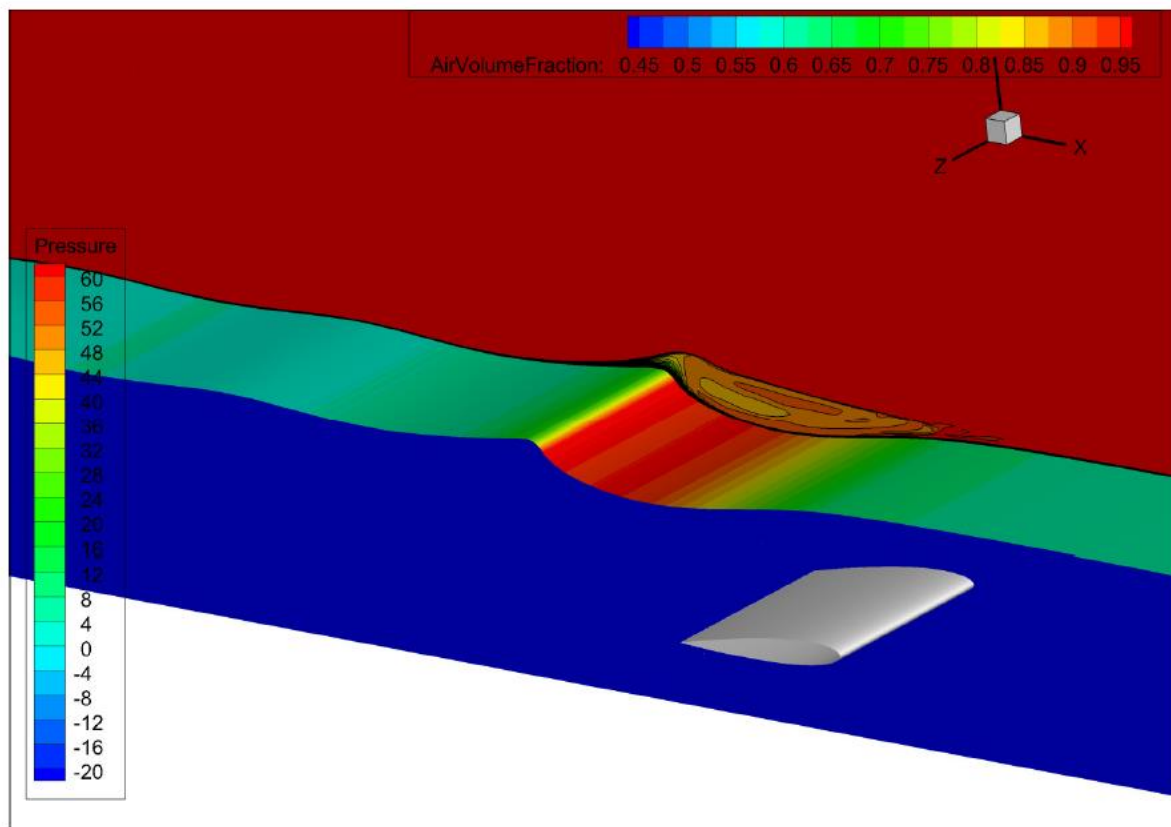


Fig. 5. Wave surface for submergence 0.159 m, with pressure distribution on it; and air volume fraction distribution shown on vertical plane.

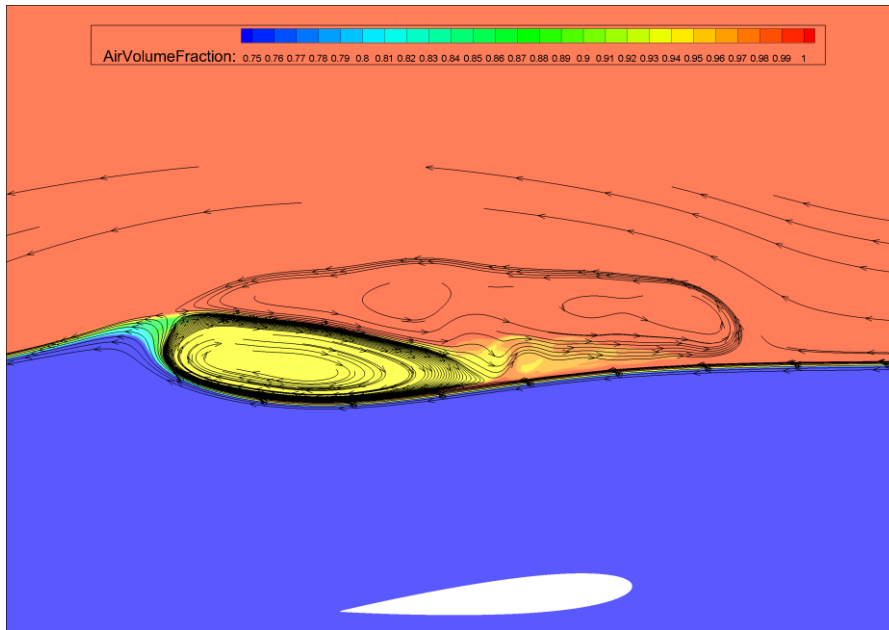


Fig. 6. Volume fraction distribution and streamline pattern, for submergence 0.159 m, for Spalart-Allmaras turbulence model.

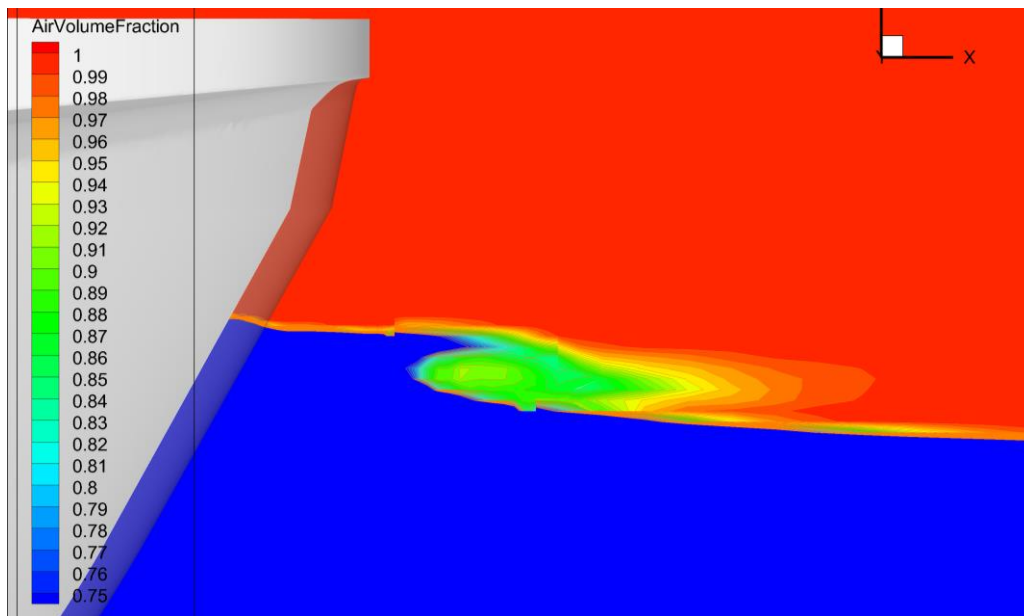


Fig. 7. Longitudinal slice through bow wave of inland ship, from REFRESCO, showing volume fraction field.

## Discussion

We thus find a superficial similarity with the simple model of breaking: there is a recirculating flow on the front face of the wave, which exerts a pressure on the underlying flow and leads to a reduction of the wave momentum deficit, converting it to a momentum loss in a surface wake. However, this recirculating flow consists of air with 10-15% of water, rather than water with air bubbles. How such an air-water mixture would look in reality is hard to imagine. Moreover, if we consider the volume fraction = 0.5 surface as the water surface, the ‘breaking waves’ computed have no overturning, no pointed wave crest, no stagnation and no recirculation.

Duncan (1981) estimated that the breaker has a density of about 60% of that of water, and mentions older estimates of 80 to 100%. The present ‘breaker’ therefore is 4 to 6 times too light. Moreover, its cross section is far too large, 2.5 times too large for submergence 0.159 m, 6 times too large for 0.185 m. For decreasing foil submergence, the computed ‘breaker’ does not get larger but its water content increases. If one would imagine to compute air entrainment by a spilling breaker in this way, there is none: the thicker interface disappears immediately aft.

In general, we need to be aware of what is modelled in the equations. In a RANS model, the volume fraction transport equation represents pure convection by the *mean* flow. No effect of turbulence is incorporated at all, as a result of the simple disregard of any correlation of turbulent velocities and fluctuations of the volume fraction gradient. As Duncan [2001] notes, Reynolds averaging for spilling breakers is not straightforward and data for closure are lacking; but disregarding the problem seems no solution. Therefore, the computation contains no turbulent mixing of air and water, which seems to be a significant feature of a spilling breaker. The only feature by which the mean flow could lead to an air/water mixture and air entrainment is an overturning wave that encapsulates air. In our calculation we notice an intermittent ejection of fluid from the crest in forward direction, also in the ‘steady’ phase of the breaking, feeding the cloud above the surface.

Therefore, in RANS-VoF models a local thickening of the interface mostly is a result of the flow retardation towards the wave crest, and numerical diffusion, but not of turbulent mixing. Simultaneously, the compressive action of the discretisation continuously tries to keep the interface thin. One needs to be very careful in attaching any physical meaning to the thickness of the computed air/water interface in VoF methods.

Finally, we go back to ship waves. In Fig 1 we had noticed a large difference in dissipation due to the breaking, between the surface-fitting and surface capturing codes, for almost equal local wave and flow fields. We now understand that the clue was to be found above the wave surface. Fig. 7 is a longitudinal slice through the flow field for the same inland ship, slightly off the centreplane, showing the volume fraction distribution. The air volume fraction 0.5 isosurface has a somewhat overhanging bow wave. Forward of it, a circulating cloud of air with 10% of water is found, which exerts a pressure on the wave front, damping the waves. We find this consistently for all computed breaking ship waves, overturning or spilling. As long as the flow behaviour is so far off the physical reality, there seems to be no reason to believe the computed wave amplitudes behind a breaking wave.

Therefore, the ability to compute wave breaking depends on what one wants to see: just the overturning of a bow wave, or also what it means for the radiated wave amplitudes or air entrainment. At least the standard RANS-VoF formulation in our code is producing weird flow fields, only identified upon a closer look. Other methods might behave differently, therefore we challenge readers to inspect their computed flow fields from a similar point of view. Until improvements have been found and further validation has been done, the physical realism of VoF predictions of steady breaking waves seems quite limited.

### **Acknowledgement**

This study was supported by the Defensie Materieel Organisatie of the Dutch Ministry of Defence. This support is gratefully acknowledged.

### **References**

- Duncan, J.H. (1981), “*An experimental investigation of breaking waves produced by a towed hydrofoil*”, Proc. Royal Soc. A, Vol.377, pp. 331-348.
- Duncan, J.H. (1983), “*The Breaking and Non-Breaking Wave Resistance of a Two-Dimensional Hydrofoil*”, Jnl. Fluid Mechanics Vol. 126, pp. 507-520.
- Duncan, J.H. (2001), “*Spilling breakers*”, Ann. Rev. Fluid Mech. Vol.33, pp 519-547.
- Hino, T. (2004), “*Numerical simulations of breaking waves around an advancing ship by an unstructured NS solver*”, 25<sup>th</sup> Symp. Naval Hydrodynamics, St.John’s, Canada.
- Klaij, C.M., Hoekstra, M., and Vaz, G. (2018), “*Design, analysis and verification of a volume-of-fluid model with interface capturing scheme*”, Comp. & Fluids, Vol. 170, pp. 324-340.
- Starke, A.R., Raven, H.C. and Van der Ploeg, A.P. (2007), “*Computation of transom stern flows using a steady free-surface fitting RANS method*”, 9<sup>th</sup> Int. Conf. Num. Ship Hydrodynamics, Ann Arbor, Michigan, USA.
- Tulin, M.P. and Cointe, R. (1986); “*A Theory of Spilling Breakers*”, Proc. 16<sup>th</sup> Symp. Naval Hydrodynamics, Washington DC, USA.
- Wang, J. and Wan, D.C., “*Breaking Wave Simulations of High-speed Surface Combatant using OpenFOAM*”, 8<sup>th</sup> Int. Conf. Comp. Methods, Guilin, China.

# A Single Cavitation Bubble Collapse in Perspective of Numerical Simulations

<sup>1</sup>Hemant Sagar; <sup>2</sup>Bettar el Moctar

<sup>1</sup>Universität Duisburg-Essen, Institute of Ship Technology, Ocean Engineering and Transport Systems; Germany

<sup>2</sup>Harbin Engineering Universität, College of Shipbuilding Engineering, Harbin, Heilongjiang, P.R. China  
corresponding author: [hjsagar.21@gmail.com](mailto:hjsagar.21@gmail.com)

## Abstract

Basics of cavitation and induced damages are not very well understood in bulk cavitation. For a better understanding of cavitation and induced damage, investigations of a single-bubble collapse are very useful and logical. Numerical simulations of cavitation bubble give out more detailed information about collapsing process, parameters than experiments. In the current work, the flow surrounding the collapse process of a single cavitation bubble near a solid surface has been numerically investigated considering compressibility. The three-dimensional flow was captured by the numerical code module CavitatingFOAM solves the compressible two-phase Navier-Stokes equations in an Euler-Euler approach with barotropic equations of state. The relative wall distance ( $\gamma$ : ratio of the distance between bubble center and solid surface to bubble's maximum radius) systematically. In computed collapse derivatives, the shape of the bubble, such as toroidal shapes of oval impacts and collapse times agreed favorably to experimental measurements. Simulated cases reflected. Flow types, pressure fields, and shear rate were also discussed. A microscopic bubble collapse near the surface was also investigated to compute collapse induced wall shear rate and flow around collapsing bubble. The results of numerical simulations were compared with the experimental data investigated in past with qualitative quantitatively good agreement. Overall, this work gives broad insight into the numerical investigation of cavitation bubble and surrounding flow.

## 1 Introduction

Cavitation is an essential part of research since the last century because of its destructive effect on high-speed hydro-machinery, propellers, pumps, rudders, and turbines (Arndt, 1981; Parsons and Cook, 1919; Silberrad, 1912; Tomita and Shima, 1986). This led an extensive research in the field of hydrodynamics cavitation and single bubble cavitation and cavitation-erosion. However, cavitation is also an essential phenomenon for assorted applications, e.g., surface cleaning (Ohl et al., 2006), dispersion (Fridman, 1972), dentistry (Walmsley et al., 1988), emulsification (Ji et al., 2006), sonophoresis (Miller et al., 2002), etc. Over 150 years, researchers were interested in how these tiny cavitation bubbles damage resilient metal surfaces. Shock waves produced during the cavitation bubble's collapse damage the adjacent solid boundary (Tomita & Shima, 1986; Philipp and Lauterborn, 1998). Although the collapse of the cavitating bubble near a solid boundary induces a counter-jet flow, even leading to single bubble sonoluminescence, its destructive action on the solid boundary has not been firmly deduced and analyzed numerically. The impact of a collapsing bubble has been extensively analyzed numerically, its surrounding flow field was hardly ever discussed (Han et al., 2015; Shukla, 2014; Ye et al., 2014). Compressibility and viscosity still pose a challenge in numerical simulations. Recent numerical investigations include (Koch et al., 2016; Ma et al., 2018; Ming et al., 2017; Reuter et al. 2018; Sagar and el Moctar, 2018), among which most investigations neglected phase changes. Furthermore, in majority of investigations, spherical symmetry was assumed, or a two-dimensional computational domain was considered for computations. Some analyses used a barotropic model to account for the phase change (condensation

and evaporation) or derived coefficients (cavitation models). Many results did not reflect rebounds and multiple collapses. Nevertheless, they were able to reflect various aspects of the collapsing bubble, such as bubble shapes, rebounds, impact velocities, and collapse times. A numerical simulation of bubble collapse that accounts for three-dimensional compressible flow using finite volume method is necessary. Here we summarized the numerical work in Sagar & el Moctar (2020) and Sagar (2018), which give broad insight into the single bubble cavitation and induced damage by numerical and experimental means. Presented work covers the numerical aspects of single collapsing bubble, mainly its flow characteristics at microscopic level.

## 2 Numerical method

An open-source the finite volume method based computational fluid dynamics code ‘OpenFOAM’ was used to perform numerical simulations of a cavitation bubble collapsing near a solid surface. Previous investigations have noted the role of compressibility during the collapse phase in past investigations Besant (1859), Mitchell & Hammitt (1973), Naudé & Ellis (1961), Rayleigh (1917). However, escaping the consideration of compressibility in the numerical investigation of Plesset and Chapman (1971), Sagar & el Moctar (2018), Sagar (2018) have shown jet formation. Especially, the investigations of Sagar & el Moctar (2018) and Sagar (2018) have reflected the first two collapses and rebounds successfully. Their computed impact velocities near the bottom surface correlated well with reference experiments of Phillip & Lauterborn (1998). However, the compressibility of flow can have a significant influence on the maximum speed and pressure. Some investigations have predicted local velocities in the range of several hundreds of m/s. Additionally, we believe that compressibility and phase change can reflect more realistic multiple collapses. Due to high pressure and velocities resulting during the collapse process of the bubble, we felt it was appropriate to use of the fully compressible solver based on the barotropic equation. That is why, we used a fully compressible two-phase flow solver “CavitatingFoam”, modeled using the barotropic equation of state. An Euler-Euler approach solved the Navier-Stokes equations on a fixed Eulerian grid, considering gas and liquid phases as a homogeneous mixture with vapor as the gas phase and water as the liquid phase. It is two-phase flow solver that applies barotropic equations of state and an Euler-Euler approach to solve the Navier-Stokes equations on a fixed Eulerian grid, considering gas and liquid phases as homogeneous mixture. More details of numerical method can be find in Sagar & el Moctar (2020). Here, the liquid and the gas phase is water and vapor, respectively. The mass fraction of the vapor in the mixture  $\alpha$  is assumed to be a continuous function of space and time. It is determined as:

$$\alpha = \frac{\rho_m - \rho_{w,sat}}{\rho_{v,sat} - \rho_{w,sat}}, \quad (1)$$

where  $\rho_m$  is the mixture mass density,  $\rho_{w,sat}$  is the density of water at saturation and  $\rho_{v,sat}$  is vapor saturation density. A drop in the saturated liquid density below vapor saturation density indicates the presence of cavitation.  $\alpha = 0$  means the presence of only the liquid phase, whereas  $\alpha = 1$  indicates cavitation zones. The mixture compressibility  $\varphi_m$  is modelled using Wallis linear model given by:

$$\varphi_m = \alpha\varphi_v + (1 - \alpha)\varphi_w, \quad (2)$$

where  $\varphi_v$  and  $\varphi_w$  are the liquid and the vapor compressibility. Further, the mixture viscosity  $\mu_m$  is computed as:

$$\mu_m = \alpha\mu_v + (1 - \alpha)\mu_w, \quad (3)$$

Here,  $\mu_w$  and  $\mu_v$  are the viscosity of water and vapor respectively. The relation between pressure and density is defined as:

$$\frac{D\rho_m}{Dt} = \varphi \frac{DP}{Dt}. \quad (4)$$

The above equation can be used directly in the continuity equation to formulate a pressure equation or integrated to obtain the pressure as a function of the density. The size of the computational domain was  $10 \times 10 \times 6 \text{ mm}^3$ . To reduce computational costs, we refined our grid only in the nearby region of bubble collapse. Figure 1(b) illustrates the finite volume discretized domain.



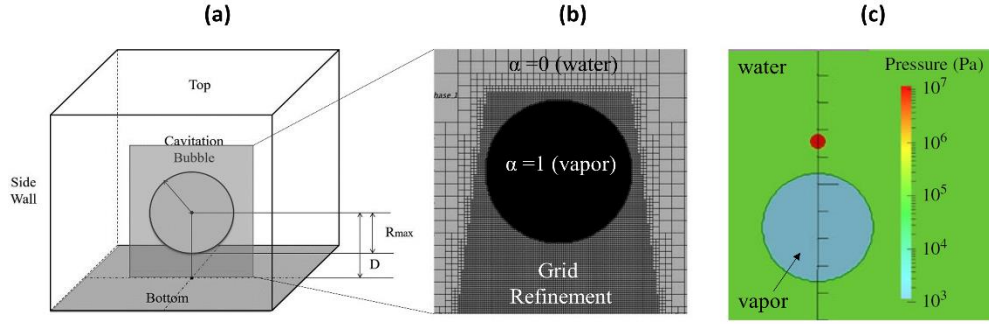


Figure 1: Illustration of numerical domain: (a) three-dimensional representation of the numerical domain, (b) grid topology along plane section shown in (a) showing grid refinement around vapor bubble and phases, (c) computed pressures in plane section [taken from Han et al. (2015)].

In figure 1 (a)  $R_{max}$  is the maximum radius of the bubble, and  $D$  is the distance between the bubble's center and the bottom surface. Instead of considering the millimeter-sized bubble, we initiated the numerical computations for the fully-grown spherical bubble having a diameter of 3mm. Based on the numerical results of Han et al. (2015) we defined our initial bubble by specifying its internal vapor pressure of 0.01bar, the bubble's wall velocity of zero, and volume fraction of vapor to 1. For grid sensitivity studies, the CPBR (cells per bubble radius) parameter was already specified for the spatial resolution of Sagar & el Moctar (2018). Here we used a similar grid resolution to perform our computations by varying the acoustic Courant number. The maximum acoustic Courant number was limited to 0.5 by choosing appropriate time steps. For shear rate validation, we choose a bubble size of 325 $\mu$ m and the minimum cell size in the grid refinement area was 6.25  $\mu$ m. As many flow effects during the collapse of the cavitation bubble are inherently three-dimensional, the computations were also carried out without the assumptions of any symmetries. The flow was assumed to be laminar.

### 3 Results

#### 3.1 Bubble dynamics

Figure 2 compares experimentally obtained and numerically simulated bubble shapes in their plane projected vapor volume fractions, for the relative wall distances of  $\gamma = 1.4$  (left) and 1.8 (right) respectively. The negative time only specifies events before the first collapse and physically insignificant. In simulations, vapor condensed at the center of the bubble during the first collapse. This phenomenon was more pronounced as  $\gamma$  increased. For the relative wall distance of  $\gamma = 0.9$ , the comparative bubble shapes of the second collapse, which differed with  $t \approx 0.04$ ms. For  $\gamma = 1.2$ , the times of the second collapse observed in the experiments and our simulations agreed well with each other. The bubble dynamics featured the microjet and flattening the bubble when it attached itself to the surface. Further on, the computed compression of the cavity and its resulting collapse was as observed in the experiments. The vertical height of the toroid in the simulation was more pronounced than in the experiments and this was also observed for further investigation of  $\gamma = 1.4$  and  $\gamma = 1.8$ .

In Figure 2 (left, for  $\gamma = 1.4$ ) Experiments and simulations reflected the similar distance between the collapsing bubble and the bottom surface before it collapses. After the first collapse in the water, the cavity translated towards the bottom surface and attached itself to the bottom surface. At the beginning of the second rebound, a clear jet was observed (until  $t = 0.04$ ms), which further disappeared by the enclosed cavity due to compression. The attached cavity indicated vertical compression and horizontal expansion during the second collapse in both, experiments and simulations. At the end of the second collapse flattened became toroidal and caused peripheral pressure impacts (see Figure 3,  $\gamma = 1.4$ ).

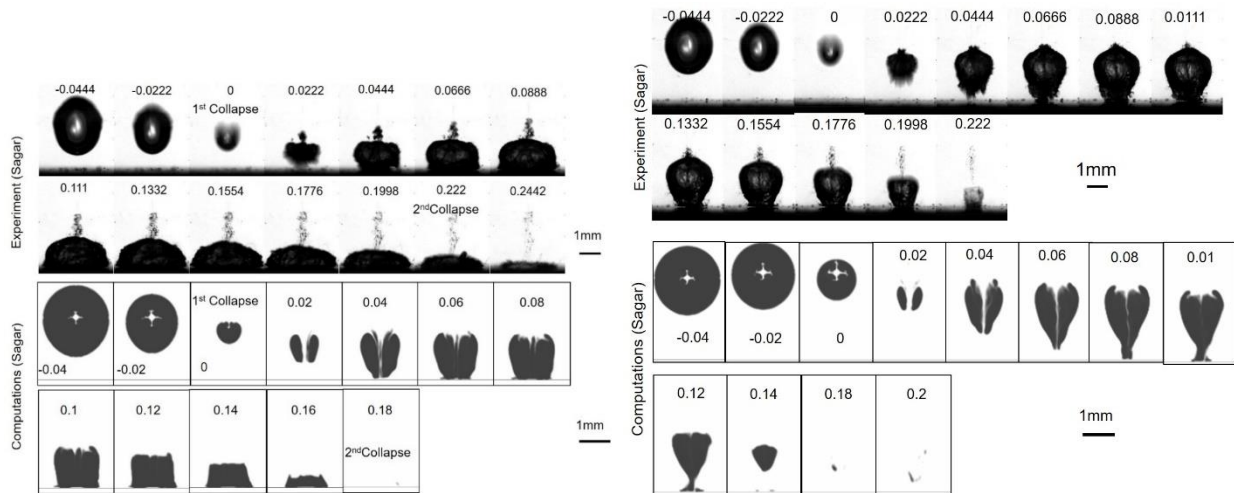


Figure 2: Comparison between bubble shapes obtained in experiments and numerical simulations for  $\gamma = 1.4$  (left) and  $1.8$  (right), [taken from Sagar & el Moctar (2020)]

Figure 2 (right) shows the comparison between experimentally captured and numerically simulated series of collapsing events of the cavitation bubble. For this case, numerical simulations reflect the rebounding bubble translation towards the solid surface after its first collapse which is also observed in experiments. A clear jet indicated in simulations until  $t=0.08\text{ms}$  during the second rebound, which was enclosed later due to compression of the cavity. The simulation did not show enough enlarged cavity as in experiments before the second collapse, as its majority content may not be vapor. The second collapse in simulations and experiments occurred at  $t \approx 0.2\text{ms}$  after the first collapse.

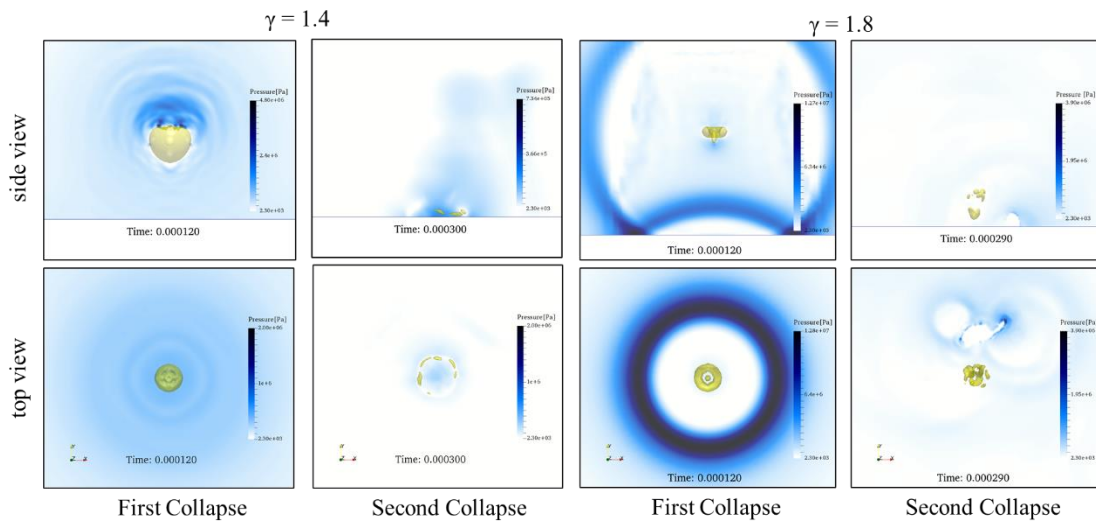


Figure 3: Computed field pressure along side and top view during first and second collapse for  $\gamma = 1.4$  and  $1.8$ . Time annotations are from the full-grown condition.

Although our simulation results indicated some differences from experiments in terms of shapes and fine features of counter jet and toroid, the essential physics associated with jet formation, translation of regrowing cavity (for larger relative wall distances), toroid, and rebound of toroid were well-reflected. The associated underestimated shaped during simulation due to the assumption of only vapor as gaseous phase, while in experiments regrowing cavity content was not only vapor but also extracted dissolved gases due to pressure shock waves. Our computed collapse times were consistent with collapse times observed in experiments. The bubble shapes during the second collapse for  $\gamma = 1.4$  and

$\gamma = 1.8$  were not resolved in the simulations. However, the bubble shapes during the second collapse were well resolved in the simulations for  $\gamma < 1.4$ . Although our computed vertical dimensions of the rebounding cavities exceeded those observed in experiments, our simulations were able to reflect consistent bubble dynamics up to the second rebound. The overall agreement of our computations with experiments was favorable.

### 3.2 Flow characteristics of a collapsing bubble

The dynamics of the bubble differed significantly even the relative wall distance varied moderately. Pressure gradient variation from top to bottom acting on the bubble's surface when the solid surface is present nearby bubble. This pressure distribution and the flow over the bubble's surface initiated the formation of a microjet. Thus, the presence of the wall itself and the associated wall distance are significant parameters affecting the initiation of the microjet rather than notch formation at the top of the bubble. The top wall velocity of the bubble exceeded the velocity of the bottom, leading to the formation of a microjet. The attached toroidal bubble surrounded by the vortex flow collapsed and rebounded many times, which resulted in the formation of tiny bubbles.

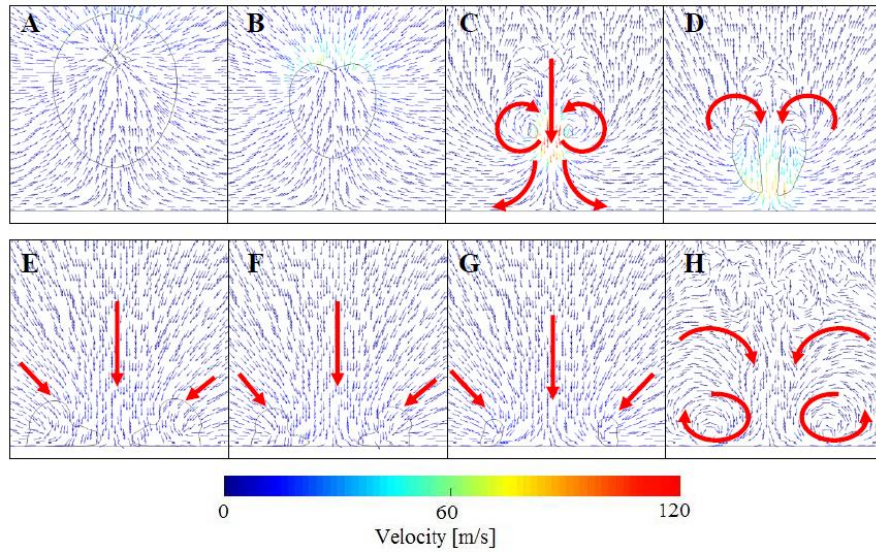


Figure 4: Different types of flow patterns observed in numerical simulation of single cavitation bubble collapse.

To model the bubble's collapse mechanism, the flow around the bubble in different phases of collapse has to be known. From our simulation, flow comprised three different kinds, namely, radial flow, translational flow, and rotational flow as illustrated in Figure 4. Asymmetric pressure distribution over the surface of a cavitation bubble during its collapse leads to the formation of a microjet. The microjet initiation caused the surrounding fluid to be sucked from the bubble's top and through the collapsing bubble. At this instance, two different kinds of flows developed. A translational flow turned into a tangential flow towards the surface, led to the rotational or vortex flow around the collapsing cavity (see Figure 4, C). This vortex flow became dominant during the first collapse. After the first collapse, when the cavity attached itself to the bottom wall, the radial flow over the toroidal cavity was initiated (see Figure 4, E). Combination of the radial flow over toroid and the translation flow during the collapse of toroid induced vortex flow. This flow along the bottom surface induced shear forces on the surface. The intensity of this flow and application are discussed in the following subsection.

### 3.3. Shear rate analysis

Above numerical results predicted high velocity flow around the surface of a collapsing bubble induced the translational flow energy of the jet to be converted to radial and rotational flow energy after impact. Someone can

expect considerable shear stresses at the wall due to such higher velocity during bubble collapses, regrows, and collapses. These wall shear rates might be significant in bulk cavitation, e.g., ultrasonic cavitation. Previously, Reuter & Mettin (2018) developed a shear rate raster microscope to measure the shear rate near the bottom surface induced by a single microscopic cavitation bubble collapse. Their measured shear rates near the surfaces were validated with our numerical method. Our numerical results also validated against their (Reuter et al. 2017) PTV results obtained during a bubble collapse for the flow around the bubble.

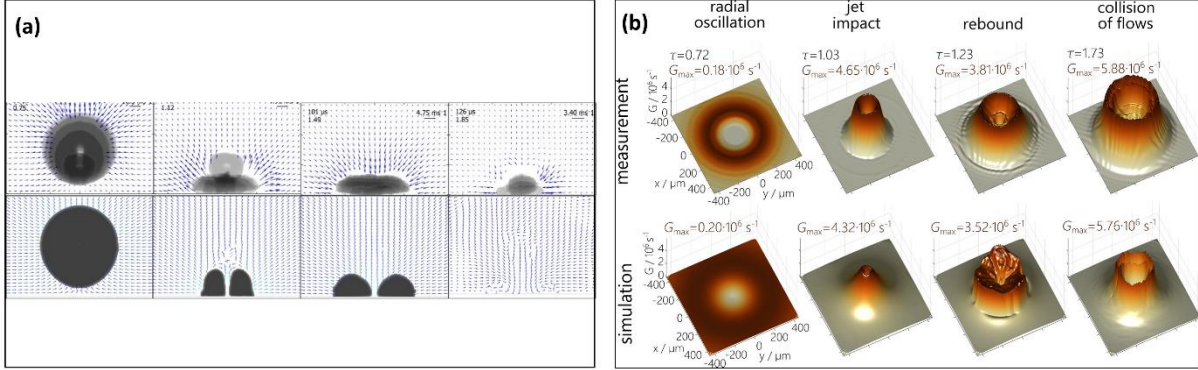


Figure 5: flow and shear rate analysis during the collapse of a single cavitation bubble. (a) comparison of flow characteristics during bubble collapse. The flow field in experiments (top) of Reuter et al. (2017) and from our computations (bottom), (b) Comparison between shear rates from experiments (top) of Reuter et al. (2017) and from computations for a bubble of  $R_{max} = 325 \mu\text{m}$  (taken from Reuter et al. (2018))

The first image of Figure 5 (b) presents the shear rate caused by the radial oscillation of the bubble just before the microjet impacted the surface. The flow stagnated flow underneath the bubble caused an almost negligible shear rate on the bottom surface. During the jet impact, the shear rates increased by a factor of 26, and they were radially distributed and limited to a certain radial distance. Shear rates during rebound were significant, and they traversed outward. Before the collapse, two annular rings, an inward and an outward ring, were formed. During the collapse of the toroid, maximum shear rates were computed with an annular ring traveling inward. The computed wall shear rates compared favorably to the experiments over all phases of the collapse although the shear rate distributions differed somewhat. The shear rate distributions obtained from the experiments were broader than those obtained from our computations. This could have been due to the fact that experimental shear rates were measured and averaged from several collapsing bubbles.

## 4 Conclusion

We considered the collapse of a single laser-induced bubble in the water near a solid surface. Our computed bubble collapses were similar to experimental ones. We found some minor disparities e.g. shape and counter jet, which our simulations could not be resolved. Computed physical features of collapsing bubble associated with jet formation, translation of regrowing cavity (for larger relative wall distances), toroid, and rebound of toroid are well reflected. Collapse times of first and second collapse were consistent with collapse times observed in experiments. Numerical simulations featured the flow around the micrometer-sized bubble especially, radially inward flow during bubble compression, radially outward flow during its second rebound, radially compressing flow during its second toroidal collapse, and vortices after its second collapse. These different flow types were consistent with previous experiments. A cavitation bubble collapse induced an intense micro-convection on the nearby bottom surface inducing wall shear rate. In our computations, these shear rates were noticeable during jet impact and toroidal collapse. The topography of the wall shear rate was consistent with the experiments. Computed wall shear rates were also quantitatively similar to

those measured in experiments. Overall, the presented numerical method is reliable where microscopic surface cleaning at a higher level of temporal and spatial precision is necessary by reducing efforts in experimental trials.

## 5 References:

- Arndt, R. E. A. (1981). Cavitation in Fluid Machinery and Hydraulic Structures. *Annual Review of Fluid Mechanics*, 13(1), 273–326. <https://doi.org/10.1146/annurev.fl.13.010181.001421>
- Besant, W. H. (1859). *Hydrostatics and Hydrodynamics*. Cambridge: Bell and Daldy.
- Fridman, V. M. (1972). The interaction mechanism between cavitation bubbles and particles of the solid and liquid phases. *Ultrasonics*, 10(4), 162–165. [https://doi.org/10.1016/0041-624X\(72\)90357-5](https://doi.org/10.1016/0041-624X(72)90357-5)
- Han, B., Köhler, K., Jungnickel, K., Mettin, R., Lauterborn, W., & Vogel, A. (2015). Dynamics of laser-induced bubble pairs. *Journal of Fluid Mechanics*, 771, 706–742. <https://doi.org/10.1017/jfm.2015.183>
- Ji, J., Wang, J., Li, Y., Yu, Y., & Xu, Z. (2006). Preparation of biodiesel with the help of ultrasonic and hydrodynamic cavitation. *Ultrasonics*, 44 Suppl 1, e411–4. <https://doi.org/10.1016/j.ultras.2006.05.020>
- Koch, M., Lechner, C., Reuter, F., Köhler, K., Mettin, R., & Lauterborn, W. (2016). Numerical modeling of laser generated cavitation bubbles with the finite volume and volume of fluid method, using OpenFOAM. *Computers and Fluids*, 126, 71–90. <https://doi.org/10.1016/j.compfluid.2015.11.008>
- Ma, X., Huang, B., Li, Y., Chang, Q., Qiu, S., Su, Z., ... Wang, G. (2018). Numerical simulation of single bubble dynamics under acoustic travelling waves. *Ultrasonics Sonochemistry*, 42, 619–630. <https://doi.org/https://doi.org/10.1016/j.ultsonch.2017.12.021>
- Miller, D. L., Pislaru, S. V., & Greenleaf, J. E. (2002). Sonoporation: mechanical DNA delivery by ultrasonic cavitation. *Somatic Cell and Molecular Genetics*, 27(1–6), 115–134. <https://doi.org/10.1023/A:1022983907223>
- Ming, L., Zhi, N., & Chunhua, S. (2017). Numerical simulation of cavitation bubble collapse within a droplet. *Computers & Fluids*, 152, 157–163. <https://doi.org/https://doi.org/10.1016/j.compfluid.2017.04.019>
- Mitchell, T. M., & Hammit, F. G. (1973). Asymmetric Cavitation Bubble Collapse. *Journal of Fluids Engineering*, 95(1), 29. <https://doi.org/10.1115/1.3446954>
- Naudé, C. F., & Ellis, A. T. (1961). On the Mechanism of Cavitation Damage by Nonhemispherical Cavities Collapsing in Contact With a Solid Boundary. *Journal of Basic Engineering*, 83(4), 648. <https://doi.org/10.1115/1.3662286>
- Ohl, C.-D., Arora, M., Dijkink, R., Janve, V., & Lohse, D. (2006). Surface cleaning from laser-induced cavitation bubbles. *Applied Physics Letters*, 89(7), 074102. <https://doi.org/10.1063/1.2337506>
- Parsons, C. A., & Cook, S. S. (1919). Investigations into the causes of corrosion or erosion of propellers. *Journal of the American Society for Naval Engineers*, Vol. 31, pp. 536–541. <https://doi.org/10.1111/j.1559-3584.1919.tb00807.x>
- Philipp, A., & Lauterborn, W. (1998). Cavitation erosion by single laser-produced bubbles. *Journal of Fluid Mechanics*, 361(1998), S0022112098008738. <https://doi.org/10.1017/S0022112098008738>
- Phillip, A., & Lauterborn, W. (1998). Cavitation Erosion by Single Laser-Produced Bubbles. *Journal of Fluid Mechanics*, 361, 75–116.
- Plesset, M. S., & Chapman, R. B. (1971). Collapse of an initially spherical Vapor Cavity in the Neighborhood of a solid Boundary. *Journal of Fluid Mechanics*, 47(2), 283–290. <https://doi.org/10.1017/S0022112071001058>
- Rayleigh, Lord. (1917). VIII. On the pressure developed in a liquid during the collapse of a spherical cavity. *Philosophical Magazine Series 6*, 34(200), 94–98. <https://doi.org/10.1080/14786440808635681>
- Reuter, F., Gonzalez-Avila, S. R., Mettin, R., & Ohl, C. D. (2017). Flow fields and vortex dynamics of bubbles collapsing near a solid boundary. *Physical Review Fluids*, 2(6). <https://doi.org/10.1103/PhysRevFluids.2.064202>
- Reuter, F., & Mettin, R. (2018). Electrochemical wall shear rate microscopy of collapsing bubbles. *Physical Review Fluids*, 3(6), 063601. <https://doi.org/10.1103/PhysRevFluids.3.063601>
- Reuter, F., Sagar, H., el Moctar, B., & Mettin, R. (2018). Wall shear rates induced by a single cavitation bubble collapse. *10th International Cavitation Symposium (Cav2018)*. Retrieved from <https://cav2018.jhu.edu/wp-content/uploads/Reuter-Fabian.pdf>
- Sagar, H., & el Moctar, O. (2018). Numerical simulation of a laser-induced cavitation bubble near a solid boundary considering phase change. *Ship Technology Research*, 65(3), 163–179. <https://doi.org/10.1080/09377255.2018.1473235>
- Sagar, H. J. (2018). *Numerical and experimental investigation of a laser induced cavitation bubble and damage on aluminum surface*. PhD Thesis (University of Duisburg-Essen). Retrieved from <http://nbn-resolving.org/urn:nbn:de:hbz:464-20181105-111935-5>
- Sagar, H. J., & el Moctar, O. (2020). Dynamics of a cavitation bubble near a solid surface and the induced damage. *Journal of Fluids and Structures*, 92. <https://doi.org/10.1016/j.jfluidstructs.2019.102799>
- Sagar, H. J., & el Moctar, O. (2020). Dynamics of a cavitation bubble near a solid surface and the induced damage. *Journal of Fluids and Structures*, 92, 102799. <https://doi.org/10.1016/j.jfluidstructs.2019.102799>
- Shukla, R. K. (2014). Numerical investigation of shock-induced bubble collapse near a rigid wall. *Proceedings of the IUTAM Symposium on Multiphase Flows with Phase Change: Challenges and Opportunities, Hyderabad, India*, 15, 158–164. <https://doi.org/10.1016/j.piutam.2015.04.022>
- Silberrad, D. (1912). Propeller erosion. *Engineering*, 33–35.
- Tomita, Y., & Shima, A. (1986). Mechanisms of impulsive pressure generation and damage pit formation by bubble collapse. *Journal of Fluid Mechanics*, 169(1), 535. <https://doi.org/10.1017/S0022112086000745>
- Walmsley, A. D., Laird, W. R. E., & Williams, A. R. (1988). Dental plaque removal by cavitation activity during ultrasonic scaling. *Journal of Clinical Periodontology*, 15(9), 539–543. <https://doi.org/10.1111/j.1600-051X.1988.tb02126.x>
- Ye, X., Yao, X.-L., Sun, L.-Q., & Wang, B. (2014). Cavitation bubble in compressible fluid near the rigid wall subjected to the acoustic wave with arbitrary incidence angle in three-dimensional. *Journal of Mechanics*, 31(03), 307–318. <https://doi.org/10.1017/jmech.2014.77>

# Validation of potential theory based resistance computations

Carsten Schumann

Ingenieurbüro SchiffsRat, Conventstr. 14, 22089 Hamburg, Germany

schumann@schiffsrat.de

## 1 Introduction

RANS-computations of resistance and propulsion become more and more a practical tool for hull and propeller design. Nevertheless, it will be shown that the "old" potential theory based methods are also still of practical use and sufficiently accurate. The validation is limited to model scale results because full scale resistance data is missing. The methods are rather suitable for full scale applications, though.

A potential flow program calculating the free surface flow around the bare hull is extended by features considering viscosity and appendages.

Most of the ideas and numerical tricks of the described method are based on Prof. Söding's publications.

## 2 Potential flow around the bare hull

The base method to compute the stationary potential flow is outlined in this section.

The boundary condition on the hull (no flux through it) is covered by Söding's patch method [1]. Here unstructured triangular meshes with nearly equilateral elements are generated with an advancing front algorithm. The hull geometry is described with an STL representation. One rim of the hull grid coincides with the wave contour on the hull. To every triangle (named patch) a point source is assigned which is slightly shifted towards inside the hull and the boundary condition is discretised in a way that the total flux over the triangle is zero. In very small hull areas (e.g. skegs) the sources are placed directly on the patch. After computing the flow potential, the velocity on a patch is found by numerical differentiation of the potentials at patch vertexes.

The applied boundary conditions at the free surface are the dynamic and the kinematic boundary condition. The wave elevation is defined as an explicit function based on the longitudinal and lateral coordinates. This formulation neglects spray and breaking waves. These conditions are solved on a quadrilateral mesh as depicted in figure 1. Point sources are located at a constant value above the free surface at still water level. The kinematic condition is fulfilled for every second element only (painted light blue in the figure) and the dynamic condition is satisfied at vertexes (marked green). To enforce the radiation condition the sources of the free surface (FS) grid are shifted one patch size downwind, simply by moving the sources of the head row behind the tail row of the grid (RHS in figure 1). Furthermore, the sources are shifted in lateral direction a quarter of the patch size towards the centreline. The boundary condition of FS vertexes located at the hull is not fulfilled at this point but is interpreted as the mean value

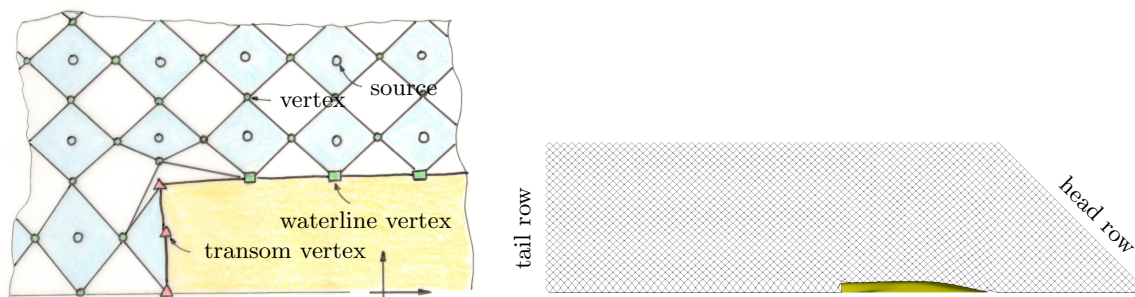


Figure 1: View on a typically free surface grid and hull, RHS; section near the transom stern, LHS

of one quarter of the attached patch. Therefore, the velocity is integrated over this sub patch solved partly analytical and partly numerical.

At a transom stern the boundary condition is defined as wave elevation being equal to the position of the transom edge (red triangles in figure 1).

This results in a large nonlinear system of equations with unknown source strengths and unknown wave elevation at FS vertexes. This approach is different to most of the known programs solving for source strength only but is very easy to program and maintain. It has also a very high numeric stability. These equations are solved iteratively with Newton's method. In every iteration step a new hull grid is created fitting the hull wave contour. In lateral direction the free surface grid vertexes are shifted on the hull grid.

Additionally, the dynamic trim and sinkage are accounted for and steep or breaking waves behind the stern are damped to avoid divergence.

### 3 Frictional force

For most ship types the frictional resistance is dominant over all other resistance components. Thus, this component has to be considered carefully and has to account for arbitrary rough surfaces because ships hull surfaces are rough. *Monty et. al.* [8] described a simple boundary layer method to compute the turbulent frictional resistance of a flat plate including roughness. Therefore, the input data "roughness function"  $\Delta U^+$  and roughness height  $k_s$  are needed. These values can be found for ship hull surfaces in *Schulz* [10]. Figure 2 shows the resistance coefficient for the boundary layer computation (BL) of a smooth surface and the well-known result of the Schoenherr friction line, see e.g. [3]. Additionally, friction lines for a containership (see section 5.4, DTC) are plotted in two conditions. "Typical newly applied anti-fouling coating" and "Deteriorated coating or light slime" have been chosen according to [10]. Dots are plotted for ship speeds between 15kn and 25kn.

For the characteristic velocity of a flat plate flow, the mean velocity on the hull surface is chosen. The characteristic length is set to the maximum wetted length. The hull force is integrated over the hull patches and the force on a patch is defined as

$$\vec{F} = C_{F0} \frac{1}{2} \rho \vec{U}_p |\vec{U}_p| S \quad (1)$$

with flat plate frictional resistance coefficient  $C_{F0}$ , local patch velocity  $\vec{U}_p$ , patch surface  $S$  and fluid density  $\rho$ .

With that, the real wetted surface, an appropriate velocity and the roughness is accounted for.

### 4 Appendages

Thruster openings, bilge keels, shaft lines with brackets and rudders are included by force coefficients considering the local flow characteristics on or near the hull.

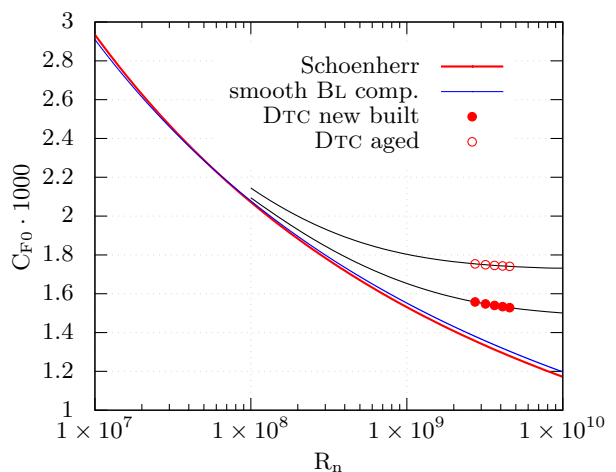


Figure 2: Frictional resistance coefficients of flat plates

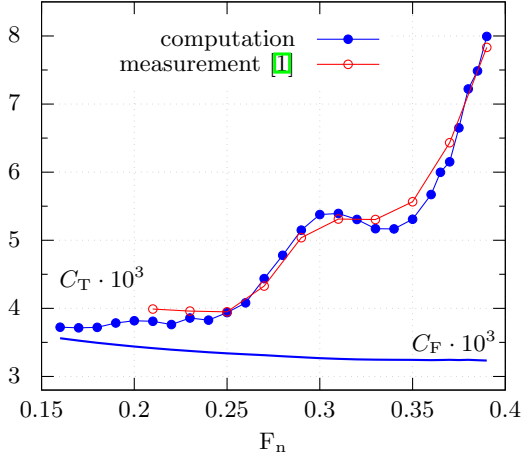


Figure 3: Total resistance coefficient of the Series 60 ship

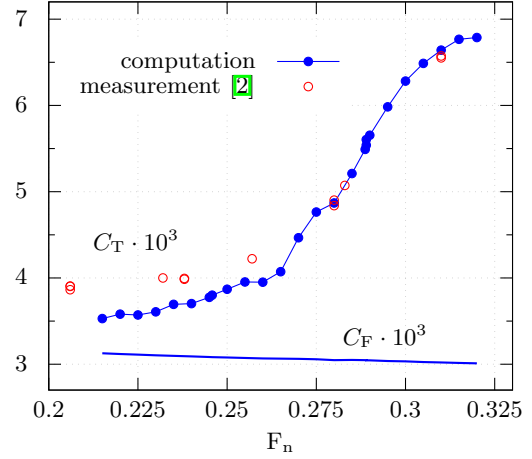


Figure 4: Total resistance coefficient of the Ville de Mercure

#### 4.1 Rudder

The rudder force is summed up by several strips chordwise (e.g. 10)

$$\vec{F} = (1 + k) C_{F0} \frac{1}{2} \rho \vec{U}_P |\vec{U}_P| S, \quad (2)$$

with local velocity  $\vec{U}_P$  at the rudder mean plane and wetted surface  $S$  of a strip. The frictional resistance coefficient  $C_{F0}$  is computed with the mean velocity and mean chord length of the rudder applying the mentioned friction line. The form factor  $k$  is approximated according to [15]  $k = 2 \delta_s + 60 \delta_s^4$  with the thickness ratio  $\delta_s$ .

#### 4.2 Thruster openings

The force on thruster openings acts in flow direction on the hull surface and is approximated with a resistance coefficient  $C_d$  based on the opening area and local flow velocity. Values in the range of  $0.004 < C_d < 0.01$  seem to be adequate [4]. The uncertainty of this force component is high and current measurements or computations are needed.

#### 4.3 Shaft lines

The total force on the shaft line is the sum of forces each acting on segments (e.g. 20) that also cover bearings and hoses by being varied in thickness. The flow at every segment is separated in two components: one in axial and one in normal direction  $\vec{U}_l$  and  $\vec{U}_n$  respectively. It is assumed that the normal component causes a force proportional to the resistance coefficient of a circular cylinder  $C_d = 1.2$ , see e.g. *Hoerner* [4]. In axial direction there are only frictional forces. The force on a segment is

$$\vec{F} = (1 + k) C_{F0} \frac{\pi}{2} \rho \vec{U}_l |\vec{U}_l| D l + C_d \frac{1}{2} \rho \vec{U}_n |\vec{U}_n| D l, \quad (3)$$

with frictional coefficient  $C_{F0}$  using the total length of the shaft line, the mean velocity along the shaft line and the hull friction line (section 3). The length of the segment is called  $l$ , the diameter of the segment is  $D$ . The form factor  $k$  takes into account bearings, hoses and the difference between plate flow and flow around a pipe, see e.g. *White* [14]. Appropriate values may be in the range of  $1.2 < k < 1.6$ .



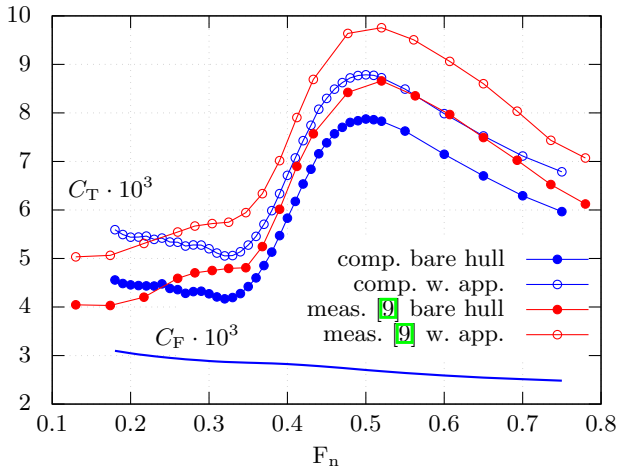


Figure 5: Total resistance coefficient of the D9 Series ship with and without appendages

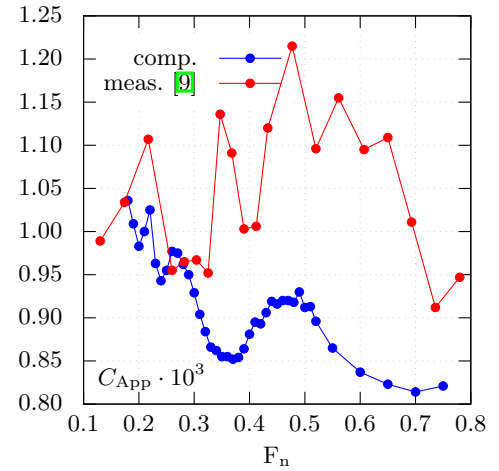


Figure 6: Appendage resistance coefficient of the D9 Series ship

#### 4.4 Shaft brackets

It is assumed that the brackets are aligned in flow direction. The resistance force is computed similar to that of rudders.

#### 4.5 Bilge keels

Bilge keel forces are computed with the same equation as the forces for shaft lines. In detail, the resistance coefficient for normal directed flow is set to  $C_d = 1.6$  due to sharper geometry. The mean flow velocity is approximated considering the hull boundary layer.

#### 4.6 Propeller hub

It is assumed that the flow separates at the aft edge of the propeller hub. The base pressure coefficient  $c_{pB}$  in the deadwater is found to be nearly unaffected by viscosity [5]. This resistance component can be significant for large controllable pitch propeller hubs, though.

### 5 Validation

Computational results and model tests of four different ship types with and without appendages are discussed in this section. To avoid the issue of separating resistance components the total resistance coefficient is compared only.

#### 5.1 Series 60

Computational results and measurements for a Series 60 ship [13] are plotted over the Froude number  $F_n$  in figure 3. The scale of the model was 30.48, the block coefficient was 0.6 and tests were carried out for the bare hull. The resistances agree well and the differences are less than 2%.

The frictional coefficient  $C_F$  due to the computed frictional force is shown in the lower part of the diagram and differs significantly from the ITTC57-value.

#### 5.2 Containership of the nineties

A more current example is a containership built in the 1990s [2], named Ville de Mercure. It has a transom stern and a bulbous bow; length is  $L_{PP} = 153.7\text{m}$ . These tests were carried out for the bare hull. Its scale was 24.

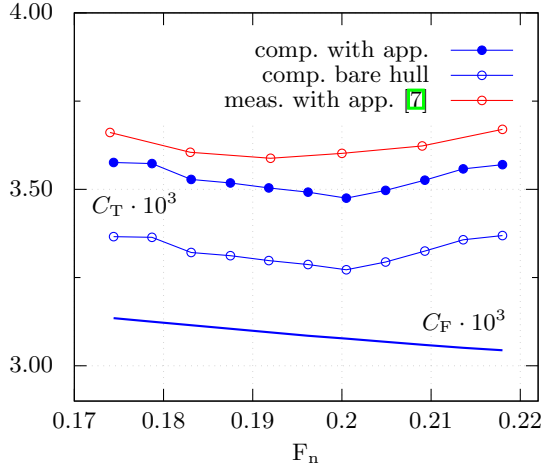


Figure 7: Total resistance coefficient of DTC

Figure 4 shows the comparison of the results: In the Froude number range of  $0.23 \leq F_n \leq 0.26$  measurement and computation differ about 6–10%. For larger Froude numbers measured and computed resistances are identical.

The following table 1 contains the results of a grid study for the Froude number  $F_n = 0.246$ . First the FS grid is refined independently from the hull grid and vice versa. The maximum resistance deviations are about  $\pm 0.7\%$  compared to the mean value.

no. patches on the hull	2200	2200	2200	2200	1200	3200	4200
no. patches on the Fs	820	900	1140	1510	820	820	820
no. vertexes at the Fs	1720	1880	2370	3120	1720	1720	1720
$C_T \cdot 10^3$	3.80	3.77	3.82	3.79	3.78	3.77	3.80

Table 1: Grid study, Ville de Mercure,  $F_n = 0.246$

### 5.3 D9 Series

This test case is a small fast twin screw vessel [9]; length is  $L_{PP} = 90\text{m}$ . It has a deeply emerged transom stern but no bulbous bow. Tests were carried out at the large circulation tank in Berlin; the scale of the model was 15. Test results are available for the bare hull condition and appended hull.

The comparison is given in figure 5. Differences between measurement and computation are in the range of 8–10%. The appendage resistance  $C_{App}$ , defined as difference between appended and bare hull resistance, is plotted in figure 6. The computed resistance coefficients of the appendages are not adjusted to meet the measurements. This will be done when more data are available.

Table 2 lists the relative appendage resistances for model and full scale condition. The full scale condition is a newly coated hull with no fouling [10].

appendages	fraction of res. in %	
	model	full scale
bilge keels	0.5	0.4
rudder	4.9	3.2
propeller hub	0.3	0.4
sum	5.7	4.0

Table 3: Resistance components of DTC;  $F_n = 0.218$

appendages	fraction of res. in %	
	model	full scale
shaft lines	3.0	2.5
I shaft brackets	0.4	0.2
V shaft brackets	1.0	0.7
rudders	5.0	3.4
propeller hubs	3.9	4.7
sum	13.3	11.5

Table 2: Resistance components of D9;  $F_n = 0.40$

## 5.4 Duisburg test case (DTC)

The DTC is a large containership [7] with a transom stern and a bulbous bow; length is  $L_{PP} = 355.0\text{m}$ . The model was fitted with a rudder having a rudder bulb, relatively small bilge keels and a propeller hub. The scale was 59.4.

The results are plotted in figure 7. The measured and computed resistances differ about 2-3%. A comparison of appendage resistances is listed in table 3 showing the fraction of appendages both for model and full scale condition.

## 6 Conclusion

The validation of the program results in moderate to good agreement with the model tests. It is expected, though, that the comparison with full scale tests would show better agreement because the viscosity effects are smaller. Having in mind the inaccuracy of model testing (considering roughness, Reynolds effects of appendages, Froude hypothesis defining the residual resistance) it is my opinion that the proposed method provides comparable accuracy to model tests and resistance extrapolation.

Work in progress are two dimensional boundary layer computations considering pressure gradients and vortex lattice computations of propeller and rudder. These results will be presented at the NuTTS 2021 conference.

The described program is part of the Uthlande software package<sup>1</sup> and can easily be applied with a graphical user interface.

## References

1. Bertram V.: Numerische Schiffshydrodynamik in der Praxis; Institut für Schiffbau der Universität Hamburg, Bericht Nr. 545, September 1994.
2. Bertram V., Chau K.Y., Lammers G., Laudan J.: Entwicklung und Verifikation numerischer Verfahren zur Antriebsleistungsprognose von Schiffen – Phase 2; HSVA-Bericht 1597, Oktober 1992.
3. Eça L., Hoekstra M.: The numerical friction line; J. Mar. Sci. Technol. 2008.
4. Hoerner S.F.: Fluid-Dynamic Drag; 1965.
5. Hucho W.-H.: Aerodynamik stumpfer Körper; Vieweg+Teubner Verlag 2011.
6. Jiménez J.: Turbulent Flows Over Rough Walls; Annu. Rev. Fluid Mech. 2004.
7. el Moctar B., Shigunov V., Zorn T.: Duisburg Test Case: Post-Panmax Container Ship for Benchmarking; Ship Technology Research, Schiffstechnik, Vol. 59, No. 3, August 2012.
8. Monty J.P., Dogan E., Hanson R., Scardino A.J., Ganapathisubramani B., Hutchins N.: An assessment of the ship drag penalty arising from light calcareous tubeworm fouling; Biofouling 2015.
9. Schmiechen M., Kracht A.: Erweiterung der D-Serie: Breite, schnelle Zweischaubenschiffe; Bericht 1267/96 der Versuchsanstalt für Wasserbau und Schiffbau, Berlin 1996.
10. Schultz M.P.: Effects of coating roughness and biofouling on ship resistance and powering; Biofouling, 2007, 23(5).
11. Söding H.: A Method for Accurate Force Calculations in Potential Flow; Schiffstechnik Bd. 40, 1993.
12. Söding H.: Resistance Decrease by Computer-Aided Hull Shape Improvements, Proc. HIPER 2001.
13. Todd F.H., Stuntz G.R., Pien P.C.: Series 60 – The Effect upon Resistance and Power of Variation in Ship Proportions; SNAME Transactions Volume 65, 1957.
14. White F. M.: viscous fluid flow; McGraw-Hill 1974.
15. The Specialist Committee on Azimuthing Podded Propulsion; Proceedings of 25th ITTC - Volume II, Fukuoka 2008.

---

<sup>1</sup>Homepage <https://www.uthlande.org>

# CFD Prediction of Cavitation Inception on Marine Propellers

Keun Woo Shin\*, Jens Ring Nielsen\* and Poul Andersen†

\*MAN Energy Solutions, Frederikshavn/Denmark,

†Technical University of Denmark (DTU), Kgs. Lyngby/Denmark

keun.shin@man-es.com

## 1 Introduction

It is desirable to predict the cavitation inception speed in designing marine propellers, because cavitation-free sailings are often required for special-purpose ships engaged in research, survey and military operations, as noise signals are amplified by cavitating flows. Hull pressure pulses can be significantly reduced by delaying cavitation inception, which results in an improvement of cargo safety and passenger comfort on general cargo and passenger ships.

Sheet cavitation inception on the suction side of a propeller blade can be predicted with acceptable accuracy by computationally efficient numerical methods like potential flow approaches. Tip vortex cavitation (TVC) is often the first propeller cavitation type observed at the lowest inception speed. Turbulent viscous flow simulations show better accuracy in considering TVC, especially on a complex blade geometry e.g. with a highly skewed or raked tip.

A CFD cavitation simulation is made on a highly skewed propeller at the cavitation inception speed obtained from a cavitation tunnel test. A threshold cavity volume for the cavitation inception is determined by the comparison between the CFD and experimental results. A new propeller is designed by modifying the blade tip geometry. The blade tip geometry is optimized by a simplified CFD approach for improving the propulsive efficiency and delaying the cavitation inception. The cavitation inception speed for the new design is estimated by repeating cavitation simulations until reaching close to the threshold value.

## 2 CFD setup

Unsteady cavitation simulations are made by the DES solver of the commercial CFD software StarCCM+ with the interphase mass transfer model of Schnerr and Sauer (2001). Multiphase flows are modelled by a single-fluid Eulerian approach of VOF method.

As shown in Fig. 1, CFD is made on a propeller and a rudder in a cylindrical fluid domain axially extending  $3\cdot D$  from the propeller plane to the inlet and  $6\cdot D$  to the outlet with a radial extent of  $4\cdot D$ , where  $D$  is the propeller diameter. An inner cylindrical subdomain axially extending  $0.25\cdot D$  from the propeller plane upstream and downstream with a radial extent of  $0.6\cdot D$  is defined around the propeller for modeling propeller rotations by the rigid body motion.

A trimmed hexahedral grid is prepared for the volumetric grid of the fluid domain. Prism-layer grid is applied to the wall surface region, which results in  $y^+ \leq 1$  on average. The surface grid size is set to  $\Delta x = 0.1\% \cdot D - 0.2\% \cdot D$  on the overall surface of the blade and hub and it is refined to  $\Delta x = 0.05\% \cdot D - 0.1\% \cdot D$  along the blade edges. The volumetric grid at the outer-radius region of  $0.8\cdot R - 1.0\cdot R$  is refined to having a consistent fine grid of  $\Delta x = 0.1\% \cdot D$ .

The nominal hull wake field measured in a towing-tank test is applied to the propeller inflow instead of including a hull model. The axial wake is applied to an inlet boundary and the transverse wake is modeled by momentum sources applied upstream from the propeller outside the rotating subdomain (Shin et al 2015). Momentum source strengths are calibrated by numerical tests without a propeller

model. Cavitation simulations in hull wake fields have been validated against experimental results for different types of propeller cavitation (Shin & Andersen 2015).

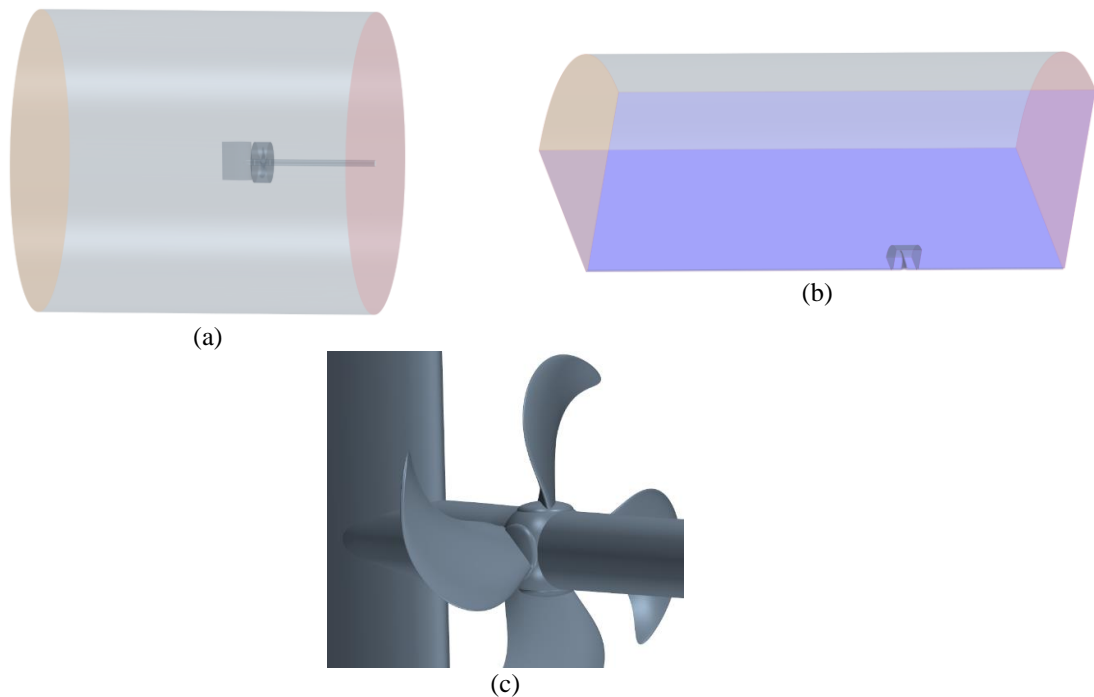


Fig. 1: (a) Cylindrical fluid domain for cavitation simulations, (b) Quarter-cylinder fluid domain for steady simulations in the design optimization, (c) Propeller and rudder models for cavitation simulations

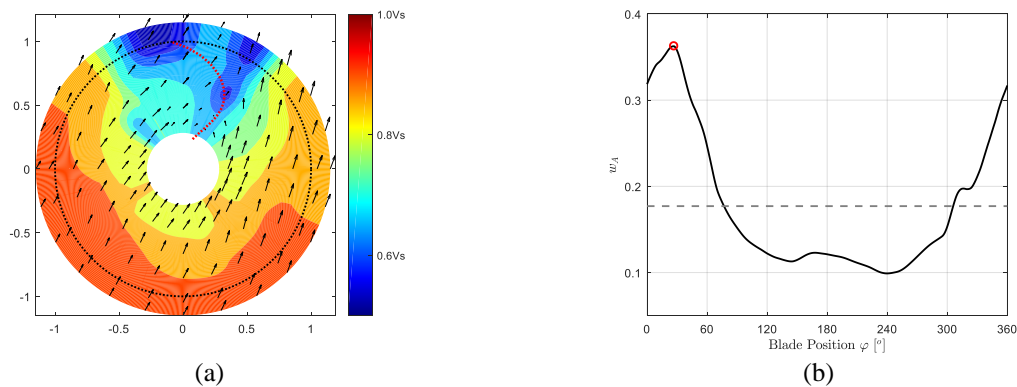


Fig. 2: (a) Nominal hull wake field, (b) Axial wake averaged along the mid-chord locus at different blade positions

Unsteady cavitation simulations are made with a full hull wake model, whereas the hull wake model is simplified to be circumferentially uniform and radially vary for representing a specific blade position in CFD for the blade tip optimization (Shin & Andersen 2018).

It is not efficient in terms of computational effort to use unsteady cavitation simulations in a propeller design optimization for considering hundreds of different designs. For the optimization, steady RANS simulations are made on a single blade with the periodic boundary condition in a quarter-cylinder domain (See Fig. 1(b)) as a computationally efficient approach taking about 1/60 of the computational time of an unsteady cavitation simulation.

### 3 Cavitation simulation

First, a cavitation simulation is made on the baseline propeller design with a straight tip at the cavitation inception speed  $V_{S,Inc0}$  obtained from experiments, which have been conducted in the large cavitation tunnel of SSPA located in Gothenburg, Sweden including a whole hull model. In Fig. 3, the cavitation patterns on the baseline propeller are compared between the experimental and CFD results. In CFD, cavitation interfaces defined by the iso-surfaces of vapor volume fractions  $\alpha_v = 0.1$  and  $0.5$  are indicated by light and dark blue contours, respectively.

CFD shows a reasonable agreement in the overall TVC extent with the experimental result at the blade positions of  $\varphi = 20 - 80^\circ$ . TVC in CFD starts earlier from the leading edge of a more inner radius than in the experiment. The extent of TVC is shorter and it is weakened to disappear earlier.

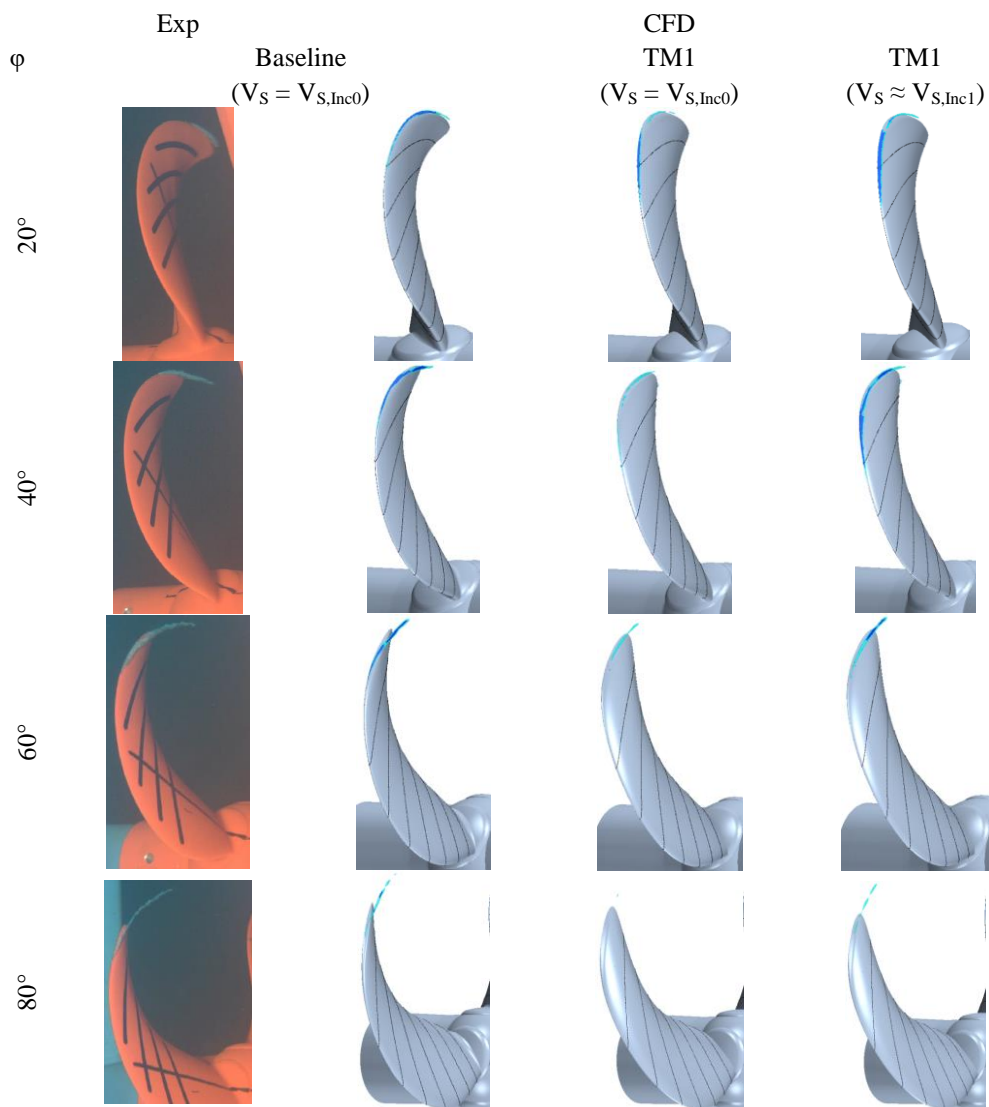


Fig. 3: Suction-side cavitation for the baseline and tip-modified propellers in the cavitation tunnel test and CFD with the full hull wake model

The variation of single-blade thrust coefficient  $K_{T,1Blade}$  from CFD is presented in Fig. 4(a). When comparing to the variation of axial wake averaged along the mid-chord locus in Fig. 2(b), the thrust peak is shown earlier than the axial wake peak, because the thrust loading is higher at the leading edge than at the mid chord.

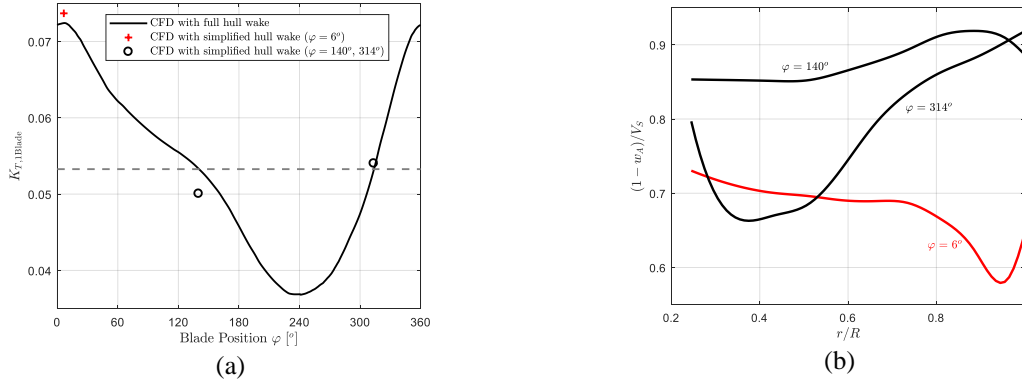


Fig. 4: (a) Variation of single-blade thrust coefficient, (b) axial wake distribution along the mid-chord locus at  $\varphi = 6^\circ, 140^\circ, 314^\circ$

The blade tip geometry is optimized based on steady CFD simulations with simplified hull wake models. A tip-modified blade design TM1 showing the largest reduction of the tip vortex volume is selected and a cavitation simulation is made on it at  $V_S = V_{S,Inc0}$ . In Fig. 3, TVC indicated by the dark blue is significantly reduced on TM1 compared to the baseline design, whereas the sheet cavitation at the leading edge of  $0.9 \cdot R$  is increased at  $\varphi = 0 - 20^\circ$ .

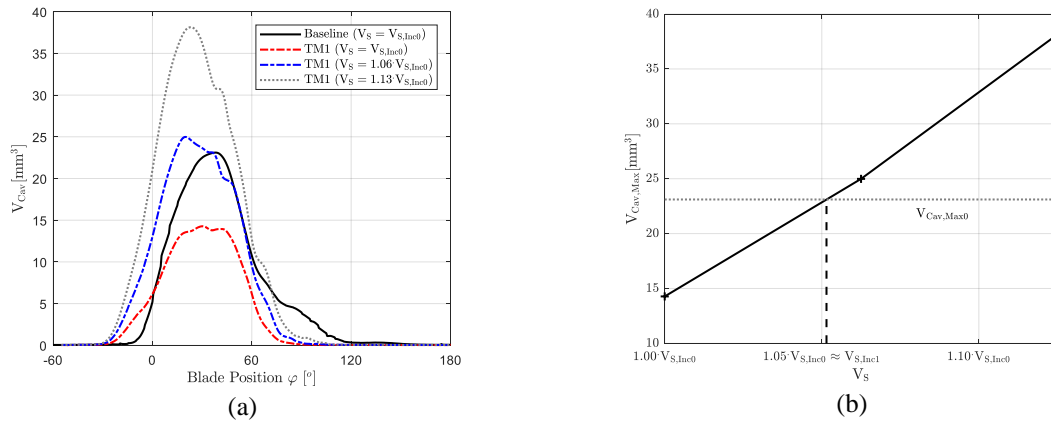


Fig. 5: (a) Variation of cavity volume around a blade with respect to the blade position, (b) Maximum cavity volume with respect to the ship speed for TM1

When comparing the variation of the cavity volume around a blade in Fig. 5(a), the maximum cavity volume  $V_{Cav,Max}$  for TM1 is 38% lower at the same value of  $V_S$ . Cavitation simulations are repeated on TM1 for the conditions corresponding to 6% and 13% higher ship speeds than  $V_{S,Inc0}$ .  $V_{Cav,Max}$  for TM1 at  $V_S = 1.06 \cdot V_{S,Inc0}$  and  $1.13 \cdot V_{S,Inc0}$  is larger by 8% and 65%, respectively, than for the baseline design at  $V_S = V_{S,Inc0}$ .

$V_{Cav,Max0} = 23 \text{ mm}^3$  on the baseline design at  $V_S = V_{S,Inc0}$  is assumed to be a threshold value for the cavitation inception. When interpolating  $V_{Cav,Max}$  for TM1 with respect to the ship speed as shown in Fig. 5(b), it is the same as  $V_{Cav,Max0}$  at  $V_S \approx 1.05 \cdot V_{S,Inc0}$  and so the cavitation inception speed for TM1 is estimated to be 5% higher than for the baseline design i.e.  $V_{S,Inc1} \approx 1.05 \cdot V_{S,Inc0}$ , where  $V_{S,Inc0}$  and  $V_{S,Inc1}$  are the cavitation inception speeds for the baseline and TM1, respectively.

#### 4 Blade tip optimization

The parameterized tip shape is optimized by a constrained heuristic optimization algorithm (Rao 2009) based on CFD simulations with a simplified hull wake model for maximizing an objective function

consisting of the tip vortex volume reduction  $-\Delta V_{TV}$  and the efficiency gain  $\Delta\eta$  compared to the baseline design. Simplified hull wake models are prepared for three blade positions showing the maximum and mean values of  $K_{T,1Blade}$  in CFD with the full hull wake.

When CFD is made with the simplified hull wake models, the differences in  $K_{T,1Blade}$  from CFD with the full hull wake are smaller than 2% for  $\varphi = 6^\circ$  &  $314^\circ$ , as shown in Fig. 4(a). The simplified hull wake models of  $\varphi = 6^\circ$  &  $314^\circ$  shown in Fig. 6 are adopted for estimating tip vortex volume and efficiency, respectively, in the tip geometry optimization. The tip vortex volume is defined by a Q-criterion iso-surface to be equal to the maximum cavity volume from CFD with the full hull wake.

Over 800 tip-modified blade designs are considered and two steady RANS simulations are made on each design. The result is summarized in Fig. 7. An approximate Pareto front is formed at the bottom right-hand side corner along TM2 – 4. More designs are located at the bottom side of the Pareto front rather than at the right-hand side, because the objective function has a higher weight on  $-\Delta V_{TV}$ .

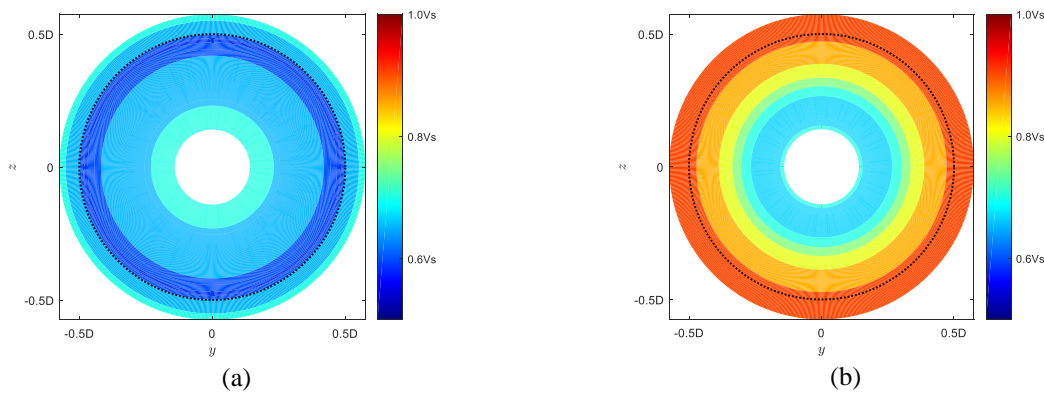


Fig. 6: Simplified hull wake models for (a)  $\varphi = 6^\circ$  and (b)  $\varphi = 314^\circ$

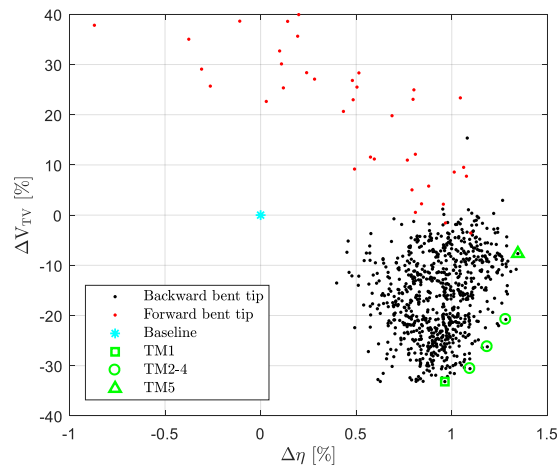


Fig. 7: Efficiency gain and tip vortex reduction for tip-modified propellers compared to the baseline propeller

The red and black dots are blade designs with tips bent forward and backward, respectively. The designs with a tip bent backward i.e. towards the pressure side of the blade show tip vortex reductions and positive efficiency gains, whereas the designs with a forward bent tip show tip vortex increases. TM1 shows the largest tip vortex reduction of  $\Delta V_{TV} = -33.2\%$  with  $\Delta\eta = 0.96\%$ . TM5 shows the highest efficiency gain of  $\Delta\eta = 1.3\%$  with  $\Delta V_{TV} = -7.7\%$ .



The cavitation simulation made on TM1 with the full hull wake model shows 38% reduction of the maximum cavity volume, which is larger than 33.2% reduction of the tip vortex volume in CFD with the simplified wake model probably due to the convection of cavity bubbles taken into account by the cavitation model.

## **7 Conclusion**

CFD with a simplified hull wake model is an efficient way to optimize the propeller blade geometry with considering characteristic hull wake flows. When the blade tip geometry of a propeller on a twin-screw ship is optimized for delaying the TVC inception and improving the propulsive efficiency, it shows 5% increase of the cavitation inception speed and almost 1% efficiency gain compared to a state-of-the-art propeller design.

The cavitation simulation with a full hull wake model is validated against a cavitation tunnel test result. The maximum cavity volume from the cavitation simulation at the cavitation inception speed obtained in the cavitation tunnel test is set to the threshold value. The cavitation inception speed of the modified propeller design with the optimized tip geometry is estimated by interpolating maximum cavity volumes in several cavitation simulations at different ship speeds.

## **References**

- S.S. Rao (2009). Engineering optimization theory and practice, Wiley
- G.H. Schnerr & J. Sauer (2001). Physical and numerical modeling of unsteady cavitation dynamics. Proceedings of 4th International Conference on Multiphase Flow (ICMF2001), New Orleans, LA, USA
- K.W. Shin & P. Andersen (2015). CFD analysis of cloud cavitation on three tip-modified propellers with systematically varied tip geometry. Proc. of 9<sup>th</sup> Int. Symp. on Cavitation (CAV2015), Lausanne, Switzerland
- K.W. Shin & P. Andersen (2018). Simplified CFD approach for simulating propeller flows in ship wake fields. Proceedings of 21<sup>st</sup> Numerical Towing Tank Symposium (NuTTS'18), Cortona, Italy
- K.W. Shin, P.B. Regener & P. Andersen (2015). Methods for cavitation prediction on tip-modified propellers in ship wake fields. Proc. of 4th International Symposium on Marine Propulsors (SMP'15), Austin, TX, USA

# DYNAMIC STABILITY ANALYSIS OF A SHIP AT HIGH FORWARD SPEED IN CALM WATER

Hendrik Simonis<sup>1</sup>, Patrick Marleaux<sup>2</sup>, Moustafa Abdel-Maksoud<sup>2</sup>, Norbert Stuntz<sup>1</sup>

hendriksimonis@bundeswehr.org, patrick.marleaux@tuhh.de, m.abdel-maksoud@tuhh.de, norbertstuntz@bundeswehr.org

<sup>1</sup>Bundeswehr Technical Center for Ships and Naval Weapons, Maritime Technology and Research

<sup>2</sup>Institute of Fluid Dynamics and Ship Theory, Hamburg University of Technology

## 1. INTRODUCTION

The dynamic stability of a ship can become more and more of an issue as the ship speed increases. While many different forms of dynamic instability are known, often very little is known about their cause and only a limited amount of research exists [1]. Therefore, an incident of dynamic instability observed during model tests of a semi-displacement vessel in calm water [2] is investigated. The incident occurred at a very high Froude number of  $Fn = 0.9$ , see Fig. 1. Despite of the restrain by the gimbal yaw and sway motions develop followed by a roll motion in the end.

First the approach used here is outlined. The numerical method and its extensions to consider sway, roll and yaw motions are introduced briefly. Then the computations carried out are described. Afterwards, the obtained results are presented and discussed.

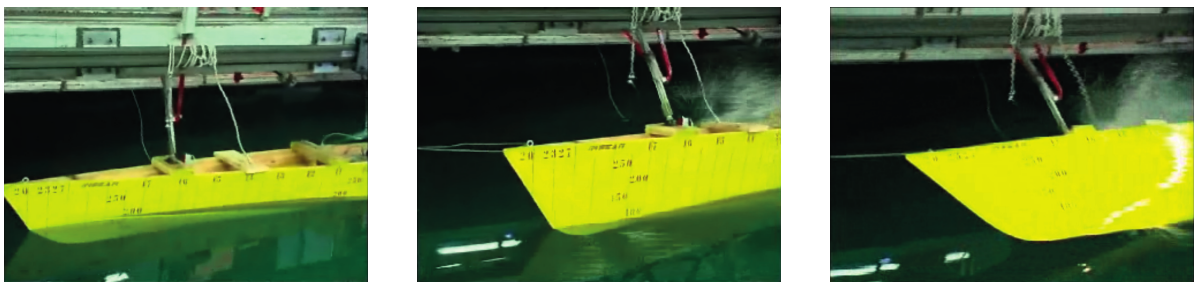


Figure 1 - Calm water broaching incident observed during experiments by Lugni et al. [2].

## 2. APPROACH

A nonlinear 2D+t method is extended and used to compute free sway, roll and yaw motions of the vessel. In such a method the three dimensional flow around the ship is replaced by several two-dimensional flows in earth-fixed transverse cross planes, see Fig. 2. The time development of the two dimensional flows caused by the ship advancing through these transverse cross planes is computed. This approach simplifies the computations significantly and is appropriate for fast and slender ships. The two-dimensional flows are treated as fully nonlinear potential flows. This means that viscous effects are neglected and that boundary conditions are kept in their nonlinear form and fulfilled on the instantaneous wetted hull and free surface. Therefore, most of the nonlinear effects can be taken into account. A boundary element method (BEM) is used to calculate the flow in each cross plane numerically. Using a BEM only the boundaries of each cross plane have to be discretised. This is done using linear elements.

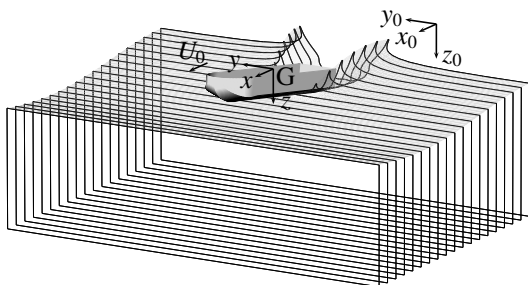


Figure 2 - Principle of the employed 2D+t method.

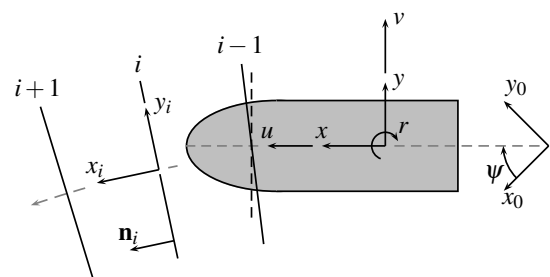


Figure 3 - Used coordinate systems.

A linear system of equations can then be set up and solved. Afterwards, the boundary conditions, which apply at the free surface, can be evaluated and used to step the free surface forward in time. This approach is called Mixed Euler-Lagrange (MEL) approach. Furthermore, the forces acting on the vessel can be computed from the flow solution and used to calculate the motions of the vessel. Simonis et al. [4] provide a more detailed description of the method and use it to analyse the heave and pitch motions of a fast semi-displacement vessel in head waves.

Here, the method is extended in such a way that also sway, roll and yaw motions can be considered. An earth-fixed coordinate system  $x_0y_0z_0$  is used in the following, see Fig. 2. This can be related to a ship-fixed coordinate system  $x_0'y_0'z_0'$  by the Euler angles  $\varphi$  (roll),  $\theta$  (pitch) and  $\psi$  (yaw). Furthermore, a coordinate system  $xyz$  is used, which has its origin at the ship's center of gravity  $G$  and follows its yaw motion but not its pitch and roll motions, see Fig. 3. While quantities used in manoeuvring theory often refer to a ship-fixed system, they will be referring to the  $xyz$  coordinate system used here in the following. Furthermore, sometimes simplifications will be made in the following, because only small transverse velocities are dealt with.

As the ship moves forward, cross planes are constantly added in front of the ship and discarded behind it. In order to also consider yaw motions, the sections are added in such a way that they are perpendicular to the instantaneous orientation of the ship's longitudinal axis, which correlates with the unit vector  $\mathbf{i}$  in the  $x$ -direction. Their current yaw velocity is also considered, so that the angle between the normal vector  $\mathbf{n}_i$  of the section and  $\mathbf{i}$  remains small while the ship advances through the section. The flow in that section is solved in a local (earth-fixed)  $x_iy_iz_i$  coordinate system, where the index  $i$  denotes the section number. Afterwards the pressures can be computed and the sectional forces are obtained by first projecting the section to a plane at a certain longitudinal location  $x$  which is perpendicular to  $\mathbf{i}$  (see section  $i - 1$  and the corresponding projected section denoted by a dashed black line in Fig. 3) and integrating the pressure afterwards. The total forces are then computed by integrating the sectional forces in the  $x$  direction.

In the analysis presented here, constant sway and yaw velocities are considered first and the results for transverse forces are compared to numerical results computed using a RANS method. Then the 2D+t method is used to calculate the free sway and yaw motions, which develop from a small initial disturbance in terms of an initial sway velocity, while the vessel is advancing at constant forward speed in calm water. Additionally, the 2D+t method is used to compute linear force coefficients in sway and yaw. These are used to solve the linearised equations of motion in sway and yaw. Furthermore, the computed coefficients are used to evaluate a yaw stability criterion. The influence of roll is also touched upon.

### 3. RESULTS

The main dimensions and most important properties of the model used in the experiments by Lugni et al. [2] are listed in Table 1. The values marked by a \* were not provided by Lugni et al. [2] and are taken from Ommani [3], who also investigated the dynamic stability of this model using a linear 3D BEM. In Fig. 4 its body plan is shown. The model is actually a demi-hull of a catamaran, which may explain its quite small beam-to-draft ratio  $B/D$ . Since the interaction of the demi-hulls was one of the aspects studied by Lugni et al. [2], they were also tested as monohulls. They also obtained values for running trim and sinkage, which are used in the computations presented here to prescribe the equilibrium running attitude. All computations are carried out in model scale.

First, the ability of the method to compute transverse forces resulting from small sway and yaw motions is studied. Fig. 6 shows the non-dimensional sectional transverse forces  $dY'/dx'$  for steady sway and yaw for two different Froude numbers  $F_n = U_0/\sqrt{gL}$ , where  $U_0$  denotes the constant forward speed in the  $x$ -direction. Furthermore,  $Y' = Y/(\rho U_0^2 LD/2)$  is the total non-dimensional transverse force in the  $y$ -direction and  $x' = x/L$ . The

Length $L$ [m]	25
Beam $B$ [m]	2
Draft $D$ [m]	1.75
Displaced volume $\nabla$ [m <sup>3</sup> ]	40.48
Roll gyradius $k_{xx}$ [m]	0.6125*
Yaw gyradius $k_{zz}$ [m]	6.5*
Longitudinal COG $LCG$ [m]	10.8
Vertical COG $VCG$ [m]	1.35*
Model scale factor $\lambda$ [-]	6.25

**Table 1 - Vessel properties.**

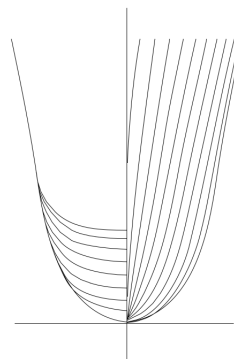


**Figure 4 - Body plan of the vessel.**

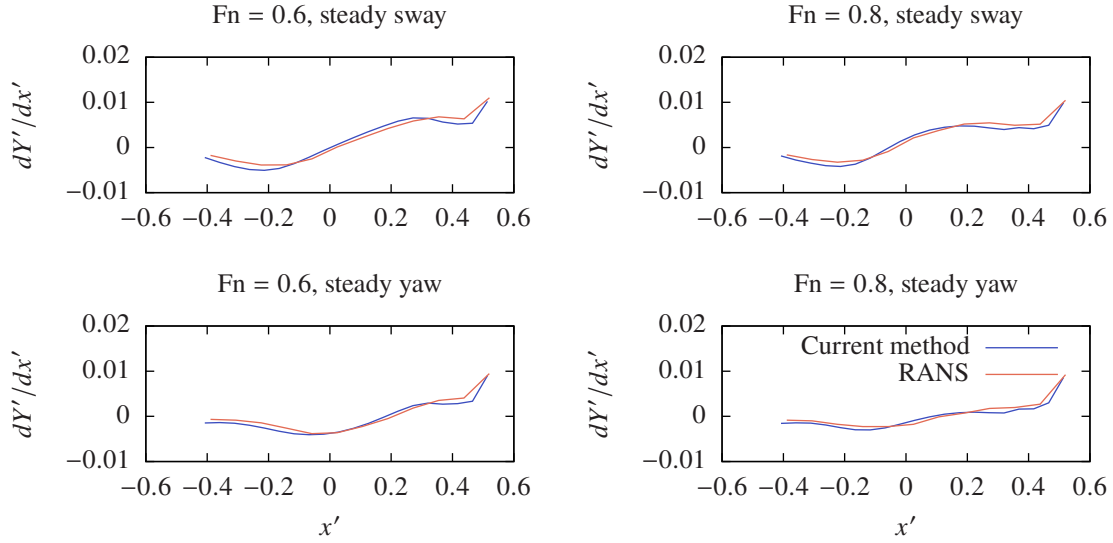


**Figure 6 - Sway force distribution for steady sway and yaw motions and two different forward speeds.**

non-dimensional sway velocity is chosen according to  $v/U_0 = -0.0087$  corresponding to a drift angle of  $\beta = 0.5^\circ$  and the non-dimensional yaw velocity is chosen as  $rL/U_0 = -0.0080$ , leading to similar transverse velocities observed at the bow. The convergence with respect to element size and time step size was checked.

The results of the method presented here are compared to results obtained using the RANSE solver STAR-CCM+. This solver employs a finite-volume method to solve the Reynolds-averaged Navier-Stokes (RANS) equations. In the simulations carried out here, turbulence is modeled using the  $k\omega$ -SST turbulence model with wall function treatment. This was considered acceptable due to the small transverse velocities dealt with here. The grid for the simulations is adjusted iteratively, so that the dimensionless wall distance  $y^+$  takes values between 40 and 100 on boundaries on which friction is considered (no-slip walls), i.e. the hull. To capture the free surface a Volume of Fluid (VoF) method is utilised. The time marching procedure is selected to be first-order accurate. Convective and viscous fluxes are handled with second-order accuracy in space.

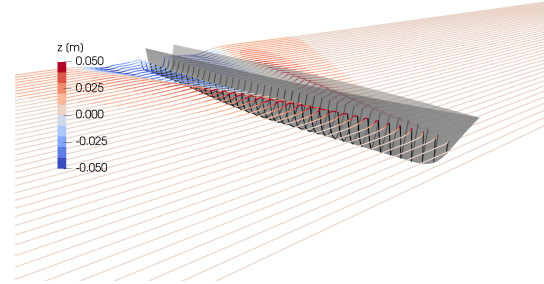


**Figure 5 - Simulation of the model at  $Fn = 0.6$  having a constant sway velocity using the presented 2D+t method.**

The distribution of the transverse force is similar for both sway and yaw motions and the two considered Froude numbers. The agreement between the current method and the RANS method appears satisfactory. Deviations mainly seem to occur where the local minima near the bow and in the aft half of the model are. In both cases the current method underestimates the forces. Separation effects are known to influence the force distribution in such a way that most of the transverse momentum is retained in the fluid in the aft half of the vessel, which leads to smaller negative forces. If the transverse forces are computed using slender body theory, the aft half is therefore often excluded from the integration of the sectional forces to some extent [6]. However, the agreement seems to improve for the higher Froude number, which could indicate the importance of accounting for the elevation of the free surface along the hull due to the steady flow caused by the forward speed. This is generally better captured by the current method the higher the Froude number is [1]. Söding [5] recommends accounting for the steady wave field for higher Froude numbers if transverse forces are computed using slender body theory. Fig. 5 shows a screenshot of the simulation at  $Fn = 0.6$  considering a constant sway velocity. It can be seen that the sectional drafts are influenced by the flow around the hull.

Next, the method is used to compute linear hydrodynamic coefficients  $Y'_v$ ,  $Y'_r$ ,  $N'_v$  and  $N'_r$ , where  $N$  refers to the yaw moment. As indicated above, the non-dimensional forms are obtained by dividing the transverse forces by  $\rho U_0^2 L D / 2$  and the yaw moment by  $\rho U_0^2 L^2 D / 2$ . The coefficients are obtained from simulations of either an

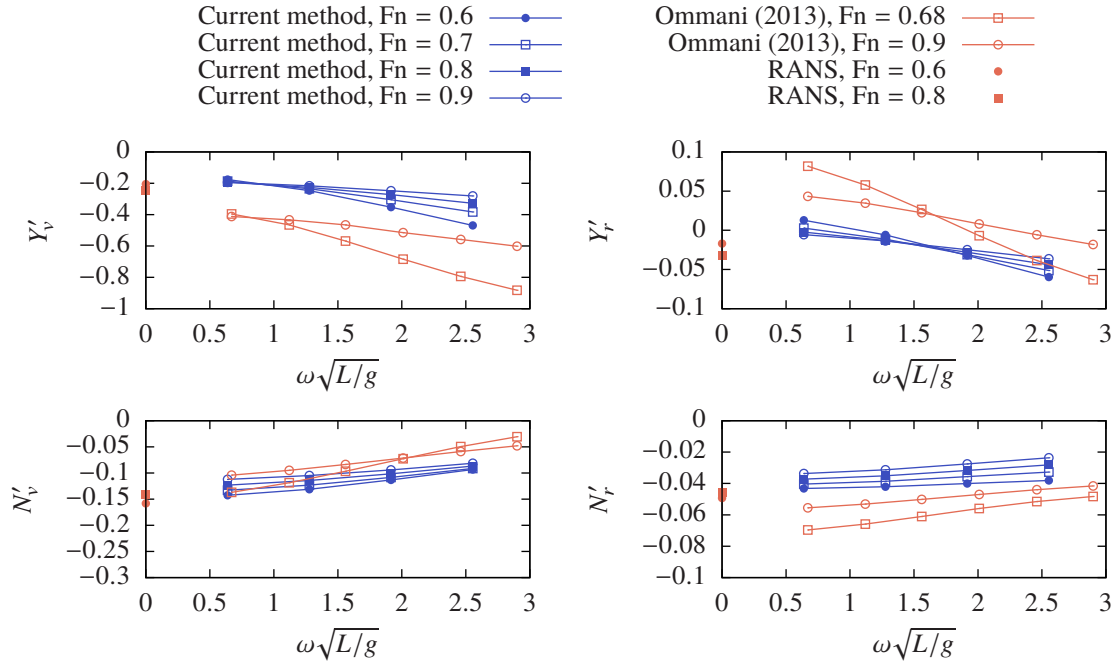


**Figure 7 - Computed damping coefficients for sway and yaw.**

oscillatory sway motion or an oscillatory yaw motion. Afterwards,  $Y$  and  $N$  can be expanded into a Fourier series and  $Y_v$ ,  $Y_r$ ,  $N_v$  and  $N_r$  and also  $Y_{\dot{v}}$ ,  $Y_{\dot{r}}$ ,  $N_{\dot{v}}$  and  $N_{\dot{r}}$  may be computed from the first-order Fourier coefficients. The results are presented in Fig. 7 together with the results obtained by Ommani [3] and the results from RANS computations discussed before. Ommani [3] used a linear 3D BEM and simplified the shape of the vessel to that of a surface piercing flat plate. Although the absolute values differ, the two methods show a very similar dependence regarding frequency  $\omega$  and speed  $U$ . The 2D+t method seems to agree better with the results obtained using the RANS method. This could indicate that accounting for the steady flow and the actual shape is of importance, as also noted by Ommani [3].

The hydrodynamic coefficients appear in the linearised equations of motion in sway and yaw. They may be written as

$$m\dot{v} + mUr = Y = Y_v v + Y_r r + Y_{\dot{v}} \dot{v} + Y_{\dot{r}} \dot{r} \quad (1)$$

$$I_{zz} \dot{r} = N = N_v v + N_r r + N_{\dot{v}} \dot{v} + N_{\dot{r}} \dot{r} \quad (2)$$

or using matrix vector notation as

$$\mathbf{M}\dot{\boldsymbol{\nu}} + \mathbf{D}\boldsymbol{\nu} = \mathbf{0}, \quad (3)$$

where

$$\mathbf{M} = \begin{bmatrix} -Y_{\dot{v}} + m & -Y_{\dot{r}} \\ -N_{\dot{v}} & -N_{\dot{r}} + I_{zz} \end{bmatrix} \quad \mathbf{D} = \begin{bmatrix} -Y_v & -Y_r + mU \\ -N_v & -N_r \end{bmatrix} \quad \boldsymbol{\nu} = \begin{bmatrix} v \\ r \end{bmatrix}.$$

Eq. (3) is solved by assuming

$$\boldsymbol{\nu} = \hat{\boldsymbol{\nu}} e^{\lambda t}, \quad (4)$$

which leads to an eigenvalue problem. After inserting Eq. (4) into Eq. (3) the eigenvalues  $\lambda$  can be determined from

$$\det(\lambda \mathbf{M} + \mathbf{D}) = A\lambda^2 + B\lambda + C = 0. \quad (5)$$

Generally,

$$\lambda = \delta + i\omega. \quad (6)$$

The general solution is then given by

$$\boldsymbol{\nu} = \sum_j c_j \hat{\boldsymbol{\nu}}_j e^{\lambda_j t}, \quad (7)$$

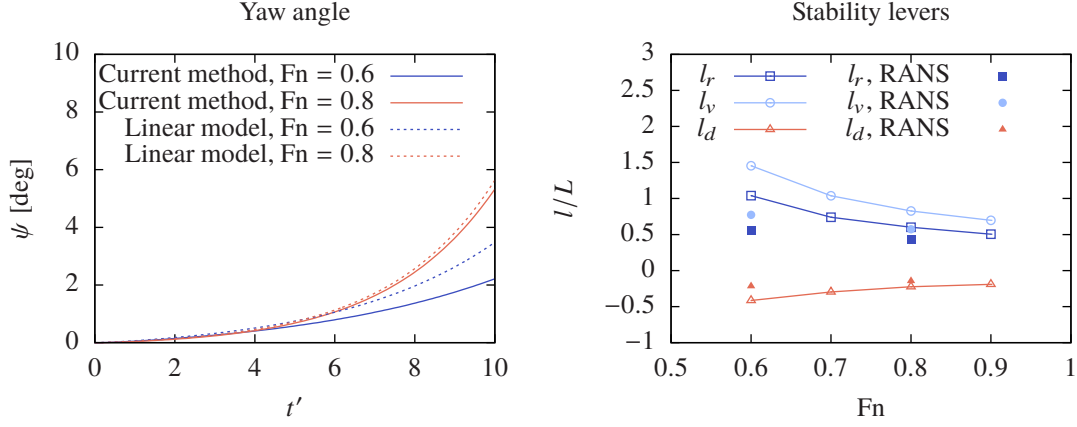


**Figure 8 - Computed yaw angle  $\psi$  using nonlinear time domain simulations and the linear coefficient based model (left) and yaw stability levers computed from the linear hydrodynamic coefficients (right).**

where the eigenvectors  $\hat{\nu}_j$  corresponding to an eigenvalue  $\lambda_j$  can be determined from

$$[\lambda_j \mathbf{M} + \mathbf{D}] \hat{\nu}_j = \mathbf{0}. \quad (8)$$

The constants  $c_j$  are determined from the initial values, i.e.  $\nu(t=0) = \nu_0$ . According to this linear analysis, the real parts  $\delta$  of the eigenvalues  $\lambda$  have to be negative for stability, meaning that sway and yaw motions decay if no additional forces are present. A further study of the characteristic polynomial according to Eq. (5) reveals that in practical cases the vessel will be directionally stable if

$$C = Y_v N_r - N_v (Y_r - mU) > 0, \quad (9)$$

or

$$l_d = l_r - l_v = \frac{N_r}{Y_r - mU} - \frac{N_v}{Y_v} > 0, \quad (10)$$

where  $l_d$  is the dynamic stability lever,  $l_r$  is the yaw damping lever and  $l_v$  is the static stability lever.

In Fig. 8 yaw motions developing from a small disturbance in terms of an initial sway velocity  $v_0 = 0.001$  m/s are shown. Results from free coupled sway-yaw simulations using the presented method are compared to results obtained using the linear model described above, i.e using Eq. (7). The agreement for  $F_n = 0.8$  is better than for  $F_n = 0.6$ . However, in both cases the same behavior is observed. The yaw angle changes increasingly faster and no new steady course can be reached, i.e. the vessel is unstable for all tested Froude numbers based on the numerical results. As is also shown in Fig. 8, this result is recovered from the evaluation of the dynamic stability levers, i.e. the dynamic stability lever  $l_d$  is negative for all tested Froude numbers. The results obtained using the RANS method also indicate directional instability. As before, the results obtained using the 2D+t method agree better with those using the RANS method at higher Froude numbers.

As instability of semi-displacement vessels at high speed may also be initiated by a loss of transverse stability, the influence of the roll motion is also investigated. Fig. 9 shows the distribution of the sway force and roll moment due to a small steady heel angle of  $\varphi = -2^\circ$ . Good agreement is found between RANS and the 2D+t method, indicating that the roll motion might be reasonably predicted. Wakeling et al. [7] investigated the transverse stability of semi-displacement vessels at high speed and found a loss of righting moment in the aft part of the hull. The same is found here, while the total righting moment does not seem to be influenced significantly, as an increase of righting moment can be observed in the forward sections. Fig. 10 shows results from free coupled sway-roll-yaw simulations using the presented method. Here, an additional disturbance in terms of an initial roll angle  $\varphi_0 = -0.5^\circ$  has been used. It can be seen that including the roll motion does not change the observed yaw motion significantly. The model is stable in roll, i.e. a decaying oscillatory roll motion can be observed.

#### 4. CONCLUSIONS

From the results it may be concluded that the presented 2D+t method can be used to compute efficiently the sway and yaw motions and associated hydrodynamic forces considering the nonlinear steady flow around the vessel. Neglecting viscous effects seems to be possible as long as the motions remain small as is the case if linear dynamic stability is considered. Judging from the obtained results yaw instability could be the cause of the observed

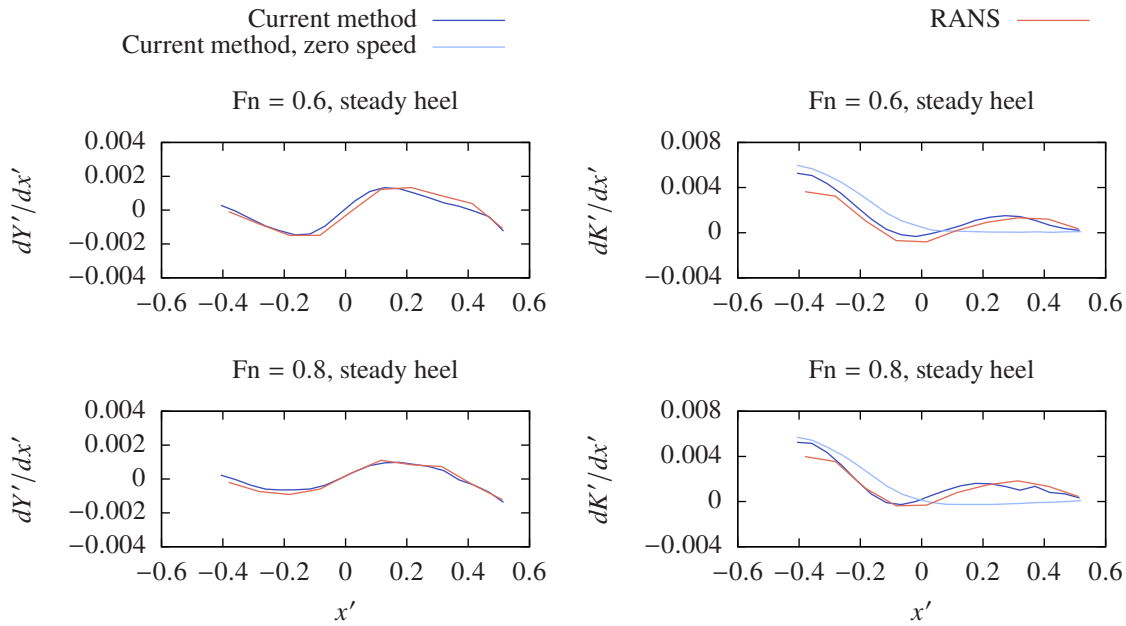


**Figure 9 - Computed sway force and roll moment distribution due to steady heel.**

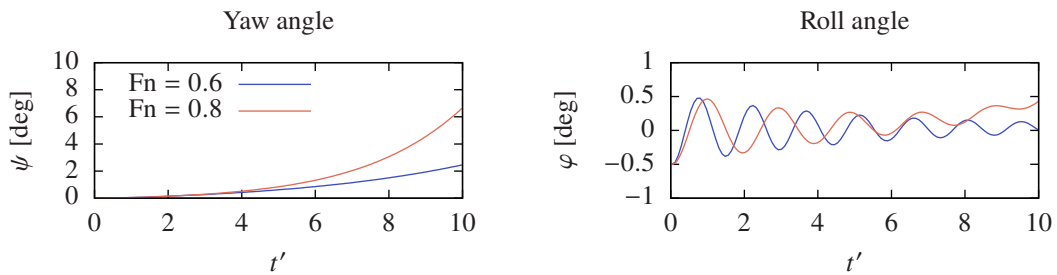


**Figure 10 - Computed yaw and roll angles using the presented method.**

instability. The restrains might be the reason why this instability was observed only at the highest Froude numbers during towing tank tests. According to the obtained results, including the roll motion in the analysis does not change dynamic behaviour of the model considerably. However, further studies are necessary in that respect.

## 5. REFERENCES

1. Faltinsen, O. M. (2005) Hydrodynamics of High-Speed Marine Vehicles. *Cambridge University Press*, Cambridge
2. Lugni, C., Colagrossi, A., Landrini, M. and Faltinsen, O. M. (2004) Experimental and Numerical Study of Semi-displacement Mono-hull and Catamaran in Calm Water and Incident Waves. *Proceedings of the 25th Symposium on Naval Hydrodynamics*, St. John's, Canada
3. Ommani, B. (2013) Potential-Flow Predictions of a Semi-Displacement Vessel Including Applications to Calm-Water Broaching. *Ph.D dissertation*, Norwegian University of Science and Technology, Norway
4. Simonis, H., Marleaux, P. and Abdel-Maksoud, M. (2020) Numerical analysis of semi-displacement vessels in head waves. *Proceedings of the 33rd Symposium on Naval Hydrodynamics*, Osaka, Japan
5. Söding, H. (1982) Prediction of Ship Steering Capabilities. *Schiffstechnik* 29, 3-29
6. Söding, H. (1993) Manoeuvring Technical Manual - Chapter 4 Body Forces. *Seehafen Verlag*, Hamburg
7. Wakeling, B. P., Sproston, J. L. and Millward, A. (1984) Transverse stability of a fast round bilge hull. *Proceedings of the International Conference on Design Considerations for Small Craft*, London, United Kingdom

# Nonlinear Seakeeping Analysis of an Elastic Ship Hull Using a Potential Method

by Heinrich Söding, Technische Universität Hamburg, h.soeding@tu-harburg.de

## 1 Introduction

For most practical problems of ship seakeeping, linear methods are sufficiently accurate. However, substantial deviations from linearity occur for large roll motions, for sloshing of fluids in ship tanks, and for ‘vertical’ bending moments (around the transverse axis) in ship cross sections. The probability distribution of these bending moments is influenced substantially by the flexibility of the ship hull. Oberhagemann [4] has shown that finite-volume methods solving the RANSE for the fluid flow around the ship are suitable for determining these bending moments, including non-linear effects and hull elasticity, both in periodical and in natural ocean waves. The present work shows that accurate results can also be determined by approximating the water flow as a potential flow. That allows to use a boundary element (panel) method (program SIS) instead of the finite-volume method, thereby decreasing the numerical effort by one to two orders of magnitude.

The present paper is confined to a ship in periodical long-crested (regular) head or following waves.

## 2 Rigid body motions

The incident wave flow is computed using Fenton’s method [2]: About 20 Fourier coefficients of the periodical long-crested wave potential are determined by solving a nonlinear equation system following from the free-surface boundary conditions. The disturbance caused by the presence of the body, on the other hand, is determined using the patch method [2, 5], a variant of the panel method. In each considered time instant, the required source strengths of 8 potentials are determined by solving a linear equation system having 8 different right-hand sides. The sources generate:

- the flow satisfying the no flux condition on the wetted surface of the moving body, and the two free-surface boundary conditions within a region around the body;
- the time derivative of the flow satisfying the conditions of no flux through the body, and giving zero potential at the free surface, for each of 6 rigid-body unit accelerations; and
- the time derivative of the flow satisfying the boundary conditions at body and free surface in case of no body accelerations.

The idea of determining not only the flow potential, but also its time derivative from the relevant boundary conditions was taken from [1]. It eliminates the problem of determining partial (at inertially fixed locations) time derivatives of the potential to compute the fluid pressure. The rigid-body added mass matrix follows from the six potentials for unit accelerations. It is used to improve the time integrations of body motions [6] by means of the 4th-order Runge-Kutta method.

A time-invariant (in body-fixed coordinates) body panel mesh is used. The panel method takes account of partly submerged panels. The panel mesh on the deformed free surface is generated anew around the actual waterline in each time instant. The disturbance potential is damped to eliminate wave reflections at the outer boundaries of the free-surface panel mesh. The surge, sway and yaw motion is controlled by PID control forces and moments. Details are given in [5].



### 3 Elastic vibrations

To catch the effect of vertical hull vibrations on wave loads approximately without substantially increasing computing time, elastic vibrations are linearized with respect to deformations, using modal shapes and eigenfrequencies for the ship with speed ahead, but in still water. Only the vibration excitation is determined nonlinearly during the simulation.

Before starting the simulation, vertical hull vibration modes are determined. The hull structure is modeled as a Timoshenko finite element beam, allowing vertical shear and bending deformations. Mode shapes are at first determined approximately using sectional added masses with 3-d corrections. For these approximate mode shapes 3-dimensional added masses are determined by a variant of the linear panel method GLRankine [8]. An eigenvalue analysis is then used to determine accurate, uncoupled vibration modes and eigenfrequencies  $\omega_j$ . Section loads are determined for unit mode vibrations, separately for contributions of deformation and acceleration. Modal damping was only guessed as 2% for all vibration modes, independent of the wave and rigid-body motion.

For linear vibrations, but nonlinear vibration excitation, each mode  $j$  satisfies the equation

$$k_j v_j(t) + d_j \dot{v}_j(t) + m_j \ddot{v}_j(t) = f_j(t), \quad (1)$$

where  $v_j(t)$  is the factor with which the unit mode deformation is to be multiplied to obtain the actual mode deformation, and  $f_j(t)$  is the mode excitation.  $k_j$ ,  $d_j$  and  $m_j$  are modal stiffness, damping and mass, respectively. The time dependence of  $v_j(t)$  is described as

$$v_j(t) = \text{Re}[\hat{v}_j(t)e^{i\omega_j t}], \quad (2)$$

where  $\omega_j$  is the eigenfrequency of mode  $j$ , and  $\hat{v}_j(t)$  is the time-dependent mode amplitude. It changes over time according to the relation following from (1) and (2):

$$\text{Re}[(d_j \dot{\hat{v}}_j + 2i\omega m_j \hat{v}_j + m_j \ddot{\hat{v}}_j)e^{i\omega_j t}] = f_j(t). \quad (3)$$

Within each half time step of the rigid-body motion integrated by the 4th order Runge-Kutta method, the excitation  $f_j(t)$  is assumed constant: the average of its values at the beginning and at the end of the time interval. Then the integrations for obtaining  $\dot{\hat{v}}_j$  and  $\hat{v}_j$  from (3) can be performed analytically. This results in an unconditionally stable integration scheme; thus the same time step size for rigid and elastic bodies can be used. Therefore both cases require practically identical computer time: for symmetrical cases of head or following waves, typically between 150 and 400 times real time on a single PC processor.

### 4 Results

Verifications were shown in [9] already for the WILS and the DTC containership. Here another example is taken: the 10 000-TEU ship used by Oberhagemann [4] (Table 1). Fig. 1 shows the ‘coarse’ body panel mesh applied to all simulations, together with an example of the free surface panel mesh. There are about 5000 body panels, of which on average about 3200 are used simultaneously because they are partly or fully submerged. The number of free-surface panels varies with wave length between about 1100 and 3100. Typically about 30 free-surface panels are generated behind each other within one wave length, and 35 Runge-Kutta time steps are used per encounter period.

Figs. 2 and 3 compare simulation results of the present program SIS for heave, pitch and midship vertical bending moment with corresponding results by Oberhagemann [4] (program COMET) and Hong (cited in [4]; model experiments). For further comparison, the results of the linear panel program GLRankine [8] are shown for two different body panel meshes. The

Table 1. Main particulars of the 10 000-TEU ship

$L$	321.0m	$B$	48.4m	$T$	15.0m
$C_B$	0.61	$x_G$	-8.08m	GM	2.00m

‘coarse’ mesh corresponds in panel size to that shown in Fig. 1; the fine one has about 4 times as many hull panels and shows that the ‘coarse’ body panel mesh is appropriate or, possibly, overly fine. The difference between the results of (a) the linear program GLRankine, and (b) all other computations and experiments, is, for the higher frequency range, largely or totally owed to the non-vanishing wave height; this is shown by the asterisks, which mark results of SIS for the small wave height 0.2m. The cause of deviations of GLRank results at low frequencies (in long waves) from those of the other methods are, possibly, inaccuracies in satisfying the radiation condition.

For one wave length (310m), Fig. 4 shows how the simulation results depend on wave height. The broken line is used to indicate that the results for 9m wave height and 20kn ship speed may be inaccurate because the upper boundary of the panel mesh (15m above the rest waterline) was temporarily submerged.

As another example, Figs. 5 to 7 show time functions of modal deformations, rigid-body motions and midship section loads in head waves of 310m length and 8m height (no submergence of the upper boundary) for a ship speed of 10 knots, which is more realistic in a severe seaway. In the plots of rigid-body motions and loads, results during the initial phase are substituted by straight lines. In this case the ratio between the lowest vibration eigenfrequency (2.703rad/s) and the encounter period is 4.9; thus deformations (Fig. 5) and cross-section loads (Fig. 7) show contributions oscillating with both the encounter period and the two-node eigenfrequency. The latter is excited by the 5th order of periodical forces induced by the wave and the ship motion.

Fig. 8 shows loads in the midship section for another wave length: 155m ( $\omega = 0.634$ ). Here the encounter frequency  $\omega_e = 0.843$ rad/s is near, but not at resonance between the third-order excitation and the 2-node eigenfrequency. The figure shows also high-frequency transients dying out after 3 to 4 encounter periods.

Fig. 9 comprises results of many simulations in head waves of normally 8m height, but not exceeding  $1/30$  wave length, for a ship speed of 10 knots. Only vertical midship bending moments  $M_y$  were evaluated. The simulations were extended until the responses were nearly periodical at least for the last three encounter periods; only these were evaluated. Amplitudes were determined by a Fourier analysis for the encounter frequency and added to and subtracted from the average bending moment. Also maximum (hogging) and minimum (sagging) values (averages of results for each of the 3 evaluated encounter periods) are given. The circles show results computed for the rigid hull; the smaller circles for average  $\pm$  amplitude are nearly coincident with the larger ones, which indicate maximum and minimum moments.

The difference between the broken lines and the neighboring full lines is, approximately, the effect of hull elasticity. The peaks in the maximum and minimum curves at  $\omega_e/\omega_2 = 1/5$  are due to resonance of the 5th excitation order with the 2-node eigenfrequency  $\omega_2$ . Corresponding peaks for the resonance of the 4th- and 3rd-order excitation are less visible or absent, respectively.

Presumably due to the moderate wave height of 8m, no obvious whipping (slam-induced vibration) occurred during these simulations. However, Fig. 10 shows a simulation in following waves of 10m height which includes whipping. No comparable CFD computations or experimental data are known; thus it remains to be clarified whether the number and intensity of the simulated slams are correct.

## 5 Conclusions

The coincidence between results of COMET and the present program SIS is, generally, better

Fig. 1. Example of panel mesh and height contours ( $\Delta z = 0.1\text{m}$ ) of disturbance wave (wave length 360m)

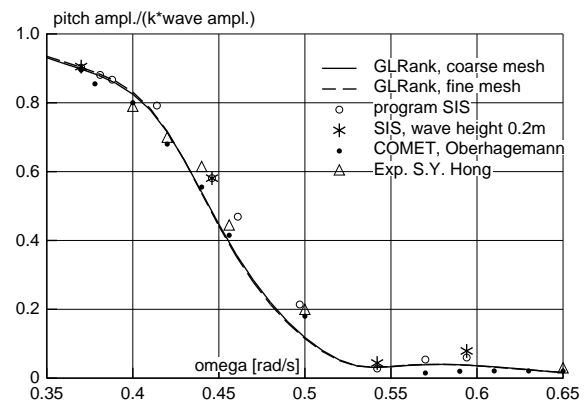
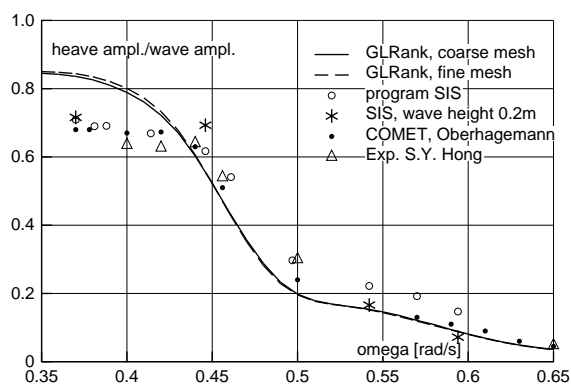
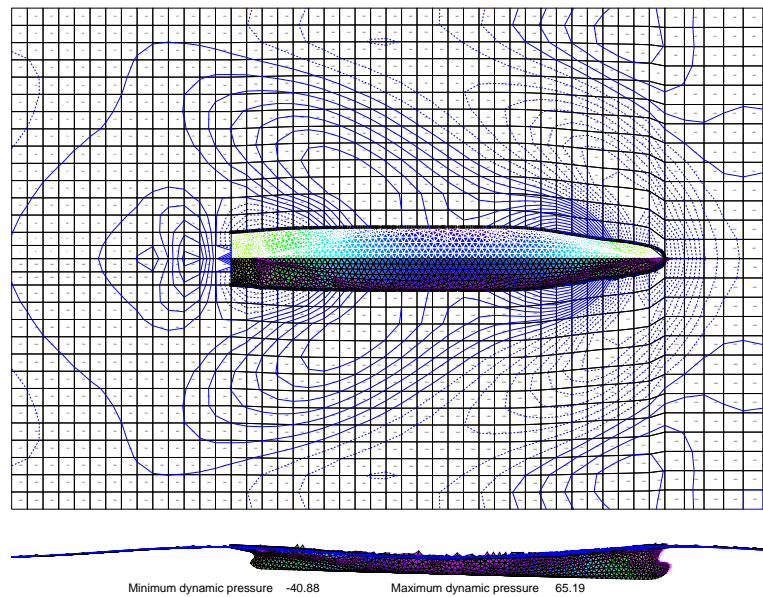


Fig. 2. Nondimensional heave and pitch motion amplitudes in periodical head waves of 3m (asterisks for 0.2m) height for 20kn ship speed

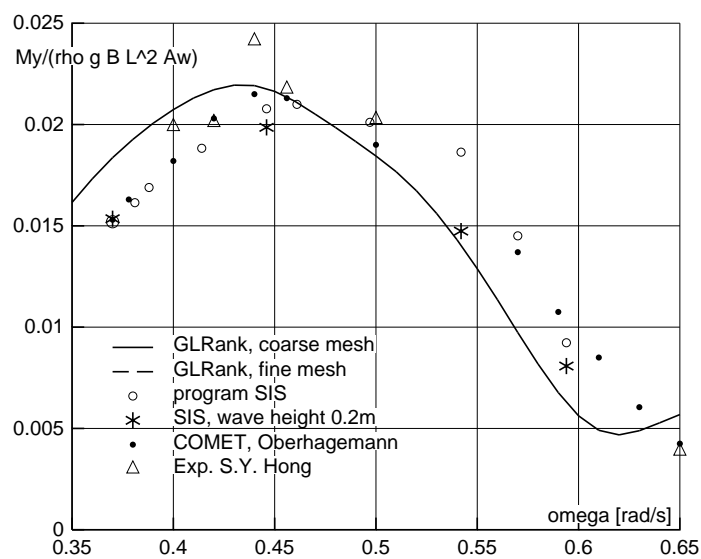


Fig. 3. Nondimensional vertical bending moment amplitude in periodical head waves of 3m (asterisks for 0.2m) height for 20kn ship speed

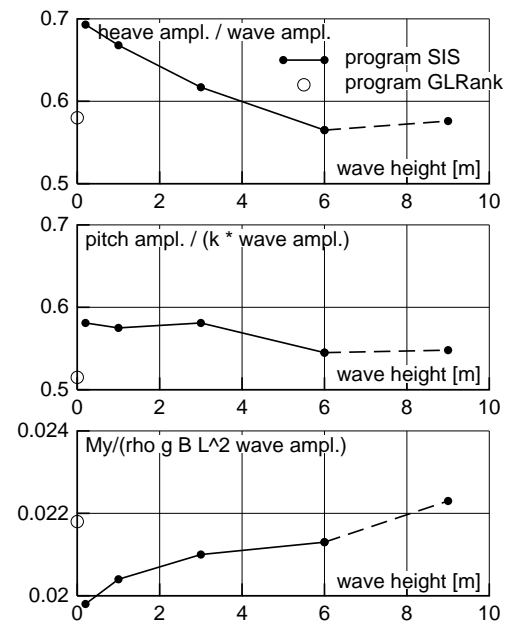


Fig. 4. Dependence of nondimensional responses on wave height in periodical head waves of 310m length; speed 20kn

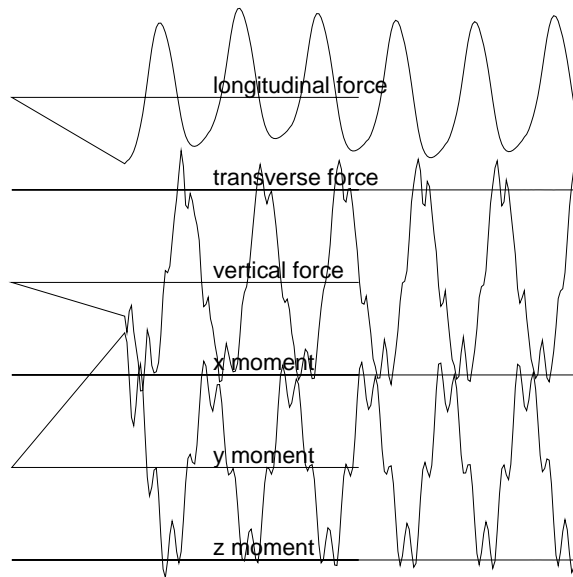
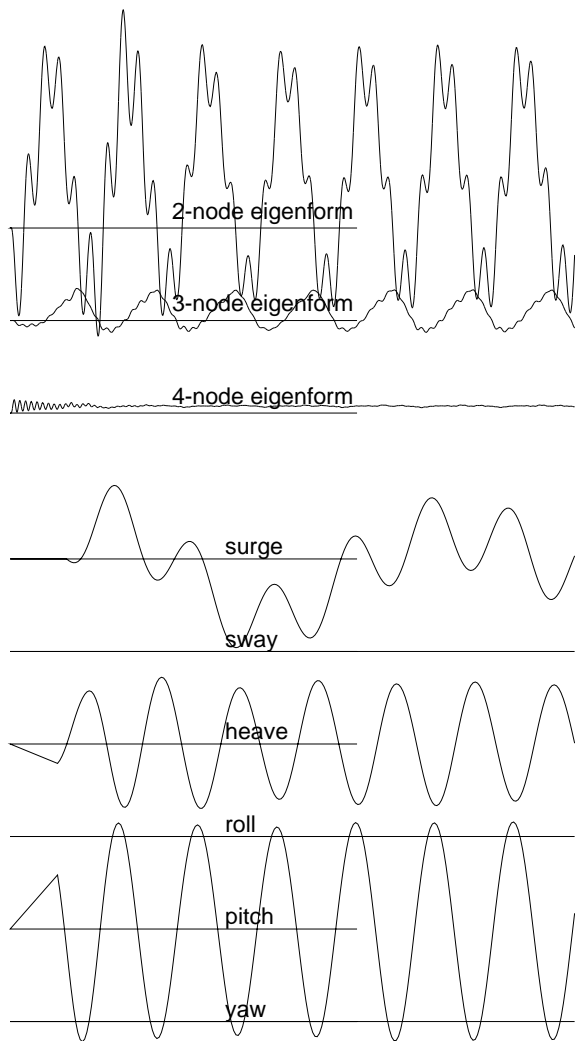


Fig. 5 (top left): Time functions of eigenform factors  $v(t)$ . Speed 10kn, wave height 8m, wave length 310m.

Fig. 6.(left): Time functions of motions; same conditions

Fig. 7 (top right): Time functions of midship loads; same conditions

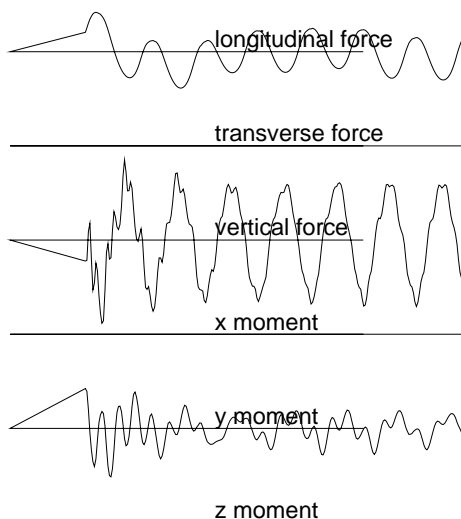


Fig. 8. Time functions of midship loads in head waves of 155m length and 5.17m height; speed 10kn

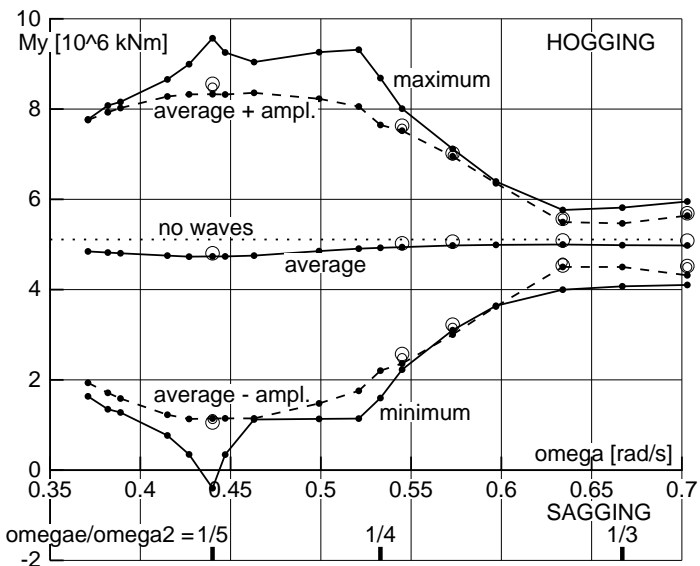


Fig. 9, Midship vertical bending moment in regular head waves of various frequencies  $\omega$ . Wave height = Min(8m, wave length/30); speed 10 knots.

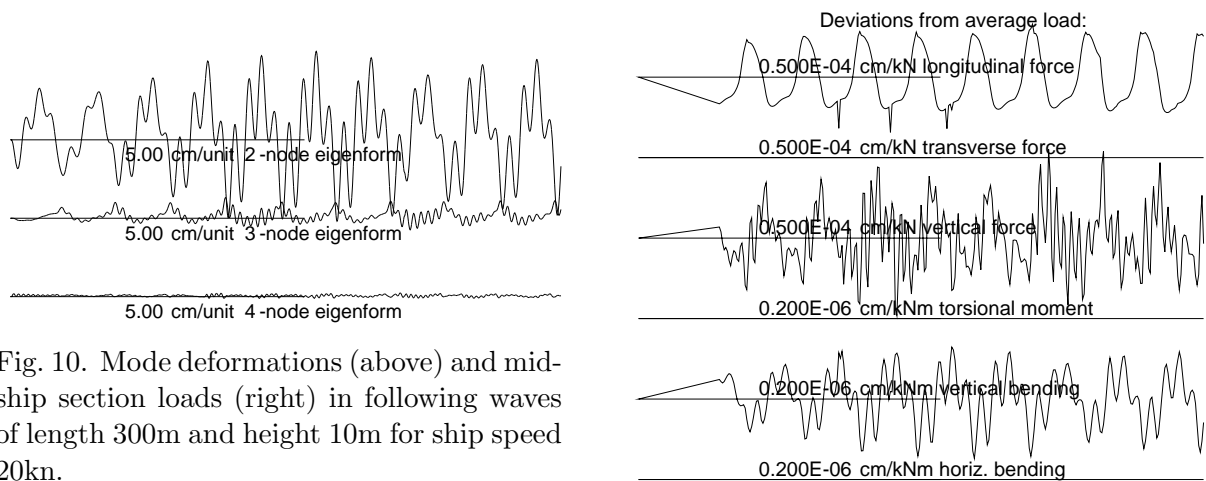


Fig. 10. Mode deformations (above) and mid-ship section loads (right) in following waves of length 300m and height 10m for ship speed 20kn.

than that between both computations and the experimental results. In my view, the experimental results by Hong belong to the best of their kind; nonetheless, the computed results presented here appear more accurate.

For a rigid and an elastic hull, the average bending moment and the oscillation amplitude (determined by a Fourier analysis for the encounter frequency) are nearly identical. However, only for an elastic hull the responses contain substantial higher-order oscillations, which lead to higher extremes of wave bending moments. Also fatigue loads are higher in elastic than in rigid hulls, not only because many more load cycles occur in an elastic hull, but also because of higher ranges between maximum and minimum moments.

The source code of the present method can be attained from the author if an adequate gift is donated to the Médecins Sans Frontières.

## 6 References

- [1] P.J. Bandyk and R.F. Beck (2011), *The acceleration potential in fluid-body interaction problems*, J. Engineering Mathematics, Vol. 70 / 1, 147-163
- [2] J.D. Fenton, J.D. (2018), *Use of the programs Fourier, Cnoidal and Stokes for steady waves*, <http://johndfenton.com>
- [3] B.O. el Moctar, T.E. Schellin, H. Söding (2021), *Numerical methods for seakeeping problems*, Springer
- [4] J. Oberhagemann (2016), *On prediction of wave-induced loads and vibration of ship structures with finite volume fluid dynamic methods*, Dr. Diss. University Duisburg-Essen 2016
- [5] H. Söding (1993), *A method for accurate force calculations in potential flow*, Ship Technology Research 40, 176-186
- [6] Söding, H. (2001), *How to integrate free motions of solids in fluids*, Proc. NuTTS 2001, Hamburg
- [7] H. Söding (2009), *Computation of springing transfer functions*, Proc. IMechE: Vol. 223 Part M: JEME 158, 291-304
- [8] H. Söding, A. von Graefe, O.E. Moctar, V. Shigunov, *Rankine source method for seakeeping predictions*, OMAE 2012, paper 83450
- [9] H. Söding (2020), *Fast accurate seakeeping predictions*, Ship Techn. Res. 67 (2020) 3, 121-135

# On the relation between measurable (*AHR*) and modelled (sand-grain) roughness heights in RANS-based full-scale ship resistance predictions

A.R. STARKE

Maritime Research Institute Netherlands (MARIN)  
2, Haagsteeg, P.O. Box 28, 6700 AA Wageningen, Netherlands  
e-mail: b.starke@marin.nl

## INTRODUCTION

The surface roughness of ship hulls is usually expressed in terms of an average height of the roughness (*AHR*), determined from measurements at a large number of locations across a hull. In viscous-flow (RANS-CFD) solvers the sand-grain height,  $h_R$ , is used to model surface roughness effects, typically through the adaptation of the wall-boundary conditions in the turbulence model. It is important to realize that these are two very different measures for the surface roughness, and to the best of the author's knowledge there is no generally valid expression that relates *AHR* to  $h_R$ . Nevertheless, for numerical simulations we are faced with the challenge to translate the texture of a ship's surface, either newly-built or after some time in service, into an equivalent roughness height.

In the present study it has been investigated how the CFD-predicted ship-resistance increase due to surface roughness compares with a well-known empirical relation that has been used in the determination of the ship resistance for quite some time. From this comparison a factor has been determined that for the present test case results in a good agreement between the two methods at higher roughness values.

## DESCRIPTION OF THE TEST CASE

The ship under consideration is the Japan Bulk Carrier (JBC), illustrated in Figure 1, that has been used as a testcase in the Tokyo 2015 Workshop on CFD in Ship Hydrodynamics [1]. Its main dimensions and some relevant flow parameters have been listed in Table 1.

Table 1: Particulars of the ship and the flow.

Symbol	Description	Value	Unit
$L_{pp}$	Length between perpendiculars	280	m
B	Breadth	45	m
T	Design draught	16.5	m
S	Wetted surface area	19556	m <sup>2</sup>
$\rho$	Water density	1025	kg/m <sup>3</sup>
$\nu$	Dynamic viscosity	$1.138 \times 10^{-6}$	m <sup>2</sup> /s



Figure 1 The geometry of the Japan Bulk Carrier (JBC).

## COMPUTATIONAL METHOD

The viscous-flow method used is PARNASSOS, a code developed by MARIN and IST [2,3]. It solves the discretised Reynolds-averaged Navier-Stokes (RANS) equations for a steady, 3D incompressible flow around a ship's hull. For all computations in this study, the two-equation  $k-\omega$  SST turbulence model from Menter [4] was used. The discretisation is of finite-difference type. All terms in the momentum and continuity equations are discretised by second or third-order accurate difference schemes. PARNASSOS can handle structured, body-fitted, generally non-orthogonal HO-type grids. The momentum and continuity equations are solved in fully coupled form. Therefore, the continuity equation need not be recast in a pressure correction or pressure Poisson equation, but can simply be solved as it is. After discretisation and linearisation, the three momentum equations and the continuity equation give rise to a matrix equation containing 4\*4 blocks, which is solved using preconditioned GMRES. This fully coupled solution has been found to be robust and quite insensitive to the mesh aspect ratio. This allows solving the discretized equations on extremely contracted grids close to the wall. As a result, wall functions are not necessary, not even at full scale.

The handling of sand-grain roughness in  $k-\omega$  models has been described in Wilcox [5]. The boundary condition for  $\omega$  at the wall is defined by

$$\omega = \frac{u_\tau^2}{\nu} S_R$$

where  $\nu$  is the kinematic viscosity of the fluid,  $u_\tau$  is the friction velocity given by

$$u_\tau = \sqrt{\frac{\tau_w}{\rho}} = \sqrt{\nu \left( \frac{\partial u_\tau}{\partial y_n} \right)_{y=0}}$$

Here,  $u_\tau$  is the velocity component tangential to the wall and  $y_n$  the coordinate normal to the wall. Furthermore,

$$S_R = \begin{cases} \left( \frac{200}{h_R^+} \right)^2 & h_R^+ \leq 5 \\ \frac{100}{h_R^+} + \left[ \left( \frac{200}{h_R^+} \right)^2 - \frac{100}{h_R^+} \right] e^{5-h_R^+} & h_R^+ > 5 \end{cases}$$

Using this formulation a limiter of the eddy viscosity in the viscous sub-layer was negatively affected in the  $k-\omega$  SST model and therefore a modified damping function was proposed in [6] which has been used in the present computations as well.

The computational domain extended from the inflow boundary, located  $0.5L_{pp}$  in front of the bow, to the outflow boundary,  $1.5L_{pp}$  behind the transom. The lateral outer boundary is a quarter of a cylinder with axis  $y=z=0$  and radius  $1L_{pp}$ . At this boundary tangential velocities and pressure found from a potential-flow computation are imposed. Due to symmetry considerations only the starboard side of the ship was taken into account. The base mesh, denoted H1, consisted of approximately 6.5M cells. From this base a coarser mesh has been generated by removing every second grid node in each direction. This mesh will be denoted

H2. Cells were contracted strongly towards the hull, to capture the gradients in the boundary layer. Two levels of contraction have been applied to both H1 and H2 to illustrate that the present combination of turbulence model and roughness model poses strong demands on the wall-grid spacing, and increasingly so with increasing roughness heights. The applied contraction levels resulted in  $y^+$  values of approximately 0.1 for the contraction that is normally used when surface roughness is ignored (hydrodynamically smooth walls) and 0.01 for the increased contraction.

The iterative convergence has been monitored using normalized maximum changes in the solution and by the changes in the resistance coefficients between successive updates. For a limited number of computations the solutions could be converged almost to machine accuracy. For the remaining computations the iterative convergence was sufficient to guarantee a negligible effect on the resistance coefficients.

## RESULTS

The approximate formula to assess the drag penalty associated with an average hull roughness as formulated by Townsin et al [7] reads

$$10^3 \Delta C_F = 44 \left[ \left( \frac{AHR}{L_{pp}} \right)^{1/3} - 10 Rn^{-1/3} \right] + 0.125$$

Here  $\Delta C_F$  corresponds to an increase of the friction coefficient,  $L_{pp}$  is the reference length of the ship,  $Rn$  the Reynolds number, and  $AHR$  corresponds to an average hull roughness.

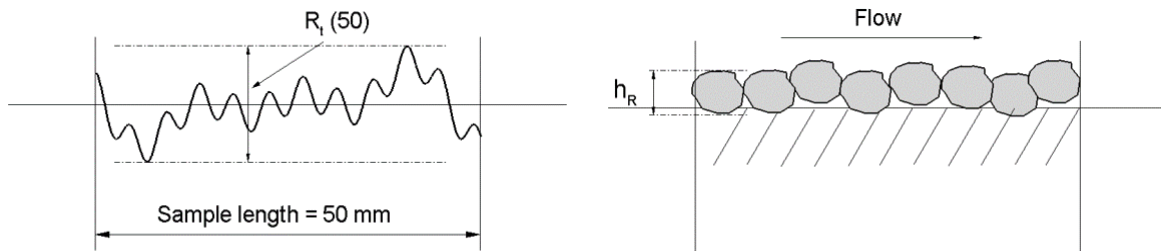


Figure 2 Illustration of the AHR (left) and equivalent sand-grain roughness (right).

According to the publication of Townsin, “the standard measure of hull roughness that has been adopted in the maritime industry is  $R_t(50)$ , see Figure 2. This is a measure of the maximum peak-to-valley height over 50 mm lengths of the hull surface. When undertaking a survey of a hull, several values of  $R_t(50)$  will be determined in a particular location on the hull and these are combined to give a Mean Hull Roughness (MHR) at that location. The Average Hull Roughness (AHR) is an attempt to combine the individual MHR values into a single parameter defining the hull conditions at a particular moment in time. Typically the vessel may have been divided up into a number of equal sections, perhaps 100 – 120, and a MHR determined for each section. These MHR values are then combined to give the AHR for the vessel”.

The first challenge for simulation roughness effects in ship flows is to find a relation between the AHR and  $h_R$ , which is not a trivial problem. In this original paper Townsin refers to a



study where  $AHR=4h_R$ , while Schultz [8] reports that  $AHR=5h_R$  for a ship with an anti-fouling coating. Later studies suggest that this relation may be case dependent.

An alternative approach to establish a relation between  $AHR$  and  $h_R$  is to use Towsin's formula as a reference line for the resistance increase found from viscous-flow computations. For that purpose viscous-flow computations have been performed at three different full-scale Reynolds numbers, namely  $Rn=1.33E9$ ,  $1.84E9$  and  $2.34E9$ , which corresponds to ship speeds of  $V_s=10.5$ ,  $14.5$  and  $18.5$  knots for the present test case, respectively. For each speed the roughness height has been varied up to  $800\ \mu m$   $h_R$ . In the set-up of the computations the ratio between  $AHR$  and  $h_R$  has been taken according to Schultz, i.e.  $AHR=5h_R$ . The resulting increase of the friction increase has been illustrated in Figure 3.

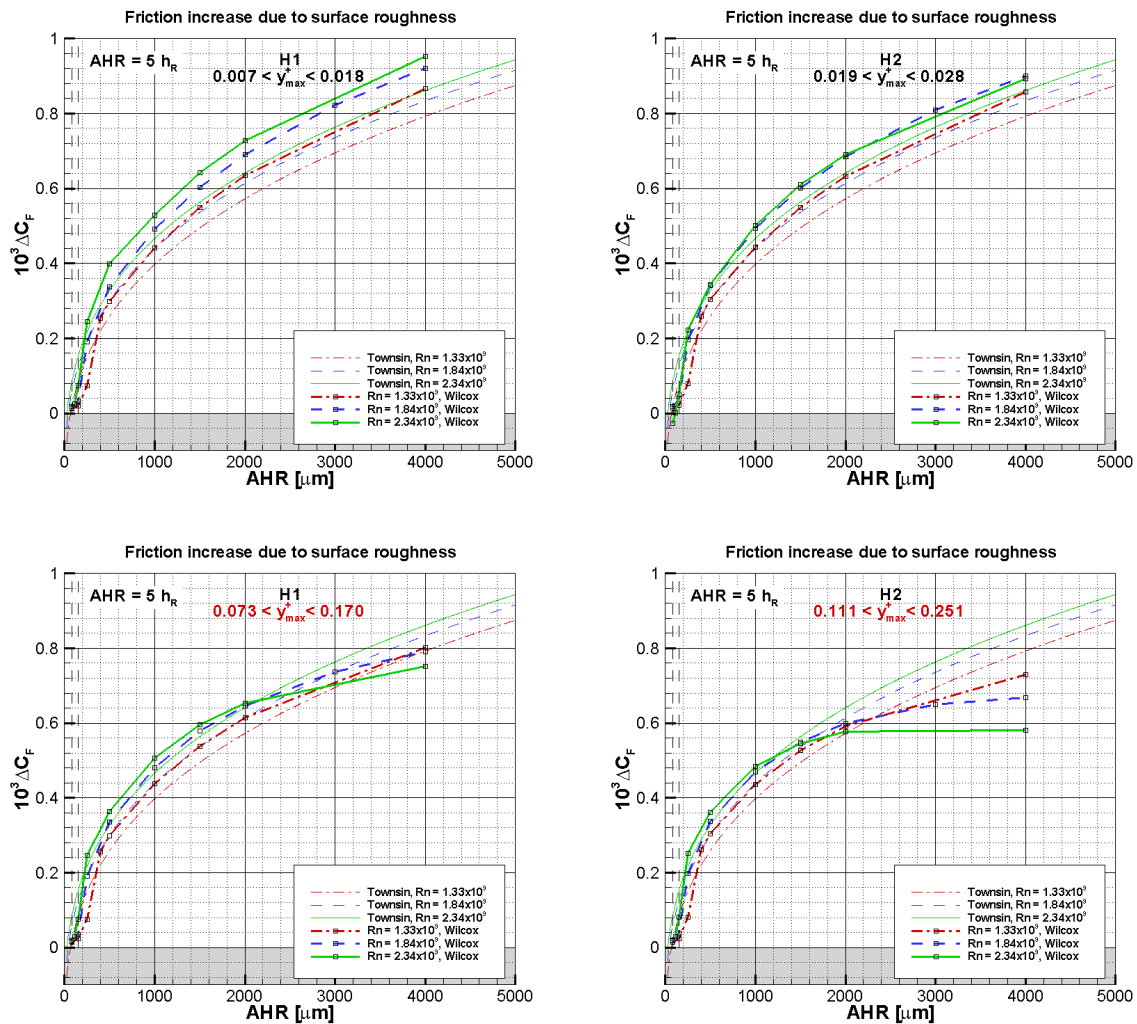


Figure 3: The increase of the friction resistance with  $AHR$  on the finest mesh (left) and the coarsened mesh (right); and with an increased (top) and more regular (bottom) near-wall spacing.

Concentrating first on the graph in the top-left corner it can be seen that with increasing roughness heights the numerical results show two inflexion points (below  $AHR=500\ \mu m$  for the present case). There the solution passes the intermediate range between the

hydrodynamically smooth and fully rough flow regimes. For reference the two vertical dashed lines indicate the roughness values that are typically claimed for newly-built ships (80-150  $\mu\text{m}$   $AHR$ ). With increasing roughness heights the predicted lines run practically parallel to each other, at higher values than the reference lines obtained from Townsin's formula.

Comparing the graphs at the top and the bottom of Figure 3 it can be observed that there is a significant dependence in the CFD results on the near-wall spacing. Outside the intermediate range the predicted friction increase increases considerably with smaller wall-grid spacing, and more so with increasing roughness heights. The results indicate that for hydrodynamically smooth flows and in the intermediate range  $y^+ < 0.1$  is sufficient, but the higher the roughness the lower this value should be:  $y^+ < 0.01$ , or possibly even lower. It can be expected that not all flow solvers will be able to meet these demands.

Comparing the graphs on the left and the right it can furthermore be seen that there is also some grid dependence left in the solution. Again, however, this is more pronounced at higher roughness heights and in this case also at higher Reynolds numbers. It can be expected that a more elaborate mesh sensitivity study will result in a further growth of the predicted friction resistance increase, most notably in the fully rough regime.

Since the predicted friction increase runs practically parallel to the lines by Townsin at higher roughness heights, it can be expected that CFD results can be made to coincide reasonably well with Townsin's lines at the fully rough regime by increasing the ratio between  $AHR$  and  $h_R$ . For the present study the lines at  $Rn=1.84 \times 10^9$  have been fitted in a least-squares sense, resulting in  $AHR = 6.36h_R$ . From Figure 4 it can be seen that using this ratio the CFD results practically coincide with Townsin's empirical formula outside the intermediate range. Note, that the friction increase has now been plotted against an  $AHR$ -based Reynolds number to collapse the numerical results at low values of  $AHR$ .

As discussed above it is expected the ratio between  $AHR$  and  $h_R$  will become somewhat higher if the remaining dependence on near-wall spacing and mesh density is removed from the solutions.

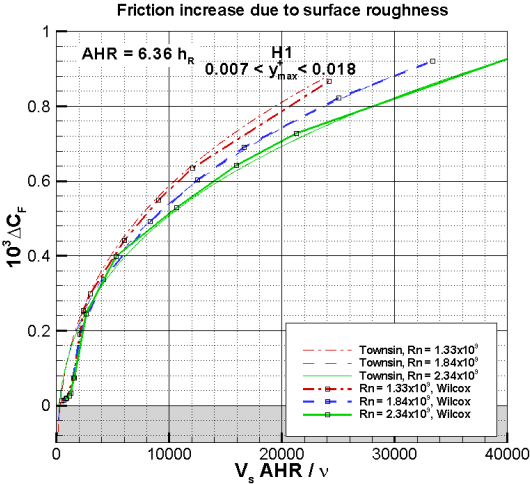


Figure 4: Comparison between the predicted (thick lines) and empirical (thin lines) friction increase due to surface roughness using  $AHR=6.36h_R$ .

Finally it is emphasized that the presently found ratio between  $AHR$  and  $h_R$  is not expected to be generally valid. There is evidence that this ratio varies between ship types, and it will be different for other combinations of turbulence models and roughness models as well. Work is continuing on this subject at MARIN [9].

## CONCLUSION

When defining  $AHR=6.36h_R$  good agreement is found for the friction increase due to surface roughness between Townsin's empirical formula and viscous-flow simulations of the flow around the JBC using the  $k-\omega$  SST turbulence model in combination with a modified Wilcox roughness model.

The present combination of turbulence model and roughness model is very sensitive to the applied near-wall spacing, and increasingly so at increasing roughness heights. The requirement that for these models  $y^+ < 0.1$  for hydrodynamically smooth hulls is not sufficient in the fully-rough regime. There the near-wall spacing should be  $y^+ < 0.01$  or even lower. If not met, the friction increase is under-estimated.

## ACKNOWLEDGEMENT

This research is partially funded by the Dutch Ministry of Economic Affairs.

## REFERENCES

- [1] Hino, T., Stern, F., Larsson, L., Visonneau, M., Hirata, N. and Kim, J. (Eds.), (2016), Numerical Ship Hydrodynamics, an assessment of the Tokyo 2015 Workshop, Tokyo, Japan.
- [2] Hoekstra, M., "*Numerical simulation of ship stern flows with a space-marching Navier Stokes method*", PhD Thesis, Technical University of Delft, Oct. 1999.
- [3] Van der Ploeg, A., Eça, L. and Hoekstra, M., "*Combining accuracy and efficiency with robustness in ship stern flow calculation*", 23rd Symp. Naval Hydrodynamics, Val de Rueil, France, Sept. 2000.
- [4] Menter, F.R., (1994), "*Two-equation eddy-viscosity turbulence models for engineering applications*", AIAA Journal, Vol. 32, No. 8, pp. 1598-1605.
- [5] Wilcox, D.C., (1998), "*Turbulence modelling for CFD – DCW Industries*", 2<sup>nd</sup> edition.
- [6] Hellsten, A., Laine, S., (1997), "*Extension of the  $k-\omega$  SST turbulence model for flows over rough surfaces*", AIAA Paper 1997-3577.
- [7] Townsin, R.L., Medhurst, J.S., Hamlin, N.A. and Sedat, B.S., "*Progress in calculating the resistance of ships with homogeneous or distributed roughness*", NECIES Centenary Conference in Marine Propulsion, 1984.
- [8] Schultz, M.P., (2007), "*Effects of coating roughness and biofouling on ship resistance and powering*", Biofouling, 23(5):331-341.
- [9] Eça, L., Starke, A.R., Kerkvliet, M. and Raven, H.C., "*On the contribution of roughness effects to the scaling of ship resistance*", 9th International Conference on Computational Methods in Marine Engineering, (MARINE 2021), online, June 2-4, 2021.

## **Hydrodynamic and Hydroacoustic Simulations of Propeller-Induced URN Effects in a Hull Wake-Field**

Joseph Praful Tomy<sup>1,2</sup>, Stephan Berger<sup>1</sup>, Keun Woo Shin<sup>1</sup>, Harry Bingham<sup>2</sup>, Poul Anderson<sup>2</sup>

<sup>1</sup>MAN Energy Solutions, Copenhagen, Denmark

<sup>2</sup>Technical University of Denmark (DTU), Lyngby, Denmark

The study of Underwater Radiated Noise (URN) from marine propellers has been garnering interest over the past few years, due to their interference with the communication channels of marine mammals [1]. The acoustic signature of the propeller is determined in its design phase, and hence, it is important to predict the acoustic performance at early stages of the propeller design.

The numerical simulation of the hydro-acoustic problem involves solving the compressible Navier-Stokes Equations (NSE) in the fluid domain. Due to the rotation of the propeller in an unsteady hull wake-field and due to the effects of cavitation, the pressure at a far-field point fluctuates; and this gives rise to the acoustic noise in the fluid domain. High frequency fluctuations are associated with a lower wavelength, and hence, in order to capture these effectively, a fine spatial discretization of the fluid domain is required. This makes the numerical computations using the Reynolds Averaged Navier-Stokes Equations (RANSE) computationally intensive for such hydroacoustic problems.

An alternative technique that is popular within the industry is to use potential flow methods, such as the Boundary Element Method (BEM). These methods obtain the solution of the 3-dimensional flow problem for a non-viscous flow, by identifying the strength of equivalent singularity potentials on the boundary surfaces. Essentially, this reduces the flow problem in the 3-D domain into a 2-D problem solving for the unknown potentials on the boundary surfaces. [2]

The direct extension of potential flow methods to the hydroacoustic problem of URN prediction involves two main challenges – the effect of viscosity and the effect of compressibility on the solution. The effect of viscosity for the hydroacoustic URN problem would be similar to that for the hydrodynamic problem. It is evident that the effect of compressibility is not so prominent for near-field points, as the speed of sound in water is high enough for these to be neglected. However, for far-field points, the effect of the potential flow solution on the pressure fluctuations could be important.

For the prediction of aero-acoustic performance of helicopter rotors, the use of an acoustic analogy with the Ffowcs-William-Hawkings (FWH) method [3] is a globally accepted method. The acoustic analogy is based on the principle that the problems of fluid dynamics and acoustics are treated separately. The flow solution on the boundary surface is obtained from fluid dynamics. The ‘noise-generating source’ is then defined by the perturbations of the pressure and flow velocities on the boundary surface. The FWH method provides a solution to the acoustic wave equation at any point in the acoustic domain, by assigning different source terms to each ‘noise-generating panel’ – the thickness and loading source terms. The integral formulation of a singularity-free solution for high speed propellers has been derived by Farassat and Brentner [4]. This technique has successfully been extended for applications involving the marine propeller as well [5]. The method can also be further extended for cavitating flow, including the effect of the cavitating tip vortex. This is currently a work in progress.

Within this paper, the hydro-acoustic simulation of a marine propeller is performed using three methods – (i) by directly obtaining the hydrodynamic pressure-fluctuations on a far-field point using BEM, (ii) by using the hydrodynamic solution from BEM on the surface of the propeller blade and then applying the FWH acoustic analogy to obtain the far-field pressure fluctuations, and (iii) RANSE-CFD simulations in a 3D fluid domain. These simulations are performed for a non-cavitating propeller within a measured wake-field and compared with available experimental results, to use as a benchmark for the study. The harmonics of the pressure fluctuations at the blade frequency are compared to establish the effect of compressibility in the URN simulation of marine propellers. The comparison is performed for multiple far-field points in the hydroacoustic domain, to study the decay rate of high-pressure pulses.

The in-house BEM program ESPPRO, originally developed at Technical University of Denmark (DTU), is used for the potential flow calculations. The Ffarrasat 1A formulation of the FWH acoustic analogy [4], is implemented within a python script and uses the potential flow solution from ESPPRO to calculate the pressure fluctuations at a far-field point. Figure 1 shows the mesh-grid used for computations, with 25 elements in the radial direction and 25 elements in the chordwise direction of the blade. The simulations are done for the open water case, case with only axial hull wake, and a case with all three hull wake components. Such an analysis aims to show the influence of the tangential hull wake component on the underwater radiated noise. A preliminary comparison of the decay rate of high-pressure pulses between the BEM hydrodynamic simulations and the FWH hydroacoustic simulations for the Open Water case, with an advance coefficient ( $J$ ) of 0.728, is shown in Figure 2.

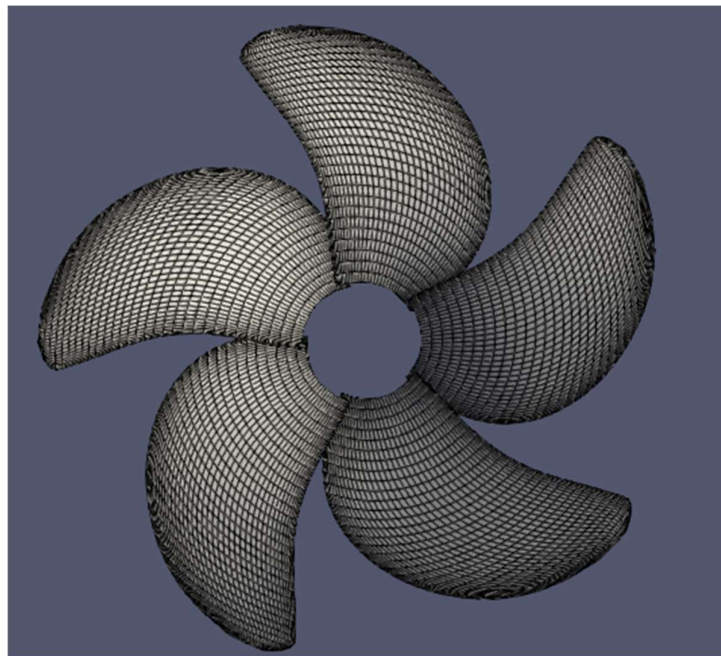


**Figure 1: Mesh-grid used for Boundary Element calculations**

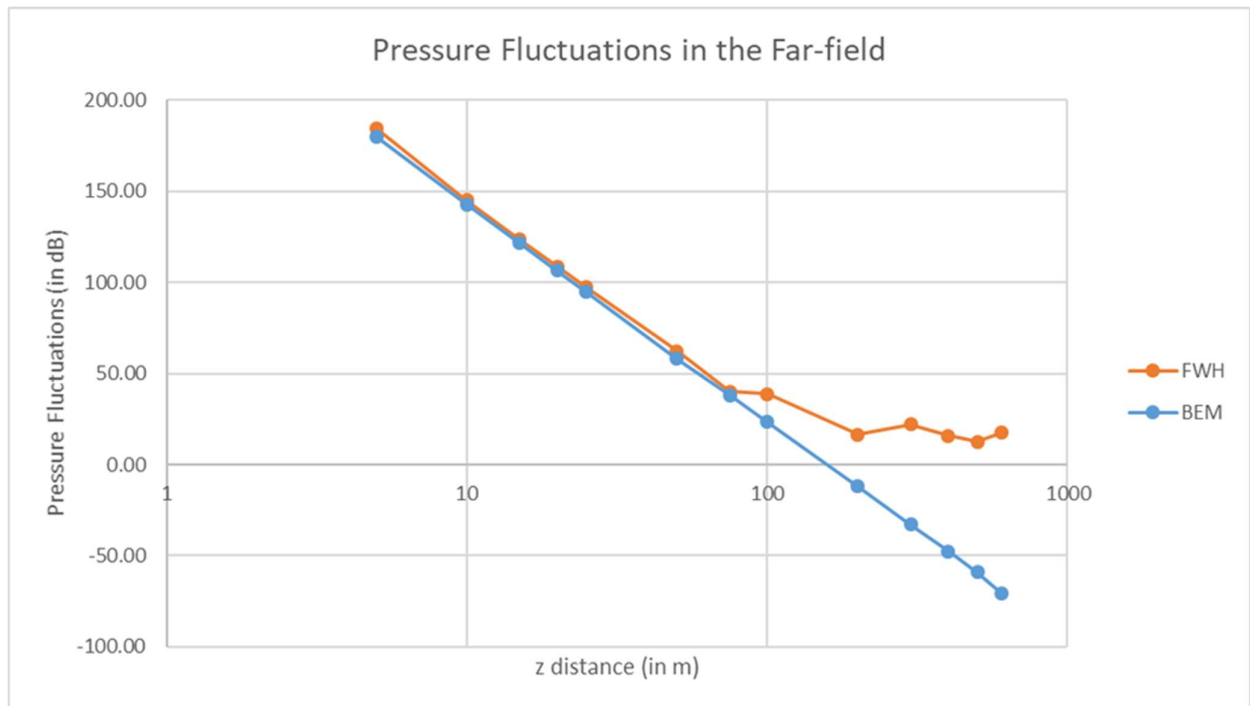


Figure 2: Comparison of decay rate of pressure fluctuations

## REFERENCES

- [1] A. J. Wright, «Shipping Noise and Marine Mammals,» Okeanos - Foundation for the Sea, Hamburg, Germany, 2014.
- [2] International Towing Tank Conference, «ITTC Recommended Procedures, 7.5-02-02-02,» Specialist Committee of 23rd ITTC: Procedures for Resistance, Propulsion and Propeller Open Water Tests, 2002.
- [3] J. F. Williams und D. Hawkings, «Sound Generation by Turbulence and Surfaces in Arbitrary Motion,» *Philosophical Transactions of the Royal Society*, Bd. 264, Nr. 1151, pp. 321-342, 8 May 1969.
- [4] F. Farassat und K. S. Brentner, «The Acoustic Analogy and the Prediction of the Noise of Rotating Blades,» *Theoretical and Computational Fluid Dynamics*, Bd. 10, pp. 155-170, 1998.
- [5] U. Gottsche, M. Scharf, S. Berger und M. Abdel-Maksoud, «A Hybrid Numerica Method for Investigating Underwater Sound Propogation of Cavitating Propellers,» in *Fifth International Symposium on Marine Propellers, SMP '17*, Espoo, Finland, June 2017.

# Accelerating marine propeller development in early design stages using machine learning

Maurits van den Boogaard<sup>a\*</sup>, Giacomo Alessi<sup>a</sup>, Benoit Mallol<sup>a</sup>, Dirk Wunsch<sup>a</sup>, Nathan Clero<sup>a</sup>, Dario Amadori<sup>a</sup>, Luca Zampieri<sup>b</sup> and Charles Hirsch<sup>a</sup>

<sup>a</sup>: NUMECA-Cadence, Ch. de La Hulpe 189, 1170 Brussels, Belgium; \*: [boogaard@cadence.com](mailto:boogaard@cadence.com)

<sup>b</sup>: Neural Concept, EPFL Innovation Park, Batiment C, 1015 Lausanne, Switzerland

## 1 Introduction

With the increase in computational power, machine learning offers new opportunities for accelerating the marine engineer's workflow during the initial design phases. Taking the example of open-water calculations, which tend to have high relative computational costs, the application of a machine learning algorithm like a Geodesic Convolutional Neural Network (GCNN) to such computations is shown in this paper to be promising and could allow increasing productivity in the initial design process by orders of magnitude. The goal of this study is therefore to describe the approach and discuss the results of applying a GCNN to open-water computations using geometries following the design of the Wageningen B-series propeller family and explore the productivity gains that can be achieved by applying artificial intelligence to marine CFD results.

## 2 Methodology

### 2.1 Geometry generation and verification using CFD

The Wageningen B-series propeller series was chosen as the 'parent' series for the design of experiments (DoE). Propellers in this series are described by four parameters: the diameter  $D$ , the expanded area ratio  $EAR$ , the number of blades  $Z$  and the propeller pitch  $P$ . If the diameter is kept constant ( $D=1\text{m}$ ), the geometry is fully described by  $EAR$ ,  $Z$  and  $P$ . The propellers were modeled using Rhino 3D in combination with Grasshopper along with a proprietary Python code containing the sectional geometry description based on the definitions described in Kuiper (1992). The two-dimensional sections were developed into three-dimensional blades using NURBS.

Van Oossanen & Oosterveld (1975) developed the description of open-water performance curves valid for any Wageningen B-series propeller based on regression analysis of earlier model tests performed at the Maritime Research Institute in the Netherlands (MARIN). The original description of the thrust and torque coefficient curves is valid at a Reynolds number of 2,000,000. These regression curves were subsequently compared to CFD results for a selected number of propellers and operating conditions to verify that the created propeller geometries yielded the expected results corresponding to the Wageningen B-series. The results indicated that thrust and torque predictions coming from CFD were within 5% of the regression-based prediction for a wide range of advance ratios  $J$ .

Very high advance ratios, where propellers generate close to zero thrust, showed lower accuracy which was already expected based on previous experience. At low values of  $J$ , the propeller is acting in bollard pull conditions and this was identified as a less interesting condition to include as most ships only spend very little amount of time operating in these conditions. Therefore, the allowed range of  $J$  values was determined by first calculating the theoretical range of positive thrust (first quadrant propeller operation) for each propeller in the design set. Subsequently, the bottom 10% was discarded to avoid bollard pull conditions and the maximum allowed  $J$  value was chosen halfway between the point of maximum efficiency and the  $J$  value corresponding to thrust breakdown, to avoid inaccuracies of the CFD solver close to the point where  $K_t = 0$ . This is visualized in Fig. 1.

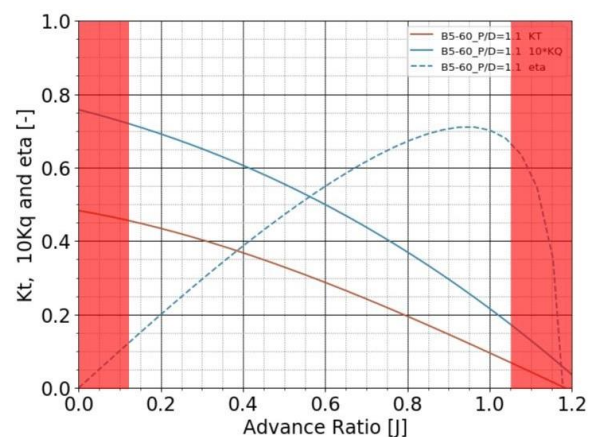


Figure 1: Indication of excluded values of  $J$  (in red) in the open-water performance curve for the Wageningen B5-60

## 2.2 Design of Experiments

The nature of machine learning requires the generation of large amounts of data obtained, in this case, from many similar propellers and operating conditions. The propeller geometries (parametrized as the Wageningen B-Series) and operating conditions must be chosen randomly by what is called the design of experiments (DoE). The DoE was managed using FINE™/Design3D. The CAD files of the propellers were generated using Rhino 3D in combination with Grasshopper, followed by an export as STL using a proprietary tool. As the process needed to be fully automated, the different patches (e.g. leading edge) were identified automatically with this tool if the number of blades was maintained equal. This created a constraint for the creation of the DoE: the design space had to be created for each blade number separately.

The design space for each blade number could therefore be defined by the geometrical parameters  $EAR$  and  $P$  (as  $D$  and  $Z$  are fixed) and by the operational parameter: the advance ratio  $J$ . The parametric ranges of the Wageningen B-Series were used for  $EAR$  and  $P$  (through the pitch-diameter ratio). The number of blades was varied between 2 and 7. Given the  $J$  value limits described in Fig. 1, the  $J$  value in the DoE was a normalized range with values between 0 and 1, corresponding to respectively the minimum and maximum of the propeller-specific allowed range. The normalized values were converted to the actual  $J$  values when setting up the computations. The Latinized CVT and Inherited LHS (for additional samples) methods were used to sample randomly across the design space for each blade number. A total of 271 STL files was created, each corresponding to a single propeller operating at a specific advance ratio  $J$ .

## 2.3 Mesh generation

The meshes were generated with OMNIS™/Hexpress using the surface-to-volume (S2V) technique. This methodology ensures superior mesh quality on curved surfaces like propeller blades, but also a more constant viscous layer height enveloping the blades, compared to the more common volume-to-surface approach. Leading and trailing edges as well as the area around the blade tip were more finely discretized compared to the blade surface. This can be clearly seen in the mesh close-ups in Fig. 2a and Fig. 2b.

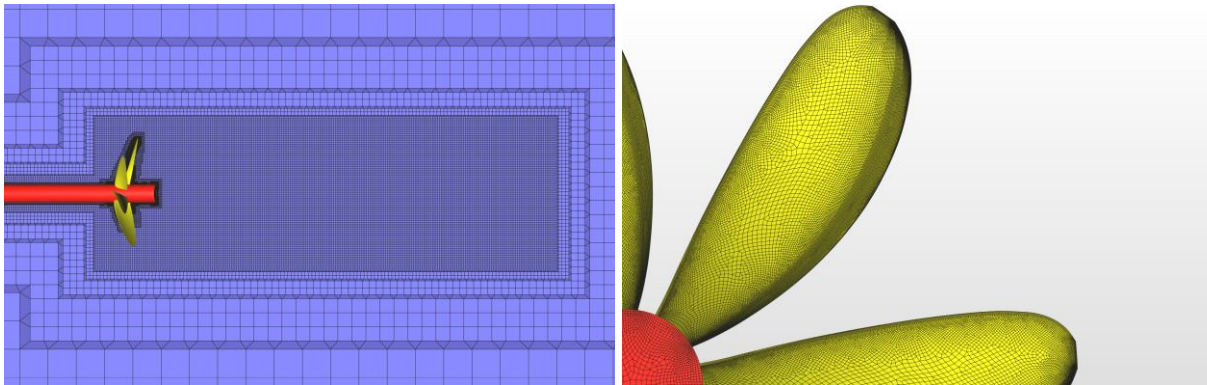


Figure 2a: Mesh far field and blade surfaces for a Wageningen B7-59 with  $P/D=1.25$ .

Viscous layers were inserted with a first layer thickness defined by  $y^+=1$  (and Reynolds number of 2,000,000). Preliminary results were compared between using a  $y^+$  value of 1 and 0.1, but no significant differences were found in the prediction of thrust and torque between both approaches. Given the lower cell count using  $y^+=1$ , this higher value was used for all meshes. The wake behind the propeller was additionally refined until 4 diameters behind the propeller location to enable an accurate calculation of the flow behind the propeller. The total number of cells for all different propellers ranged from 25 to 35 million cells. The meshing procedure was completely automated with the use of Python.

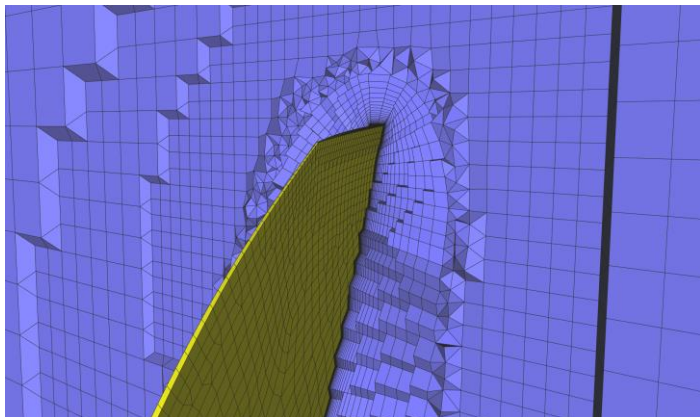


Figure 2b: Tip close-up with viscous layers for a Wageningen B7-59 with  $P/D=1.25$ .



## 2.4 Computation details

As the model tests at the basis of the regression curves were performed at Reynolds number of 2,000,000, all computations were set up in such a way that the Reynolds number (based on the reference velocity and propeller radius) was kept as close as possible to this value. The reference velocity  $u_{ref}$  for propeller was defined as:

$$u_{ref} = \sqrt{u_{x,\infty}^2 + (0.7R\omega)^2}, \quad (1)$$

where  $u_{x,\infty}$  is the inflow velocity in the far field in [m/s],  $R$  is the propeller radius in [m] and  $\omega$  is the propeller rotational speed in [rad/s]. Additionally, the advance ratio of the propeller  $J$  is defined as:

$$J = u_{x,\infty} / 2nR, \quad (2)$$

where  $n$  is the rotational speed in [rps].  $n$  can be converted to  $\omega$  as  $\omega = 2\pi n$ .

The goal was to obtain a fixed value of propeller rotation rate  $n$  across computations so that only the inflow velocity needed to be varied to simulate different values of  $J$ , as the Reynolds number is much more sensitive to changes in the propeller rotation speed than to the inflow velocity (as  $\omega^2 \gg u_{x,\infty}^2$ ) through Eq. 1.

After initially fixing the rotational speed  $n = 1.97418$  rps (by fixing  $\omega$ , see below) and the Reynolds number  $Re = 2e6$ , the value of  $u_{x,\infty}$  could be determined for a target  $J$  value using the following formula:

$$u_{x,\infty} = J \cdot (2nR) \quad (3)$$

The value of  $\omega$  was determined from the definitions of  $Re$  and  $u_{ref}$  as:

$$\omega = \nu Re / R \cdot \sqrt{1 / R^2 \left( \frac{J_0^2}{\pi^2} + 0.7^2 \right)}, \quad (4)$$

where  $J_0 = 0.7$ , but this can be set to any realistic value.

The k- $\omega$  SST model (Menter, 1994) was used as a turbulence model. The model was chosen after comparison with the SSG EARSM model of Speziale et al. (1991) and the SST 2003 formulation by Menter et al. (2003), with and without transition modeling (using the  $\gamma$ -model of Menter et al. (2015)). The original SST model showed the best agreement with the regression-based predictions. The propeller was accelerated from stand-still in an unsteady simulation and the rotating-frame method (also known as multiple reference frame method) was used to reduce the computational cost. Second-order discretization methods were used for the time, momentum and turbulence equations.

All computations were set up using the C-Wizard and run using FINE<sup>TM</sup>/Marine version 10.1 on a Linux-based HPC cluster using 96 CPU cores (2x Intel Xeon Platinum CLX-9242 48C). As the total number of time steps was fixed and equal for every computation, the total runtime of each computation was between 2 and 3 hours (clock time) depending on the mesh density. Only propellers for which thrust convergence was reached within a 1% tolerance of the average were included in the training sets for the neural network. The average was calculated over the last 30% of time steps.

## 2.5 Machine learning algorithm

For the presented study, a deep learning approach was used, implemented in the form of a geodesic convolutional neural network (GCNN). Such a neural network is trained on a large amount of training data obtained from CFD computations. The data can be in the form of integral values or field data plotted on two- and three-dimensional surfaces. Using a geodesic convolutional neural network is ideal for CFD computations because it does not require equidistant data points in the original data (i.e. CFD output) and accepts surface manifolds as input data. A thorough description of the underlying theory can be found in Baqué et al. (2018).

Of the initial number of 271 computations, 239 yielded converged results based on the previously defined criteria. The computations were subsequently divided into two sets using a 90-10 split; 90% of the computation formed the training set, while 10% of the computations were designated as the validation set to test the model.

Two sets of inputs for the neural network can be distinguished. First, data needs to be provided only for the training data set, consisting of the converged values of the thrust coefficient  $K_t$ , torque coefficient  $K_q$  and open-water

efficiency  $\eta$  (the “integrated quantities”) as well as the field quantities. The field quantities consist of the nondimensional axial velocity  $u'_x$  in the propeller wake and the pressure coefficient  $C_p$  on the propeller blades. Both are defined as:

$$u'_x = u_x/u_{x,\infty} \text{ and } C_p = P/1/2 \rho u_{ref}^2 \quad (5)$$

The field quantities were saved as surface CGNS data, while the integrated quantities were saved in comma-separated value files. A support grid needed to be constructed to represent the field quantities for the GCNN.

The second set of data needs to be provided for both the training and the exploitation of the model, and consisted of the STL definition of the blade geometry and the advance ratio  $J$ . For the research described in this paper, the geometry parameters pitch  $P$ , number of blades  $Z$  and the expanded area ratio  $EAR$  were explicitly provided to the neural network. However, the GCNN can learn straight from the provided STL without this explicit input, which can be exploited in future applications.

The GCNN was trained for approximately 240 thousand iterations, whereby at each iteration, the model is trained on results from a single propeller geometry. This means that the model training enters a new epoch every 239 iterations (i.e. equal to the number of propellers in the training set). The total training time of the neural network is 65 hours on a single GPU (Nvidia Tesla V100). Once the model has been trained, it takes roughly 0.3 seconds to interrogate the model and another 19.7 seconds to represent the data visually. This brings the total to 20 seconds that are needed to obtain a full performance curve and corresponding velocity and pressure fields for a new propeller geometry.

### 3 Results

The results for the integrated quantities and field quantities can be discussed using, on the one hand, the  $R^2$ -metric and on the other by checking differences between the AI prediction and the CFD result using the  $L_1$ -norm. The former relates to an entire set of samples (i.e. the training and the validation set), while the latter can be done on a sample-by-sample basis. The  $R^2$ -metric of the training and validation sets is the main indicator for conclusions regarding predictability and generality of the trained model. The  $R^2$ - and  $L_1$ -norms are defined as:

$$R^2 = 1 - \frac{\sum(\phi_{CFD} - \phi_{AI})^2}{\sum(\phi_{CFD} - \overline{\phi_{CFD}})^2} \text{ and } L_1 = \phi_{CFD} - \phi_{AI} , \quad (6)$$

where  $\overline{\phi_{CFD}}$  indicates the average of all CFD-values and  $\phi_{CFD}$  and  $\phi_{AI}$  denote respectively the CFD value and prediction by the GCNN. From Eq. 6 follows that if  $R^2$  is equal to 1, the predicted result exactly equals the CFD result for the entire set, while if  $L_1$  equals 0, there are no differences for a specific sample between the AI prediction and the CFD result.

#### 3.1 Integrated quantities

The values of  $R^2$  in Fig. 3 are very close to 1, indicating very good predictability of the model. The line of the validation set is very close to the line of the training set, indicating that the model generalizes well, i.e. it not only predicts  $K_t$ ,  $10K_q$  and  $\eta$  well on already seen data (training set), but also on unseen data (validation set). Tab. 1 shows the averaged sample-by-sample error (the difference between the AI prediction and the CFD result) for all three integrated quantities. The averaged error is at most 1.5% for all three quantities, and as such of the same order of magnitude of the modeling error usually accepted in CFD.

Table 1: Averaged sample-by sample error for integrated quantities

Quantity	Error $ \phi_{AI} - \phi_{CFD} $
$K_t$	<b>1.21%</b>
$10K_q$	<b>1.48%</b>
$\eta$	<b>1.50%</b>

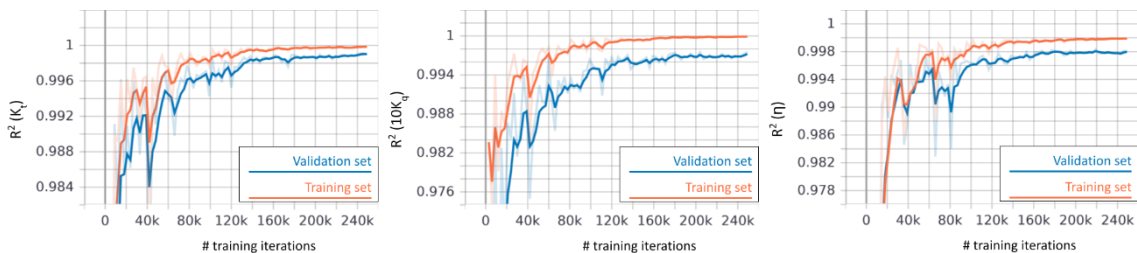


Figure 3 (f.l.t.r.): Evolution of  $R^2$  in function of the number of training iterations for  $K_t$ ,  $10K_q$  and  $\eta$ .

### 3.2 Field quantities

The  $R^2$  value for the field quantities  $u'_x$  and  $C_p$  is slightly lower than for the integrated quantities, as visualized in Fig. 4. The  $R^2$  value of the velocity field prediction on the validation set stagnates after the first 80,000 iterations around  $R^2 = 0.94$ . The value is slightly higher at  $R^2 = 0.98$  for the pressure. Given the proximity to  $R^2 = 1$  for both quantities and for both sets, it can be concluded that also for the field quantities, the currently trained model generalizes and predicts the solution well. The stagnation of the  $R^2$  value in the case of  $u'_x$  indicates that there may be an input-data related issue. This issue is addressed in more detail below.

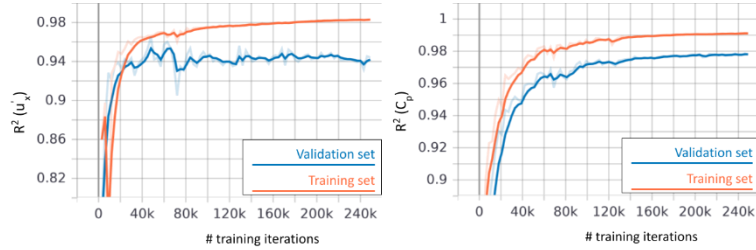


Figure 4 (f.l.t.r.): Evolution of  $R^2$  in function of the number of training iterations for  $u'_x$  and  $C_p$ .

Fig. 5 shows the best samples for the pressure coefficient of the 7- and 3-bladed Wageningen B-Series propellers that were tested. These were selected from the validation set and represented thus unseen data for the model. While the overall value of  $L_1$  is very low, especially on the blade surfaces, particularly the 7-bladed propeller displays slightly larger differences of around 5-8% between CFD and AI results closer to the tip.

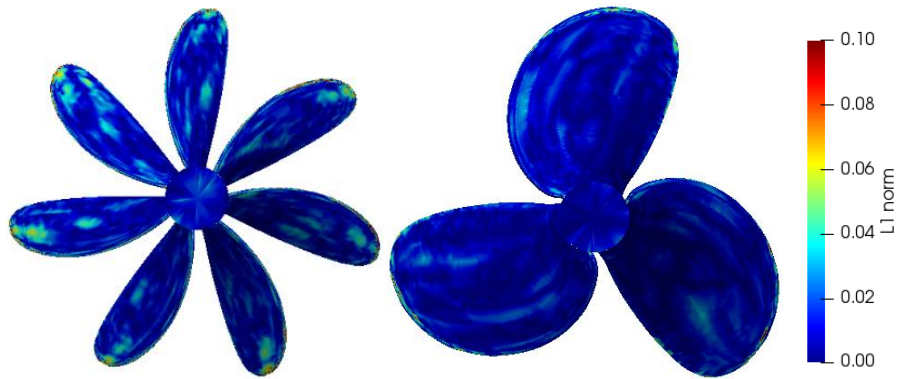


Figure 5: Value of the  $L_1$  norm on the best samples of 7-bladed and 3-bladed Wageningen B-Series propellers.

The plots in Fig. 6 comparing the axial velocity field at the different indicated stations A through E also show local differences in the order of a few percent. Results are given for the same 7-bladed propeller as in Fig. 5. Differences are largest around the radial location of maximal thrust (i.e.  $0.7R$ ). This difference may be due to unsteadiness of the flow field, present for some of the samples. It is probable that this is connected to the stagnating and relatively lower value of the  $R^2$  metric for the  $u'_x$  velocity field.

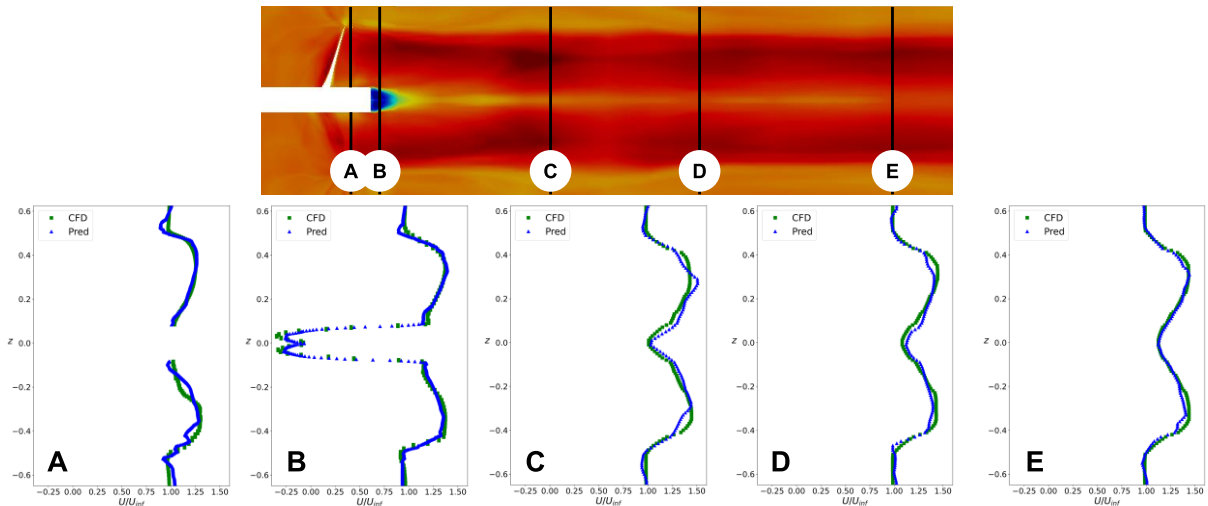


Figure 6: Nondimensional axial velocity field  $u'_x$  compared at different stations indicated above.

The earlier mentioned unsteadiness relates to the nature of the input for the machine learning algorithm. Given that the GCNN is trained based on field values, ideally those field values should represent a steady solution. If some of the results are unsteady, this perturbs the training of the GCNN. Unsteadiness in the wake of the propeller was found for some of the samples used to train the model, see Fig. 7. The unsteadiness was found for low values of  $J$  and follows from the longer time needed for the flow to stabilize at low inflow speeds. Given that the unsteadiness is linked to the transient solution, the computations should have run approximately twice as long in order to obtain only fully steady fields for all propellers and operating conditions.

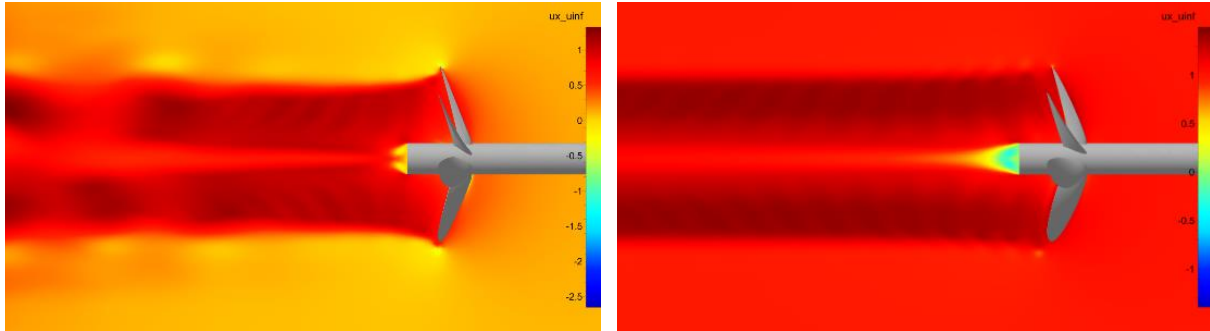


Figure 7: Unsteadiness present in the wake for low  $J$  values (left), compared to the expected steady wake result (right).

## 4 Conclusion

A working application of machine learning to a marine propeller has been demonstrated, where a geodesic convolutional neural network (GCNN) has been trained to predict both the integral quantities of an open-water performance curve and local field values of velocity and pressure on two-dimensional planes for Wageningen B-Series propellers. The GCNN was trained on 239 samples, of which 90% constituted the training set and the remainder the validation set. The values of the  $R^2$  metric were almost equal to 1 for the integrated quantities  $K_t$ ,  $K_q$  and  $\eta$  on both training and validation sets, indicating a very good prediction and generalization capability of the trained model for propellers in the Wageningen B-Series regarding integrated quantities. The average difference between the predicted and CFD-obtained value remained below 1.5% for all three integrated quantities. The local field quantities of nondimensional wake velocity  $u'_x$  and  $C_p$  showed slightly lower  $R^2$  values of respectively 0.94 and 0.98 for the validation set. Still, capabilities of the model to predict the local flow fields and its generalizability can be qualified as good, but improvement is possible. Unsteadiness in the flow field was identified for several cases with low advance ratios, perturbing the training of the GCNN and reducing the accuracy of the prediction for the  $u'_x$  field values. This underlines the importance of careful data selection prior to feeding the data to the GCNN as well as the requirement of understanding the present limitations of neural networks in dealing with unsteady data. It has been shown that when proper care is taken in data selection and computation parameters, machine learning can, in fact, enhance productivity for marine engineers in the initial design process of propellers by orders of magnitude. This is possible due to a drastic reduction in interrogation time from more than 200 CPU-hours per operating point in CFD to 20 seconds for an entire performance curve using a machine learning approach. A logical next step is testing the presented concept on resistance and self-propulsion applications.

## 5 References

- Baqu e, P., Remelli, E., Fleuret, F., & Fua, P. (2018, July). Geodesic convolutional shape optimization. In the International Conference on Machine Learning (pp. 472-481). PMLR.
- Kuiper, G. (1992). The Wageningen propeller series. *MARIN Wageningen, The Netherlands*.
- Menter, F. R. (1994). Two-equation eddy-viscosity turbulence models for engineering applications. *AIAA journal*, 32(8), 1598-1605.
- Menter, F. R., Kuntz, M., & Langtry, R. (2003). Ten years of industrial experience with the SST turbulence model. *Turbulence, heat and mass transfer*, 4(1), 625-632.
- Menter, F. R., Smirnov, P. E., Liu, T., & Avancha, R. (2015). A one-equation local correlation-based transition model. *Flow, Turbulence and Combustion*, 95(4), 583-619.
- Oosterveld, M. W. C., & van Oossanen, P. (1975). Further computer-analyzed data of the Wageningen B-screw series. *International shipbuilding progress*, 22(251), 251-262.
- Speziale, C. G., Sarkar, S., & Gatski, T. B. (1991). Modelling the pressure-strain correlation of turbulence: an invariant dynamical systems approach. *Journal of fluid mechanics*, 227, 245-272.

# Anderson Acceleration for Maritime Applications

Auke van der Ploeg

MARIN, Wageningen/Netherlands, a.v.d.ploeg@marin.nl

## 1 INTRODUCTION

In general, most of the computational effort required to do numerical simulations for maritime applications is spent to solve systems of non-linear equations. For time-dependent simulations such systems have to be solved every time step, and to be sure a correct time-dependent behavior is simulated, the time step cannot be chosen too large. To ensure that the accuracy of the simulations is not spoiled by grid dependence, sufficiently fine meshes have to be used, which causes these systems to become large. Therefore, in Ploeg, 2019 we studied the effectiveness of an acceleration strategy introduced in Anderson, 1965 to reduce the computational effort. In the sequel of this report, this strategy will be referred to as Anderson Acceleration (AA).

In Ploeg, 2019 it was shown that AA can significantly speed up the solution of the systems of non-linear equations as they occur in the computation of incompressible flows. Especially for 2D problems without turbulence, the improvement in convergence rate can be spectacular and a reduction in the required wall clock time of more than one order of magnitude can be obtained. However, for more realistic 3D test cases with turbulence, with meshes suited to resolve boundary layers, the reduction of the wall clock time was not as spectacular. Typically, a reduction of only 30% could be achieved. Moreover, the solution of the minimization problem required by the AA algorithm was not yet parallelized. In this paper, we address these issues. We will describe a parallelizable algorithm of AA including a proper scaling that improves the convergence also for realistic 3D cases.

## 2 DERIVATION AND ALGORITHM

The basic idea of Anderson Acceleration is to accelerate an existing iterative method by using information from previous iterates. This information is used to improve the approximate solution of the current iteration. Suppose that after discretization of the transport equations a system of non-linear equations is obtained that can be denoted by

$$\mathbf{r}(\mathbf{x}) = \mathbf{0} \quad \text{with} \quad \mathbf{r} : \mathbb{R}^n \rightarrow \mathbb{R}^n \quad (1)$$

The vector-valued function  $\mathbf{r}$  contains the values of the residual for the transport equations that have to be solved in each cell center. For example, if only the coupled system of momentum and mass equation have to be solved in three dimensions,  $\mathbf{r}$  contains four residual values for each cell center: three components from the momentum equation and the residual of the mass equation. Hence in that case the vector length  $n$  is four times the number of cells. In general,  $\mathbf{r}$  will also contain the residuals from other transport equations like those coming from a turbulence model or a transport equation for the volume fraction.

Equation (1) can be solved by a basic solution method without acceleration like SIMPLE (Semi-Implicit Method for Pressure-Linked Equations) Patankar and Spalding, 1972 or one of its variants like SIMPLER (SIMPLE Revised) Tannehill et al., 1997. Such a basic method constructs a sequence of estimates of the solution vectors  $\mathbf{x}_k$ ,  $k = 1, 2, \dots$ . In this paper, one step of such a method without acceleration will be denoted by  $\mathbf{B}$ . Without AA, at iteration  $k$  a new estimate is constructed as

$$\mathbf{x}_{k+1} = \mathbf{B}(\mathbf{x}_k) \quad (2)$$

If AA is applied at the  $k$ -th step of the iteration, first an 'optimized' update  $\tilde{\mathbf{x}}_k$  is constructed. Next, (2) is replaced by

$$\mathbf{x}_{k+1} = \mathbf{B}(\tilde{\mathbf{x}}_k)$$

To be able to construct  $\tilde{\mathbf{x}}_k$ , the residual vectors together with the solution vectors of some previous iterations have to be stored in memory. Of course, we have to choose a maximum number of such vectors. This number will be denoted by  $m$ , and the resulting AA method to accelerate the computation will be

denoted by  $AAm$ . We use a so-called first-in-first-out strategy. At each iteration the vectors are shifted: the current residual vector and solution vector are added and, if the resulting number of residual vectors exceeds  $m$ , the 'oldest' vectors are deleted.

For ease of presentation, we will first assume that  $k > m$ . Solving  $\mathbf{r}(\mathbf{x}) = \mathbf{0}$  is equivalent to solving the fixed point problem  $\mathbf{x} = \mathbf{g}(\mathbf{x})$  in which the operator  $\mathbf{g}$  is defined by

$$\mathbf{g}(\mathbf{y}) = \alpha \mathbf{r}(\mathbf{y}) + \mathbf{y} \quad \text{for any given vector } \mathbf{y}. \quad (3)$$

Herein  $\alpha$  is a positive parameter to be chosen in advance.

The  $AAm$ -algorithm updates the solution vector as

$$\tilde{\mathbf{x}}_k = \sum_{i=0}^m \theta_i \mathbf{g}(\mathbf{x}_{k-i}) \quad \text{satisfying the constraint} \quad \sum_{i=0}^m \theta_i = 1. \quad (4)$$

The vector  $\mathbf{x}_{k-1}$  indicates the solution from the previous iteration, the vector  $\mathbf{x}_{k-2}$  the solution from the previous previous iteration etc. The zero-sum constraint is necessary to guarantee that at a converged stage at which  $\mathbf{x} = \mathbf{x}_{k-i}$  for  $i = 0, \dots, m$ ,  $\tilde{\mathbf{x}}_k = \mathbf{g}(\tilde{\mathbf{x}}_k)$ . From this constraint it follows that  $\theta_0 = 1 - \sum_{i=1}^m \theta_i$ . To ensure that new information is incorporated into  $\tilde{\mathbf{x}}_k$ ,  $\theta_0$  should be positive.

The coefficients  $\theta_1, \dots, \theta_m$  are determined in such a way that in the special case in which  $\mathbf{r}$  is linear

$$\|\mathbf{r}(\tilde{\mathbf{x}}_k)\|_2 \quad \text{is minimized.} \quad (5)$$

Therefore  $\mathbf{r}(\tilde{\mathbf{x}}_k)$  is expressed as a function of  $\theta_1, \dots, \theta_m$ :

$$\mathbf{r}(\tilde{\mathbf{x}}_k) = \mathbf{g}(\mathbf{r}(\mathbf{x}_k) - \mathbf{R}\boldsymbol{\theta}) \quad (6)$$

in which the  $i$ -th column of the  $n \times m$  matrix  $\mathbf{R}$  consist of  $\mathbf{r}(\mathbf{x}_k) - \mathbf{r}(\mathbf{x}_{k-i})$  and the vector  $\boldsymbol{\theta} = (\theta_1, \dots, \theta_m)^T$ .

To prove this equation we rewrite  $\tilde{\mathbf{x}}_k$  using (4):

$$\tilde{\mathbf{x}}_k = \left(1 - \sum_{i=1}^m \theta_i\right) \mathbf{g}(\mathbf{x}_k) + \sum_{i=1}^m \theta_i \mathbf{g}(\mathbf{x}_{k-i}) \quad (7)$$

$$= \mathbf{g}(\mathbf{x}_k) + \sum_{i=1}^m \theta_i [\mathbf{g}(\mathbf{x}_{k-i}) - \mathbf{g}(\mathbf{x}_k)] \quad \implies \quad (8)$$

$$\mathbf{r}(\tilde{\mathbf{x}}_k) = \mathbf{r} \left( \mathbf{g}(\mathbf{x}_k) + \sum_{i=1}^m \theta_i [\mathbf{g}(\mathbf{x}_{k-i}) - \mathbf{g}(\mathbf{x}_k)] \right) \quad (9)$$

Note that, if  $\mathbf{r}$  is linear, the operators  $\mathbf{r}$  and  $\mathbf{g}$  commute:

$$\mathbf{r}(\mathbf{g}(\mathbf{y})) = \mathbf{r}(\alpha \mathbf{r}(\mathbf{y}) + \mathbf{y}) = \alpha \mathbf{r}(\mathbf{r}(\mathbf{y})) + \mathbf{r}(\mathbf{y}) = \mathbf{g}(\mathbf{r}(\mathbf{y})) \quad \text{for any given vector } \mathbf{y}.$$

Therefore, from (9) we obtain

$$\begin{aligned} \mathbf{r}(\tilde{\mathbf{x}}_k) &= \mathbf{g} \left( \mathbf{r}(\mathbf{x}_k) + \sum_{i=1}^m \theta_i [\mathbf{r}(\mathbf{x}_{k-i}) - \mathbf{r}(\mathbf{x}_k)] \right) \\ &= \mathbf{g}(\mathbf{r}(\mathbf{x}_k) - \mathbf{R}\boldsymbol{\theta}) \end{aligned}$$

which proves (6) for  $\alpha > 0$ . If  $\alpha = 0$ ,  $\mathbf{g}$  is the identity operator and in that case (6) holds as well.

From (5) and (6) it follows that  $\|\mathbf{r}(\mathbf{x}_k) - \mathbf{R}\boldsymbol{\theta}\|_2$  must be minimized, independent of the value of  $\alpha$ . This is done by solving the system of linear equations  $\mathbf{R}\boldsymbol{\theta} = \mathbf{r}(\mathbf{x}_k)$  in a least-squares sense. In other words,  $\boldsymbol{\theta} = (\theta_1, \dots, \theta_m)^T$  follows from the solution of

$$\mathbf{R}^T \mathbf{R} \boldsymbol{\theta} = \mathbf{R}^T \mathbf{r}(\mathbf{x}_k) \quad (10)$$

## 2.1 Parallelization

Building the coefficient matrix and the right-hand side vector of the linear system (10) is computationally expensive, because each entry of both the matrix  $\mathbf{R}^T \mathbf{R}$  and the right-hand side vector  $\mathbf{R}^T \mathbf{r}(\mathbf{x}_k)$  consists of an inner-product of two vectors having as many components as the number of cells times the number of unknowns per cell. Suppose that a domain decomposition approach is combined with an MPI parallelization approach, in which the data corresponding to each sub-domain is stored on a separate processor. In that case, all vectors are distributed over all processors, and computing the matrix and right-hand side vector in (10) can easily be parallelized. Inner-products of only the local parts of the vectors can be computed locally on each processor without needing any communication. Next, all these local parts can be summed in only one simultaneous step that needs communication.

The size of (10) is  $m$ , which is typically between 5 and 10. It hardly takes any memory to store this small system and, once the matrix and right-hand side have been built, the computational effort to solve it is also negligible. Therefore, (10) is solved on every processor so it is not necessary to distribute the solution over all processors afterwards.

## 2.2 Scaling of the residuals

As mentioned before, the  $i$ -th column of the  $n \times m$  matrix  $\mathbf{R}$  consist of  $\mathbf{r}(\mathbf{x}_k) - \mathbf{r}(\mathbf{x}_{k-i})$ . For some applications, the effect of AA can be improved considerably by using a proper scaling of the residual vectors. To be precise, by replacing  $\mathbf{R}$  in (10) with  $\mathbf{D}^{-1} \mathbf{R}$  in which  $\mathbf{D}$  is a proper chosen diagonal matrix. We choose as  $\mathbf{D}$  the diagonal matrix taken from the discretized momentum equations. The effect of this scaling will be demonstrated in Section 3.1.

## 2.3 Algorithm

The AA acceleration can be applied at every step of the iteration, but to reduce the overhead, it is also possible to apply it only every second, third or fourth iteration. The frequency to apply AA can be controlled by the parameter `frequency_AA`. Summarizing, a pseudo-code of the algorithm is given by:

### Algorithm 1: Basic method B accelerated by Anderson Acceleration:

```
Given  $\mathbf{x}_0$  and  $m \geq 1$ :
Set  $\mathbf{x}_1 = \mathbf{B}(\mathbf{x}_0)$ ;
For  $k = 1, 2, \dots$ 
  IF mod(k, frequency_AA) == 0 THEN
    Compute the residual  $\mathbf{r}(\mathbf{x}_k)$ ;
    Set  $m_k = \min(m, k)$ ;
    Set  $\mathbf{R} = \mathbf{D}^{-1} \mathbf{R}$ ;
    Determine  $\boldsymbol{\theta} = (\theta_1, \dots, \theta_{m_k})^T$  from  $\mathbf{R}^T \mathbf{R} \boldsymbol{\theta} = \mathbf{R}^T \mathbf{r}(\mathbf{x}_k)$ 
    IF  $\sum_{i=1}^{m_k} \theta_i < 1.0$  Set  $\mathbf{x}_k = \mathbf{g}(\mathbf{x}_k) + \sum_{i=1}^{m_k} \theta_i [\mathbf{g}(\mathbf{x}_{k-i}) - \mathbf{g}(\mathbf{x}_k)]$ 
  ENDIF
Set  $\mathbf{x}_{k+1} = \mathbf{B}(\mathbf{x}_k)$ 
```

## 3 RESULTS

The results described in this section were obtained with the RANS code REFRESCO ([www.refresco.org](http://www.refresco.org)), a community based CFD code for the maritime world. It solves multiphase (unsteady) incompressible viscous flows using the Navier-Stokes equations, complemented with turbulence models, cavitation models and volume-fraction transport equations for different phases. The equations are discretised using a finite-volume approach with cell-centered collocated variables, in strong-conservation form.

In Ploeg, 2019 it was already shown that for applications without turbulence, especially for easy 2D cases, Anderson Acceleration (AA) can significantly speed up the computation. To illustrate the effect of AA for real-life 3D cases including turbulence, the flow around a propeller and around a ship is computed. The k-omega SST-turbulence model is used and the transport equations are solved up to the walls at which no-slip boundary conditions are applied. In order to capture the boundary layer, a strong refinement of the mesh towards these walls is used:  $y^+$ -values are all below 1.

### 3.1 Propeller

The flow around the four-bladed skewed INSEAN E779A propeller is computed for advance coefficient  $J = 0.845$ , using a structured mesh with 1.2 million cells. The Reynolds number is  $5 \cdot 10^5$ . The left picture in Fig. 1 shows the wall mesh and the right-picture shows the effect of AA on the convergence behavior. The text in the boxes has the same color as the corresponding line, and shows the required wall clock times. As mentioned before,  $AA_m$  denotes the AA method in which the dimension of the search space is  $m$ . Hence the solution method without AA is indicated by AA0. Implicit and explicit relaxation parameters were determined in such a way that the solution method without AA gives the best convergence behavior.

Initially, the effect of AA was rather disappointing, as shown by the black line: AA worsens the convergence behavior. It appeared that the effect of AA could be improved considerably by scaling the residual vectors as described in Section 2.2. With this scaling, AA shows an improvement of the convergence behavior as is illustrated by the blue line, and decreases the wall clock time from 161 seconds to 98 seconds. The relatively strong effect of this scaling can probably be explained by the strong refinement of the mesh towards the walls. For the 'easy' test cases described in Ploeg, 2019 the scaling of the residuals did not have a significant effect.

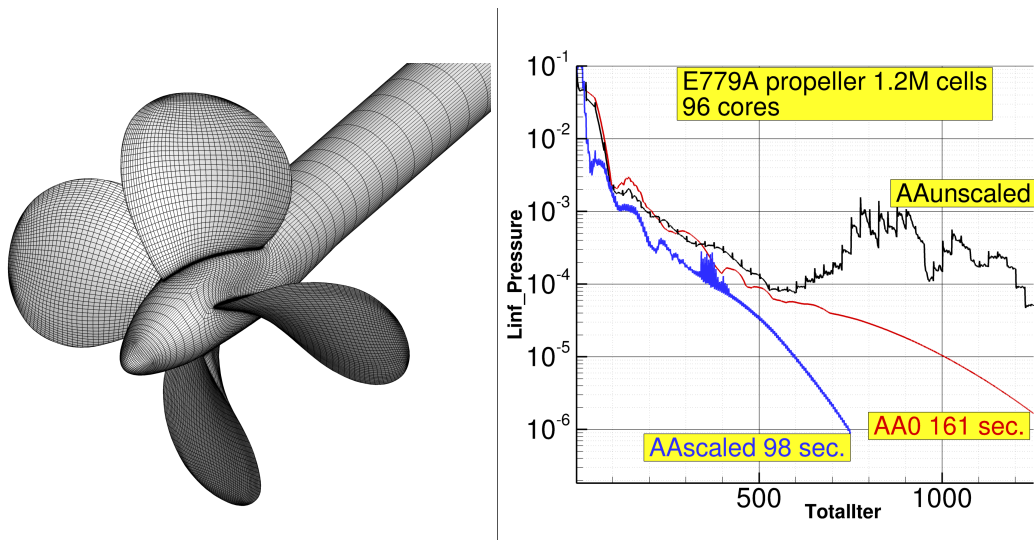


Fig. 1: Left: illustration of the wall mesh on the E779A propeller. Right: Effect of AA10 with  $frequency\_AA=5$ .

### 3.2 KVLCC2

The flow around the model-scale KVLCC2 tanker is computed, using two types of meshes, a relatively coarse unstructured mesh that contains 0.18M cells and two relatively fine structured meshes that contain 2.7M and 10M cells. The Reynolds number is  $4.7 \cdot 10^6$ . Fig. 2 illustrates the two mesh types on the undisturbed water surface. For illustration purposes, the left picture shows a much coarser mesh than used in the computations. The wall mesh on the aft part of the ship is shown in the left picture of Fig. 3. The right picture shows the effect of AA on the convergence behavior and the wall clock time in case the unstructured mesh is used. Herein for example AA10f5 indicates the AA method in which the parameters  $m = 10$  and  $frequency\_AA = 5$ . To demonstrate the effect of AA on the convergence behavior, we use a more tight convergence criterion than required in practice. A typical convergence criterion in practice for the maximum norm of the residual would be around  $10^{-4}$ . It appears that at the early stage of the iteration AA gives no improvement, but at the later stage it does. Increasing the parameter  $frequency\_AA$  from 1 to 5 hardly affects the convergence behavior but it significantly reduces the overhead of AA, making the computation with AA more than twice as fast than without.

Fig. 4 shows the effect of AA10, when applied only every fifth iteration, on the convergence of the



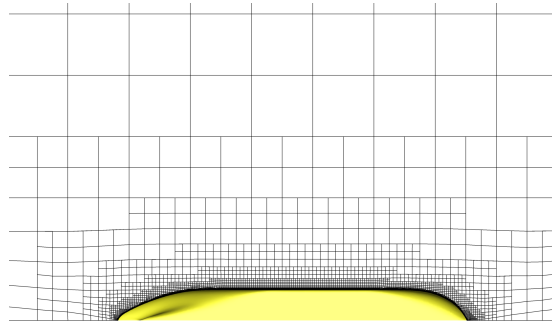
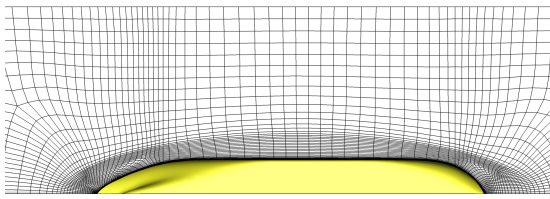


Fig. 2: Mesh types used for the KVLCC2 case. Left: structured. Right: unstructured.

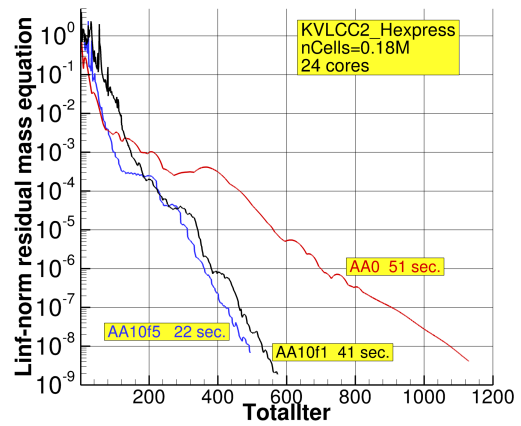
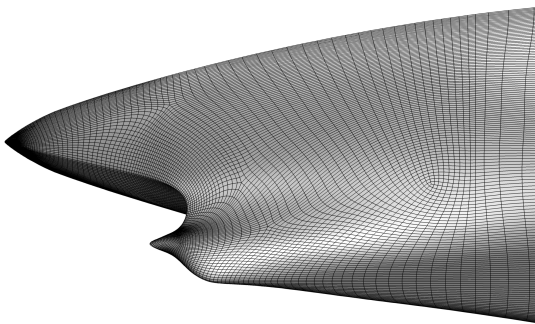


Fig. 3: Left: Illustration of the wall mesh around the aft body of the KVLCC2 tanker using an unstructured mesh. Right: effect of AA10 on the convergence of the segregated solver.

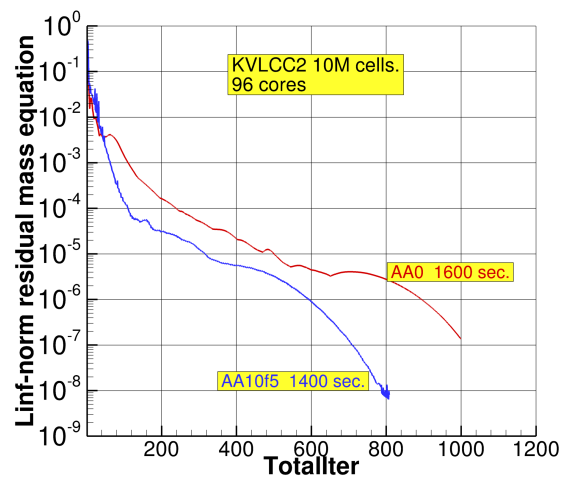
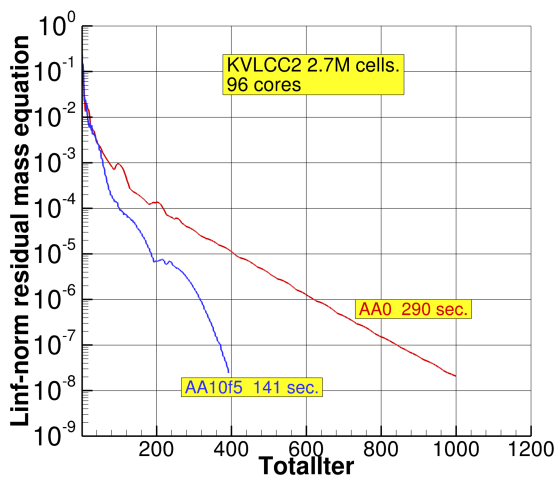


Fig. 4: Effect of AA10 on the convergence of the segregated solver when computing the flow around the KVLCC2 tanker using structured meshes. Frequency\_AA=5. Left: 2.7M cells. Right: 10M cells.

segregated solver when using both structured meshes. From this figure, we can conclude the following

- Again Anderson Acceleration significantly improves the convergence behavior.
- For the mesh containing  $2.7M$  cells AA reduces the wall clock time with more than a factor of two. For the finest mesh, without AA the tight acceptance criterion  $10^{-8}$  is not reached within 1000 iterations, whereas with AA this criterion is reached in 800 iterations.
- For this case, with the above-mentioned acceptance criterion for practical application  $10^{-4}$ , AA also improves the convergence behavior.

#### 4 Conclusions

In this paper, we have described a parallelizable version of Anderson Acceleration (AA) that can reduce the computational effort required to do numerical simulations for maritime applications. The main overhead of AA is the construction of a minimization problem which can easily be parallelized. Because the corresponding system of linear equations is very small, its actual solution hardly takes any computational effort and can be done on every processor to avoid communication.

Realistic 3D cases with meshes suited to resolve viscous boundary layers require a proper scaling of the residuals that are used to set up the minimization problem in AA. With such a scaling, AA can significantly improve the convergence also for these cases but the reduction of the wall clock time is not as spectacular as for easy problems without turbulence. Still, if the turbulent flow around a propeller or a ship is computed, a reduction of more than a factor of 2 can be achieved. Similar results are obtained with both structured and unstructured meshes.

In this research AA was used to accelerate only the coupling between the mass and momentum equations. Future research should focus on how AA can be used to accelerate the complete set of equations, including those coming from turbulence or cavitation models and volume-fraction transport equations for different phases.

#### References

- Anderson, D. (1965). Iterative Procedures for Nonlinear Integral Equations. *Journal of the Association for Computing Machinery*, 12(4):547–560.
- Patankar, S. V. and Spalding, D. B. (1972). A calculation procedure for heat, mass and momentum transfer in three-dimensional parabolic flows. *Int. J. Heat Mass Transfer*, 15:1787–1806.
- Ploeg, A. v. d. (2019). Anderson-Accelerated Convergence for Incompressible Navier-Stokes Equations. *In Proceedings of 22nd Numerical Towing Tank Symposium (NuTTS'19), Tomar, Portugal*.
- Tannehill, J. C., Anderson, D. A., and Pletcher, R. H. (1997). *Computational Fluid Mechanics and Heat Transfer*. Taylor & Francis.

## Eulerian-Eulerian multiphase flow and turbulence modelling of hydrofoil cavitation

V. Viitanen<sup>1,\*</sup>, J. Peltola<sup>1</sup>, A. Jaatinen-Värri<sup>2</sup>

<sup>1</sup>VTT Technical Research Centre of Finland Ltd.

<sup>2</sup>Lappeenranta University of Technology, Lappeenranta, Finland.

\*Corresponding author: ville.viitanen@vtt.fi

### 1. Introduction

Cavitating flow problems are commonly assessed numerically with homogeneous mixture flow models. The multiphase flow is then treated using single continuity, momentum and turbulence equations for the mixture of phases, at the same time ignoring many phase interaction mechanisms in dispersed systems. The cavitation can appear in a range of different forms such as sheet, cloud and vortex cavitation that occur at different temporal and spatial scales. An inhomogeneous Euler-Euler (EE) modelling relies on conservation equations for each phase, and interfacial transfer terms are included which can allow a physically more sound framework for cavitating flow predictions.

We investigate steady and unsteady cavitation on a planar hydrofoil in a cavitation tunnel, as well as tip vortex cavitation on an elliptic hydrofoil. The flow solutions with a volume-of-fluid (VOF) cavitation mixture and EE models are compared, and different turbulence modelling approaches are utilized. We use the OpenFOAM flow solver.

### 2. Numerical methods

The used homogeneous flow solver application `interPhaseChangeFoam` is based on the Navier-Stokes equations for two incompressible, isothermal and immiscible fluids with phase-change accounted for by mass-transfer models. The continuity and momentum equations as well as the turbulence modelling is applied for the mixture. Several mass-transfer models such as those of Kunz [1] and Schnerr [2] are readily available, and we have recently implemented the Zwart [3] model for this solver as well.

The employed EE multiphase solver is a general-purpose CFD solver in OpenFOAM Foundation release [4, 5] for  $n$ -phase compressible and incompressible flow problems featuring heat transfer, chemistry and mass transfer. The solver application is called `multiphaseEulerFoam`. Continuity and momentum equations are used for each phase. A selection of interfacial force and transfer models is available, as well as single-phase and multiphase specific turbulence modelling approaches for RANS and LES applications. Interfacial transfer models are used for each phase pair. The interfacial momentum transfer terms consist in general of drag, lift, virtual mass, turbulent dispersion and wall lubrication forces, and there are numerous run-time selectable options for modelling of each interfacial forces, applicable for different multiphase flow configurations and flow topologies. A population balance modelling is used to predict the local mean dispersed phase diameter. The turbulence models can be chosen for each phase separately, and both liquid and gas phases are primarily modelled with SST  $k-\omega$  RANS model. Selected cases are simulated also with a DDES (delayed detached eddy simulation) hybrid RANS-LES approach.

Several cavitation mass-transfer models have been developed, and the mass-transfer rate is typically proportional to a pressure difference from the saturated state, or to the square root of that. In the present work, we applied the mass-transfer term to the phase continuity equations in the EE model via user-defined source terms. The evaporation and condensation are accounted for with either the Kunz or Schnerr model.

### 3. Test cases

The first test case is a NACA66mod a=0.8 hydrofoil in a cavitation tunnel [6]. The chord length is  $c = 0.15$  m. We conducted the simulations using the free stream velocity of  $V_\infty = 5.33$  m/s with the foil at an angle of attack of  $6^\circ$ . Two conditions are investigated with different cavitation numbers  $\sigma = 2(p - p_{\text{sat}})/(\rho_\infty V_\infty^2) = 1.41$  and  $1.25$ . These give steady and unsteady cavitation, respectively. The second test case is a foil with elliptical planform and a NACA66<sub>2</sub>-415 cross section [7]. The foil chord  $c = 0.1254$  m, its span is  $0.15$  m, and it is set at an angle of attack of  $7^\circ$ . The free stream velocity is  $V_\infty = 6.8$  m/s, and we consider a single case with  $\sigma = 0.87$ .

The two-dimensional grid for the planar hydrofoil is shown in Fig. 1, which consists of roughly 63k cells. The inlet is located  $4c$  and the outlet  $8c$  from the leading edge (LE). Fig. 2 shows the computational domain and grid for the elliptical foil. Two grids were constructed for this case. The coarse grid consists of around 1.8M cells, and the fine grid consists of roughly 8.8M cells. Specific attention was put on the grid resolution near the tip vortex, as shown in Figs. 2(b) and (c), and we mainly increased the grid resolution in the vicinity of the tip vortex for the finer grid. The inlet is located  $4c$  and the outlet  $10c$  from the LE. Grid points were clustered toward solid surfaces for all investigated cases to obtain an average  $y^+ \approx 20$  for use with turbulence model wall functions.

The hydrofoils are modelled with no-slip boundary condition. The top and bottom tunnel walls for the planar hydrofoil and the side to which the elliptic hydrofoil is attached (Fig. 2) are modelled as no-slip boundaries. For the elliptical foil, the other tunnel walls are modelled as slip boundaries. The velocity is set at the inlet to the prescribed value of  $V_\infty$ , and the pressure is

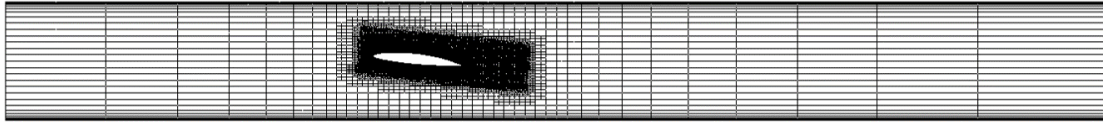
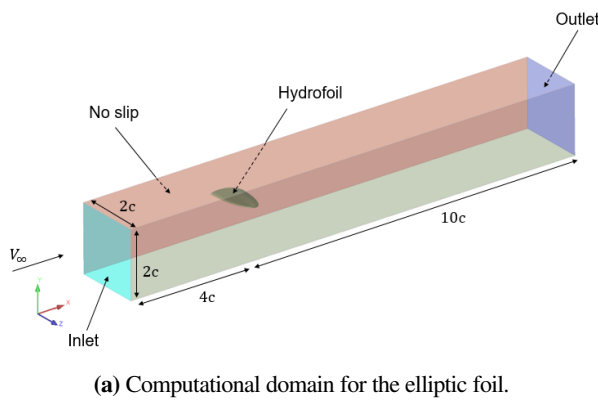
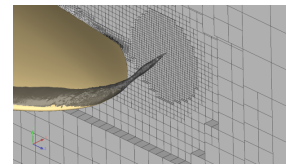


**Figure 1:** Computational grid for the planar hydrofoil. The flow is from left to right.

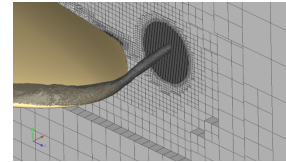
extrapolated. At the outlet, the pressure is specified to the free stream pressure, and all other quantities are extrapolated from the computational domain. The finite volume method with second-order spatial discretization is used for the flow equations. Simulations are conducted as time-accurate using an Euler implicit scheme for the time derivatives. The physical time-step is adjusted adaptively during the solution based on a maximum Courant number criterion of  $Co \leq 1$ . A compressive discretization is applied for the convection terms of the volume fraction equations in both the VOF and EE approaches. A TVD limited central difference scheme was used for the convection terms in the momentum equations. Convection terms for turbulence quantities were evaluated with a second-order upwind-biased scheme. We applied the mass-transfer models in all cases using their "default" parameter values. The wall-clock time consumed by the EE model for an iteration cycle within a time step was around three times that of the VOF model for the present simulations. The maximum time steps attained in the simulations were around  $1 \times 10^{-5}$  s for both modelling approaches which were limited by the chosen maximum Courant numbers.



**(a)** Computational domain for the elliptic foil.



**(b)** Coarse grid close to the tip.



**(c)** Fine grid close to the tip.

**Figure 2:** Utilized numerical grid for the elliptic hydrofoil.

## 4. Results

### 4.1. Planar hydrofoil

For the case of steady cavitation and  $\sigma = 1.41$ , the measured and simulated pressure distributions ( $C_p = 2(p - p_\infty) / (\rho_\infty V_\infty^2)$ ) on the hydrofoil are shown in Fig. 3. The cavitation extents are visualized in Fig. 4. The sharp pressure gradient is visible at around  $x/c \approx 0.3 \dots 0.4$  corresponding to the closure of the sheet cavity. VOF methods with Zwart and Schnerr mass-transfer models predict a steep pressure drop occurring a bit later, and consequently also a bit longer cavity extents as seen in Fig. 4, although the deviations there do not appear to be as great. The Kunz model shows clearly shorter predicted cavity, and we see

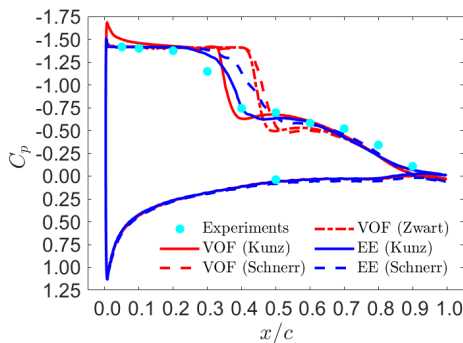


**Figure 3:** Pressure distributions on the hydrofoil at  $\sigma = 1.41$ .

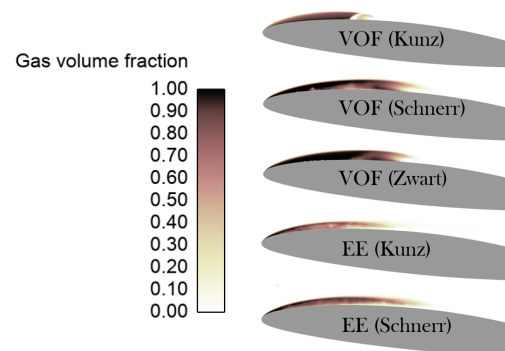


**Figure 4:** Cavitation extent at  $\sigma = 1.41$ .

a corresponding  $C_p$  drop to take place earlier matching the experimental result. The cavitation extents in Fig. 4 predicted by the EE approaches appear as a bit thinner than those given by the VOF models, and they also yield a cavity 'tail' downstream of the station  $x/c \approx 0.3$  whereas very close to the foil surface there is next to no vapour present but rather a liquid film after this station, contrary to the VOF predictions. EE simulations with Kunz model have very good correspondence with the

experiments in terms of the surface pressure distribution. Also the results with Schnerr model agree well with the experiments. We note that in previous studies a second-order upwind biased scheme for momentum equations for the homogeneous model turned out too diffusive to allow capturing of the steep pressure gradient. Instead, a low diffusive limited central difference scheme was needed. Additionally, it is known that homogeneous model results can be sensitive to the parameters used for the mass-transfer models. An interesting remark is that the Kunz model predicts negative pressure magnitudes close to the LE, whereas the Schnerr or Zwart models give the smallest pressure in the simulations to be approximately equal to the vapour pressure. We can observe this also in the  $C_p$  plots in Fig. 3. A similar behaviour occurred in the EE simulations with Kunz and Schnerr models, which we also noted in the simulations with the elliptic hydrofoil.

The case with  $\sigma = 1.25$  featured unsteady cavitation with a periodic growth and destabilization cycle. The frequencies corresponding to the periodic cavity shedding were 3.6 Hz in the experiments, and 3.8 Hz in VOF and 3.9 Hz in EE simulations with the Kunz mass-transfer model. One cycle is depicted in Fig. 5 which shows the experimental results together with the VOF and EE solutions. The cavity extent grows until reaching a maximum length after which a vapour cloud is broken off and shed to the wake and then convected downstream. Having travelled about half a chord length downstream the vapour clouds collapse, which leads to disappearance of the remaining attached sheet cavitation on the hydrofoil. This completes one cavitation shedding cycle. Two mechanisms control the cavitation dynamics, namely the formation of the re-entrant jet which is responsible of the initial cloud break-off, and a pressure wave induced by the collapse of the shed cavity cloud.

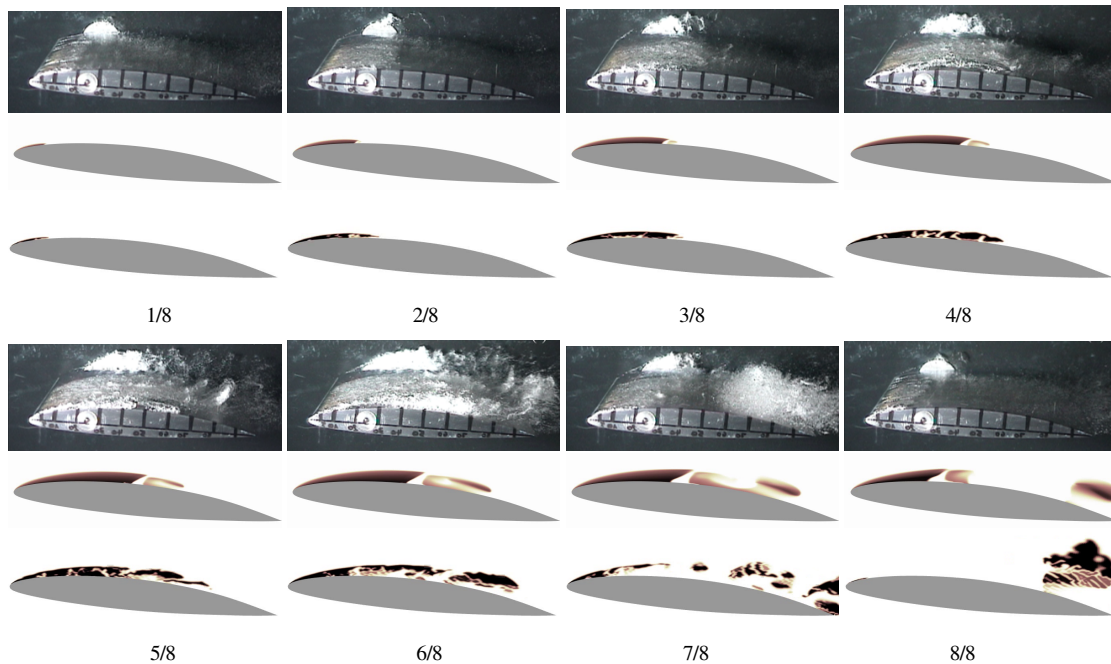


**Figure 5:** Visualization of cavitation growth and destabilization at  $\sigma = 1.25$ . The time between two consecutive images is 25 ms. Top row: experiments [6]. Second row: VOF model. Third row: EE model. Same colour scale as in Fig. 4.

#### 4.2. Elliptic hydrofoil

The measured lift coefficient was 0.58 [7]. CFD predicted values using the SST were 0.59 with the VOF model and 0.58 with the EE model. Here, mainly the Schnerr mass-transfer model was applied. We obtained similar numerical results with the coarse and fine grids used, which was expected since the grid was refined mainly in the tip vortex region. DDES on the fine grid using the VOF model gave the  $C_L = 0.59$ , and the EE model gave the  $C_L = 0.57$ . The predicted lift coefficients are very close to the experimental result; the VOF model simulations give a bit greater  $C_L$  values and the EE model simulations slightly smaller  $C_L$  values.

Fig. 6 shows the cavitation extent with a photograph from the experiments together with numerical results where we used the iso-surface of the void fraction of 0.1 to depict the cavitation. The foil has a strong tip vortex cavitation with several modes visible. Based on the numerical results, the foil exhibits also a short attached sheet cavitation near the LE as seen also in Figs. 7, 10 and 11. The simulations underpredict the size as well as the modes of the vortex cavitation. The vapour distributions with VOF and EE models in the cavitating tip vortex are displayed in Fig. 8 at  $x/c = 0.1$  together with the grid lines. Around 10 cells covered the cavitating tip vortex. Vapour concentration at the tip vortex core was greater with the EE model. A similar observation can be made from Fig. 10. Fig. 9 shows the diameters of the cavitating tip vortex at  $yz$ -planes on different  $x/c$  values from the corresponding simulations. We see that the predicted diameters near the foil are similar between the different models, and the VOF model yields a bit greater values farther from the foil. Some modes are visible in the tip vortex diameter graphs although not as distinctively as observed in the experiments. The resolution of the cavitating tip vortex is sensitive to the utilized grid density (Fig. 7), and the coarse grid simulations predicted the

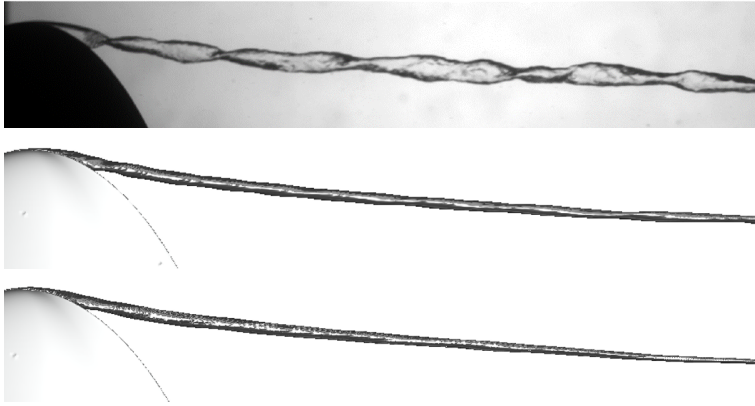


**Figure 6:** Tip vortex cavitation extent. Top: experiments. Middle: VOF model. Bottom: EE model. DDES on fine grid, and iso-surfaces of  $\alpha_g = 0.1$  shown.

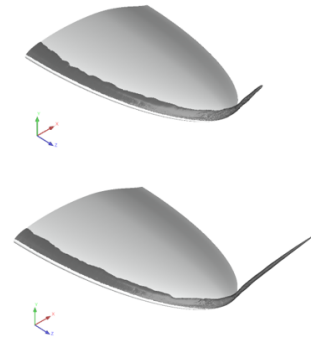


**Figure 7:** Results on different grids. EE with SST. Coarse (top) and fine (bottom) grids.

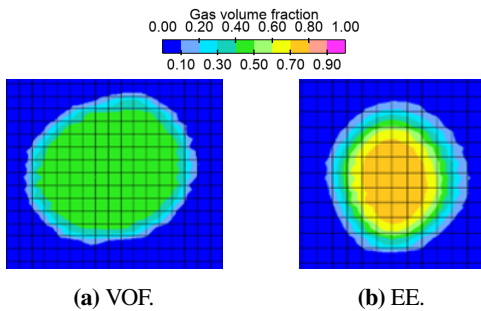


**Figure 8:** Gas fraction in the cavitating tip vortex at  $x/c = 0.1$ .

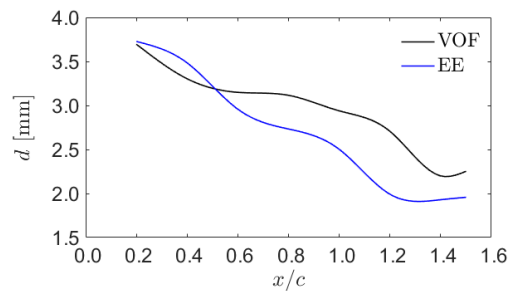


**Figure 9:** Diameters of the cavitating tip vortex at different  $x/c$  planes.

tip vortex extent to just reach the foil TE. It is clear from Fig. 6 that also the utilized fine grid is too coarse to capture properly the extent of the cavitation and especially its modes. In terms of the cavitation prediction, not much difference was seen in EE results between Schnerr and Kunz models, although this comparison is not shown here.

Fig. 10 visualizes the cavitation extent with different void fraction iso-surfaces. The VOF simulations predict a smaller vapour content than the EE method in the tip vortex as evidenced by the quick disappearance of the cavity with the greater gas volume fraction iso-surfaces. This is visible also in Fig. 8.

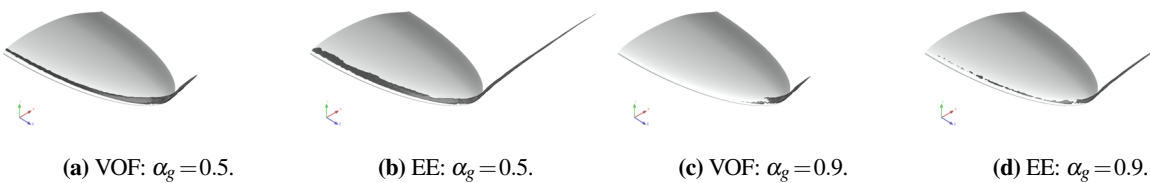


**Figure 10:** Visualization of cavitation extent with different void fraction iso-surfaces. DDES on fine grid.

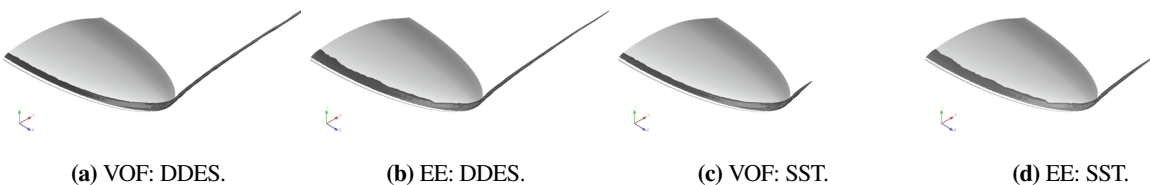


**Figure 11:** Visualization of cavitation extent  $\alpha_g = 0.1$  with different turbulence modelling approaches. Fine grid.

Fig. 11 compares the predicted cavitation extents with different turbulence modelling approaches for the VOF and EE simulations. Additionally, Fig. 12 compares the EE model predictions from different turbulence modelling approaches in terms of vortical flow structures based on the mixture velocity  $Q$ -criterion. The DDES improves the prediction of the tip vortex extent. This is evident also comparing Figs. 6 and 7. Although not shown here, this improvement was due to the fact that the predicted gas eddy viscosity levels were an order of magnitude larger with the SST model than with the DDES

as noted also in earlier studies [8, 9], which then quickly dissipate the vortical and cavitating flow. Vortical flow drawn up from the pressure side is more pronounced with DDES. We observed a corresponding tendency for eddy viscosity with the VOF method utilizing the SST and DDES turbulence modelling approaches.



**Figure 12:** Vortical flow near the tip as viewed from the suction side with different turbulence modelling. EE simulations on the fine grid. Visualization with  $Q=5 \times 10^4$  based on volumetric mixture velocity.

## 5. Summary

Hydrofoil cavitation predictions with the utilized VOF and EE models gave results matching quite well with corresponding experiments. The foil pressure distribution was somewhat better predicted by the EE models although differences were not major. Applications of different cavitation mass-transfer models can influence the results, and this effect seemed less for the EE models in the considered steady case. Tip vortex cavitation predictions can be improved by utilizing high-fidelity turbulence modelling approaches such as hybrid RANS-LES ones, or non-linear eddy viscosity closures. Still, its resolution can be quite sensitive to the utilized grid density. The tip vortex cavitation in the present case appeared as quite stationary and well segregated and thus the application of an inhomogeneous approach may not affect a lot the numerical prediction in such cases. Unsteady cavitation phenomena that feature a wider range of multiphase phenomena are also considered in the future. A grid sensitivity study is planned to further evaluate the abilities of the different models for the steady and unsteady cavitating flow predictions. In addition, interesting alternatives for combinations of mass-transfer models and predicted dispersed phase composition available from the EE solution are possible in the future.

## Acknowledgements

V. Viitanen and J. Peltola would like to express their gratitude for the support granted by Business Finland within the project “ModProp”. The authors also wish to thank Prof. J. Andre Astolfi from Research Institute of the Naval Academy, France, for kindly providing the experimental results for the planar hydrofoil. The numerical simulations were performed on HPC cluster of VTT (“The Doctor”) and CSC – IT Center for Science, Finland.

## References

1. R.F. Kunz, D.A. Boger, D.R. Stinebring, T.S. Chyczewski, Jules W. Lindau, H.J. Gibeling, S. Venkateswaran, and T.R. Govindan. A preconditioned Navier–Stokes method for two-phase flows with application to cavitation prediction. *Computers & Fluids*, 29(8):849–875, 2000.
2. G.H. Schnerr and J. Sauer. Physical and numerical modeling of unsteady cavitation dynamics. In *Fourth international conference on multiphase flow*, volume 1. ICMF New Orleans, 2001.
3. P.J. Zwart, A.G. Gerber, and T. Belamri. A two-phase flow model for predicting cavitation dynamics. In *Fifth international conference on multiphase flow, Yokohama, Japan*, volume 152, 2004.
4. J. Peltola, T. Pättikangas, W. Bainbridge, R. Lehnigk, and F. Schlegel. On development and validation of subcooled nucleate boiling models for OpenFOAM Foundation release. In *18th International Topical Meeting on Nuclear Reactor Thermal Hydraulics, NURETH 2019*, pages 2149–2163. American Nuclear Society ANS, 2019.
5. V. Viitanen and J. Peltola. Hydrodynamic cavitation investigations with homogeneous and inhomogeneous multiphase flow models in OpenFOAM context. In *Proceedings of 11th International Symposium on Cavitation*, Daejeon, Korea, 2021.
6. J.-B. Leroux, J.A. Astolfi, and J.Y. Billard. An experimental study of unsteady partial cavitation. *J. Fluids Eng.*, 126(1):94–101, 2004.
7. P. C. Pennings, J. Bosschers, J. Westerweel, and T. J. C. Van Terwisga. Dynamics of isolated vortex cavitation. *J. Fluid Mech.*, 778:288–313, 2015.
8. A. Asnaghi, R.E. Bensow, and U. Svanberg. Comparative analysis of tip vortex flow using RANS and LES. In *MARINE VII: proceedings of the VII International Conference on Computational Methods in Marine Engineering*, pages 836–847. CIMNE, 2017.
9. V.M. Viitanen and T. Siikonen. Numerical simulation of cavitating marine propeller flows. In *9th National Conference on Computational Mechanics (MekIT'17)*, Trondheim, Norway, May 11 – 12 2017. International Center for Numerical Methods in Engineering (CIMNE), pp. 385–409. Trondheim, Norway. ISBN: 978-84-947311-1-2.

# Simulating the transport of suspended superquadric shapes with a fully-resolved CFD-DEM algorithm

Leonie Walter<sup>1</sup>, Jann Strybny<sup>1</sup>, Reinhard Hinkelmann<sup>2</sup>

<sup>1</sup>Maritime Environmental Technology & Fluid Dynamics, Faculty of Maritime Sciences, University of Applied Sciences Emden/Leer, Bergmannstraße 36, 26789 Leer, Germany

<sup>2</sup>Water Resources Management and Modeling of Hydrosystems, Institute of Civil Engineering, Technische Universität Berlin, Berlin, Germany

## 1. Introduction

Fluid-particle systems occur in varying fields of application, such as mechanical engineering, coastal and fluvial research, medicine and many more. Although the description and prediction of their temporal evolution has been a subject of interest for more than a century, in fact little is known about the detailed physical processes on particle scale, even for the supposedly simple case of single sedimenting non-spherical particles. Therefore problems like determining and increasing the stability of nourishments and marine foundations or understanding enclosure processes of microplastic particles in marine sediment lack fundamental knowledge. Due to the extremely small length scales, especially in case of natural mixtures of sediment and fluid, numerical simulations, for instance with a CFD-DEM method as presented here, offer the chance to gain more insights about microscopic fluid-particle interaction schemes. This knowledge in turn is supposed to contribute to the derivation of new and the validation or improvement of already existing algorithms for systems on larger scales, like for instance sediment entrainment in rivers.

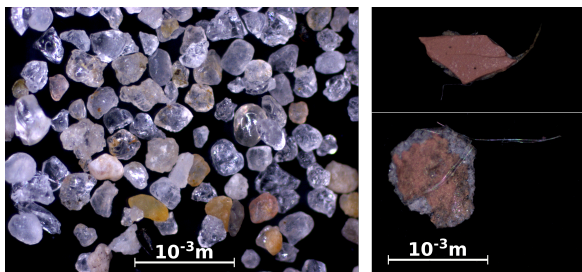


**Figure 1:** Microscopic pictures of sand grains (left) from a probe taken at the shore of Hvide Sande, Denmark (North Sea) and examples of common microplastic particles floating in the North Sea (right), originating from ship paint.

Studying the interaction of fluid and particle motion in detail, however, requires a realistic numer-

ical depiction of different particle shapes on the one hand, without increasing the complexity of the numerical algorithm too much on the other. So far particle shape has been implemented mostly in terms of drag and lift correlations, without resolving the individual particle (see e.g. [5], [11]), or a spherical shape has been assumed if particles were resolved on the numerical CFD-grid (cf. [10], [15]). However, especially in natural sediments, the deviations from spherical shapes can be immense (see e.g. microscopy in figure 1).

## 2. Numerical methods

The applied numerical algorithm of the authors [16], optimising the approaches of Hager [6] and Podlozhnyuk [14] in terms of accuracy and efficiency, therefore makes use of a family of generalised ellipsoidal shapes, called *superquadrics*, for particle representation. In a particle-fixed coordinate system their surface is implicitly described by the following continuous function in canonical form, as introduced by Barr [2] in 1981:

$$f(x, y, z) = \left( \left| \frac{x}{a} \right|^{n_2} + \left| \frac{y}{b} \right|^{n_2} \right)^{\frac{n_1}{n_2}} + \left| \frac{z}{c} \right|^{n_1} - 1, \quad (1)$$

with  $f(x, y, z) = 0$ . The shape parameters  $a$ ,  $b$ ,  $c$  determine the length of the three semi-axes and the blockiness parameters  $n_1$  and  $n_2$  influence the local curvature and therefore directly the particle shape (see fig. 2). For numerical reasons a restriction to convex shapes ( $n_1, n_2 \geq 2$ ) is required so far [14]. Each particle is resolved by the numerical grid in the CFD calculations, conveyed with OpenFOAM [9]. Particle collisions, translational and rotational motions are captured by the Discrete Element Method (DEM) developed in 1979 by Cundall and Strack [4], and implemented in the open-source software LIGGGHTS [12]. In the DEM method Newtons equations of motion (translational and rotational) are solved for each particle individually. It is suitable for both, dense and dilute particulate systems, which makes it a good choice for generalised particle transport applica-



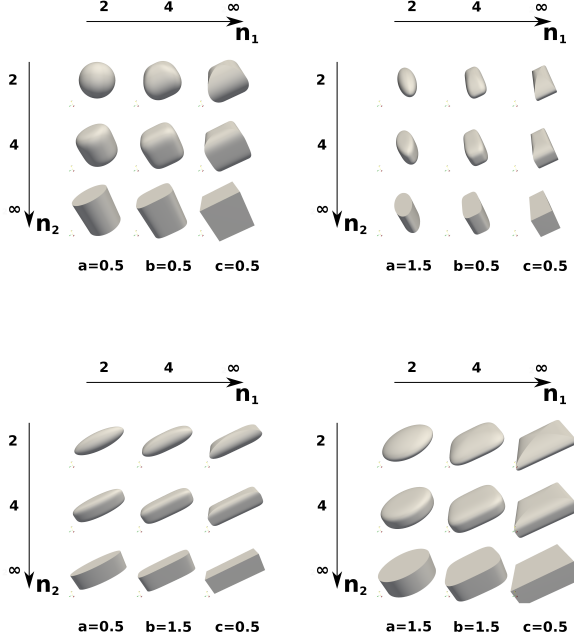


**Figure 2:** Differing convex superquadric shapes for varying blockiness parameters  $n_1$  and  $n_2$  and semi-axis  $a$ ,  $b$  and  $c$ .

tions. Both methods are coupled to each other in the CFDEMcoupling framework [13], allowing an exchange of information regarding particle motion and forces the fluid exerts on individual particles.

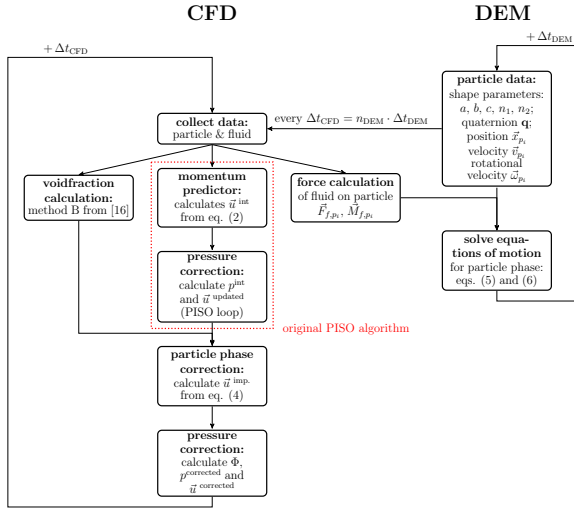


**Figure 3:** Schematic visualization of the applied fully-resolved CFD-DEM algorithm as adapted from Hager [6].

The overall numerical algorithm is based on the PISO algorithm [9] and has been proposed by Hager [6]. The simplified graphical overview in figure 3 reveals that in one timestep at first particle data is transferred from the DEM calculation to the CFD side. Consecutively a voidfraction field  $\alpha$ , representing the particle phase on the numer-

ical grid, is established, applying a novel method by the authors [16]. Relevant fluid forces  $\vec{F}_{f,p_i}$  resulting from pressure differences and viscosity are determined in a fictitious domain approach as outlined in [6]. Details regarding the explicit formulations and methodologies for voidfraction and force calculations are summarised in [16].

At the same time a momentum predictor and a pressure corrector are calculated according to the basic PISO algorithm, applying the Navier-Stokes and the continuity equation

$$\int_V \rho_f \frac{\partial \vec{u}}{\partial t} d^3r + \int_V \rho_f \vec{u} \cdot \nabla \vec{u} d^3r - \int_V \rho_f \nu \Delta \vec{u} d^3r = - \int_V \nabla p d^3r, \quad (2)$$

$$\int_V \rho_f \nabla \cdot \vec{u} d^3r = 0 \quad \text{on } \mathcal{D}, \quad (3)$$

with  $\rho_f$  being the fluid density,  $\nu$  its viscosity and  $p$  the dynamical pressure. Subsequently the velocity field  $\vec{u}$  in the computational domain  $\mathcal{D}$  is altered, accounting for the presence of the particle phase by imposing the translational and rotational velocity,  $\vec{v}_{p_i}$  and  $\vec{\omega}_{p_i}$  of the respective particle  $i$ , located in the domain  $\mathcal{D}_{p_i}$ :

$$\vec{u}^{\text{imp.}} = \begin{cases} \vec{u} & \text{on } \mathcal{D} \setminus \mathcal{D}_{p_i}, \\ \vec{v}_{p_i} + \vec{\omega}_{p_i} \times \vec{r}_c & \text{on } \mathcal{D}_{p_i}, \quad i = 1, \dots, n_p. \end{cases} \quad (4)$$

The vector  $\vec{r}_c$  denotes the distance to the particle centre of gravity. Afterwards a pressure correction step again includes the continuity equation (3). Meanwhile the DEM algorithm solves Newtons equations of motion for translation and rotation for each particle with mass  $m_{p_i}$ :

$$m_{p_i} \frac{d\vec{v}_{p_i}}{dt} = m_{p_i} \vec{g} + \vec{F}_{f,p_i} + \vec{F}_{\text{coll.}} \quad \text{and} \quad (5)$$

$$\frac{d\vec{N}}{dt} = \frac{d}{dt} [\hat{I}_{p_i} \cdot \vec{\omega}_{p_i}] = \vec{M}_{f,p_i} + \vec{M}_{\text{coll.}}. \quad (6)$$

The contributions  $\vec{F}_{\text{coll.}}$  and  $\vec{M}_{\text{coll.}}$  are forces and moments resulting from particle-particle and particle-wall collisions, which are calculated with a soft-sphere approach by Podlozhnyuk [14]. For superquadric particles this is already implemented in the public version of LIGGGHTS. Formula for calculating the principle and the transformed tensor of inertia  $\hat{I}^*$  and  $\hat{I}$  for isotropic superquadric particles are given in [14], accurate derivations of the same in [7] and [8]. The timestep of the DEM algorithm,  $\Delta t_{\text{DEM}}$ , has to be much smaller than on the CFD side,  $\Delta t_{\text{CFD}}$ , to depict collision forces to a sufficiently exact extend in most cases.

### 3. Case studies

The idea of the current study is to compare the temporal evolution of systems with superquadric particles with systems in which they are replaced by volume equivalent spheres. This is done for a single sedimenting particle as well as for an initially resting particle mixture in a channel flow. A detailed validation of the outlined numerical algorithm for the case of a single sedimenting sphere in a resting fluid is presented in [16], together with an extensive grid sensitivity study. This study revealed that the resolution of the particle interface strongly affects its terminal falling velocity, whereas the resulting drag is almost independent for physical reasons. Furthermore extremely smooth surface representations lead to decreasing particle velocities, which was explained by the lack of surface roughness in these cases. An ideal grid spacing has been proposed using 6 basic grid cells per (spherical) particle diameter with a refinement level of 3 at the particle surface. With these prerequisites known  $c_D - Re$  as well as  $v^* - d^*$  relations could be perfectly depicted. These considerations are taken into account in the following two studies, which represent two different possible starting points for future work.

#### 3.1. Sedimenting oblate ellipsoid

In the previous study [16] it has already been pointed out that an oblate ellipsoid with aspect ratio  $\mathcal{AR} = \frac{a}{b} = \frac{1}{3}$  (see fig. 4) and a Galileo number

$$Ga = \sqrt{\frac{|\frac{\rho_p}{\rho_f} - 1| g D_{\text{eq}}^3}{\nu^2}} \quad (7)$$

of 100, is sedimenting steadily with a terminal Reynolds number of  $Re_t \approx 75$ . An equivalent sphere with the same Galileo number ( $D_{\text{eq}} = 1.943 \cdot 10^{-3}$  m) instead reaches a terminal Reynolds number of about  $Re_t^{\text{eq. sph.}} \approx 112$  due to the smaller cross sectional area. This example inductively reveals that particle shape and orientation play a crucial role in the dynamics of a particle-fluid system.

For increasing Galileo numbers even the qualitative behaviour of the system changes. It is known that the dynamical state of a non-spherical particle undergoes several bifurcations for increasing Galileo numbers until a chaotic motion regime is reached. The phase-diagrams displaying the individual motion regimes, however, are a matter of active research, with, sometimes contradicting, theoretical, experimental and numerical contributions (see e.g. [3]).

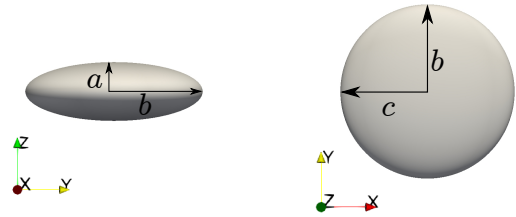


**Figure 4:** Shape of an oblate ellipsoid ( $b = c$ ) with aspect ratio  $\mathcal{AR} = \frac{a}{b} = \frac{1}{3}$ , displayed in the observer-fixed coordinate system.

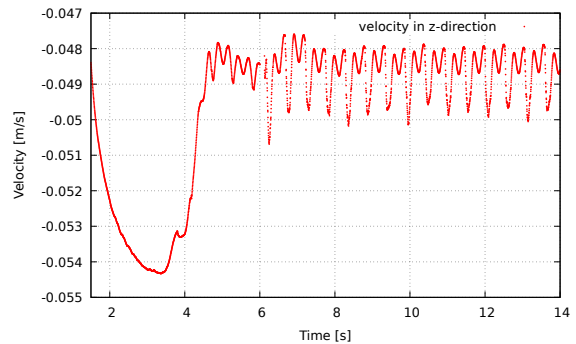


**Figure 5:** Sedimentation velocity of an oblate ellipsoid ( $b = c$ ) with aspect ratio  $\mathcal{AR} = \frac{a}{b} = \frac{1}{3}$ , and  $Ga = 170$  in the transition to periodic oscillatory motion.

In the numerical study of Ardekani et al. [1] it has been stated that a planar oscillatory motion is observed for a Galileo number of  $Ga = 170$  and the oblate ellipsoid defined above. With the same Galileo number and particle shape, a fluid viscosity of  $\nu = 1.004 \cdot 10^{-6} \frac{\text{m}^2}{\text{s}}$ , fluid density of  $\rho_f = 998.21 \frac{\text{kg}}{\text{m}^3}$  and particle density of  $\rho_p = 1137.9594 \frac{\text{kg}}{\text{m}^3}$  a simulation is conducted with the presented algorithm. Therefore a cuboid computational domain of  $X = Y = 0.02$  m width and  $Z = 0.12$  m length is constructed. Then the sedimentation is simulated in a fixed reference frame until an almost constant terminal velocity is reached. Afterwards a moving reference frame is applied to save computational time. Numerical schemes and temporal and spatial discretisation are chosen according to the ones in the previous study of the authors [16].

In a first transitional state the oblate particle sediments almost straightly along the z-direction, though in a non-axisymmetric state. Then, when a certain degree of perturbation is reached, suddenly greater deviations in x- and y-direction occur, which leads to a reduction of the velocity in z-direction as revealed by figure 5. This phase transition results from a Hopf bifurcation [3] and therefore also depends on numerical perturbations and accuracy. After a short settling time an oscil-

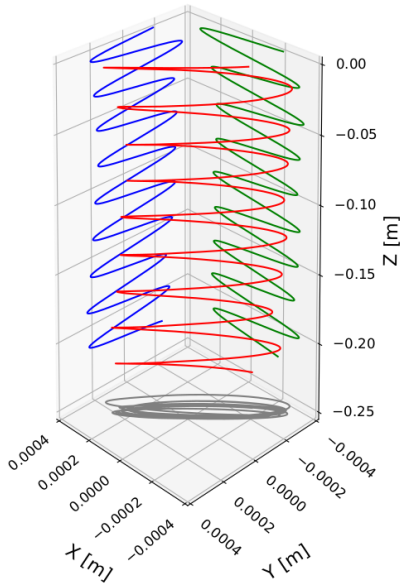


**Figure 6:** Oscillatory trajectory of an oblate ellipsoid ( $b = c$ ) with aspect ratio  $\mathcal{AR} = \frac{a}{b} = \frac{1}{3}$ , and  $Ga = 170$  and its projections into the coordinate planes.

latory motion state occurs as expected, though the trajectory is not planar in our case as shown in figure 6, contrasting the results in [1] and [3]. Instead the oblate particle precesses elliptically around an axis pointing into z-direction with a frequency of  $f = 1.71$  Hz, while still sedimenting. This leads to a flat spiral motion, with a pitch of  $9.4 \frac{z}{D_{eq}}$ . In the equivalent calculation in [1] a pitch of about  $10.7 \frac{z}{D_{eq}}$  is observed. Furthermore the particle in the current study nutates periodically, which can be visualised by the angle between the z-axis in the observer-fixed and the particle-based coordinate system (cf. figure 7), which oscillates between about 1 and 15 degrees. The maximum values of this inclination angle belong to the extremal positions in the trajectory (negative and positive corresponding x- and y-coordinates), whereas the minimum ones to the extremal positions with altering respective sign. The particle is always tilted towards the precession axis. However no rotational motion of the particle itself is observed.

The terminal Reynolds number, using the equivalent particle diameter  $D_{eq}$  as length scale is approximately  $Re_t \approx 134.3$ , which deviates from the one calculated from the linearly fitted relationship to the Galileo number

$$Re_t = 0.83 Ga - 9 = 132.1, \quad (8)$$

proposed in [1], by only 1.7 %.

### 3.2. Particle mixture in channel flow

A second study aims at outlining the differences of particle representation onto the motion of a par-

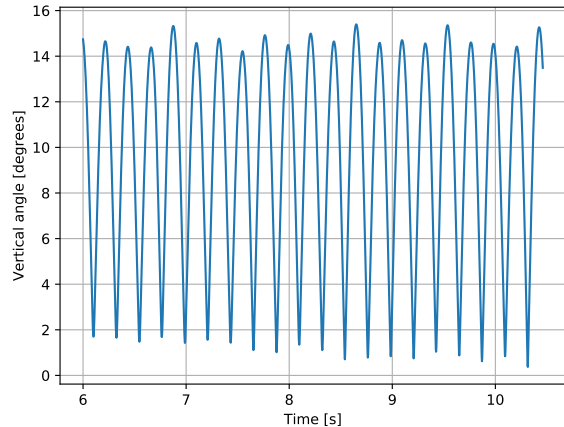


**Figure 7:** Inclination angle of an oblate ellipsoid ( $b = c$ ) with aspect ratio  $\mathcal{AR} = \frac{a}{b} = \frac{1}{3}$ , and  $Ga = 170$  with respect to the z-axis, moving on a flat spiral trajectory.

title mixture in a channel flow. Therefore a numerical channel with a length of  $X = 0.09$  m, a width of  $Y = 0.06$  m and a height of  $Z = 0.008$  m is set up. A cuboid hole of  $D = 0.003$  m depth, a width of  $W = 0.04$  m and a length of  $L = 0.02$  m is added to the channel bottom at a distance of  $X_1 = 0.02$  m to the inlet (see figure 8). Water with a density of  $\rho_f = 1000 \frac{\text{kg}}{\text{m}^3}$  and a kinematic viscosity of  $\nu = 1 \cdot 10^{-6} \frac{\text{m}^2}{\text{s}}$  flows into the domain in positive x-direction with a spatially constant velocity of  $0.5 \frac{\text{m}}{\text{s}}$ , which is ramped up from zero until  $t = 0.105$  s. Before starting the coupled CFD-DEM calculation 215 particles with three different shapes (and diameters) are placed in a face-centered-cubic grid (fcc) in and above the cuboid hole, by assuming a constant diameter of  $d_{\text{max}} = 0.003$  m for position calculation. In the first simulation three different superquadric particle shapes are encountered, in the second one they are replaced by respective volume-equivalent spheres at exactly the same initial locations. Shape data is summarised in table 1. Particle density is assumed to be  $\rho_p = 2300 \frac{\text{kg}}{\text{m}^3}$ . Then a small DEM simulation is conveyed, in which all particles settle into the prescribed hole. This is then the initial state for the coupled CFD-DEM calculation, which is revealed in figure 8.

Type	$a$ [m]	$b$ [m]	$c$ [m]	$n_1$	$n_2$
SQ 1	0.0015	0.0015	0.0005	4	4
SQ 2	0.0005	0.0005	0.0015	2	2
SQ 3	0.001	0.001	0.001	2	2
SP 1	0.0012	0.0012	0.0012	2	2
SP 2	0.0007	0.0007	0.0007	2	2
SP 3	0.001	0.001	0.001	2	2

**Table 1:** Shape data of particle mixtures with superquadric (SQ) and spherical (SP) shapes.

Numerical schemes in the simulation are chosen

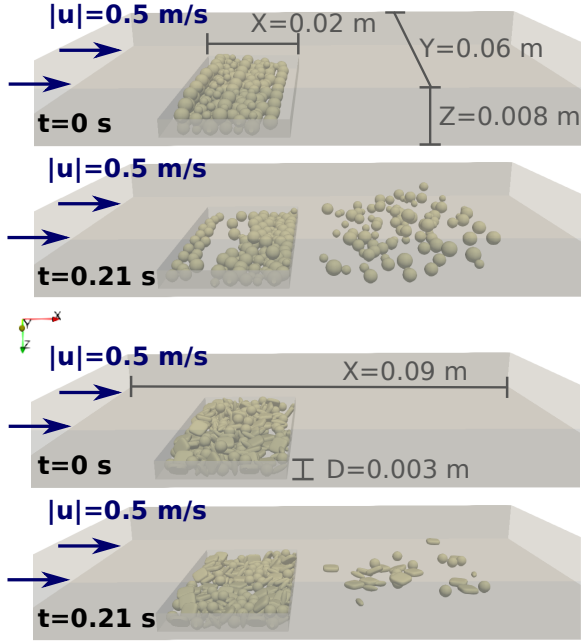


**Figure 8:** Comparison of two timesteps of equivalent particle mixtures with spherical (top) and superquadratic particles (bottom) in a channel flow.

as described in [16]. For the present calculations, however, a basic grid cell size of  $\Delta x = 2.5 \cdot 10^{-4}$  m with a refinement level of one is employed to save computational time. Both the DEM-timestep  $\Delta t_{\text{DEM}} = 2.5 \cdot 10^{-5}$  s and the CFD-timestep  $\Delta t_{\text{CFD}} = 1.75 \cdot 10^{-4}$  s are reduced compared to the previous calculations to capture particle collisions and preserve a maximum Courant number below 2. As revealed in figure 8 already

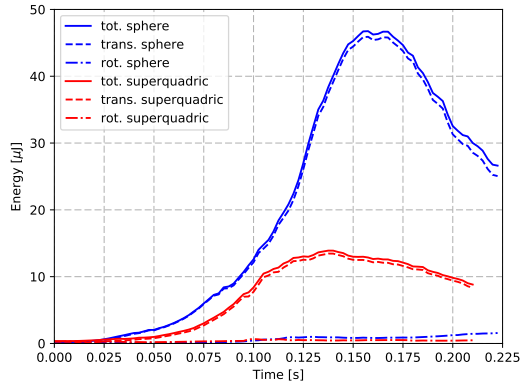


**Figure 9:** Comparison of total, translational and rotational kinetic energy of equivalent particle mixtures with superquadratic and spherical particles in a channel flow.

the initial condition for the coupled CFD-DEM calculation differs for the cases of superquadratic and spherical particles. The packed bed with spherical particles retains the structure of the initial grid for insertion and therefore creates a higher pile,

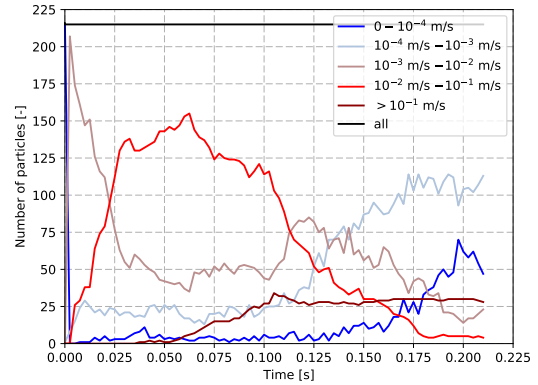
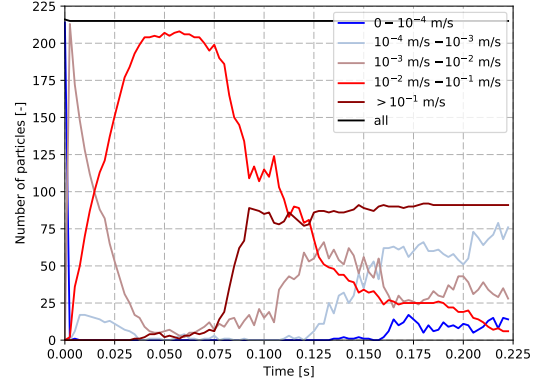


**Figure 10:** Number of spherical (top) and superquadratic (bottom) particles sorted in different velocity bins over time.

whereas in case of the superquadratic particles an almost chaotic mixture is produced, which fills the whole width and length of the hole. This is a direct consequence of the geometrical difference and influences the behaviour of the particulate phase in the channel flow. On the one hand about a factor three more particles are washed out of the hole in the spherical case, compared to the superquadratic one (cf. figs. 8 and 10), which consequently leads to almost the same factor in the peak kinetic energies of the whole particle phases (see fig. 9).

On the other hand also the phases in the temporal development differ. In the spherical case again, almost all particles start to move inside the cuboid hole with a velocity between  $10^{-1}$  and  $10^{-2} \frac{\text{m}}{\text{s}}$  as revealed by figure 10 until most of them reach its boundaries at about  $t = 0.085$  s. Then an amount of 91 particles is entrained (compared to 30 in the superquadratic case), reaching a velocity above  $10^{-1} \frac{\text{m}}{\text{s}}$  and contributing most to its kinetic energy. In case of superquadratic particles the initial motion of particles inside the hole occurs with significantly smaller velocities (see fig. 10), being a consequence of the deeper location inside the hole and of a denser packing. The moment of entrainment therefore occurs a little later at about

$t = 0.11$  s. The entrained particles similarly reach a velocity above  $10^{-1} \frac{\text{m}}{\text{s}}$ , but less motion is observed inside the hole. The velocity of suspended particles (inside their velocity bin), however, stays more constant than in case of the spherical particles, resulting in a slower decay of the total kinetic energy (cf. fig. 9).

#### 4. Conclusion

Both studies, the single sedimenting particle as well as a particle mixture in channel flow, reveal that assuming spherical particles instead of applying close to natural particle shapes crucially influences the results of fully-resolved simulations. Consequently a superquadric particle representation can contribute to a better understanding of the behaviour and characteristics of different particle mixtures in fluid flows. In the first example the shape variation has a strong effect on particle drag. However, as shown by the second example altering the particle shape does not only change the motion of an individual particle, but also integral values like the maximum kinetic energy in the particle phase, its temporal evolution and the amount of carried particles. Here particle geometry particularly influences the initial position and consequently the evolution of the system. The latter effect will be studied for cases of different particle mixtures and initial configurations in the future. Furthermore conveying validation experiments which make use of multi-particle systems is favourable to adjust material parameters to sensible values. For these achievements statistical modelling and evaluation are inevitable.

#### References

- [1] M. Ardekani, P. Costa, W. P. Breugem, and L. Brandt. Numerical study of the sedimentation of spheroidal particles. *International Journal of Multiphase Flows*, 87:16–34, 2016.
- [2] Alan H. Barr. Superquadrics and angle-preserving transformations. *IEEE Computational Graphical Animation*, 1:1–23, 1981.
- [3] M. Chrust. *Etude numérique de la chute libre d'objets axisymétriques dans un fluide newtonien*. PhD thesis, Université de Strasbourg, 2012.
- [4] P. A. Cundall and O. D. L. Strack. A discrete numerical model for granular assemblies. *Geotechnique*, 21:47–65, 1979.
- [5] J. Finn, M. Li, and S. Apte. Particle based modelling and simulation of natural sand dynamics in the wave bottom boundary layer. *Journal of Fluid Mechanics*, 796:340–385, 2016.
- [6] A. Hager. *CFD-DEM on Multiple Scales - An Extensive Investigation of Particle-Fluid Interactions*. PhD thesis, Johannes Kepler University Linz, 2014.
- [7] A. Jaklič, A. Leonardis, and F. Solina. *Segmentation and Recovery of Superquadrics*, volume 20. Springer Netherlands, Dordrecht, 2000.
- [8] A. Jaklič and F. Solina. Moments of superellipsoids and their application to range image registration. *IEEE transactions on systems, man and cybernetics. Part B, Cybernetics: a publication of the IEEE Systems, Man and Cybernetics Society*, 33:648–657, 2003.
- [9] H. Jasak. *Error Analysis and Estimation for the Finite Volume Method with applications to Fluid Flows*. PhD thesis, Imperial College of Science, Technology and Medicine, 1996.
- [10] T. Kempe, B. Vowinkel, and J. Fröhlich. On the relevance of collision modeling for interface-resolving simulations of sediment transport in open channel flow. *International Journal of Multiphase Flow*, 58:214–235, 2014.
- [11] A. Kidanemariam and M. Uhlmann. Direct numerical simulation of pattern formation in subaqueous sediment. *Journal of Fluid Mechanics*, 750:R2, 2014.
- [12] C. Kloss and C. Goniva. LIGGGHTS - open source discrete element simulations of granular materials based on LAMMPS. *The Minerals, Metals & Materials Society (TMS), Supplemented Proceedings*, 2011.
- [13] C. Kloss, C. Goniva, A. Hager, S. Amberger, and S. Pirker. Models, algorithms and validation for opensource DEM and CFD-DEM. *Progress in Computational Fluid Dynamics*, 12, 2012.
- [14] A. Podlozhnyuk. *Modelling superquadric particles in DEM and CFD-DEM: implementation, validation and application in an open-source framework*. PhD thesis, JKU Linz, 2018.
- [15] M. Uhlmann. Interface resolved direct numerical simulation of vertical particulate channel flow in the turbulent regime. *Physics of Fluids*, 20(5), 2008.
- [16] L. Walter, J. Strybny, and R. Hinkelmann. Extension of a fully-resolved CFD-DEM method for superquadric shapes: Sensitivity study on a single falling particle. *Computers and Fluids*, (submitted: 20.04.2021).

# Comparative Study on Numerical Hydroelastic Analysis of Impact-induced Loads

Dongni Yan<sup>1</sup>, Saeed Hosseinzadeh<sup>1,2</sup>, Arun Lakshmyanarayanan<sup>1</sup>, Tommi Mikkola<sup>1</sup>, Spyros Hirdaris<sup>1</sup>

<sup>1</sup>Marine Technology Group, Department of Mechanical Engineering, Aalto University, Espoo, Finland

<sup>2</sup>Department of Civil Engineering and Architecture, Tallinn University of Technology, Tallinn, Estonia  
[dongni.yan@aalto.fi](mailto:dongni.yan@aalto.fi)

## 1 Introduction

Ships and floating offshore installations are commonly exposed to impact pressures induced by waves. Suitable idealization of impulse induced slamming phenomena is possible by advanced “*Fluid Structure Interaction (FSI)*” models making combined use of principles of structural and fluid dynamics within the context of finite discretization methods. In such methods the fluid domain can be idealized using the “*Finite Volume method (FVM)*”, while the structural domain can be discretized by “*Finite Element Analysis (FEA)*”. Dynamic implicit solution strategies for FSI simulations are divided into one- and two-way coupling. In the former, the effect of deformation of the structure on fluid mesh deformation and the variation of added mass effects at different time steps of the numerical idealization may be neglected. Accordingly, the structure is assumed to be rigid and resulting pressures are applied as loading history onto the structural model. In two-way coupling methods, fluid pressures are transferred to the structural solver at each time increment and the corresponding structural deformation is transferred back to the fluid solver. Mesh morphing (also known as mesh adaption technique) may be utilized to ensure that the fluid mesh matches the deformed structural geometry. Recently, Lakshmyanarayanan and Hirdaris (2020) presented a comparative study of nonlinear one- and two-way “*Flexible FSI (FFSI)*” methods for the case of global symmetric hydroelastic container ship responses. Results demonstrated that two-way FFSI coupling is essential in terms of idealising the influence of stochastically induced hydrodynamic actions on resonant ship responses. This paper presents FFSI modelling methods that may be used for the prediction of local slamming loads. As applicable, computations are assessed and compared for the cases of flat bottom plate and wedge-shaped structures against experimental results from Tödter et al. (2020) and KRISO (2014).

## 2 Methodology

In slamming problems, both impact and response are transient and strongly interactive. Complex free surface deformations, highly localised pressure distributions and high velocities are always associated with slamming impact. Whereas hydroelasticity may influence the peak magnitude of impact loads, overprediction of results would lead to significant inaccuracies (Kapsenberg, 2011). This is because the variation of fluid pressures acting on a structure may modify its dynamic state, and consequently motions and dynamic response may lead to variable fluid state perturbations. With the later in mind FFSI models may be considered as useful alternative in terms of studying the influence of hydro-structural resonances in stochastic seaways (Hirdaris and Temarel, 2009). Whereas fluid viscosity may be neglected (Southall et al., 2014), hydrodynamic actions are governed by the continuity and Euler assumptions, expressed by equations (1), (2) respectively.

$$\frac{\partial}{\partial t} \int_V \rho dV + \oint_A \rho \mathbf{v} \cdot d\mathbf{a} = 0 \quad (1)$$

$$\frac{\partial}{\partial t} \int_V \rho \mathbf{v} dV + \oint_A \rho \mathbf{v} \otimes \mathbf{v} \cdot d\mathbf{a} = - \oint_A p \mathbf{I} \cdot d\mathbf{a} + \int_V \mathbf{f}_b dV \quad (2)$$

where  $\rho$  is the density,  $\mathbf{v}$  is the continuum velocity,  $\otimes$  is the outer product,  $\mathbf{f}_b$  is the resultant of the body forces (e.g. gravity) per unit volume acting on the continuum, and  $p$  is the pressure. The integral forms of the governing equations are solved using a FVM approach.

Hydromechanics are solved based on Newton’s 2<sup>nd</sup> Law of motion using FEA (Harding et al., 2006). Accordingly, the governing equation for the dynamic response of an elastic body is represented as:

$$M\ddot{x} + C\dot{x} + Kx = F \quad (3)$$

where  $M$ ,  $C$ ,  $K$  are the mass, damping and stiffness matrices,  $F$  is the external load applied,  $\ddot{x}$ ,  $\dot{x}$ ,  $x$  are the acceleration, velocity, and displacement vectors on finite element nodes.

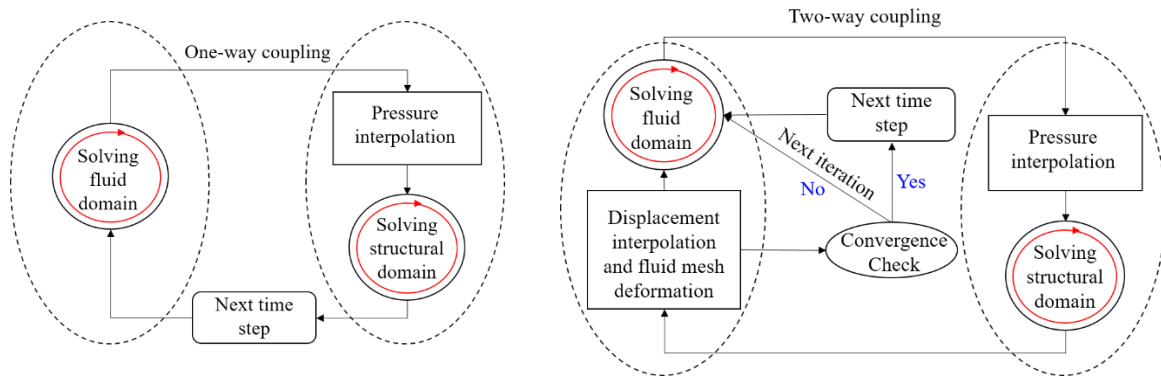


Figure 1 Flowcharts of one-way coupling method (left) and two-way coupling method (right)

A partitioned approach may be applied by either one-way or two-way coupling methods (see Figure 1). In one-way coupling, the fluid field is solved until convergence criteria are reached. Impact pressures in way of FSI boundaries are then transferred to the structural domain, where a set of simultaneous nonlinear dynamic equilibrium equations are solved iteratively at each time increment until the error in the residuals is less than 0.5% (Dassault Systèmes, 2016). In two-way coupling both fluid pressure and structural displacement on FSI boundaries are constantly transferred between the fluid and structural domains. Accordingly, fluid mesh deformation is accounted for at each time step.

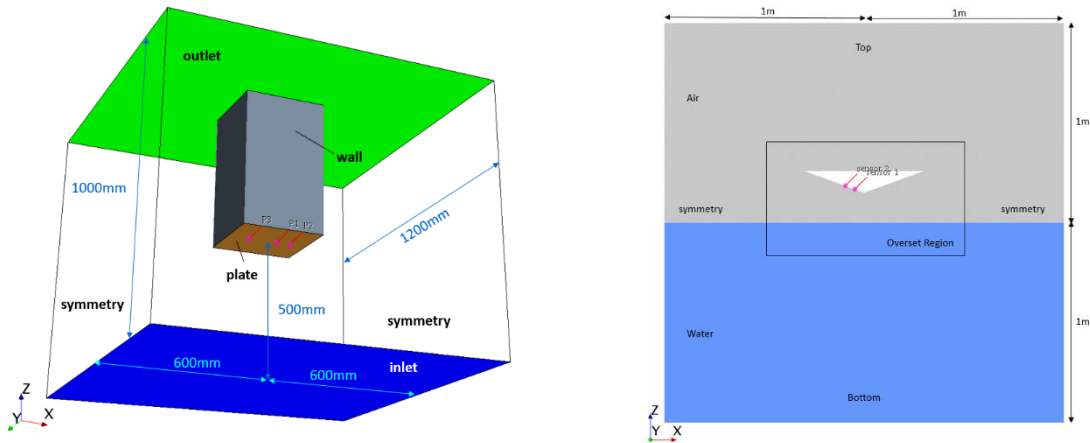


Figure 2 Fluid domain idealization (a) plate type structure (b) wedge-shaped structure with  $20^\circ$  deadrise angle (red dots idealise the positioning of pressure sensors) (Yan et al., 2021)

The fluid domain models of bottom plate and wedge type models studied in this paper are illustrated in Figure 2. In both cases the fluid domain consisted of both air and water idealised by unstructured hexahedral cells based on trimmed Cartesian grids. Mesh refinements were carried out by volumetric blocks. A 5 mm mesh size was used in way of the wedge surface. For the plate surface, 3mm of grid size was considered adequate in terms of capturing pressure peaks and high gradients. Water compressibility was modelled artificially. Thus, density dependency to pressure and speed of sound were modelled as per Yan et al. (2021). The free surface interface was modelled by a Volume of Fluid (VOF) surface capturing technique in which an additional transport equation was solved for the volume fraction  $c$  (Hirt and Nichols, 1981). For the case of the bottom plate, the FSI domain was idealized in 3D ( $x, y = 1200 \text{ mm}; z = 1000 \text{ mm}$ ). Accordingly, the plate structure was positioned 500 mm above the domain's bottom and the water entry velocity of the plate was assumed constant. For meaningful validation of results, sensors mapped the experimental topology used by Tödter et al. (2020). For the wedge structure, a very thin CFD domain was used to simulate the symmetric free fall of wedge with  $20^\circ$  deadrise angle. In this case, the  $x$ - $z$  reference domain size was specified as  $2 \text{ m} \times 2 \text{ m}$  and the wedge apex was located on the vertical middle line of the domain. To enable useful validation of results, numerical pressure sensors were attached on the lower part of the wedge-shaped edge (KRISO, 2014). To ensure accuracy of interpolation mapping, the structural element sizes on plate/wedge bottom surface matched the fluid mesh. Flexible material of polyoxymethylene (Tödter et al., 2020) were applied on both plate and wedge structural modelling for one- and two-way simulation cases in this paper. Coupling of STAR-CCM+ fluid dynamics with ABAQUS FEA was mainly implemented for simulations and results comparison in this paper as per Yan et al., (2021). Coupling of fluid dynamics with hexahedral solid element implemented in STAR CCM+ as per Hosseinzadeh and Tabri (2021) was applied to study one way coupling.

### 3 Results and discussion

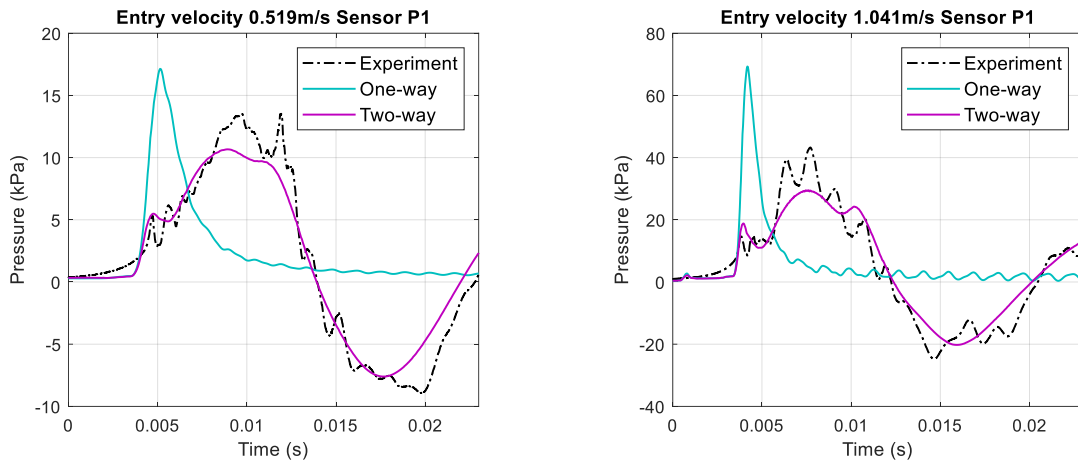


Figure 3 Loading history on pressure sensor P1 (35mm from plate center) of one-way and two-way plate simulations with experimental results for cases with entry velocity  $v=0.519$  and  $1.041$  m/s respectively

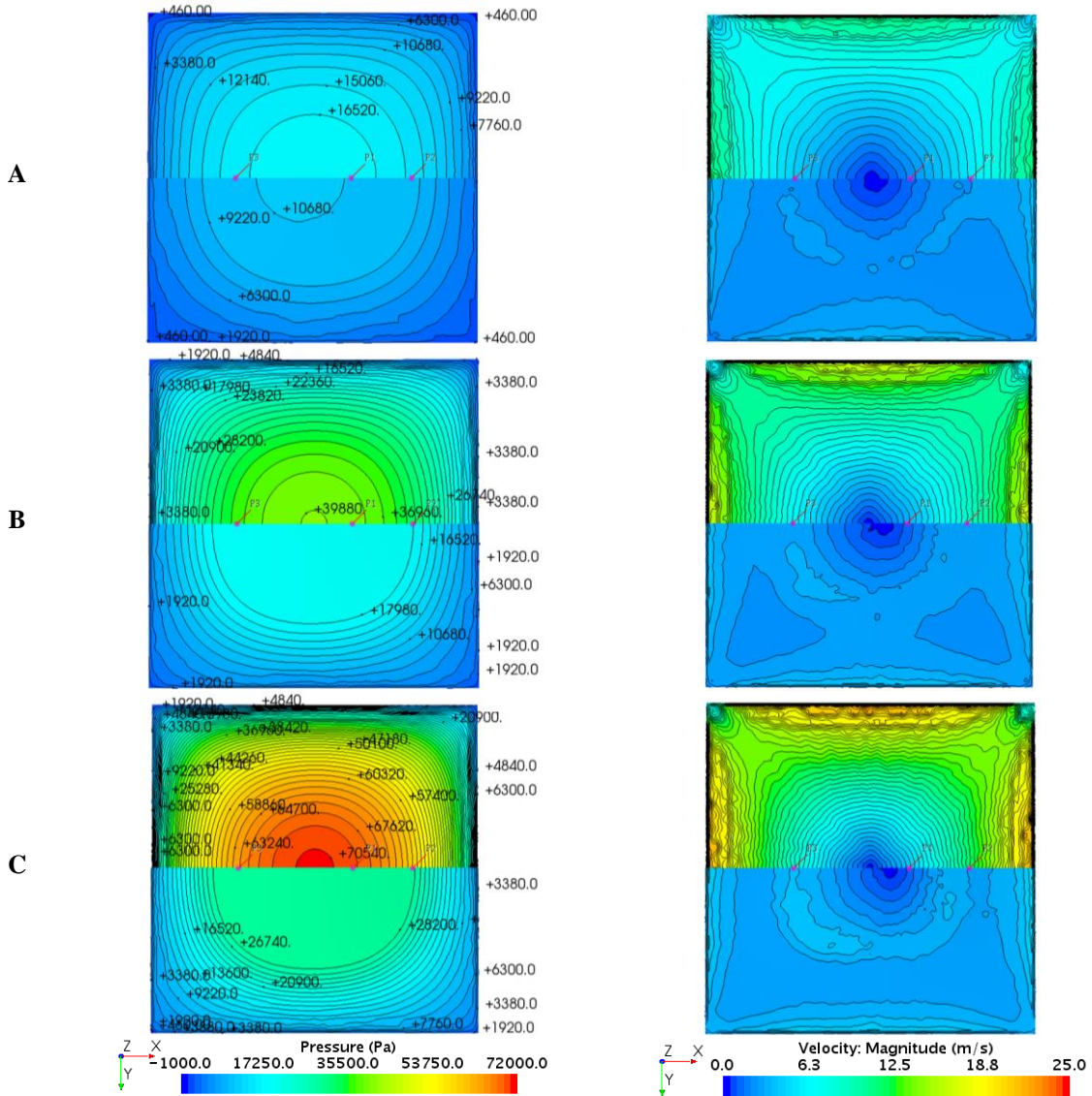


Figure 4 Pressure and velocity distribution at the pressure sensor P1 peak time of impact of one-way (upper half plate) and two-way (bottom half plate) simulations for cases with entry velocity of  $v=0.519$  m/s (A) and  $0.782$  m/s (B), and  $1.041$  m/s (C) respectively



Comparisons of FFSI simulations against the experimental results of Tödler et al. (2020) for the case of the flexible polyoxymethylene bottom plate at water entry phase are demonstrated in Figure 3. The difference in pressures predicted by the one-way coupling method is significant and may be attributed to the fact that the method does not idealise the influence of structural deformation on dynamic response. The pressure in two-way approach shows closer trend to the experiment, where the pressure rises relatively slowly and vibrates in lower frequency. This may include the effect of the interaction between fluid and structure and added mass.

The spatial distribution of pressure and velocity components are shown in Figure 4. The top and bottom halves of the plate demonstrated on each sub-figure (A, B, C) represent results from the one- and two-way idealisations respectively. One-way coupled simulations demonstrate higher magnitudes and wider pressure range. They also demonstrate high velocities and velocity gradients in way of the plate edge. Whereas in the one-way FFSI, the velocity distribution is symmetric, an obvious asymmetric distribution of velocity near the plate center becomes evident as the water entry velocity increases with two-way FFSI distribution. This indicates that higher vibration modes may significantly influence the results of two-way coupling.

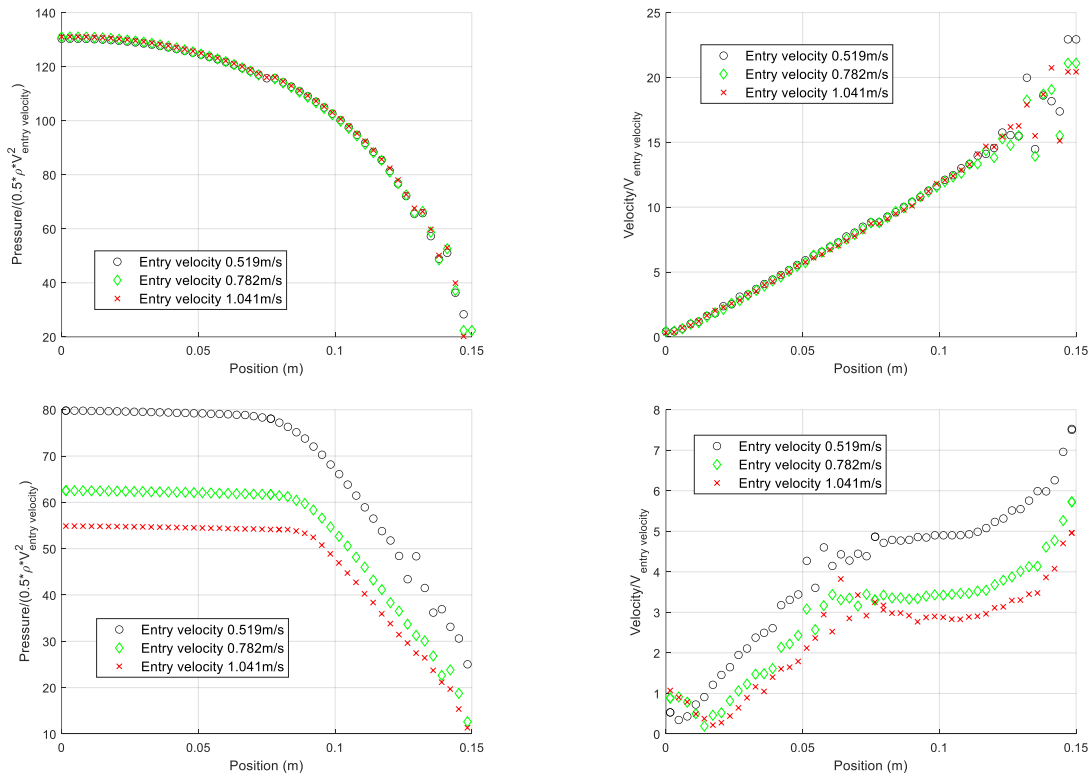


Figure 5 Nondimensional pressure and velocity distribution along the plate center to edge at the P1 peak time of impact of one-way (upper figure) and two-way (bottom figure) simulations for cases with entry velocity  $v=0.519$  and  $0.782$ , and  $1.041$  m/s respectively

The distribution of nondimensional pressures and velocities in way of the area between the plate center and edge are shown in Figure 5. The overall magnitude of the nondimensional pressure in two-way approach is nearly half of that predicted by the one-way FFSI model. In one-way coupling, nondimensional pressures and velocity distributions do not show disagreement, except near the edge. In two-way coupling, nondimensional pressure magnitudes decreases while the water entry velocity rises. This may indicate that when the entry velocity is higher, a smaller proportion of the kinetic energy is transformed to impact pressure while more energy is absorbed by the deformation of the flexible plate, which can be more accurately reflected by the two-way approach.

Representative strain sensor histories are presented in Figure 6. As expected, the magnitudes of strains predicted by one- and two-way coupling methods differ significantly. The strains predicted by two-way FFSI correspond generally well to the experimental results, except some deviations associated to the use of different FEA idealizations (i.e., solid versus continuum shell elements as explained in the papers of Hosseinzadeh and Tabri., 2021 and Yan et al., 2021). The coupling of STAR-CCM+ fluid dynamics with ABAQUS FEA seems to show more accurately the variation in the strain field. The strain in one-way approach is higher. This could be attributed to the fact that the first peak of the response nearly reflects the fluid loading process and then self-vibration

dominates the response. Therefore, it may be concluded that the one-way coupling does not suitably simulate flexible dynamic response.

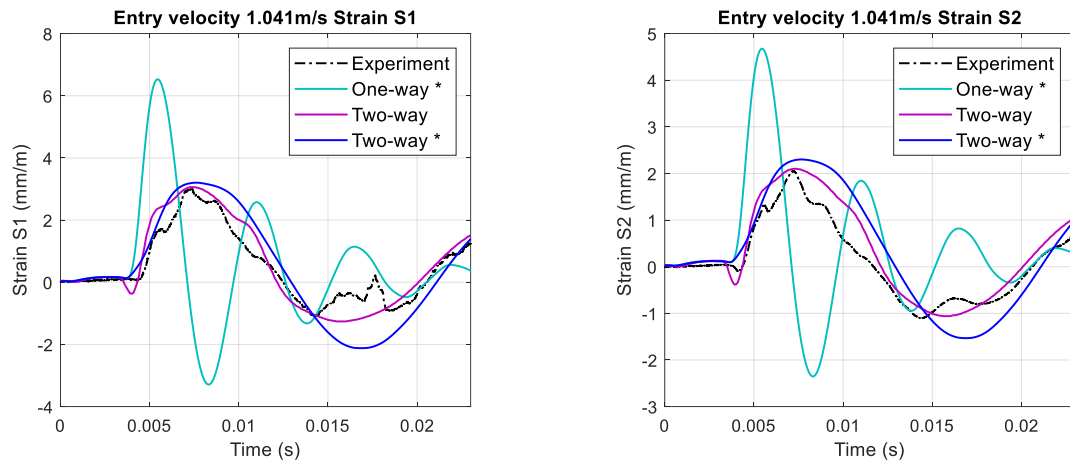


Figure 6 Response history of strain sensor S1 (plate center) and S2 (50mm from plate center) of one-way and two-way plate simulations with experimental results for cases with entry velocity  $v=1.041$  m/s (\* corresponds to STAR CCM+ solid FEA formulation)

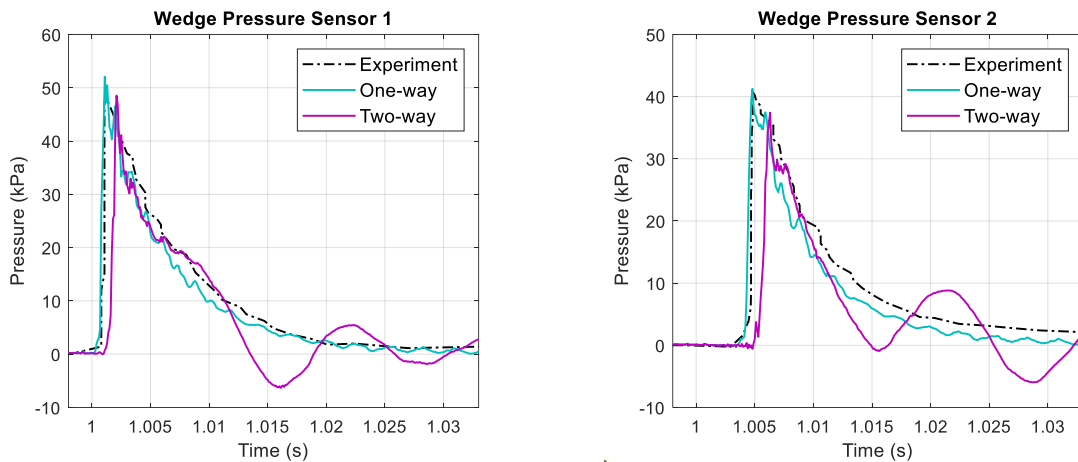


Figure 7 Loading history on pressure sensor P1 and P2 of one-way and two-way flexible wedge simulations with experimental results for cases of wedge with deadrise angle  $\theta=20$  deg

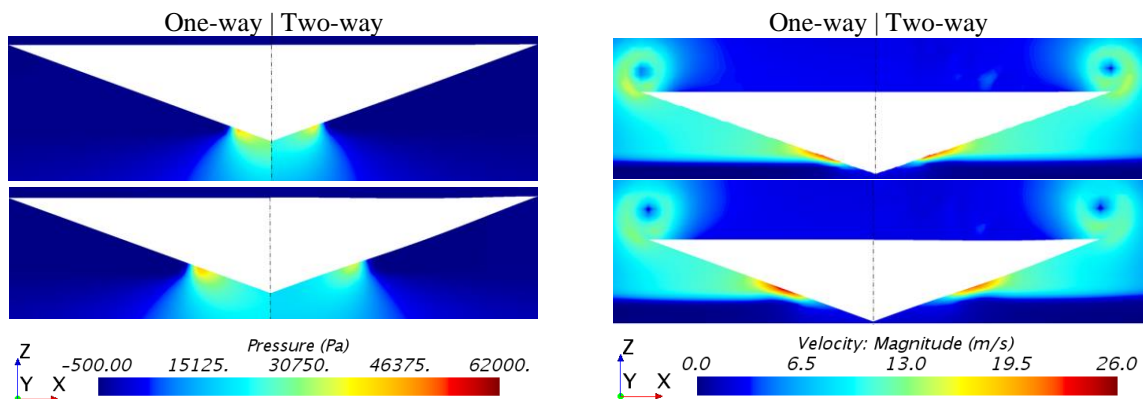


Figure 8 Pressure and velocity distribution at the peak time of P1(left figure) and P2 (right figure) of one-way (left half) and two-way (right half) simulations for cases of wedge with deadrise angle  $\theta=20$  deg

Loading predictions and comparisons against experimental results for the wedge structure are presented in Figure 7. The experimental material used in the wedge drop tests (KRISO, 2014) is aluminum (i.e., rigid material). Therefore, only one-way (i.e. rigid) hydrodynamic loading was one to one comparable with experimental data. Two-way FSI simulations show marginally lower peaks and a late pressure rise and peak.

Distributions of pressure and velocity at the pressure peak time of sensor P1 (upper row figures) and sensor P2 (lower row figures) of one-way and two-way simulations are plotted in Figure 8. Similarly to the flexible plate case, both pressure and velocity values evaluated from one-way coupling are higher. However, for the plate structure high pressure distribution was observed around the plate center, while high velocity and the velocity gradient peaked near plate edge. On the other hand, for the case of the wedge high pressure and velocity were observed at close by locations.

#### 4 Conclusions

This paper presented a comparative study of wave loads by one- and two-way FSI simulations. Following comparisons against available experimental results (Tödter et al., 2020 and KRISO, 2014), it may be concluded that the two-way hydroelastic coupling idealisations may be critical for flexible plate and wedge structures. In addition, there may be a negative correlation between the nondimensional pressure and water entry velocity for plate cases with two-way FSI, i.e., the nondimensional pressure magnitudes decrease while the water entry velocity rises.

#### References

- Dassault Systèmes. (2016). Abaqus Theory Guide, Providence, Rhode Island, U.S.A.
- Harding, R.D., Hirdaris, S.E., Miao, S.H., Pittilo, M., Temarel, P. (2006). Use of hydroelasticity analysis in design. *Proceedings of the 4th International Conference on Hydroelasticity in Marine Technology*, pp. 1 – 12, 10 – 14 September 2006, ISBN: 7-118-04728-7, Published by National Defense Industry Press, Beijing, China.
- Hirdaris, S.E. & Temarel, P. (2009). Hydroelasticity of Ships: Recent Advances and Future Trends. *Proceedings of the Institution of Mechanical Engineers Part M: Journal of Engineering for the Maritime Environment* 223(3): 305–30.
- Hirt, C. & Nichols, B. (1981). Volume of fluid method for the dynamics of free boundaries. *Journal of Computational Physics*. Vol. 39.
- Hosseinzadeh, S. & Tabri, K. (2021). Hydroelastic effects of slamming impact Loads During free-Fall water entry. *Ships and Offshore Structures*, 16:sup1, 68-84
- Kapsenberg, G.K. (2011). Slamming of ships: Where are we now? *Philosophical Transactions of the Royal Society A: Mathematical, Physical and Engineering Sciences*, 369(1947), 2892–2919.
- KRISO. (2014). Wave Induced Loads on Ships – Joint Industry Project III – Interim Report, MOERI Technical Report No. BSPIS7230-10572-6.
- Lakshmyanarayanan, P.A.K. & Hirdaris, S. (2020). Comparison of nonlinear one- and two-way FFSI methods for the prediction of the symmetric response of a containership in waves. *Ocean Engineering*. 203(2020) 107179.
- Southall, N., Lee, Y., Michael, C., Hirdaris, S., White, N. (2014). Towards a Pragmatic Method for Prediction of Whipping: Wedge Impact Simulations using OpenFOAM, *In proceedings of the 24th International Ocean and Polar Engineering Conference*, Busan, South Korea, ISOPE-I-14-341.
- Tödter, S., el Moctar, O., Neugebauer, J., Schellin, T.E. (2020). Experimentally Measured Hydroelastic Effects on Impact-Induced Loads During Flat Water Entry and Related Uncertainties. *Journal of Offshore Mechanics and Arctic Engineering*, Vol.142, 011604-1.
- Yan, D., Lakshmyanarayanan, A., Mikkola, T., Kujala, P., Hirdaris, S. (2021). Numerical simulation of the water entry of rigid and elastic structures with hydroelastic coupling. *International Conference on Ships and Offshore Structures*, Hamburg, Germany.

# Numerical Simulations of KCS self-propulsion in Regular Head Waves

Jiawei Yu, Chaobang Yao, Liwei Liu, Zhiguo Zhang, Dakui Feng

*School of Naval Architecture and Ocean Engineering, Huazhong University of Science and Technology, Key Laboratory of Ship and Ocean Hydrodynamics of Hubei Province, Wuhan, Hubei 430074, China. Email: yu\_jiaw@hust.edu.cn*

## 1. INTRODUCTION

Traditionally, the ship resistance and propulsion performance in calm water conditions are mainly considered for ship design (Zhang et al., 2021). However, during the actual voyage, ships will inevitably be affected by environmental factors such as wind, waves and currents which can induce significant ship motions and then affect resistance and speed of the ship. Both wave environment and rotating propeller can't be ignored for seakeeping performance prediction which will induce dynamic conditions including time-varying wake distribution, propulsion factors, ship motions, and speed loss. With the development of ship design, the seakeeping performance predicted by towing model or towing simulation can no longer satisfy the need of engineering practice and the propeller load fluctuations in waves are thought important for ship operations which will lead to great fluctuations of engine power and revolutions. Therefore, it is essential for ship safety and economy to evaluate and optimize ship motions and seakeeping behaviors of ships operating in waves rather than in calm waters, especially self-propelled ships in waves.

This paper describes simulations of the KCS self-propulsion in head waves using the improved body-force model (MOUM, modified Osaka University Method). Firstly, uncertainty analyses are performed on resistance of hull and thrust of propeller in calm water and ship motions and added resistance in wave. Then, towing simulations in calm water and waves are performed to obtain the ship attitudes, resistance, ship motions response and added resistance. Self-propulsion simulations in waves are performed to obtain the propeller rotation speed and ship motions. Four wave lengths ( $\lambda/L_{pp}=0.65, 0.85, 1.15, 1.95$ ) of regular head waves with  $1/60$  wave steepness are taken into account according to the benchmark case in Tokyo 2015 CFD Workshop. The self-propulsion computational results of thrust, torque and ship motions using the improved body-force model will be compared with these using discretized propeller model (DPM) to prove that this approach is applicable to these complex situations. Finally, we discussed how it is different from the towing tests when self-propulsion simulations were used for ship motion response prediction in head waves. All computations are carried out using an inhouse CFD code to solve the RANS equations coupled with three-degree-of-freedom (3DOF) solid body motion equations including surge, heave and pitch. The RANS equations are solved using a finite difference method and pressure-implicit with splitting of operators (PISO) arithmetic. The computations use a structured grid with overset technology.

## 2. COMPUTATIONAL METHOD

All the CFD simulations included open water, towing and self-propulsion simulations in calm water and waves are carried out in house CFD code. In house CFD code has been validated by lots of simulations for various propellers, ships and underwater vehicles in calm water and waves (Zhang et al., 2020; Wang et al., 2020; Feng et al., 2020a; Feng et al., 2020b). URANS approach with two-equation eddy-viscosity SST k-w model (Menter, 1994) is selected for turbulence modeling. Inhouse CFD code discretizes the governing equations using a structured finite-difference method.

The RANS equations can be obtained by time-averaging the continuity equation and the momentum conservation equation:

$$\frac{\partial U_i}{\partial x_i} = 0 \quad (1)$$

$$\frac{\partial U_i}{\partial t} + U_j \frac{\partial U_i}{\partial x_j} = -\frac{\partial \hat{p}}{\partial x_i} + \frac{1}{Re} \frac{\partial^2 U_i}{\partial x_j^2} - \frac{\partial}{\partial x_j} \overline{u_i' u_j'} + f_{b_i}^* \quad (2)$$

where  $U_i$  is the component of Reynolds-averaged speed in the  $x_i$  direction of the independent coordinates,  $\hat{p} = \left( \frac{p-p_\infty}{\rho U_0^2} + \frac{z}{Fr^2} \right)$  is the dimensionless dynamic pressure coefficient,  $\overline{u_i' u_j'}$  is the Reynolds stress tensor,  $\nu$  is the kinematic viscosity, and  $Re = U_0 L_{pp} / \nu$  is the Reynolds number. For the body-force model, the RANS solution for the propeller is omitted and the body-force source term  $f_{b_i}^*$  is added in the momentum equation to replace the propeller. For the improved body-force model, the blade thrust and torque of each element can be calculated based on blade element momentum theory and considers the three-dimensional viscous effect of the propeller (Feng et al., 2020a; Feng et al., 2020b). The free surface is captured by solving the single-phase level-set method (Burg, 2005). In self-propulsion computation in calm water, PI (proportional–integral) speed controller (Carrica et al., 2010) is used. Boundary wave-generation approach is utilized to realize regular wave generation in inhouse CFD code. To avoid the wave reflection due to limited border effectively, two approaches of wave elimination are adopted near the exit of numerical tank, including grid attenuation and adding damping source term to the momentum equation. In addition, wave damping range is set as  $2.5 \leq x \leq 4$  for wave simulations in this paper.

### 3. GRIDS AND WORKING CONDITIONS

The computational ship and propeller models are KCS appended with a rudder and KP505 with scale ratios of 1:37.89, whose open-water, resistance, self-propulsion and ship motion responses experiments data is available from Tokyo (2015). According to Tokyo 2015 benchmark cases, the CFD wave simulations are performed as listed in Table 1, each identified by their case numbers. The rotation speed in waves at  $Fr = 0.26$  will be matched using PI speed controller ( $U_0 = 2.017m/s$ ).

**Table 1.** The CFD simulation cases in wave.

Case No.	$Fr = U_0 / \sqrt{gL_{pp}}$	Rotation speed ( $n/U_0 * L_{pp}$ )	wave length ( $\lambda/L_{pp}$ )	Wave Height ( $H/L_{pp}$ )	DOF	Propeller model
1	0.26	—	Calm water		2DOF	w/o
2			0.65	0.0108		
3			0.85	0.0142		
4			1.15	0.0192		
5			1.95	0.0325		
6		PI speed controller	1.95	0.0325	3DOF	DPM
7			0.65	0.0108		MOUM
8			0.85	0.0142		
9			1.15	0.0192		
10			1.95	0.0325		

The structured dynamic overset grids are used for all simulations in this paper which are dealt with by the self-developed code. In house overset grid code is based on the grid point overset of structured grid and consists of three steps: hole cutting, identification of the interpolation points and identification

of the donor cells. The hole mapping method based on Cartesian coordinate grid of uniform structured grid is adopted for hole cutting, the donors of interpolation points are found using ADT (an alternative digital tree) based on the data structure while the relationship between the donor points and interpolation points is obtained by trilinear interpolation method (Li et al., 2005; Zhang et al., 2020). The near-wall grid spacing  $\Delta s = 8.6 \cdot y^+ LR_e^{-\left(\frac{13}{14}\right)}$  and  $y^+ = 1$  is selected. As seen in Fig.6 and Fig.7, to capture the detailed flow around the hull and the propeller, lots of refinements are used in the simulations. The ability to freely refine according to specific needs is also a major advantage of overset grids.

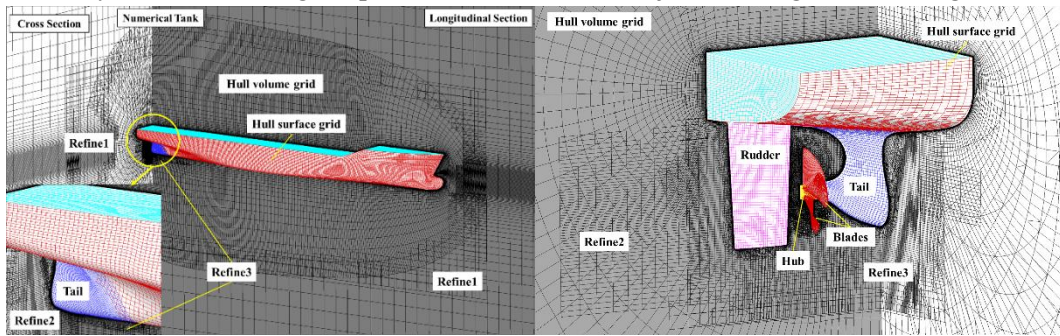


Fig.1 Structured overset grid for self-propulsion case.

## 4. RESULTS

### 4.1 Towing computations in wave

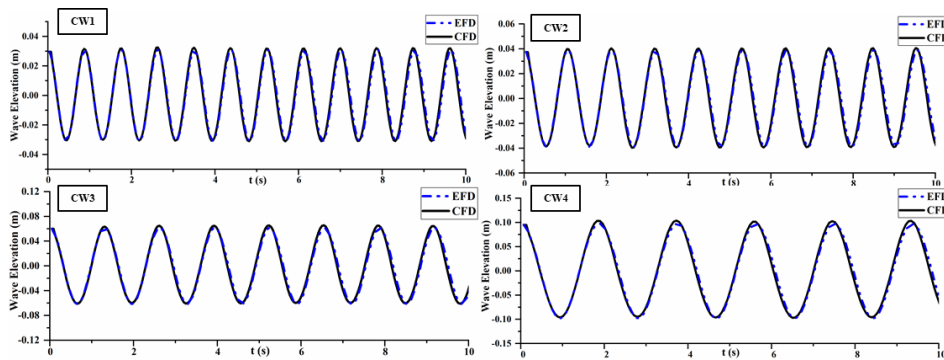


Fig. 2 comparison of wave simulation results with theoretical results

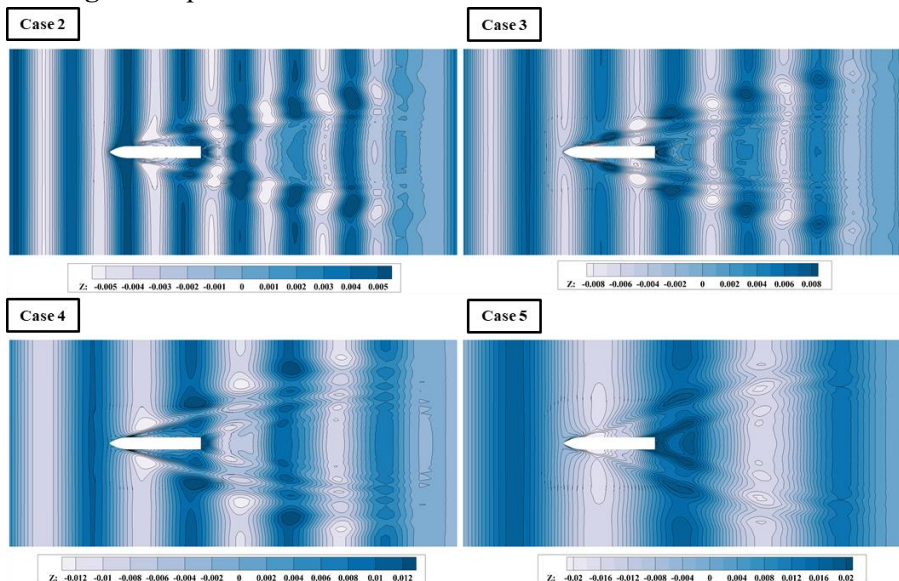


Fig. 3 Wave pattern of KCS in head waves.

**Table 2.** The grid and time step uncertainty study results for CW4.

	$r_G$	Solutions			$U_G$ (%D)	$r_T$	Solutions			$U_T$ (%D)
		$S_{G1}$	$S_{G2}$	$S_{G3}$			$S_{T1}$	$S_{T2}$	$S_{T3}$	
$C_T \times 10^3$	$\sqrt{2}$	10.542	11.811	11.999	4.04	2	10.552	11.811	11.914	0.29
$TF_3^{1st}$		0.922	0.935	0.938	1.12		0.920	0.935	0.942	1.42
$TF_5^{1st}$		1.136	1.111	1.107	0.95		1.131	1.111	1.103	1.20

Simulations were performed for the ship free to heave and pitch in regular head waves at wave lengths covering a range of 0.65~1.95 with the constant wave steepness  $H/\lambda = 1/60$  which can ensure linear and comparable wave profiles. The time histories of the wave elevation have been validated for all wave conditions in Fig.2. The results with the different grids and time steps are listed in Table 2. The results of the validation study are presented in Table 3. The results of this validation study show that all the comparison errors E are less than the validation uncertainty  $U_V$ , which validates the computation results at the  $U_V$  level. As seen in Fig.3, the ship wake in wave is clearly visible and the wave amplitude attenuation is very obvious in wave-elimination region which can avoid the wave reflection effectively.

**Table 3.** Results of validation study.

	$U_G$ (%D)	$U_T$ (%D)	$U_{SN}$ (%D)	$U_D$ (%D)	$U_V$ (%D)	E (%D)
$C_T \times 10^3$	4.04	0.29	4.33	8	9.10	8.94
$TF_3^{1st}$	1.12	1.42	2.54	4	4.74	0.37
$TF_5^{1st}$	0.95	1.20	2.15	4	4.54	0.65

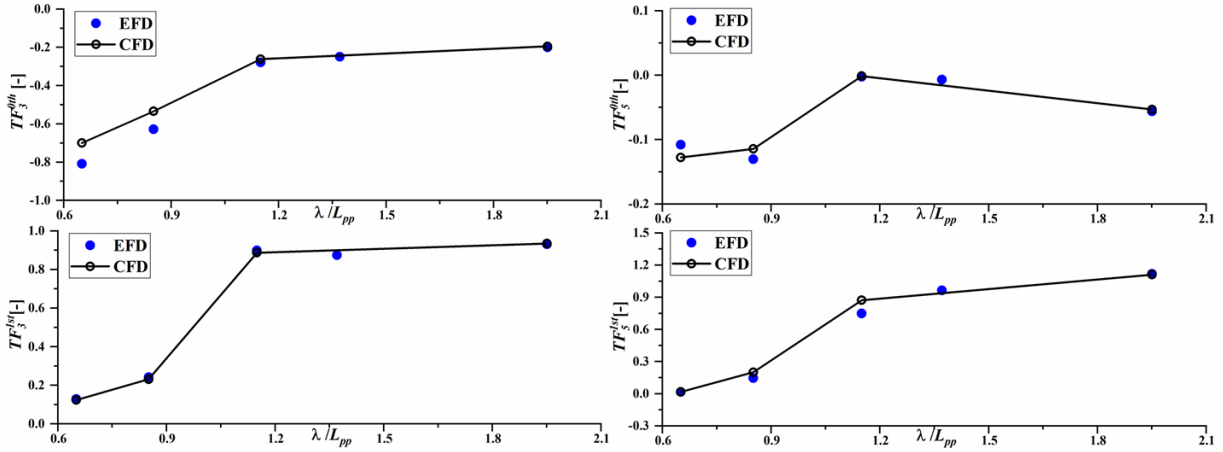


**Fig. 4** Comparison between CFD and EFD of 0<sup>th</sup>/1<sup>st</sup> heave/pitch transfer function  $TF_3/TF_5$ .

Fig.4 shows the comparison of 0<sup>th</sup>/1<sup>st</sup> heave and pitch transfer functions between CFD and EFD where good agreements are achieved. The peaks can be observed near  $\lambda/L_{pp}=1.15$  which can be explained by resonance. Resonance takes place when the encounter frequency of waves  $f_e$  equals, or is close to, the natural frequency of the ship  $f_n$ . The natural heave and pitch frequencies were close to  $f_n = 0.763 \text{ Hz}$  for KCS with scale ratios 1:37.89 according to the calculation of Simonsen et al. (2013). The encounter frequencies are  $f_n = 1.140, 0.941, 0.762$  and  $0.534 \text{ Hz}$  corresponding to  $\lambda/L_{pp}=0.65, 0.85, 1.15, 1.95$  calculated by  $f_e = \sqrt{g/(2\pi\lambda)} + U_0/\lambda$ . As a result, the peaks of ship motions and added resistance will occur when  $f_e \cong f_n = 0.763 \text{ Hz}$ , which is consistent with the simulation results.

## 4.2 Self-propulsion computations in Head Waves

As seen in Fig.5, motion variations using MOUM and DPM have been compared each other. The sea-keeping performance using MOUM is under-/over-predicted ~3% to DPM, so MOUM is applicable for sea-keeping performance prediction of self-propelled ships. PI control method is used to match the propeller rotating speed where the target velocity is 2.017m/s. Propeller rotation speed and ship speed for KCS self-propulsion simulations in head waves are shown in Fig.6.

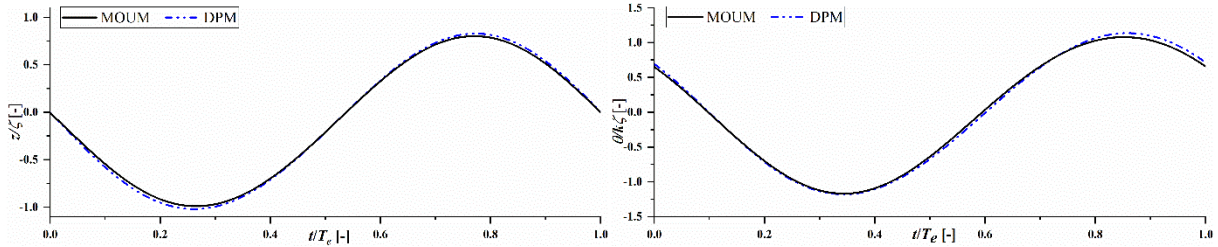


**Fig. 5** Heave and pitch variations using MOUM and DPM at an encounter period of waves.

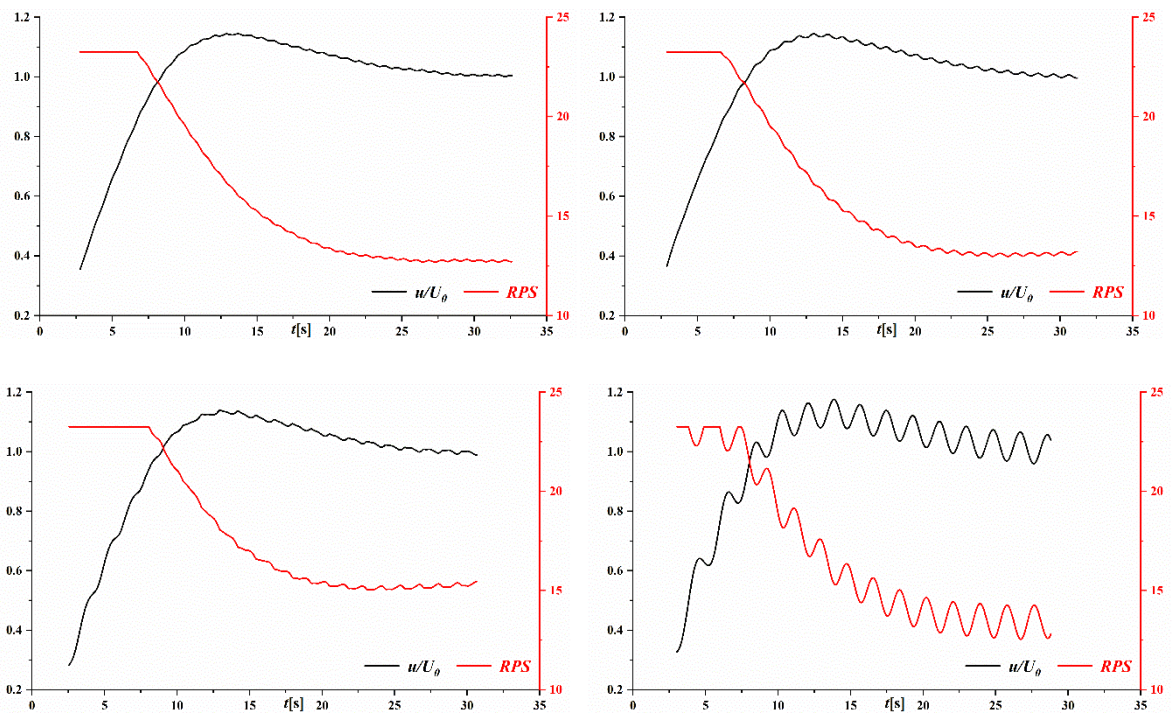


**Fig. 6** Propeller rotation speed and ship speed for KCS self-propulsion simulations in head waves.

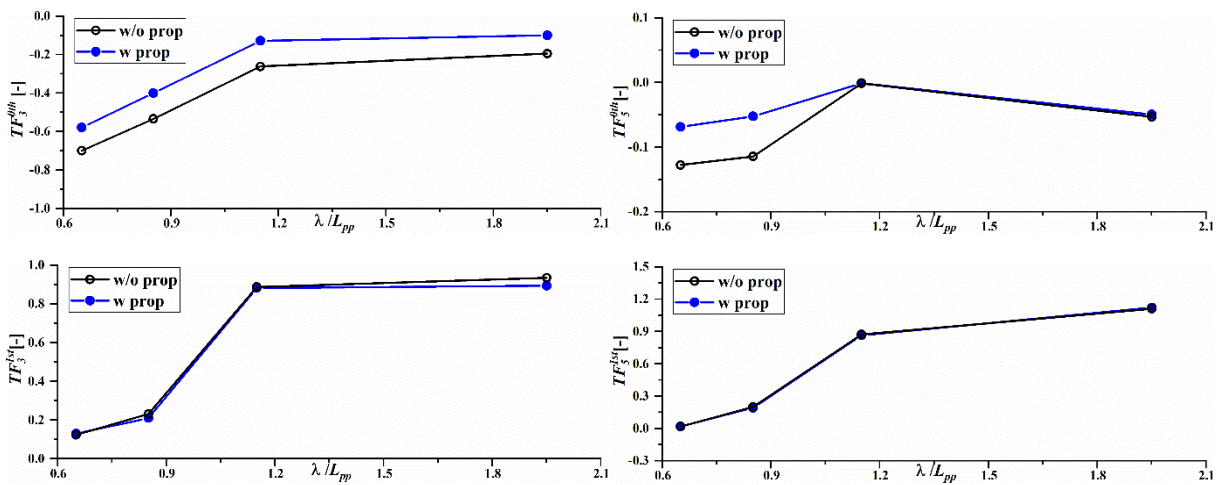


**Fig. 7** Comparison between w and w/o prop of 0<sup>th</sup>/1<sup>st</sup> heave/pitch transfer function  $TF_3/TF_5$ .



Ship motions using MOUM in all wave conditions for self-propelled KCS are shown in Figs.7. It can be found in Fig.7 that the amplitudes of ship motions for self-propelled KCS in head waves are reduced compared with the motions of towing tests, but all the differences are less than 5%. The mean values of pitch and heave are increased, and the differences are more than 20%. Therefore, the propeller has almost no effect on the amplitudes of ship motions and it is reasonable to predict the motion responses using towing tests.

## 5. CONCLUSIONS

In the present study, URANS simulations were carried out to determine the KCS self-propulsion performance in waves using inhouse CFD code. We discussed how it is different from the towing tests when self-propulsion simulations were used for ship motion response prediction in head waves. It can be concluded that the propeller has almost no effect on the amplitudes of ship motions (the differences are less than 5%) and it is reasonable to predict the motion responses using towing tests.

## REFERENCES

- Burg, C.O.E., 2005. Single-phase level set simulations for unstructured incompressible flows. 17th AIAA Computational Fluid Dynamics Conference, June 6, 2005 - June 9, 2005. Toronto, ON, Canada: American Institute of Aeronautics and Astronautics Inc.
- Carrica, P.M., Castro, A.M., Stern, F., 2010. Self-Propulsion Computations Using a Speed Controller and a Discretized Propeller with Dynamic Overset Grids. *Journal of Marine Science and Technology*. 15(4), 316-330.
- Feng, D., Yu, J., He, R., Zhang, Z. and Wang, X., 2020a. Improved body force propulsion model for ship propeller simulation. *Applied Ocean Research*. 104, 102328.
- Feng, D., Yu, J., He, R., Zhang, Z. and Wang, X., 2020b. Free running computations of KCS with different propulsion models. *Ocean Engineering*. 214, 107563.
- Li, T., Yan, C., 2005. Investigation of automatic generation technique for two-dimensional DRAGON grid. *Acta Aerodynamica Sinica*, 23(1):88-92.
- Menter, F.R., 1994. Two-Equation Eddy-Viscosity Turbulence Models for Engineering Applications. *Aiaa Journal*. 32(8), 1598-1605.
- Simonsen, C.D., Otzen, J.F., Joncquez, S., Stern, F., 2013. EFD and CFD for KCS Heaving and Pitching in Regular Head Waves. *Journal of Marine Science and Technology*. 18(4), 435-459.
- Tokyo 2015 CFD Workshop organizers. Tokyo 2015 CFD Workshop website. [https://t2015.nmri.go.jp/Instructions\\_KCS/Case\\_2.7/Case\\_2-7.html](https://t2015.nmri.go.jp/Instructions_KCS/Case_2.7/Case_2-7.html).
- Wang, X., Liu, L., Zhang, Z., Feng, D., 2020. Numerical Study of the Stern Flap Effect On Catamaran' Seakeeping Characteristic in Regular Head Waves. *Ocean Engineering*. 206, 107172.
- Zhang, Z., Guo, L., Wei, P., Wang, X., Feng, D., 2020. Numerical Simulation of Submarine Surfacing Motion in Regular Waves. *Iranian Journal of Science and Technology, Transactions of Mechanical Engineering*. 44(2), 359-372.
- Zhang, L., Zhang, J., Shang, Y., 2021. A Practical Direct URANS CFD Approach for the Speed Loss and Propulsion Performance Evaluation in Short-Crested Irregular Head Waves. *Ocean Engineering*. 219, 108287.

# Evaluating the effects of drift angle on the self-propelled ship using Blade Element Momentum Theory

Yifu Zhang\*, Dominic Hudson\*, Björn Windén†, Stephen Turnock\*

\*Maritime Engineering Research Group, University of Southampton, UK

†SHORTCUt CFD LLC, College Station, Texas, USA

Corresponding email: yz26g15@soton.ac.uk

## 1 Introduction

Ship maneuverability is one of the most essential performance indicators in the ship design process. Common practice for predicting a ship's maneuvering characteristics and force derivatives includes theoretical methods, towing tank tests and numerical approaches via Computational Fluid Dynamics (CFD). Theoretical methods are mainly applicable to slender bodies and the interactions between the hull, the propeller and the rudder are usually not considered. In a towing tank test, forces and moments on the model ship can be measured in static and dynamic Planar Motion Mechanism (PMM) tests or Circular Motion Test (CMT) (Islam and Soares, 2018). However, conducting maneuvering tests in a towing tank or wave basin requires more accurate test facilities and ship models, which are very costly. Although traditional experimental tests in a conventional towing tank plays a significant role in evaluating ship's maneuvering performance, with rapid development in high performance computers and numerical techniques, CFD tools provides researchers with a more efficient and economic method to compute ship maneuvering characteristics on more complex and realistic ship geometries.

Carrica et al.(2013) conducted model and full-scale CFD computations of a surface combatant undergoing turning circle and zig-zag maneuvers using a simplified body force propeller model and adopted an overset grid approach to capture the ship motions and rudder movement. The URANS code CFDShip-Iowa was used for simulations and results agreed well with experimental data. Sigmund and el Moctar (2017) applied a sliding mesh approach to compute the complex hull-propeller-rudder interaction and predicted free running ship behavior in waves. This demonstrates the capability of numerical method in simulating ship maneuvering performance. More recently, Sanada et al. (2021) investigated the hull-propeller-rudder interactions of the KRISO Container Ship (KCS) with the aim of providing a physical explanation for the differences between the port and starboard turning circles using a combined experimental and CFD method. Although numerical methods can, in principle, provide an adequate description of all physics, this kind of analysis is still considered as state-of-art research rather than engineering practice (Zhang et al., 2017). On the one hand, large computational resources and long CPU time are required in numerical approaches. On the other hand, according to Skejic (2013), many technical difficulties concerning the analysis of ship maneuvering in realistic seaway are still not solved, such as the accuracy of the selected turbulence model, the adequacy of the propeller and rudder models under large angles of attack, the appearance of the crossflow shed vortices and more.

Therefore, this paper aims to study the self-propelled KCS at a series of fixed drift angles, which represent different stages of a maneuver. This is done instead of studying the complete time varying maneuver. This kind of modelling not only significantly reduces the computational cost but also helps to guide future experimental measurements of rudder and propeller forces. Detailed results and discussion on the influence of a series of drift angles on resistance, wake velocity contours, side force and yaw moment will be presented. All simulations are conducted in calm water condition using the open source RANS solver simpleFoam which is part of OpenFOAM v7.

## 2 Methodology

### 2.1 Numerical model

The flow is modelled using the Reynolds Averaged Navier-Stokes equations. With the assumption of an incompressible fluid, the set of equations can be written in the form:

$$\frac{\partial \bar{U}_i}{\partial x_i} = 0 \quad (1)$$

$$\frac{\partial \bar{U}_i}{\partial t} + \frac{\partial \bar{U}_j \bar{U}_i}{\partial x_j} = -\frac{1}{\rho} \frac{\partial \bar{P}}{\partial x_i} + \frac{\partial}{\partial x_j} \left( \nu \left( \frac{\partial \bar{U}_i}{\partial x_j} + \frac{\partial \bar{U}_j}{\partial x_i} \right) \right) - \frac{\partial \overline{u'_i u'_j}}{\partial x_j} + \bar{f}_i \quad (2)$$

Where  $x_i$  represents the Cartesian coordinates (X, Y, Z) and  $\bar{U}_i$  are the Cartesian mean velocity components ( $\bar{U}_x, \bar{U}_y, \bar{U}_z$ ). The Reynolds stress is expressed as  $\overline{u'_i u'_j}$  and must be modelled using an appropriate turbulence model. The SST k- $\omega$  turbulence model is adopted to achieve turbulence closure. The SST k- $\omega$  model has previously been successfully used for wakefield analysis and hull-propeller-rudder interaction (Larsson et al., 2015). Pressure-velocity coupling is obtained by using the SIMPLE algorithm. Only the underwater body of the KCS hull is included and a symmetry plane boundary condition is enforced at the still water plane to emulate a double model flow. Discretisation of the convection terms are achieved using a Gauss linear second order upwind scheme and the diffusion terms are resolved using the central difference scheme.

## 2.2 Propeller model

To reduce the computational cost in the self-propelled calculations, propeller modelling using a body force model is used. This eliminates the need to mesh the propeller geometry. This means that the momentum generated by the rotating blades is directly inserted in the Navier-Stokes equation as an extra momentum source term or body force. Considering the momentum equation in Cartesian coordinates, the flow  $\bar{u} = (u, v, w)$  is accelerated by the body force  $\bar{F}_{\bar{v}} = (F_{vx}, F_{vy}, F_{vz})$ . This force is only non-zero where the propeller is acting on the fluid.

$$\frac{\partial(\rho u)}{\partial t} + \nabla \cdot (\rho u \bar{u}) = -\frac{\partial p}{\partial x} + \frac{\partial \tau_{xx}}{\partial x} + \frac{\partial \tau_{yx}}{\partial y} + \frac{\partial \tau_{zx}}{\partial z} + \rho F_{vx} \quad (3)$$

$$\frac{\partial(\rho v)}{\partial t} + \nabla \cdot (\rho v \bar{u}) = -\frac{\partial p}{\partial y} + \frac{\partial \tau_{xy}}{\partial x} + \frac{\partial \tau_{yy}}{\partial y} + \frac{\partial \tau_{zy}}{\partial z} + \rho F_{vy} \quad (4)$$

$$\frac{\partial(\rho w)}{\partial t} + \nabla \cdot (\rho w \bar{u}) = -\frac{\partial p}{\partial z} + \frac{\partial \tau_{xz}}{\partial x} + \frac{\partial \tau_{yz}}{\partial y} + \frac{\partial \tau_{zz}}{\partial z} + \rho F_{vz} \quad (5)$$

There are various methods to compute the distribution of this force  $\bar{F}_{\bar{v}}$ , how it relates to the propeller geometry and how it is affected by the propeller inflow. A range of models with various levels of complexity exist; from a simple actuator disk where the force is spread over the radius according to an ideal distribution, to a full panel code for the propeller where the force is obtained from the pressure on each panel.

In this paper, Blade Element Momentum theory (BEMt) is used to model the propeller. Blade Element Momentum theory combines axial momentum theory and 2D blade element theory, which was first suggested by Burrill (1944). The theory is suitable for calculations on marine propellers close to the design working condition. It is based on the lift and drag generated by an airfoil with the angle of attack being determined by the local pitch and the incidence of the incoming velocity. This is obtained by the rotation of the propeller as well as the characteristics of the nominal wake (Windén, 2014). The coupling between blade element and momentum theory is achieved by equating their two estimates of efficiency. BEMt also requires the lift and drag properties of the blade section to be known *a priori*. Here,  $C_L$  is estimated from the force balance of thrust in the previous iteration and  $C_D$  is obtained by curve fitting to an experimentally measured  $C_D - \alpha$  curve. The implementation of the BEMt in this paper follows the procedure by Molland et al. (2017). Such a coupling of RANS and BEMt has been successfully achieved in predicting ship hydrodynamic performance and hull-propeller-rudder interaction (Phillips et al., 2010; Windén, 2014; Badoe, 2015). Likewise, BEMt has been proved to be an accurate and cost-effective method for evaluation of maneuvering coefficients of a self-propelled ship (Phillips et al., 2009).

## 3 Computational implementations

The model ship used in this research for simulation is the KRISO Container Ship (KCS), which is a benchmark case for determining the flow around a modern container ship. Experimental data regarding

the self propulsion performance of the KCS was released as part of the Tokyo 2015 workshop on numerical hydrodynamics (Hino et al., 2020).

Table 1: Calculation conditions of KCS

Property	Model Scale	Full Scale
Lpp	7.2786m	230m
Fn(Lpp)	0.260 (2.196m/s)	0.260 (24kn)
Wetted surface area	9.4379 m <sup>2</sup>	9424 m <sup>2</sup>
Propeller		
Diameter	0.25m	7.9m
No. Blades	5	5
Rotation direction	Clockwise	Clockwise

Table 2: Total mesh sizes for cases with different drift angles

Drift Angle $\beta$ (°)	Total Mesh Size
0	11.1M
5	13.8M
10	17.0M
15	20.3M
20	19.7M

The OpenFOAM utilities blockMesh and snappyHexMesh are used to generate the mesh. For each simulation, the first 1000 iterations are conducted as a bare hull resistance test using simpleFoam. Another 1000 iterations are then conducted as a self propulsion test, with BEMt propeller model, using the custom solver selfPropSimpleFoam, which is part of the SHORTCUt open source framework for ship performance analysis (Winden, 2021). Five cases are simulated in calm water condition, with drift angles of  $\beta = 0^\circ, 5^\circ, 10^\circ, 15^\circ, 20^\circ$  respectively. In all cases, Lpp is set to 1. Fig 1 shows the computational domain. The inlet is located  $2.5L_{pp}$  from the bow; the outlet is  $5L_{pp}$  from the stern; the side and the bottom are both  $1.5L_{pp}$  from the hull surface.

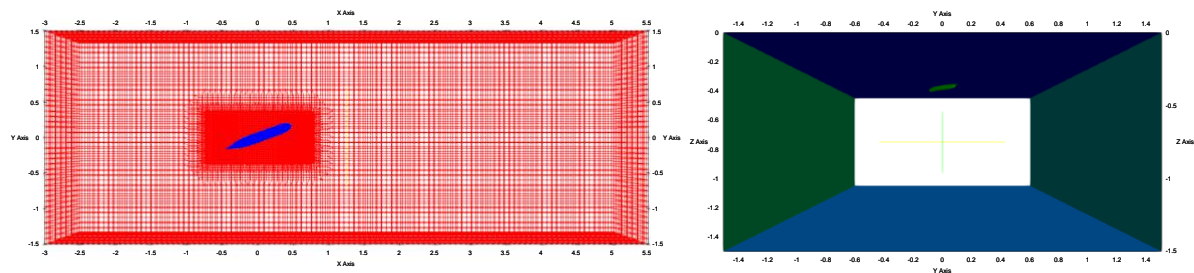


Fig. 1: Computational domain: top view and rear view

## 4 Results and discussion

### 4.1 Resistance coefficients and side force, yaw moment

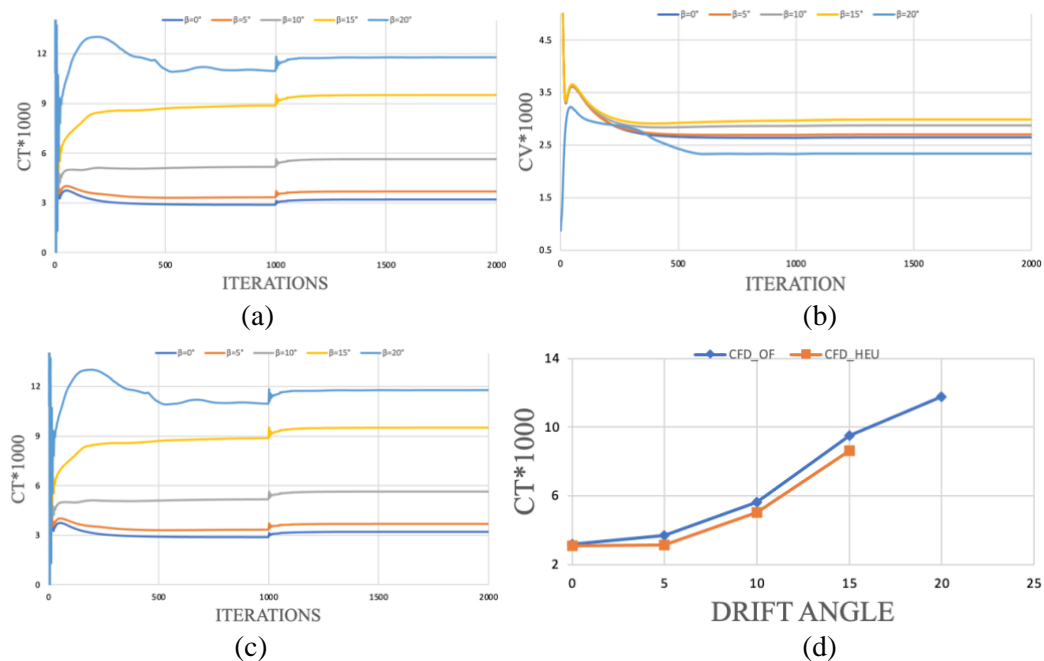


Fig 2: Resistance coefficients of KCS for different drift angles  $\beta$ .

As shown in Fig 2 (c), with the increase in static drift angle, the total resistance coefficient for the ship also increases. In terms of the viscous resistance component Fig 2 (b), it increases slightly with increasing drift angle ranging from 0° to 15°, and the value of viscous resistance coefficient is 0.00275. However, when the drift angle increases to 20°, the viscous resistance coefficient reduces to about 0.0024. The trend of pressure resistance and total resistance is very similar once the value of the viscous resistance converges after about 500 iterations. The addition of propeller forcing does not significantly change the value of the viscous resistance component. Experimental data for the drag force is not available, comparisons have been made with other simulation results seen in Fig 2 (d) (Sun et al., 2018), with which good agreement can be found. The difference is due to the fact that Sun et al. (2018) measured the different wetted surface areas for each drift angle while the constant experimental value of wetted surface is used in the current study.

Side force and yaw moment on the hull are calculated and both values are non-dimensionalised as shown below. To validate the accuracy of the results, two sets of experimental data and one set of numerical results are used, these are presented by Kim et al.(2015) and Islam and Guedes Soares (2018).

$$F'_Y = \frac{f_y(N)}{\rho \times U^2 \times L_{pp}^2} \text{ and } M'_Z = \frac{m_z}{\rho \times U^2 \times L_{pp}^3} \quad (6)$$

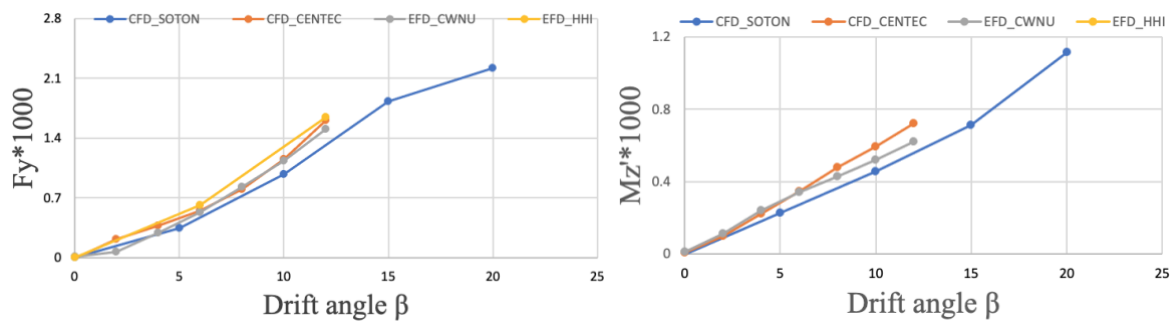


Fig 3: Non-dimensional sideforce and yaw moment experienced by KCS for different drift angles  $\beta$

As shown in Fig 3, the simulations can capture the trend of side force and yaw moment. Two sets of experimental data display slight disagreement with each other, which could be due to different scales of the ship models and test facilities used. The current results, derived from OpenFOAM, show both a slightly lower side force and yaw moment compared to the other results. But the trend is similar, and deviation is less than 10%. The reason for that difference could be the absence of the free surface effect in current study. Overall, the simulations indicate that, with increasing static drift angle, the lateral force and yaw moment encountered by the KCS model increases.

#### 4.2 Axial velocity contours and pressure distribution

The axial flow contour behind the propeller of the KCS was presented as part of the benchmarking data in the 2015 Tokyo workshop. This is compared with that calculated by the BEMt model below.

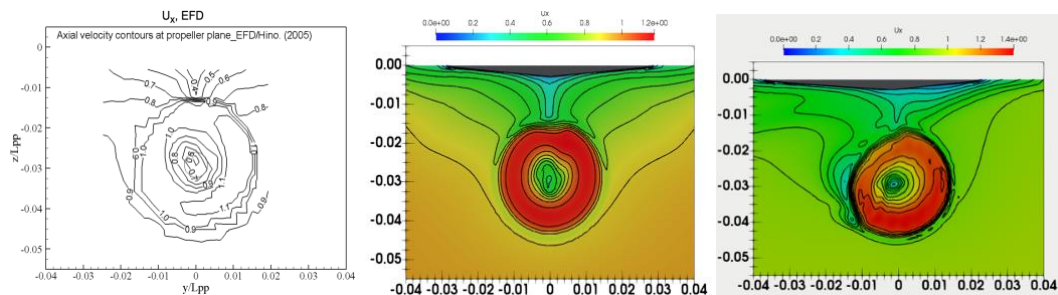


Fig 4: Local axial flow ( $U_x$ ) at  $x/L_{pp}=0.4911$ . Middle:  $\beta = 0^\circ$ , Right:  $\beta = 10^\circ$

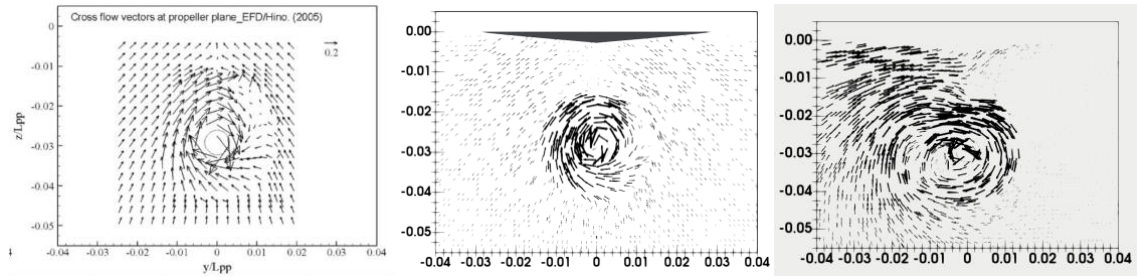


Fig 5: Cross flow vectors at  $x/L_{pp}=0.4911$ . Middle:  $\beta = 0^\circ$ , Right:  $\beta = 10^\circ$

Because of the addition of the angular momentum term, the dominant velocity component can be seen at the left-hand side of the graph in both experimental and numerical results. When the drift angle of  $10^\circ$  is applied, the asymmetric wake profile is more evident. This indicates that results obtained from BEMt are quite promising.

Fig 6 shows the pressure distribution on the surface of the KCS bow at different drift angles. As can be seen, in drift motions, the maximum pressure peak is encountered by the front of the bow. With the increase in drift angle, pressure encountered by the KCS model also increases and the pressure peak shifts to the side.

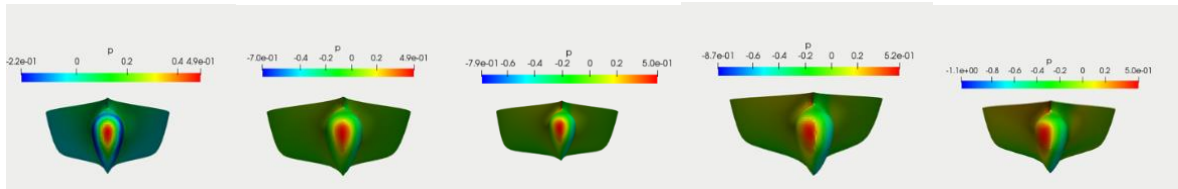


Fig 6: Hydrodynamic pressure distribution at bow of KCS at  $0^\circ, 5^\circ, 10^\circ, 15^\circ, 20^\circ$  drift angle.

### 4.3 Self-propulsion coefficients

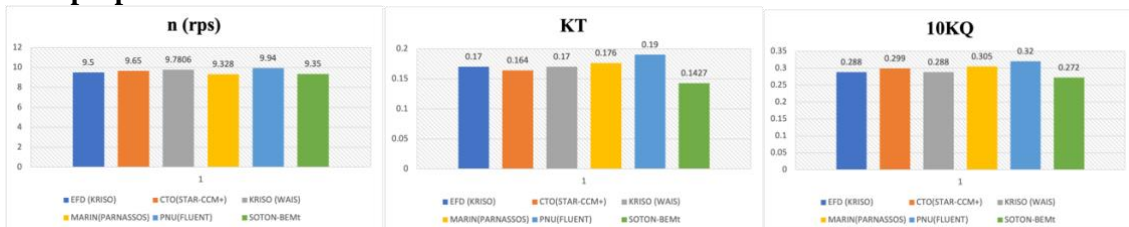


Fig 7: Comparison of estimated RPM for self propulsion and propulsion coefficients of KCS at  $\beta=0^\circ$ .

There were only four submissions to the 2015 Tokyo workshop which presented results for a calculated self propulsion point of the KCS. The results in the current study are shown together with the submission that vary the RPM in Fig7. The results obtained by RANS-BEMt coupling method fares slightly less well against that of other institutions. This is likely due to the increased importance of the free surface effect for the KCS; in terms of the pressure distribution on the hull and the propeller. Fig 8 shows the variation of KT and 10KQ value with the increase of the drift angle.

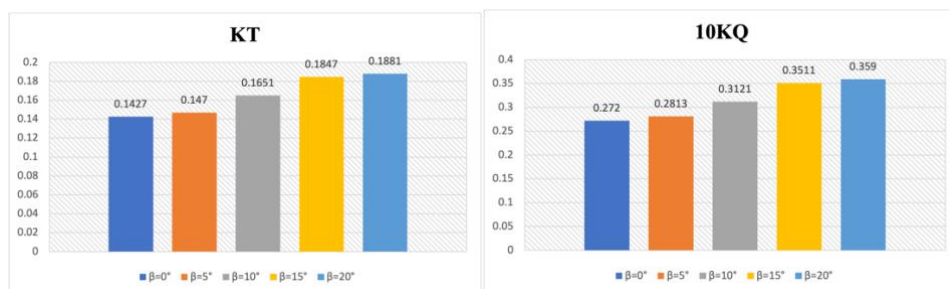


Fig 8: KT and 10KQ values for different drift angles.

## 5 Conclusion and future work

This paper presents simulations of the KCS model at different static drift angles in calm water. The results, including resistance, lateral force, yaw moment, axial velocity, pressure distribution and self-propulsion coefficients, show good agreement with experimental data. It is concluded that OpenFOAM is capable of performing maneuverability related calculations with reasonable accuracy and computational cost. The BEMt can capture the hydrodynamic performance of a ship in static drifting condition. Further investigations will include the simulation of a hull in different waves condition with drifting and the detailed influence of drift angle on hull-propeller-rudder interaction in real seaways.

## References

- Badoe, C.E., 2015. Design practice for the stern hull of a future twin-skeg ship using a high fidelity numerical approach. University of Southampton. <https://doi.org/10.1109/fie.2016.7757408>
- Burrill, L., 1944. Calculation of marine propeller performance characteristics. *Trans. NECIES*. 60.
- Carrica, P.M., Ismail, F., Hyman, M., Bhushan, S., Stern, F., 2013. Turn and zigzag maneuvers of a surface combatant using a URANS approach with dynamic overset grids. *J. Mar. Sci. Technol.* 18. <https://doi.org/10.1007/s00773-012-0196-8>
- Hino, T., Larsson, L., Stern, F., Visonneau, M., Hirata, N., Kim, J., 2020. *Numerical Ship Hydrodynamics: An Assessment of the Tokyo 2015 Workshop*. Springer.
- Islam, H., Guedes Soares, C., 2018. Estimation of hydrodynamic derivatives of a container ship using PMM simulation in OpenFOAM. *Ocean Eng.* 164. <https://doi.org/10.1016/j.oceaneng.2018.06.063>
- Islam, H., Soares, C.G., 2018. A CFD study of a ship moving with constant drift angle in calm water and waves, in: *Progress in Maritime Technology and Engineering - Proceedings of the 4th International Conference on Maritime Technology and Engineering, MARTECH 2018*. <https://doi.org/10.1201/9780429505294-22>
- Kim, H., Akimoto, H., Islam, H., 2015. Estimation of the hydrodynamic derivatives by RANS simulation of planar motion mechanism test. *Ocean Eng.* 108. <https://doi.org/10.1016/j.oceaneng.2015.08.010>
- Larsson, L., Stern, F., Visonneau, M., Hino, T., Hirata, N., Kim, J., 2015. *Proceedings, Tokyo 2015 Workshop on CFD in Ship Hydrodynamics*, in: *Tokyo CFD Workshop*.
- Molland, A.F., Turnock, S.R., Hudson, D.A., 2017. Ship resistance and propulsion, Marine Propellers and Propulsion. <https://doi.org/10.1016/B978-075068150-6/50014-0>
- Phillips, A.B., Turnock, S.R., Furlong, M., 2010. Accurate capture of propeller-rudder interaction using a coupled blade element momentum-RANS approach. *Sh. Technol. Res.* 57. <https://doi.org/10.1179/str.2010.57.2.005>
- Phillips, A.B., Turnock, S.R., Furlong, M., 2009. Evaluation of manoeuvring coefficients of a self-propelled ship using a blade element momentum propeller model coupled to a Reynolds averaged Navier Stokes flow solver. *Ocean Eng.* 36. <https://doi.org/10.1016/j.oceaneng.2009.07.019>
- Sanada, Y., Park, S., Kim, D.H., Wang, Z., Stern, F., 2021. Experimental and CFD Study of KCS Hull-Propeller-Rudder Interaction for Steady Turning Circles 1–17.
- Sigmund, S., el Moctar, O., 2017. Numerical and experimental investigation of propulsion in waves. *Ocean Eng.* 144. <https://doi.org/10.1016/j.oceaneng.2017.08.016>
- Skejjic, R., 2013. Ships Maneuvering Simulations in a Seaway - How close are we to reality ? *Int. Work. Next Gener. Naut. Traffic Model.* 91–101.
- Sun, S., Li, L., Wang, C., Zhang, H., 2018. Numerical prediction analysis of propeller exciting force for hull-propeller-rudder system in oblique flow. *Int. J. Nav. Archit. Ocean Eng.* 10. <https://doi.org/10.1016/j.ijnaoe.2017.03.005>
- Windén, B., 2021. *An Open-Source Framework for Ship Performance CFD*. <https://doi.org/10.5957/tos-2021-22>
- Windén, B., 2014. *Powering Performance of a Self Propelled Ship in Waves*. University of Southampton.
- Zhang, W., Zou, Z.J., Deng, D.H., 2017. A study on prediction of ship maneuvering in regular waves. *Ocean Eng.* 137. <https://doi.org/10.1016/j.oceaneng.2017.03.046>